


Spring 2016

Energy harvesting using photovoltaic and betavoltaic devices

Ashish Sharma

Follow this and additional works at: <https://digitalcommons.latech.edu/dissertations>

 Part of the [Electrical and Computer Engineering Commons](#), and the [Nanoscience and Nanotechnology Commons](#)

**ENERGY HARVESTING USING PHOTOVOLTAIC AND
BETAVOLTAIC DEVICES**

by

Ashish Sharma, B.Eng., M.S.

**A Dissertation Presented in Partial Fulfillment
of the Requirements of the Degree of
Doctor of Philosophy**

**COLLEGE OF ENGINEERING AND SCIENCE
LOUISIANA TECH UNIVERSITY**

May 2016

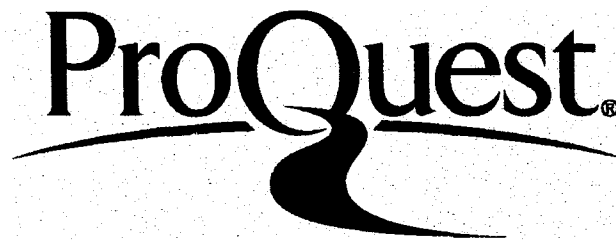
ProQuest Number: 10301363

All rights reserved

INFORMATION TO ALL USERS

The quality of this reproduction is dependent upon the quality of the copy submitted.

In the unlikely event that the author did not send a complete manuscript and there are missing pages, these will be noted. Also, if material had to be removed, a note will indicate the deletion.



ProQuest 10301363

Published by ProQuest LLC(2017). Copyright of the Dissertation is held by the Author.

All rights reserved.

This work is protected against unauthorized copying under Title 17, United States Code.
Microform Edition © ProQuest LLC.

ProQuest LLC
789 East Eisenhower Parkway
P.O. Box 1346
Ann Arbor, MI 48106-1346

LOUISIANA TECH UNIVERSITY
THE GRADUATE SCHOOL

MARCH 22, 2016
Date

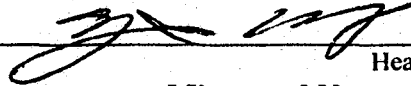
We hereby recommend that the Dissertation prepared under our supervision by
Ashish Sharma, B.Eng., M.S.

entitled Energy Harvesting Using Photovoltaic and
Betavoltaic Devices

be accepted in partial fulfillment of the requirements for the Degree of
Doctor of Philosophy in Engineering

Sandra Zivauovic

Supervisor of Dissertation Research

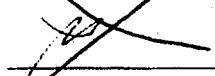


Head of Department

Micro and Nanoscale Systems

Department

Recommendation concurred in:

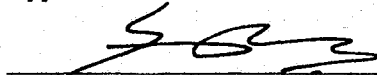
~~~~
Phil Rowe

Yuri Lvov


Richard Weis

Advisory Committee

Approved:


Director of Graduate Studies

Approved:


Dean of the Graduate School

Muhammad Megahed / SD
Dean of the College

ABSTRACT

There is an important need for improvement in both cost and efficiency of photovoltaic cells. For improved efficiency, a better understanding of solar cell performance is required. An analytical model of thin-film silicon solar cell, which can provide an intuitive understanding of the effect of illumination on its charge carriers and electric current, is proposed. The separate cases of homogeneous and inhomogeneous charge carrier generation rates across the device are investigated. This model also provides for the study of the charge carrier transport within the quasi-neutral and depletion regions of the device, which is of an importance for thin-film solar cells. Two boundary conditions, one based on a fixed charge carrier surface recombination velocities at the electrodes and another based on intrinsic conditions for large size devices are explored. The device's short circuit current and open circuit voltage are found to increase with a decrease of surface recombination velocity at the electrodes. The power conversion efficiency of thin film solar cells is observed to depend strongly on impurity doping concentrations. The developed analytical model can be used to optimize the design and performance of thin-film solar cells without involving highly complicated numerical codes to solve the corresponding drift-diffusion equations.

The third generation polymer photovoltaic solar cells, the first generation includes monocrystalline silicon solar cells and second generation being thin-film solar cells, and photodetectors are researched widely in the last few years due to their low device

processing cost, mechanical flexibility, and lightweight. Organic photovoltaic materials such as poly(3-hexylthiophene):[6,6]-phenyl-C61-butyric acid methyl ester (P3HT:PCBM) blend are usually cheaper than inorganic materials, but have a limitation of lower power conversion efficiency (*PCE*) than their inorganic (for example, Si) counterparts. These organic devices need to be optimized to achieve the maximum possible *PCE*. One way to do this is to achieve the optimal thickness of the optically active layer of P3HT:PCBM while fabricating these organic photovoltaic devices. The influence of the active layer's thickness of P3HT:PCBM blend on performance of polymer solar cells and photodetectors are experimentally investigated. The fabricated device structure is glass/ITO/PEDOT:PSS/P3HT:PCBM/Al, where ITO is the indium tin oxide, and PEDOT:PSS stands for poly(3,4-ethylenedioxythiophene):poly(styrenesulfonate) used as a buffer layer to collect holes effectively at the ITO anode. Aluminum is used as a cathode. Chlorobenzene is used as a solvent to prepare the polymer-fullerene blend. Spin coating technique was utilized to deposit the active layer and the concentration of P3HT, PCBM, and spin-coating speeds were varied to achieve a wide range of the active layer's thicknesses from 20 nm to 345 nm. The *PCE* of solar cell devices and the external quantum efficiency (*EQE*) of the photodetectors are found to increase with the thickness of the active layer. The maximum *PCE* of 1.09% is obtained for the active layer's thickness of 345 nm.

The ongoing advanced space exploration requires the novel energy sources that can generate power for extreme duration without need of refill. The need for such extreme-duration lightweight power sources for space and terrestrial applications motivates the study and development of polymer-based betavoltaic devices. The

betavoltaic devices based on the semiconductive polymer-fullerene blend of P3HT:ICBA, where ICBA is indene-C₆₀ bisadduct, are demonstrated here for the first time. Both direct and indirect energy conversion methods were explored. For the indirect conversion method, a scintillator intermediate layer of cerium-doped yttrium aluminum garnet (Ce:YAG) was used. A high open circuit voltage of 0.56 V has been achieved in the betavoltaic device fabricated on polyethylene terephthalate (PET) substrate with the indirect energy conversion method at 30 keV electron kinetic energy. The directional and external interaction losses are significantly reduced using thin PET substrates. The maximum output electrical power of 62 nW was achieved at 30 keV input electron beam energy. The highest betavoltaic *PCE* of 0.78% was achieved at 10 keV of electron beam energy.

The performance of two different scintillators, Ce:YAG and Thallium doped Cesium Iodide (CsI:Tl), were compared in the indirect conversion betavoltaic devices experimentally and the interaction of electron beam with Ce:YAG and CsI:Tl was studied using Monte Carlo simulations. The catholuminescence profiles from simulation showed that CsI:Tl is more-efficient to generate photons when hit by electron beam compared to Ce:YAG, which is further verified experimentally with 20% *PCE* enhancement using CsI:Tl at 30 kV e-beam compared to betavoltaic devices with Ce:YAG. The directional loss in the indirect conversion devices is further reduced by applying thin reflecting aluminum film on top of the scintillator. The *PCE* increased by 26.7% with 30 nm thin aluminum film on top of Ce:YAG scintillator at 30 keV electron beam energy. The experimental results showed that the output electrical power from betavoltaic devices increased with the increase in incident electron beam energy.

APPROVAL FOR SCHOLARLY DISSEMINATION

The author grants to the Prescott Memorial Library of Louisiana Tech University the right to reproduce, by appropriate methods, upon request, any or all portions of this Dissertation. It is understood that "proper request" consists of the agreement, on the part of the requesting party, that said reproduction is for his personal use and that subsequent reproduction will not occur without written approval of the author of this Dissertation. Further, any portions of the Dissertation used in books, papers, and other works must be appropriately referenced to this Dissertation.

Finally, the author of this Dissertation reserves the right to publish freely, in the literature, at any time, any or all portions of this Dissertation.

Author

A. Smith

Date

4/20/2016

DEDICATION

To my mother, Mrs. Mohan Maya Sharma Bohara; father, Mr. Parmanand Sharma Bohara; wife, Mrs. Aruna Shah; sister, Mrs. Bhawana Sharma Bohara and brother, Mr. Nishant Sharma, and all science lovers.

TABLE OF CONTENTS

ABSTRACT.....	iii
DEDICATION.....	vii
LIST OF TABLES.....	xii
LIST OF FIGURES.....	xiv
ACKNOWLEDGEMENTS.....	xxi
CHAPTER 1 INTRODUCTION.....	1
1.1 Motivation.....	1
1.2 Objectives and Outline.....	4
CHAPTER 2 ANALYTICAL MODEL OF THIN-FILM SILICON SOLAR CELLS.....	6
2.1 Introduction.....	6
2.2 Background.....	10
2.2.1 Inorganic Photovoltaic.....	11
2.2.2 Solar Cell Characterization and Parameters.....	15
2.3 Device Architecture.....	18
2.4 Analytical Modeling.....	19
2.4.1 Ambipolar Transport Equations.....	19
2.4.2 Intrinsic Boundary Condition for Thick Devices.....	20
2.4.3 Surface Recombination Boundary Condition.....	20
2.4.4 Homogeneous Generation.....	21
2.4.4.1 Solution in QNR.....	22
2.4.4.2 Solution in DR.....	23
2.4.4.3 Current Calculation.....	27

2.4.5	Inhomogeneous Generation	32
2.5	Results and Discussion.....	36
2.5.1	Surface Plasmon Enhanced Thin-Film Silicon Solar Cell.....	44
2.6	Conclusions.....	48
CHAPTER 3 POLYMER SOLAR CELLS AND PHOTODETECTORS.....		50
3.1	Introduction	50
3.2	Background	54
3.2.1	Conjugated Polymers.....	54
3.2.2	Fullerene Derivatives.....	56
3.2.3	Polymer Solar Cells	58
3.2.4	Polymer Photodetectors	61
3.2.5	General Device Characterization and Parameters.....	62
3.2.5.1	Solar Cell.....	62
3.2.5.2	Photodetector.....	62
3.3	Experimental Methods	63
3.3.1	Fabrication	63
3.3.2	Test Setup	71
3.3.2.1	Solar Cell Testing.....	71
3.3.2.2	Photodetector Testing.....	72
3.4	Results and Discussion.....	74
3.4.1	Imaging of Surface Morphology of P3HT:PCBM Film.....	74
3.4.2	Optical Characterization	75
3.4.3	Thickness Measurement	79
3.4.4	Solar Cell Electrical Characterization.....	79
3.4.4.1	Effect of Active Layer Thickness on Short Circuit Current.....	81
3.4.4.2	Effect of Active Layer Thickness on Open Circuit Voltage	82
3.4.4.3	Effect of Active Layer Thickness on Resistance.....	83
3.4.4.4	Effect of Active Layer Thickness on FF and PCE	84
3.4.5	Photodetector Electrical Characterization	85
3.4.5.1	Effect of Bias Voltage on EQE.....	87

3.4.5.2	Effect of Active Layer Thickness on EQE	90
3.4.6	P3HT:ICBA Solar Cells with Silver Nanoparticles.....	91
3.5	Conclusions	97
CHAPTER 4 POLYMER BETAVOLTAIC DEVICES		99
4.1	Introduction	99
4.2	Background	103
4.2.1	Betavoltaic	103
4.2.2	Organic Betavoltaic	105
4.2.3	Betavoltaic Characterization and Parameters	106
4.2.4	Beta Sources	107
4.3	Direct Conversion Betavoltaic	109
4.3.1	Device Architecture	109
4.3.2	Fabrication	110
4.3.3	Test Setup	115
4.3.3.1	Optical Characterization	115
4.3.3.2	Input E-Beam Power	115
4.3.3.3	Betavoltaic Testing	116
4.3.3.4	Raman Spectroscopy	117
4.3.4	Results and Discussion	118
4.4	Indirect Conversion Betavoltaic.....	124
4.4.1	Device Architecture	124
4.4.2	Scintillator for Indirect Conversion Betavoltaic.....	125
4.4.3	Test Setup	127
4.4.4	Fabrication	127
4.4.4.1	Scintillator Deposition.....	127
4.4.5	Results and Discussion	128
4.4.5.1	Comparison of Ce:YAG and CsI:Tl Scintillators.....	136
4.4.5.1.1	Monte-Carlo Simulations of Ce:YAG and CsI:Tl.....	136
4.4.5.1.2	Experimental Results.....	139
4.4.5.2	Role of Thin Reflecting Film on Scintillator.....	143

4.4.5.2.1	Monte-Carlo Simulations with Al Thin-Film on Scintillator	146
4.4.5.2.2	Experimental Results	149
4.5	Conclusion.....	155
CHAPTER 5 CONCLUSIONS AND FUTURE RECOMMENDATIONS		157
5.1	Conclusions.....	157
5.2	Future Recommendations.....	159
APPENDIX A KEITHLEY INSTRUMENTS SPECIFICATIONS.....		161
APPENDIX B MEASUREMENT ERROR CALCULATION.....		163
B.1	Solar Cell.....	164
B.2	Betavoltaic Device	164
BIBLIOGRAPHY		166

LIST OF TABLES

Table 2-1: Numerical parameters and properties of mC-Si used in model [59].....	25
Table 3-1: Fabrication parameters for solar cells and photodetectors.	69
Table 3-2: Solar cell characteristics for different P3HT:PCBM active layer's thickness.....	81
Table 3-3: Fabrication parameters of P3HT:ICBA solar cells with Ag nanoparticles. ...	93
Table 3-4: Solar cell parameters for benchmark (BM) and surface plasmon (SP) devices.	95
Table 4-1: Various beta sources and their properties [128], [143]–[145].....	108
Table 4-2: Fabrication parameters for direct conversion betavoltaic devices.	119
Table 4-3: Fabrication parameters for indirect conversion betavoltaic devices.	130
Table 4-4: Input e-beam current, accelerating voltage, e-beam power and <i>PCE</i> for indirect conversion G devices.	131
Table 4-5: Fabrication parameters for G, P, PP indirect conversion betavoltaic devices.	133
Table 4-6: Different betavoltaic device parameters of indirect conversion G, P and PP devices.	135
Table 4-7: Fabrication parameters for indirect conversion betavoltaic devices with Ce:YAG and CsI:Tl scintillators.....	140
Table 4-8: Electron beam and betavoltaic device parameters obtained when tested with Ce:YAG and CsI:Tl scintillators.	142
Table 4-9: Fabrication parameters for indirect conversion betavoltaic devices with Al thin-film on top of Ce:YAG scintillator.	150

Table 4-10: Accelerating voltage, e-beam current and e-beam power used to test indirect conversion betavoltaic devices with and without aluminum reflecting film on top of Ce:YAG scintillator.....	152
Table 4-11: <i>PCE</i> and other betavoltaic device parameters with and without thin aluminum reflecting film on top of Ce:YAG scintillator.....	152
Table A-1: Keithley 2400 sourcemeter voltage measurement accuracy (local or remote) [168].	162
Table A-2: Keithley 2400 sourcemeter current measurement accuracy (local or remote) [168].	162
Table A-3: Keithley 6487 picoammeter specifications [169].....	162

LIST OF FIGURES

Figure 1-1: The EIA global energy consumption projection by 2040 [1].	1
Figure 1-2: Global carbon emission trend [4].	2
Figure 2-1: Solar spectral power density with AM0 and AM1.5 solar radiations [41]. ..	11
Figure 2-2: Physics of p-n junction solar cell.	12
Figure 2-3: Maximum <i>PCE</i> of the solar cell for the black body spectrum at 6000 K, the AM0 and AM1.5 solar radiation spectra as a function of bandgap energy of absorber layer limited by spectral mismatch [49].	13
Figure 2-4: Absorption coefficient for different types of silicon as a function of photon energy [50].	14
Figure 2-5: Market share of different inorganic photovoltaic technologies in 2014 [51].	15
Figure 2-6: Progress of various photovoltaic technologies [9].	15
Figure 2-7: Typical <i>J-V</i> and <i>P-V</i> characteristics of a solar cell.	16
Figure 2-8: Device architecture of p-n junction solar cell for the analytical model.	18
Figure 2-9: Electron and hole concentration profiles at the homogenous generation rate of $10^{24} \text{ m}^{-3}\text{s}^{-1}$ for a) zero bias, b) forward, and c) reverse bias.	26
Figure 2-10: <i>J-V</i> characteristics of a p-n junction silicon solar cell for constant generation rates of $10^{24} \text{ m}^{-3}\text{s}^{-1}$, $5 \times 10^{24} \text{ m}^{-3}\text{s}^{-1}$ and $10^{25} \text{ m}^{-3}\text{s}^{-1}$	28
Figure 2-11: a) <i>J-V</i> characteristics, and b) <i>P-V</i> characteristics of silicon solar cell for surface recombination (SR) and intrinsic boundary (IB) conditions for homogeneous generation under AM1.5 solar irradiation with 100 mW/cm^2 power density.	31
Figure 2-12: (a) Refractive index and extinction coefficients of c-Si, and (b) Transmittance and Reflectance for c-Si-Air interface.	33

Figure 2-13: Spectral generation rate for inhomogeneous generation under AM1.5 solar irradiance of 100 mW/cm² optical power density.....	34
Figure 2-14: a) <i>J-V</i> characteristics and b) <i>P-V</i> characteristics of silicon solar cell for intrinsic (IB) and surface recombination (SR) boundary conditions with inhomogeneous generation rate under AM1.5 (100 mW/cm²) solar irradiation plotted against experimental data by Tsuno <i>et al.</i> [60].....	36
Figure 2-15: Short circuit current density for intrinsic and surface recombination boundary conditions in the case of inhomogeneous generation for various surface recombination velocities.	38
Figure 2-16: The <i>J-V</i> characteristics for different surface recombination velocities for inhomogeneous generation and surface recombination boundary condition.	39
Figure 2-17: <i>EQE</i> for intrinsic and surface recombination boundary conditions with inhomogeneous generation at zero bias.	40
Figure 2-18: The optimal current for various front and back layers thicknesses of thin film solar cell.	41
Figure 2-19: The <i>J-V</i> characteristics for different minority carrier lifetimes, monocrystalline Si (37.2 μs) [66], poly-crystalline Si (3.68 μs) [66], amorphous Si(11.29 μs) [66], GaN (6.5 ns) [67], In_{0.14}Ga_{0.86}As (110 ns) [68].	42
Figure 2-20: The <i>J-V</i> characteristics of PN junction silicon solar cell for various donor impurity concentrations N_d for a) $N_d = 10^{26} \text{ m}^{-3}$, and b) $N_d = 10^{22} \text{ m}^{-3}$.....	43
Figure 2-21: The <i>J-V</i> characteristics of PN junction silicon solar cell for various acceptor impurity concentrations N_a for a) $N_a = 10^{26} \text{ m}^{-3}$, and b) $N_a = 10^{22} \text{ m}^{-3}$.....	44
Figure 2-22: Schematic of the glass/ITO/MDC/Si/ZnO/Al based surface plasmon enhanced thin-film silicon solar cell.	45
Figure 2-23: Optical efficiency of glass/ITO/MDC/Si/ZnO/Al solar cell as a function of the silicon active layer's thickness and metal concentration in 20 nm MDC layer.	46
Figure 2-24: Optimal <i>PCE</i> of glass/ITO/ MDC/Si/ZnO/Al surface plasmon enhanced solar cell as a function of the silicon active layer's thickness and metal concentration in 20 nm MDC.	48
Figure 3-1: The molecular structure of P3HT (left) [83] and PCBM (right) [84].	52

Figure 3-2: The wide range of conductivity of conjugated polymers from insulator to conductor [106].	54
Figure 3-3: Common conjugated polymers [107].	56
Figure 3-4: Different fullerene derivatives with LUMO and HOMO energy levels used in organic solar cells and photodetectors [109].	57
Figure 3-5: The electrical power generation process in polymer solar cell following photon absorption, exciton pair generation, exciton pair dissociation, and carrier collection.	59
Figure 3-6: Three device architectures of polymer solar cells, a) planar heterojunction, b) checkerboard type architecture, and c) bulk heterojunction architecture.	60
Figure 3-7: Equivalent circuit model of photodetector [111].	61
Figure 3-8: Glass/ITO/PEDOT:PSS/P3HT:PCBM/Al device cross section and charge generation and separation when illuminated with light (left) and molecular formula of PEDOT:PSS (right).	64
Figure 3-9: Energy level diagram of ITO/PEDOT:PSS/P3HT:PCBM/Al solar cell [80].	65
Figure 3-10: Shared anode transparency mask for photolithography to pattern ITO on glass substrate (left), and stainless steel shadow mask to define cathode regions (right).	66
Figure 3-11: P3HT:PCBM active layer thickness, versus spin coating speed with concentration processing solution of both P3HT and PCBM in chlorobenzene as a parameter.	69
Figure 3-12: The step-by-step fabrication process of photovoltaic stack with P3HT:PCBM active layer.	70
Figure 3-13: The top view of six polymer devices on a single substrate and cross section of a single device (left), and ready to test device (right).	71
Figure 3-14: Schematic of the solar cell testing setup.	72
Figure 3-15: Schematic of the photodetector testing setup.	73

- Figure 3-16:** a) Optical microscope image of P3HT:PCBM thin film surface at 100x magnification, b) Optical microscope image of the interface of P3HT:PCBM film and aluminum cathode at 20x magnification, c) Top view of SEM image of P3HT:PCBM blend layer under SEM, and d) Cross-section of PET/ITO/PEDOT:PSS/P3HT:PCBM/Al film under SEM..... 74
- Figure 3-17:** a) Transmittance, and b) Absorbance spectra of various thicknesses of P3HT:PCBM thin-films on a quartz substrate, c) Transmittance, reflectance and absorbance of quartz substrate measured with Filmetrics F10-RT reflectometer. 77
- Figure 3-18:** Optical constants of P3HT:PCBM blend of various thicknesses, a) refractive index (n), b) extinction coefficient (k), c) absorption coefficient (α) calculated from extinction coefficient, and d) absorption coefficient (α) calculated from transmittance. 78
- Figure 3-19:** a) J - V characteristics, and b) P - V characteristics of polymer solar cells for different P3HT:PCBM active layer's thicknesses..... 80
- Figure 3-20:** Short circuit current density (J_{SC}) and open circuit voltage (V_{OC}) of P3HT:PCBM polymer solar cells for various active layer's thicknesses. 82
- Figure 3-21:** Series and shunt resistance for various active layer thicknesses of fabricated P3HT:PCBM polymer solar cells. 83
- Figure 3-22:** Power conversion efficiency (PCE) and fill-factor (FF) of P3HT:PCBM heterojunction polymer solar cells for various active layer thicknesses... 85
- Figure 3-23:** Optical power density of the 100 W tungsten halogen white light source of monochromator used in photodetector testing measured with the calibrated silicon photodiode (Newport 818-UV) and power meter (Newport 1936-R)..... 86
- Figure 3-24:** a) Spectral photocurrent density of photodetectors at reverse bias voltage of -4 V, and b) J - V characteristics of each device measured with solar simulator, with various P3HT:PCBM active layer thicknesses. 87
- Figure 3-25:** External quantum efficiency (EQE) of a) 330 nm, b) 230 nm and c) 37 nm thick P3HT:PCBM active layers of photodetector at various reverse bias voltages. 89
- Figure 3-26:** External quantum efficiency (EQE) of polymer photodetectors for various active layer thicknesses at reverse bias voltage of -4 V..... 90

Figure 3-27: External quantum efficiency (<i>EQE</i>) and responsivity of P3HT:PCBM polymer photodetectors for various active layer thicknesses at reverse bias voltage of -4 V for 580 nm wavelength.	91
Figure 3-28: The SEM images of Ag nanoparticles sputtered on the ITO coated glass substrates, a) 5 nm Ag before annealing, b) 5 nm Ag after annealing at 300°C for 1 hour, c) nucleated nanoparticle with small particles attached to the sides, and d) 13 nm Ag after annealing at 300°C for 1 hour. The beam voltage of SEM was set to 3 kV and the working distance was 5 mm.	92
Figure 3-29: a) Transmittance profiles of 5 nm, 6 nm and 13 nm annealed Ag thin-films on ITO coated glass substrate and without Ag thin-film, and b) transmittance, reflectance and absorbance of a 355 nm thick P3HT:ICBA film on a quartz substrate. ..	94
Figure 3-30: <i>J-V</i> characteristics of benchmark (BM) devices compared with surface plasmon (SP) devices with a) 5 nm Ag, b) 6 nm Ag, and c) 13 nm Ag layers.	96
Figure 4-1: Basic device architecture and operation of betavoltaic device.	104
Figure 4-2: Indirect conversion device architecture of organic betavoltaic device with intermediate scintillator layer.	106
Figure 4-3: Direct conversion polymer-fullerene heterostructure betavoltaic device architecture.	110
Figure 4-4: The step-by-step fabrication process of photovoltaic stack with P3HT:ICBA active layer.	114
Figure 4-5: The top view of six polymer devices on a single substrate and cross section of a single device (left), and ready to test device with scintillator screen (right).	114
Figure 4-6: The SEM image of Faraday cup (left) and the zoomed view of central hole of Faraday cup (right) used to measure e-beam power from AMRAY 1830 SEM.	116
Figure 4-7: SEM images of betavoltaic devices under testing.	117
Figure 4-8: Schematic of betavoltaic device testing setup using AMRAY 1830 SEM.	117
Figure 4-9: <i>I-V</i> characteristics of glass/ITO/PEDOT:PSS/P3HT:ICBA/Al, direct conversion betavoltaic devices for electron kinetic energies of 5, 8, 9, and 10 keV.	119

- Figure 4-10:** *I-V* characteristics of direct conversion polymer betavoltaic devices with a) 225 nm, b) 180 nm, or c) 55 nm thick P3HT:ICBA active layer measured in different time intervals under direct exposure of 10 keV e-beam. The e-beam current from the SEM was 69 pA. 121
- Figure 4-11:** Raman spectrum of a) 160 nm, and b) 120 nm, P3HT:ICBA thin-films with and without e-beam exposure. The samples were exposed under 20 kV e-beam for 15 minutes inside AMRAY 1830 SEM. 123
- Figure 4-12:** Indirect conversion polymer-fullerene heterostructure betavoltaic device architecture. 125
- Figure 4-13:** The absorption spectrum of 260 nm thick P3HT:ICBA blend on a quartz substrate, the emission spectrum of Ce:YAG and CsI:Tl scintillators. The emission spectrum of CsI:Tl is obtained from Phosphor Technology Ltd. [159]. 126
- Figure 4-14:** Ce:YAG scintillator screen deposition on quartz substrate using sedimentation process. 128
- Figure 4-15:** Optical characteristics of the 160 nm thick P3HT:ICBA 1:1 wt. thin film on a quartz substrate. 129
- Figure 4-16:** *I-V* characteristics of indirect conversion betavoltaic G devices (polymer device on glass substrate and scintillator on quartz) for 7 kV (low current 27 pA, high current 158 pA) and 10 kV (low current 60 pA, high current 300 pA). 130
- Figure 4-17:** Betavoltaic *PCE* at different e-beam powers of G devices (polymer device on glass substrate and scintillator on quartz). 131
- Figure 4-18:** *I-V* characteristics of indirect conversion betavoltaic devices: a) G device, b) P device, c) PP device in dark (i.e. no e-beam) and for 10, 20 and 30 keV e-beams. 134
- Figure 4-19:** The 30 keV electron beam trajectories of 10,000 electrons in (a) Ce:YAG and (b) CsI:Tl obtained from CASINO Monte Carlo simulations. 137
- Figure 4-20:** The Catholuminescence intensity profile of Ce:YAG and CsI:Tl scintillators for 30 keV electron kinetic energy obtained from CASINO Monte Carlo simulations. 138
- Figure 4-21:** The optical characteristics of the 260 nm thick P3HT:ICBA (1:1 wt.) thin film on a quartz substrate obtained from Filmetrics F10-RT reflectometer. 139

- Figure 4-22:** The betavoltaic I - V characteristics compared with Ce:YAG and CsI:Tl scintillators at (a) 10 kV, (b) 20 kV and (c) 30 kV e-beam accelerated voltage. 141
- Figure 4-23:** Cross section of indirect conversion betavoltaic device without thin reflecting film on top of the scintillator to study the directional loss. 144
- Figure 4-24:** Cross section of indirect conversion betavoltaic device with a 30 nm aluminum thin reflecting film on top of the scintillator to study the directional loss. 146
- Figure 4-25:** Catholuminescence intensity profiles of Al/Ce:YAG/PET device architecture for 10 kV, 20 kV and 30 kV accelerating voltages obtained from CASINO Monte-Carlo simulations. 147
- Figure 4-26:** Cross-sectional view of absorbed e-beam energy in Al/Ce:YAG/PET device architecture for a) 10 kV, b) 20 kV, and c) 30 kV accelerating voltages. 148
- Figure 4-27:** a) Ce:YAG film, b) Ce:YAG with a 10 nm aluminum film, and c) Ce:YAG with a 30 nm aluminum film. 149
- Figure 4-28:** Transmittance, reflectance and absorbance of 235 nm P3HT:ICBA film on a quartz substrate. 149
- Figure 4-29:** Betavoltaic I - V characteristics with and without Al reflecting layer on Ce:YAG scintillator for a) 10 kV, b) 20 kV, and c) 30 kV accelerating voltages. 151
- Figure 4-30:** Power conversions in indirect conversion betavoltaic devices and overall efficiency calculation. 153

ACKNOWLEDGEMENTS

I would like to thank my research advisor, Dr. Sandra R. Zivanovic, for her continuous support and guidance throughout my PhD study and providing me opportunity to work on such an interesting and state-of-art technology for my PhD research. It would not have been possible without her strong belief in me, and her valuable suggestions and understanding. My sincere gratitude goes to my co-advisor, Dr. Dentcho A. Genov, for helping in building my program solving skills. I would like to thank the members of my advisory committee, Dr. Leland Weiss, Dr. Yuri Lvov and Dr. Niel Crews, for providing support in making this research possible and motivating me throughout my graduate career to keep up the good work. I would like to thank Dr. Adarsh Radadia for assisting me on Raman spectroscopy.

I would like to take this opportunity to thank Dr. Alfred Gunasekaran, Mr. Davis Bailey, Ms. Debbie Wood and other IfM staff member for providing training in various instruments, helping with process development, suggesting alternate approaches, and taking care of IfM facilities so that I could run my experiments smoothly.

My thanks go to lab colleague, Justin M. Melancon, for acquainting me with the lab equipment, device fabrication process, and being there to help me every time. I would like to thank Dr. Gaurav Parekh, R&D Delivery Scientist II (Glanbia Nutritionals) for helping on FTIR (DRIFTS) spectroscopy and Shravan R. Animilli for helping with

device modeling. I would also like to thank Mir A. Galib, Tyler Sonsalla and Shelby Maddox for being fantastic lab mates.

Finally, I would like to thank my family and friends. I have no word to show my gratitude towards my family for unconditional love and support.

CHAPTER 1

INTRODUCTION

1.1 Motivation

There is a growing need for clean and sustainable energy due to population growth, industrialization, economic development, and expanding access to the electronic gadgets around the world. Energy information administration (EIA) predicted that the global energy consumption will increase by 56% in 2040 compared to 2010 as shown in **Figure 1-1** [1]. While the energy consumption is increasing day by day, currently a considerable percentage of the population in the world are out of reach of energy. In 2013, 1.2 billion people, about 17% of the world's population, did not have access to electricity [2]. Therefore, there is a big challenge to address the growing energy demands and the need of focused research on novel energy sources to fulfill these demands.

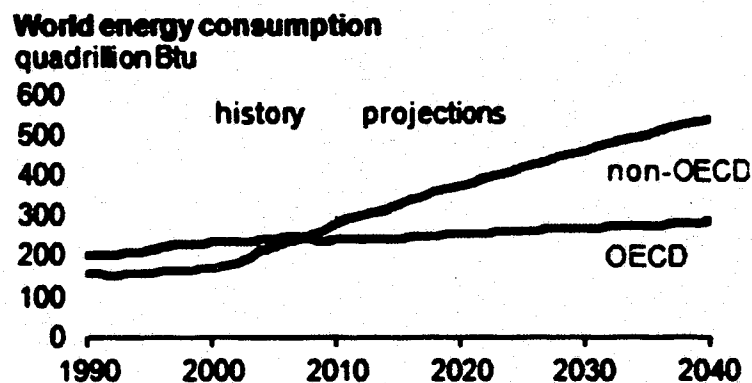


Figure 1-1: The EIA global energy consumption projection by 2040 [1].

The current primary source of energy is based on fossil fuels that are in limited supply and have negative environmental impact such as carbon emission, climate change and global warming. About 67% of the electricity generated in the USA in 2014 is from fossil fuels [3]. The carbon emission in 2013 was 61% over compared to 1990 as shown in Figure 1-2 [4]. As the energy demand increase the carbon emission increases accordingly.

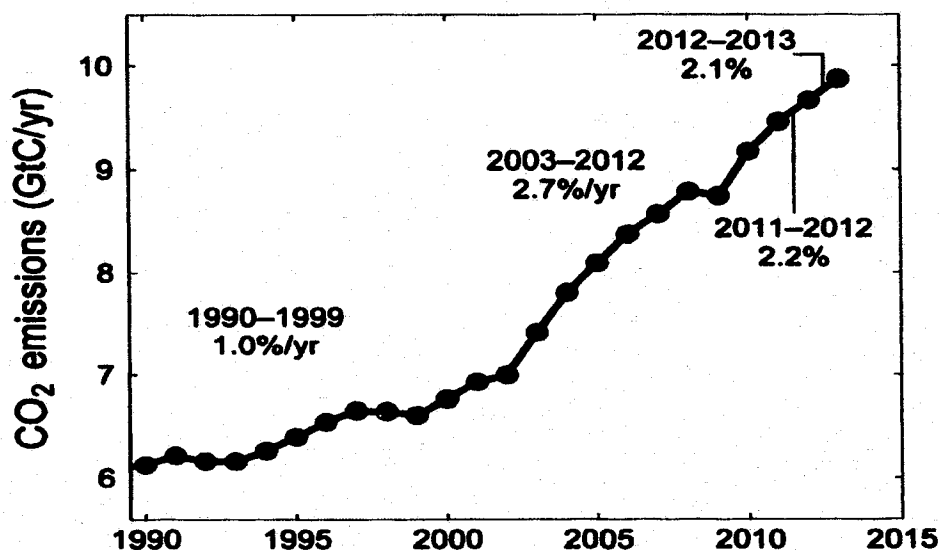


Figure 1-2: Global carbon emission trend [4].

Use of renewable energy sources such as solar, wind, etc. helps to fulfill the future energy demand and protects the environment from carbon emission resulting from burning fossil fuels. Harvesting of solar energy using photovoltaic solar cells is one of the clean and sustainable energy sources. These solar cells are virtually non-polluting with low operating cost and long duration power sources for terrestrial and space applications. At each moment, Earth receives $\sim 1.2 \times 10^{17}$ W of solar power while our total energy consumption is only $\sim 1.3 \times 10^{13}$ W [5]. A small portion of the solar energy is sufficient to fulfill the global energy demand. Another advantage of solar energy is its open access at

any location in the Earth's surface and is not limited by the transportation facilities, inter-country relationship, etc. On the other hand, the fossil fuels are only available at certain locations and require extensive transportation facilities to transfer from one place to another.

Despite the abundance of solar energy and large benefits of photovoltaic solar cells, the use of photovoltaic solar cells (usually Silicon based) is limited due to their high production cost and lower average efficiency. Scientists are working to reduce the production cost and increase efficiency of solar cells from the last few decades. One way to reduce the cost of silicon based inorganic solar cells is the development of less material consuming thin-film solar cells. However, the efficiency of solar cells also reduces while using a thin absorbing layer. The modeling approach can be used to understand the working principle of the device and optimize the device's parameters to achieve the highest possible efficiency for thin-film solar cells. Other efficiency enhancement schemes such as light trapping, surface plasmon, etc. can be used to further enhance the performance of thin-film solar cells.

Solar cells based on conjugated polymers are the other classes of solar cells made from low cost, lightweight and flexible semiconductive polymer materials with reduced fabrication cost. The efficiency is still below 12% for these polymer solar cells [6]. However, the discovery and applications of new conjugated polymers in recent research presented the polymer photovoltaic as a very promising field for solar energy harvesting.

Solar cells are required to be exposed to sunlight all the time to generate electricity. Under certain circumstances such as the shadow or dark regions, inside buildings, spaceships and outside the solar system, the use of solar cell is not viable.

Unlike the solar cells, betavoltaic devices are not affected by the weather such as clouds, snow, rain, etc. Betavoltaic devices that harvest kinetic energy of beta particles from radioisotopes into electricity can be the ideal candidates for long duration power sources for space and terrestrial applications.

1.2 Objectives and Outline

The main purpose of this research is to explore and study the thin-film photovoltaic solar cells (silicon or organic) and betavoltaic devices as an alternate source of clean energy to address the growing energy demand. The objectives of this research are:

1. To develop a generation dependent analytical model of thin-film silicon solar cell.
2. To study the role of the device's dimensions and other parameters of thin-film silicon solar cell such as doping concentration, carrier lifetime, surface recombination velocity, etc. on the device's performance.
3. To investigate the role of active layer thickness of P3HT:PCBM based polymer solar cells and photodetectors on the device's performance.
4. To provide the guidelines for fabricating polymer solar cells and photodetectors via process development.
5. To study the use of conjugated polymer in polymer betavoltaic devices.
6. To investigate the optical properties of phosphor material and semiconducting polymer to ensure the greatest possible efficiency of the betavoltaic devices.
7. To study the degradation of the conjugated polymer from exposure to beta sources.

8. To investigate the various loss mechanisms in betavoltaic devices and minimize them by modifying the device architecture to enhance performance.

This dissertation is divided into five chapters. Chapter 2 describes the analytical model of thin-film p-n junction silicon solar cells. First, the homogeneous generation rate is considered to compute and plot the carrier concentration profiles and current-voltage characteristics. Then, the more realistic inhomogeneous generation case is used to develop the model. In both cases, two boundary conditions, intrinsic and surface recombination boundary conditions, are studied.

Chapter 3 discusses the experimental optimization of the active layer thickness of P3HT:PCBM polymer solar cells and photodetectors. The role of P3HT:PCBM active layer thickness on optical properties, different solar cell parameters, such as short circuit current density, fill factor, power conversion efficiency, etc. and photodetector parameters, such as external quantum efficiency, etc. is investigated experimentally by fabricating and characterizing the polymer devices with various thickness.

Chapter 4 presents the design and development of P3HT:ICBA based polymer betavoltaic devices. Direct and indirect conversion betavoltaic devices were designed, fabricated and tested under various e-beam powers. The loss mechanism in betavoltaic devices were investigated and minimized. Different device modification schemes were utilized to further enhance the performance of the betavoltaic devices. Monte-Carlo simulations were utilized to study the interaction of high-energy e-beam with scintillators.

Finally, Chapter 5 provides the overall conclusion of the research work presented in this dissertation and future recommendations.

CHAPTER 2

ANALYTICAL MODEL OF THIN-FILM SILICON SOLAR CELLS

2.1 Introduction

The growing demand of energy with rapid population growth and economic development attracts the attention of the scientific community in the photovoltaic related research. The fossil fuel based energy sources provide about 80% of the total energy demand in our society [7]. These fossil fuels that are limited in supply cannot address future energy demands and also contribute to the 90% of greenhouse gas emission [7]. These competing trends demand the utilization of novel sources of energy such as solar, wind, etc. The photovoltaic solar cells have potential as a sustainable future global energy resource with pollution free environment. The photovoltaic solar cells have been used to harvest the solar energy into electricity and gone through substantial technical developments in the past few years [8]–[10]. The photovoltaic (PV) p-n junction solar cell is the main optoelectronic element used to harness the energy of the sun. Upon absorption of the photon, the exciton pair is formed within the PV cell, which dissociates almost instantaneously into free electrons and holes. The charge carriers then diffuse and drift under the influence of an internal electric field to the electrodes, and an electrical current can be released on a load. The silicon-based solar cells are still dominating the

photovoltaic industry due to its abundance existence, non-toxicity, high efficiency, long-term stability and well established technology [11]–[14].

Despite being a relatively well-developed technology, maximum efficiency of these silicon solar cells is still low. The highest *PCE* reported so far for crystalline silicon and thin-film amorphous silicon solar cells are below 26% and 11%, respectively [15]. Also, the cost of silicon solar cells is high due to its highly sophisticated production technology [16]. There are challenges on both the theoretical and experimental aspects of silicon-based solar cells to increase the *PCE* and decrease the production cost. Thin-film solar cells have been introduced in recent years due to its low cost [17]–[19]. These thin-film solar cells use less semiconductor material and can be cost effective [20] thus reducing the payback period to less than a year [21]. However, thin-film solar cells rely on a thin layer of absorbing material; hence, light management and device optimization are very crucial in this technology [22]–[24]. Different efficiency enhancement techniques based on light trapping and surface plasmon resonances has been proposed [13], [25]–[27]. Nanophotonic techniques [28], [29] are very effective for the light trapping since they provide flexibility to control the flow of light on the scale of several 100 nm to a few micrometers, which is best suited for thin-film solar cells [30].

To better understand the working mechanism of a solar cell, it is crucial to be able to model the behavior of the electrons and holes under different illumination and spatial conditions. An analytical model explicitly helps to study the critical parameters and working conditions that may lead to improved performance. It also provides insight regarding the dependencies of electrical current and *PCE* on various device parameters such as the device's thickness, minority carrier lifetime, impurity concentration, surface

recombination velocity of the charge carrier, etc. The dependency of short-circuit current in silicon solar cells on various device parameters is reported by Rostron [31]. The short-circuit current increases almost linearly with the minority carrier diffusion length but decreases with increase in surface recombination velocity, showing a surface region contribution up to 13% on the short-circuit current [31]. The thickness of the active layer has an important role in the device's performance, which is more dominant in thin-film solar cells as shown by McElheny *et al.* in their research [23]. Therefore, the solar cell device modeling has the advantage of investigating the critical issues and optimizing them before the manufacturing of high performing solar cells.

Computational time consuming numerical approaches have been used extensively to study the behavior of solar cell devices [32]–[39]. Ringhofer *et al.* have modified the Gummel method for iterative solution of the basic semiconductor device equation by approximating the Jacobian matrix to improve the convergence [33]. Significantly smaller growth rate of convergence with increased bias voltage was obtained compared with the Gummel method, and the quadratic convergence was demonstrated compared to the linear convergence of Gummel scheme for 0.6 V forward bias [33]. The finite-element approach has been applied to study the influence of various device parameters on performance of p-n junction solar cells, and the increase of *PCE* was reported with an increase in dopant concentration and a decrease of emitter width [39]. The increase in *PCE* was shown with a decrease in surface recombination velocity of the charge carriers at the surface, suggesting the materials with low surface recombination velocity must be used as electrodes for high performing solar cells [40].

Despite the accuracy offered by the numerical calculations of solar cell devices, they require more sophisticated software tools that need to be specifically modified for a particular device architecture [32], and they also require more computational time. The other major disadvantage of numerical calculations involving solar cell analysis is that they do not provide the explicit mathematical relationship between electrical current or *PCE* with various device parameters and illuminations conditions, and limit the understanding about the physical insight of the device's operation. In that case, the analytical modeling can provide the explicit analytical theory of solar cell device. Specifically, it provides the analytical expressions of total current density within the device that can explain the dependency of *PCE* on different device parameters such as the device's thickness, generation rate, surface recombination velocities, carrier lifetime, etc.

This chapter focuses on the analytical modeling of thin-film silicon solar cell for homogeneous and inhomogeneous generation rates. The concept of thin-film solar cell is introduced to reduce the cost per watt of photovoltaic power by reducing the thickness of the device. However, the traditional modeling approach of bulk solar cell does not provide the accuracy while applying a similar modeling approach to the thin-film solar cell. The more feasible boundary conditions must be applied while studying thin-film solar cells. Also, the thickness of the thin-film device and other critical parameters must be optimized to achieve maximum *PCE*. Here, two different boundary conditions, one based on surface recombination of the charge carrier at the electrode and another based on intrinsic boundary conditions are proposed. The analytical model describing the carrier transport in all regions of a p-n junction based device with analytical expressions of electron and hole carrier profiles is presented. In addition, the analytical expressions

for the generation dependent electrical current and *PCE* is developed. Moreover, the effect of the boundary conditions and various device parameters on the device's performance are explored.

2.2 Background

Photovoltaic is a process of generating electricity directly from electromagnetic (light, including infrared, visible, and ultraviolet) energy by the optoelectronic device called solar cell [42]. Photovoltaic effect is first discovered by Edmund Becquerel in 1839 [43] and has been through tremendous technological advancement in the last few decades [10] [44]–[48]. The underlying electronic process for the operation of solar cell is generation of free electron-hole pair upon the absorption of a photon. The sun generates a tremendous amount of light energy via nuclear fusion converting a huge amount of hydrogen into helium. Before it reaches the Earth's surface, the solar energy attenuates while passing through the atmosphere. The solar irradiance is represented in terms of air mass (AM) which accounts for attenuation, other losses in the Earth's atmosphere and global tilt. If θ is the angle of the sun to the zenith, the air mass is given by $AM = (\cos \theta)^{-1}$ [41]. The AM0 represents extraterrestrial spectrum of solar radiation outside the Earth's surface. The AM1.5 is the widely accepted standard solar irradiation on the Earth's surface with 1000 W/m^2 power density. The **Figure 2-1** shows the solar spectral power density for black body radiation at 6000 K, AM0 and AM1.5 solar radiations.

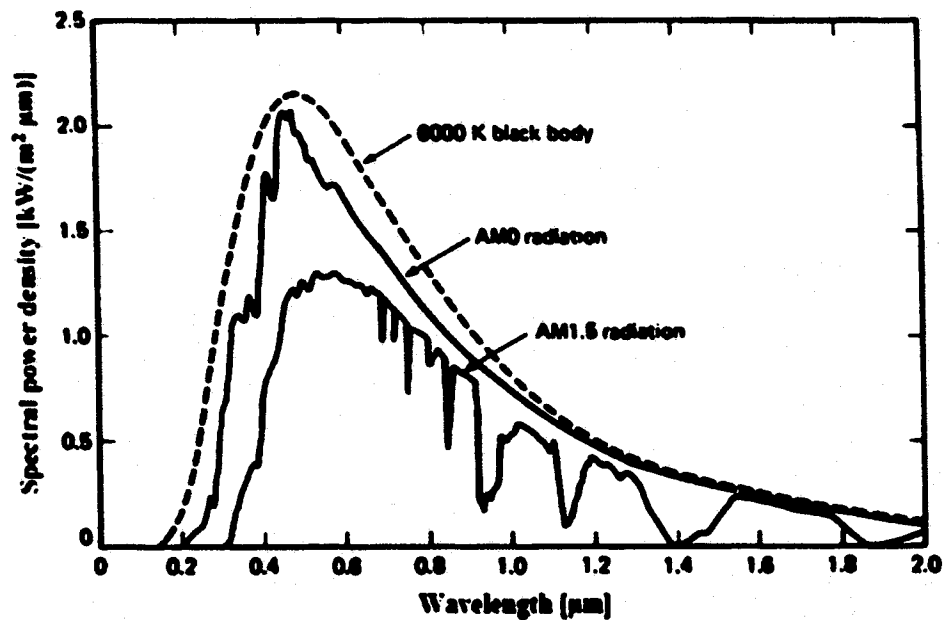


Figure 2-1: Solar spectral power density with AM0 and AM1.5 solar radiations [41].

2.2.1 Inorganic Photovoltaic

The crystalline silicon (c-Si) is the widely used inorganic semiconductor material for solar cell applications due to high *PCE*. The bandgap of c-Si is 1.1 eV [43]. The maximum *PCE* of c-Si solar cell is more than 25% [6]. The c-Si has proper order in atomic structure and minimum defects, which results in high mobility of charge carriers and minimum recombination loss. The **Figure 2-2** explains the generation of electrical power from p-n junction based solar cell, which is governed by four steps, absorption of photon, generation of free electron-hole pair, separation of electron and hole, and collection of electron and hole at the electrodes.

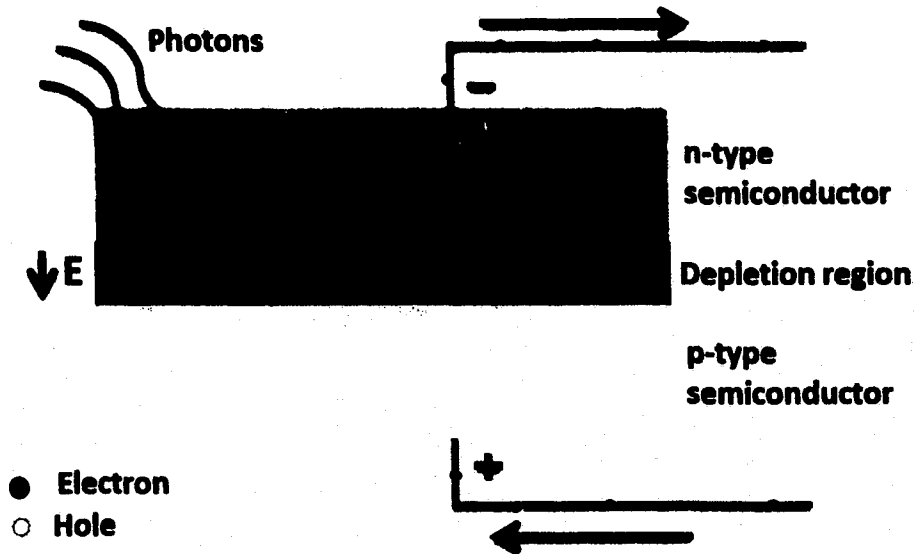


Figure 2-2: Physics of p-n junction solar cell.

If the photon of energy $E_{ph} \geq E_g$, where E_g is the bandgap energy, incidents on the solar cell, it gets absorbed and an electron-hole pair generates by the excitation of an electron from the valence band to the conduction band. Then the electron-hole pair dissociates instantaneously due to the thermal energy at room temperature. The electron and hole are then collected at cathode and anode, respectively, via diffusion and drift under the influence of the internal electric field at p-n junction. As the photon energy depends on the wavelength, $E_{ph} = hc/\lambda$, where h is Planck constant, c is the speed of light and λ is the wavelength of the photon, not all photons can generate an electron-hole pair. If the energy of the photon is less than the bandgap energy, it is not absorbed, and if it is higher than the bandgap energy, the excess energy is lost in thermalization. This photon energy mismatch with the bandgap energy of the solar cell material is the principal limitation of solar cell efficiency. **Figure 2-3** shows the maximum *PCE* as a function of bandgap energy of solar cell material [49].

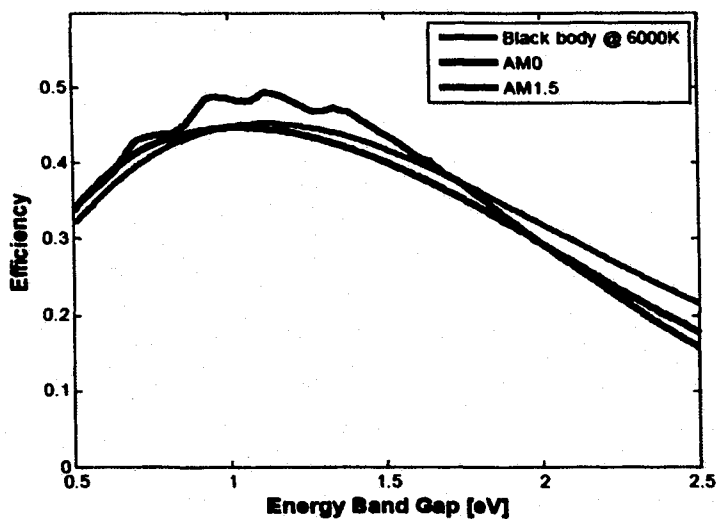


Figure 2-3: Maximum *PCE* of the solar cell for the black body spectrum at 6000 K, the AM0 and AM1.5 solar radiation spectra as a function of bandgap energy of absorber layer limited by spectral mismatch [49].

Despite the high efficiency of the crystalline silicon solar cells, the high production cost limits its application in wide range. The low cost production process such as evaporation and sputtering can be used to deposit pure silicon but with disordered atomic structure resulting in amorphous silicon. Amorphous silicon is a low cost material but has high defect density (10^{19} defects/cm³) due to the presence of dangling bonds [12]. However, the defects density can be significantly reduced to 10^{16} defects/cm³ by passivating with hydrogen in hydrogenated amorphous silicon (a-Si:H) [12]. The a-Si:H has a higher absorption coefficient in the visible range due to the presence of extended states in the forbidden gap or band gap, and only 1 μ m thick a-Si:H is enough to absorb 90% of the solar spectrum [50]. The a-Si:H has a bandgap of 1.7 eV [48]. **Figure 2-4** shows the absorption coefficient of the different types of silicon as a function of photon energy. Due to the presence of higher defects in a-Si:H, usually it is used in thin-film solar cells to ensure the efficient collection of photo-generated charge carriers, further reducing the cost of the solar cells. The a-Si:H also has low mobility of charge carriers,

so p-i-n type solar cells are used to extend the inter electric field and immediately separate electrons and holes to avoid recombination loss [12].

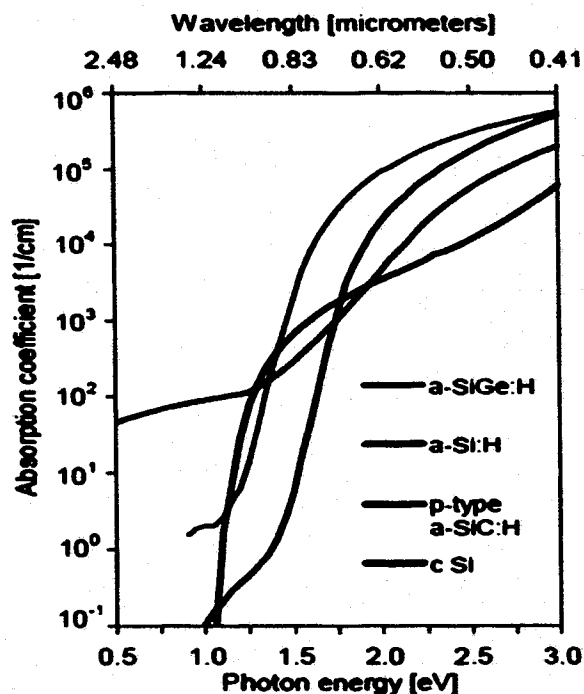


Figure 2-4: Absorption coefficient for different types of silicon as a function of photon energy [50].

Photovoltaic technologies based on other types of inorganic materials including cadmium telluride (CdTe) and cadmium sulphide (CdS), copper indium gallium diselenide (CIGS), etc. have been developed [44], [48]. The tandem and multi-junction solar cells implementing different semiconductor materials with different bandgap to absorb maximum optical power have been explored [52] [12]. Each of these technologies has its own benefits and limitations. **Figure 2-5** shows the market share of the different types of inorganic photovoltaic technologies in 2014 [51]. **Figure 2-6** shows the progress of various photovoltaic technologies and maximum efficiency achieved in each of these technologies [9].

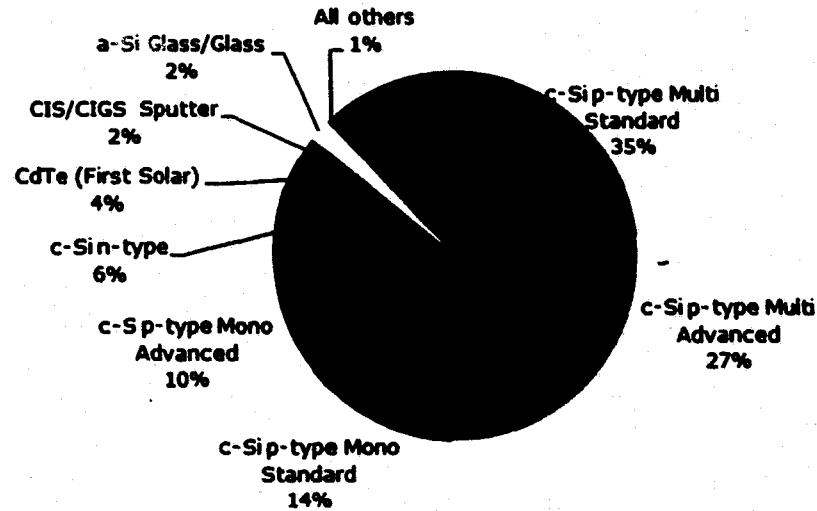


Figure 2-5: Market share of different inorganic photovoltaic technologies in 2014 [51].

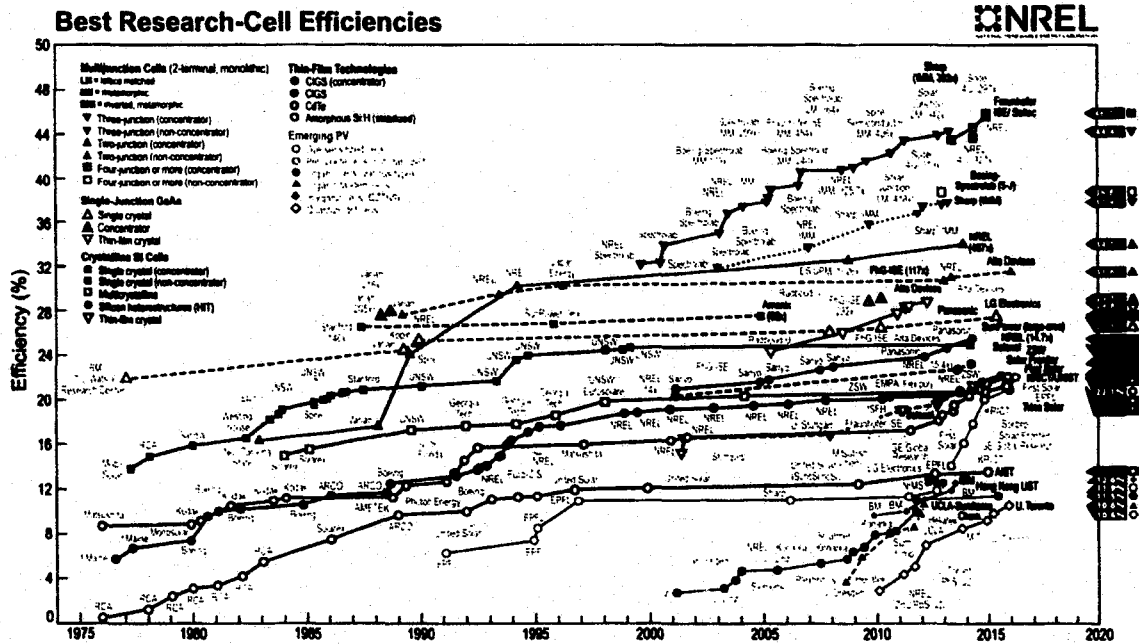


Figure 2-6: Progress of various photovoltaic technologies [9].

2.2.2 Solar Cell Characterization and Parameters

Figure 2-7 shows the typical $J-V$ and $P-V$ characteristics of a solar cell. The solar cell is generally characterized by plotting the current-voltage relationship under illumination. The fourth quadrant of the $J-V$ characteristics under illumination is the

working region of the solar cell. The primary parameters to characterize the solar cell under illumination are short circuit current, open circuit voltage, maximum power point, series and shunt resistances, fill factor, and power conversion efficiency.

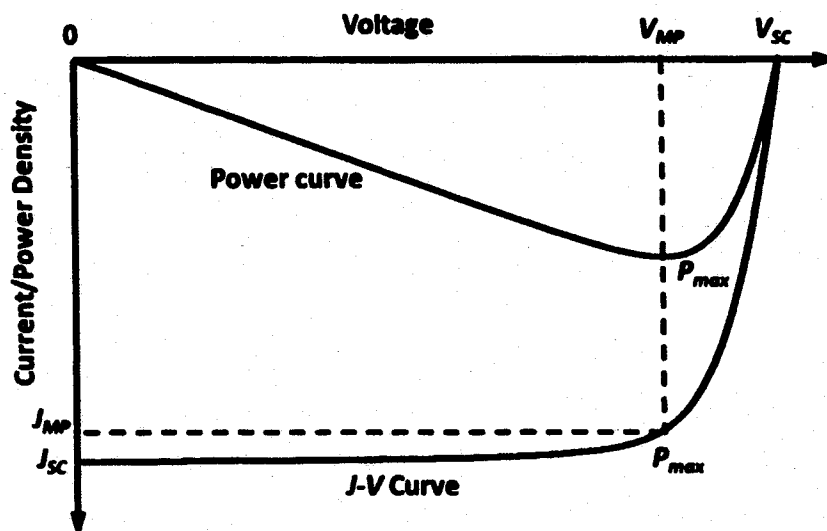


Figure 2-7: Typical J - V and P - V characteristics of a solar cell.

Short circuit current density, J_{sc} (mA/cm^2): It is the current density retrieved from the solar cell when the electrodes are shorted. In J - V characteristics, it is the current density when the bias voltage is zero. The short circuit current density is linearly dependent on generation rate and incident optical power density.

Open circuit voltage, V_{oc} (V): It is the voltage developed across the electrodes of the solar cell when no load is connected and no current is flowing through the circuit. Open circuit voltage is the theoretical maximum voltage that can be released to a load. The open circuit voltage depends on the work functions of the electrodes and energy level of the active layer.

Maximum power point, J_{MP} (mA/cm^2) and V_{MP} (V): The electrical power density generated by the solar cell is the product of current density and voltage. The

maximum power point is the peak value in the P - V curve, which corresponds to the current density and voltage at which maximum power from the solar cell is harvested.

Series, R_S (Ω) and shunt resistance, R_{SH} (Ω): The series resistance represents the inverse of the slope of the I - V curve at open circuit voltage point and shunt resistance represents the inverse of the slope of the I - V curve at short circuit current point given as

$$\begin{aligned} R_S &= \left(\frac{dV}{dI} \right)_{V=V_{OC}} \\ R_{SH} &= \left(\frac{dV}{dI} \right)_{I=I_{SC}} \end{aligned} \quad \text{Eq. 2-1}$$

Fill factor, FF (%): The fill factor is the charge extraction capability of the solar cell. It is the ratio of maximum power produced by the solar cell to the theoretical maximum power it could produce based on the J_{SC} and V_{OC} , and is given by

$$FF = \frac{J_{MP} V_{MP}}{J_{SC} V_{OC}} \quad \text{Eq. 2-2}$$

Power conversion efficiency, PCE (%): It is the ratio of maximum electrical power generated to the total incident optical power. Since the solar cell generates the maximum electrical power at maximum power point, if P_{in} is the incident optical power density, then PCE is given by

$$PCE = \frac{J_{MP} V_{MP}}{P_{in}} = \frac{J_{SC} V_{OC} FF}{P_{in}} \quad \text{Eq. 2-3}$$

2.3 Device Architecture

The p-n junction diode is the primary architecture of the silicon solar cell in which an n-type semiconductor layer is sandwiched with a p-type semiconductor layer creating a depletion region at the junction as shown in Figure 2-8. The device architecture is divided into four regions: n-type quasi-neutral region (n-QNR), n-type depletion region (n-DR), p-type depletion region (p-DR), and p-type quasi-neutral region (p-QNR). The transport of charge carriers, electrons and holes, in the p-n junction based solar cell is mainly governed by two mechanisms: drift under the influence of the internal electric field, and diffusion due to uneven carrier concentration profiles throughout the device. Under illumination, a generation of charge carriers creates new free electrons and holes, and the recombination process annihilates the free electrons and holes within the device. The direction of the internal electric field developed at the depletion region is from the n-region to the p-region. This electric field drifts photo-generated electrons towards the n-region and holes towards the p-region developing a potential difference across the p-n junction, which releases the electric power to the external load connected across the device.

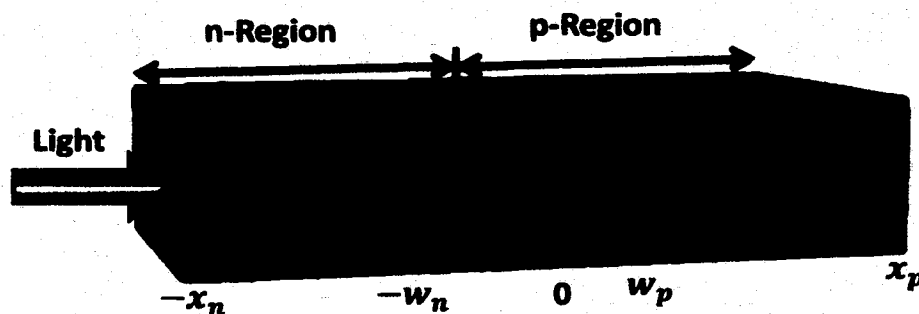


Figure 2-8: Device architecture of p-n junction solar cell for the analytical model.

2.4 Analytical Modeling

2.4.1 Ambipolar Transport Equations

The general steady state drift-diffusion equations of electron and hole including the effect of generation and recombination process in a p-n junction silicon solar cell are [53]

$$\begin{aligned} D_n \frac{d^2 n(x)}{dx^2} + \mu_n \frac{d[n(x)E(x)]}{dx} - R_n(x) + G_n(x) &= 0 \\ D_p \frac{d^2 p(x)}{dx^2} - \mu_p \frac{d[p(x)E(x)]}{dx} - R_p(x) + G_p(x) &= 0 \end{aligned} \quad \text{Eq. 2-4}$$

Where $D_n(D_p)$ is the diffusion coefficient for the electron (hole), $\mu_n(\mu_p)$ is the electron (hole) mobility, $R_n(x) = (n(x) - n_{p0})/\tau_n$ ($R_p(x) = (p(x) - p_{n0})/\tau_p$) is the recombination rate of the electrons (holes), $G_n(G_p)$ is the generation rate of the electrons (holes), $n_{p0}(p_{n0})$ is the equilibrium electron (hole) minority concentration, $\tau_n(\tau_p)$ is the electron (hole) minority carrier life-time, and $E(x)$ is the internal static electric field given as [53], [54]

$$E(x) = V_t \begin{cases} \frac{w_n + x}{L_{nD}^2}, & -w_n \leq x \leq 0 \\ \frac{w_p - x}{L_{pD}^2}, & 0 \leq x \leq w_p \end{cases} \quad \text{Eq. 2-5}$$

Where $V_t = kT/q$ is thermal voltage, $L_{nD} = \sqrt{\frac{\epsilon_r \epsilon_0 kT}{q^2 N_d}}$ and $L_{pD} = \sqrt{\frac{\epsilon_r \epsilon_0 kT}{q^2 N_a}}$ are electron and hole Debye lengths, respectively, w_n is the depletion width in n-side, and w_p is the depletion width in p-side given as [55]

$$\begin{aligned}
 w_n &= \sqrt{\frac{2\epsilon_r\epsilon_0(|V_{bi} - V|)}{q} \frac{N_a}{N_d(N_a + N_d)}} \\
 w_p &= \sqrt{\frac{2\epsilon_r\epsilon_0(|V_{bi} - V|)}{q} \frac{N_d}{N_a(N_a + N_d)}}
 \end{aligned}
 \tag{Eq. 2-6}$$

Where $V_{bi} = V_t \ln(N_a N_d / n_i^2)$ is the build-in potential [54], V is the external bias voltage, n_i is the intrinsic concentration, and N_a and N_d are the acceptor and donor impurity doping concentrations, respectively. The total depletion width of the p-n junction is $w = w_n + w_p$.

2.4.2 Intrinsic Boundary Condition for Thick Devices

The transport equations of electron and hole in QNR require two boundary conditions each. The widely used intrinsic boundary condition to solve transport equations in p-n junction diodes assumes that the device is infinitely thick. Here, intrinsic refers to the traditionally used boundary condition. Namely, the minority carrier concentrations are assumed to have a finite values, as the device's thickness tends to reach infinity. Due to this assumption, intrinsic boundary condition is only suitable for thick devices and is inappropriate for thin-film solar cells. The intrinsic boundary conditions for electron and holes in the analysis of bulk p-n junction solar cells are given as [53] [56]

$$\begin{aligned}
 n(w_p) &= n_{p0}(e^{V/V_t} - 1), & n(x \rightarrow \infty) &= n_{p0} \\
 p(-w_n) &= p_{n0}(e^{V/V_t} - 1), & p(x \rightarrow -\infty) &= p_{n0}
 \end{aligned}
 \tag{Eq. 2-7}$$

2.4.3 Surface Recombination Boundary Condition

As mentioned above that the intrinsic boundary condition is not physical for thin devices, one must be careful when considering short devices. In that case, it is probably more meaningful to consider a finite surface recombination velocity based boundary

condition. The recombination process of the charge carriers at the surface of the solar cell due to the presence of defects and dangling bonds is called surface recombination and the speed at which the charge carriers recombine at the surface is known as surface recombination velocity. The surface recombination boundary condition has no limitation for the device dimension instead, the physical phenomenon explaining the surface recombination of the charge carriers at the surface near to the electrodes is considered. With surface recombination velocity of electron S_n [cm^{-1}] and surface recombination velocity of hole S_p [cm^{-1}], the surface recombination boundary condition for electron and holes are given as [56], [57]

$$\begin{aligned} n(w_p) &= n_{p0}(e^{V/V_t} - 1), & qD_n \partial_x [n(x)] \big|_{x=x_p} &= -qn(x_p)S_n \\ p(-w_n) &= p_{n0}(e^{V/V_t} - 1), & qD_p \partial_x [p(x)] \big|_{x=-x_n} &= qp(-x_n)S_p \end{aligned} \quad \text{Eq. 2-8}$$

2.4.4 Homogeneous Generation

The generation of free charge carriers upon absorption of photons by the solar cell material is the basis for the generation of electrical power via photovoltaic. The generation rate decays exponentially as the optical power gets absorbed while penetrating inside the solar cell. However, for the thin-film solar cells, where the device's thickness is smaller than the photon penetration depth $d_p = 1/\alpha$, where $\alpha = \text{Im}(\omega\sqrt{\epsilon}/c)$ is the absorption coefficient of solar cell material, the homogeneous generation can be assumed. In such case, the homogeneous generation rate due to the infinitesimal band of wavelength $\Delta\lambda$ in a solar spectrum centered at any wavelength λ can be approximated as

$$G(\lambda) = \frac{P_0 T(\lambda) \lambda}{(x_p + x_n) hc} P_a(\lambda) \Delta\lambda. \quad \text{Eq. 2-9}$$

Where h is Planck's constant, c is the speed of light, $P_0 = 100 \text{ mW/cm}^2$ is the total solar power density for AM1.5, T is the transmission coefficient at the front face of the solar cell and P_d is the Planck's distribution of solar spectrum given as

$$P_d(\lambda) = \frac{15(ch)^4}{(\pi k_B T_c)^4 \lambda^5} \frac{1}{\left(\text{Exp} \left[\frac{ch}{k_B T_c \lambda} \right] - 1 \right)}. \quad \text{Eq. 2-10}$$

Where k_B is Boltzmann constant, T_c is temperature at the surface of the sun and $\int_0^\infty P_d d\lambda = 1$. For normal incident [58],

$$T = \frac{n_{si}}{n_{air}} \left| \frac{2n_{air}}{n_{air} + n_{si} + i\kappa_{si}} \right|^2. \quad \text{Eq. 2-11}$$

Where n_{air} and n_{si} are refractive indices of surrounding media and solar cell material, respectively, and κ_{si} is the extinction coefficient of solar cell material, silicon in this case.

2.4.4.1 Solution in QNR

In quasi-neutral regions, the internal electric field is zero ($E = 0$) and the drift-diffusion equations given in Eq. 2-4 simplifies to diffusion equation only. The solution of the hole diffusion only transport equation in n-QNR and electron transport equation in p-QNR using intrinsic boundary condition (Eq. 2-7) with homogeneous generation rate G are given as

n-QNR

$$p(x) = G\tau_p + p_{n0} - e^{\frac{w_n+x}{L_p}} \left(G\tau_p + p_{n0}(1 - e^{V/V_t}) \right). \quad \text{Eq. 2-12}$$

p-QNR

$$n(x) = G\tau_n + n_{p0} - e^{\frac{w_p-x}{L_n}} \left(G\tau_n + n_{p0}(1 - e^{V/V_t}) \right). \quad \text{Eq. 2-13}$$

Where $L_n = \sqrt{\tau_n D_n}$ and $L_p = \sqrt{\tau_p D_p}$ are electron and hole diffusion lengths, respectively.

2.4.4.2 Solution in DR

After finding the solution of charge transport equations in quasi neutral regions, the transport equations in depletion regions with electric field are calculated in quasi neutral regions. The solution of electron and hole transport equations in the depletion regions are given by

n-DR

$$n(x) = e^{\frac{-x(2w_n+x)}{2L_{nd}^2}} c_2 - \frac{GL_{nd}^2}{D_n} + \sqrt{2}L_{nd} \left(c_1 + \frac{Gw_n}{D_n} \right) D_+ \left[\frac{w_n + x}{\sqrt{2}L_{nd}} \right]. \quad \text{Eq. 2-14}$$

$$p(x) = \sqrt{\frac{\pi}{2}} L_{nd} e^{\frac{(w_n+x)^2}{2L_{nd}^2}} \left(c_1 + \frac{Gw_n}{D_p} \right) \text{erf} \left[\frac{w_n + x}{\sqrt{2}L_{nd}} \right] + \frac{GL_{nd}^2}{D_p} + c_2 e^{\frac{x(2w_n+x)}{2L_{nd}^2}}. \quad \text{Eq. 2-15}$$

p-DR

$$n(x) = \sqrt{\frac{\pi}{2}} L_{pd} e^{\frac{(w_p-x)^2}{2L_{pd}^2}} \left(c_4 - \frac{Gw_p}{D_n} \right) \text{erf} \left[\frac{x - w_p}{\sqrt{2}L_{pd}} \right] + \frac{GL_{pd}^2}{D_n} + c_3 e^{\frac{-x(2w_p-x)}{2L_{pd}^2}}. \quad \text{Eq. 2-16}$$

$$p(x) = e^{\frac{x(2w_p-x)}{2L_{pd}^2}} c_4 - \frac{GL_{pd}^2}{D_p} + \sqrt{2}L_{pd} \left(c_3 - \frac{Gw_p}{D_p} \right) D_+ \left[\frac{x - w_p}{\sqrt{2}L_{pd}} \right]. \quad \text{Eq. 2-17}$$

Where D_+ is the Dawson function. Each of the solution of the electron and hole transport equations in the depletion region have four constant parameters c_1 , c_2 , c_3 , and c_4 . As the solution of the electron and hole transport equations are already obtained in QNR, to calculate the charge carriers concentration profiles in the depletion regions, the continuity of the charge concentrations and currents are enforced at the boundaries of n-QNR, n-DR, p-DR and p-QNR.

Different parameters, their values and units used in the model are listed in **Table 2-1**. **Figure 2-9** shows the electron and hole concentration profiles at (a) zero, (b) forward and (c) reverse bias in all regions. Since the majority concentration are not much affected by the generation of charge carriers, the majority carrier concentrations are assumed to be the same as the impurity doping concentrations, such as the electron concentration in n-QNR region is N_d and hole concentration in p-QNR region is N_a . A constant generation rate of $10^{24} \text{ m}^{-3}\text{s}^{-1}$ is used in the calculations, which is the typical generation rate for AM1.5 solar irradiation. When the p-n junction solar cell is forward biased, the width of the depletion region decreases and the majority carriers make it across the junction, thus increasing the minority carrier concentration on the other side of the junction. On the other hand, reverse bias decreases the number of minority carriers and restricts the current flow through the device.

Table 2-1: Numerical parameters and properties of mc-Si used in model [59].

Parameter	Symbol	Value	Unit
Permittivity of vacuum	ϵ_0	8.854×10^{-12}	F/m
Dielectric constant of monocrystalline silicon	ϵ_{rSi}	11.7	
Boltzmann constant	k_B	1.38×10^{-23}	J/K
Planck constant	h	6.626×10^{-34}	Js
Speed of light in space	c	3×10^8	m/s
Intrinsic concentration of silicon	N_i	1×10^{16}	m^{-3}
Donor (Phosphorus) concentration	N_d	$10^{23} - 10^{27}$	m^{-3}
Acceptor (Boron) concentration	N_a	$10^{22} - 10^{25}$	m^{-3}
n-type layer thickness	x_n	300	nm
p-type layer thickness	x_p	200	μm
Electron mobility of mc-Si	μ_n	1360	$cm^2/(Vs)$
Hole mobility of mc-Si	μ_p	450	$cm^2/(Vs)$
Diffusion coefficient of electron	D_n	36	cm^2/s
Diffusion coefficient of hole	D_p	12	cm^2/s
Hole (electron) surface recombination velocity	$S_p(S_n)$	$10 - 10^4$	m/s
Minority carrier lifetime of electron	τ_n	23.5×10^{-6}	s
Minority carrier lifetime of hole	τ_p	1.5×10^{-6}	s
Operating temperature	T_0	300	K

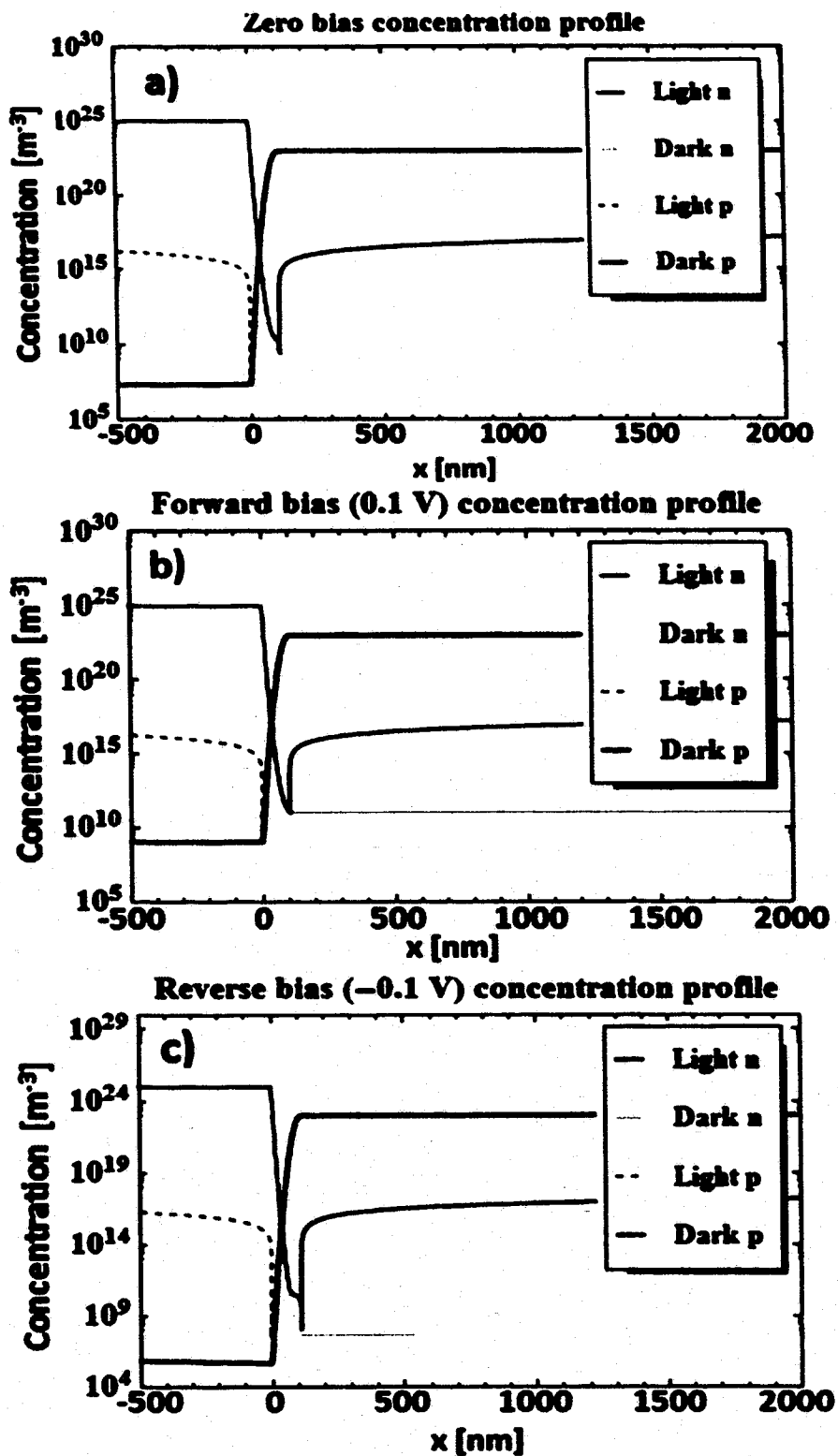


Figure 2-9: Electron and hole concentration profiles at the homogenous generation rate of $10^{24} \text{ m}^{-3} \text{ s}^{-1}$ for a) zero bias, b) forward, and c) reverse bias.

2.4.4.3 Current Calculation

Once the analytical expressions of the charge carriers were obtained, an analytical expression for the current depending on the generation rate was calculated. The electron and hole diffusion currents are calculated at the edge of the depletion regions using solution of electron and hole transport equations in QNR. The electron diffusion current j_n is calculated at w_p , the hole current j_p is calculated at $-w_n$, and the total current j_t is the summation of electron and hole current, $j_t = j_n + j_p$. The optical power in the solar spectrum is distributed in a band of wavelength. Therefore, the total current is the summation of currents contributed by each wavelength which can be expressed as

$$j_t = \sum_{\lambda=0}^{\infty} (j_{G\lambda}(\lambda) - j_s(e^{V/V_t} - 1)) = \sum_{\lambda=0}^{\infty} j_{G\lambda}(\lambda) - j_s(e^{V/V_t} - 1). \quad \text{Eq. 2-18}$$

Where the wavelength dependent generation current and saturation current are introduced as

$$j_{G\lambda}(\lambda) = qG(\lambda) \left(L_n \tanh \left[\frac{l_p}{2L_n} \right] + L_p \tanh \left[\frac{l_n}{2L_p} \right] \right) \\ j_s = q \left(\frac{p_{n0}L_p}{\tau_p} \coth \left[\frac{l_n}{L_p} \right] + \frac{n_{p0}L_n}{\tau_n} \coth \left[\frac{l_p}{L_n} \right] \right). \quad \text{Eq. 2-19}$$

Where $l_n = x_n - w_n$ and $l_p = x_p - w_p$, the homogeneous generation rate $G(\lambda)$ is given in Eq. 2-9. At zero generation ($G = 0$) and large devices ($l_p \gg L_n + L_p$ and $l_n \gg L_n + L_p$), the standard p-n junction diode response in dark can be obtained because $\coth(\infty) = 1$. Here, the total current is linearly dependent on the generation rate and is independent of the device spatial characteristics. This is an expected deficiency of the model, which follows directly from the assumption for a position independent generation of carriers, i.e. homogeneous generation rate. As the total current is linearly dependent on generation,

to demonstrate this relationship, the J - V characteristics are calculated and plotted for three different constant generation rates of $10^{24} \text{ m}^{-3}\text{s}^{-1}$, $5 \times 10^{24} \text{ m}^{-3}\text{s}^{-1}$ and $10^{25} \text{ m}^{-3}\text{s}^{-1}$. In this case, the generation is assumed to be both wavelength and position independent. **Figure 2-10** shows the J - V characteristics of solar cell under dark condition and with various constant generation rates. From **Figure 2-10**, it is seen that with an increase in the charge generation rate the short circuit current density and open circuit voltage increased.

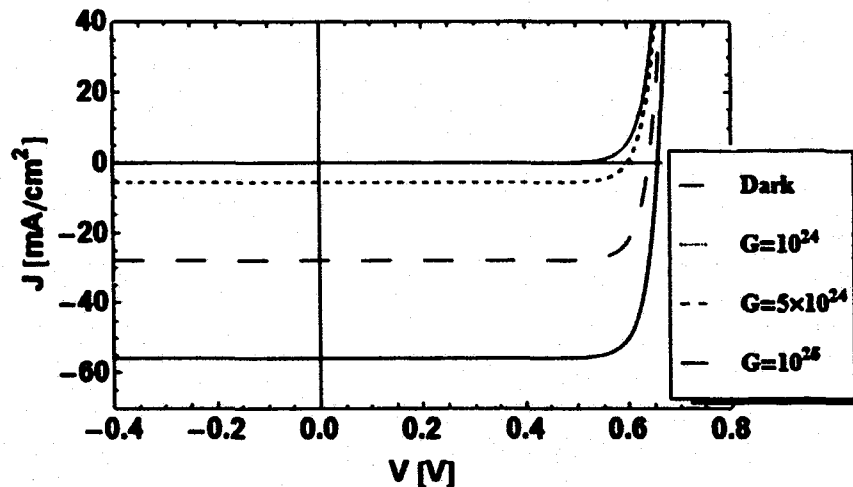


Figure 2-10: J - V characteristics of a p-n junction silicon solar cell for constant generation rates of $10^{24} \text{ m}^{-3}\text{s}^{-1}$, $5 \times 10^{24} \text{ m}^{-3}\text{s}^{-1}$ and $10^{25} \text{ m}^{-3}\text{s}^{-1}$.

The generation and recombination currents in the depletion region are calculated to include the effect of generation and recombination within the depletion region in the total electrical current from the solar cell. Assuming the homogeneous generation in the depletion region with thin depletion width (w), the generation and recombination current in the depletion region can be written as

$$j_{G,DR}(\lambda) = q \int_{-w_n}^{w_p} G(\lambda) dx = qwG(\lambda)$$

$$j_{R,DR} = q \int_{-w_n}^{w_p} R(x) dx = qwR_{max}$$

Eq. 2-20

Where R_{max} is the recombination rate at the center of the depletion region and is given as

$$R_{max} = R(x = 0) = \frac{n(x)p(x) - n_i^2}{\tau_p(n(x) + n_i) + \tau_n(p(x) + n_i)}. \quad \text{Eq. 2-21}$$

The concentration of charge carriers at the center are given as $n(x = 0) = p(x = 0) = n_i e^{V/2V_t}$, which simplifies R_{max} as

$$R_{max} = \frac{n_i}{\tau_p + \tau_n} (e^{V/2V_t} - 1). \quad \text{Eq. 2-22}$$

Now the recombination current simplifies to

$$j_{R,DR} = \frac{qWn_i}{\tau_p + \tau_n} (e^{V/2V_t} - 1) = j_R (e^{V/2V_t} - 1). \quad \text{Eq. 2-23}$$

Hence, including generation and recombination currents at the depletion region, the total electrical current from the solar cell in Eq. 2-18 modifies to

$$j_t = \sum_{\lambda=0}^{\infty} (j_{G\lambda}(\lambda) + j_{G\lambda,DR}(\lambda)) - j_s (e^{V/V_t} - 1) - j_R (e^{V/2V_t} - 1). \quad \text{Eq. 2-24}$$

From Eq. 2-19, it is demonstrated that for large devices ($l_p \gg L_n + L_p$ and $l_n \gg L_n + L_p$), the generation and saturation currents obtained with the intrinsic boundary conditions has finite values due to the facts that $\coth(\infty) = 1$ and $\tanh(\infty) = 1$. However, for thin devices, $l_p \ll L_n$, $l_n \ll L_p$, the saturation current tends to blow up and attained very high unphysical value as $\coth(0) \rightarrow \infty$. This shows that the traditional intrinsic boundary condition is not the right choice when considering thin devices. This is due to the assumption of an infinitely thick device in such boundary conditions as explained before. For thin devices, the surface recombination boundary condition is probably more physical. Next, the surface recombination boundary conditions are used to find the solution of the electron and hole transport equations, and calculate the total

current from the solar cell. The total current from the solar cell is given in Eq. 2-24, where the surface recombination boundary condition based generation and saturation currents are given as

$$j_{G\lambda}(\lambda) = qG(\lambda) \left(L_n \frac{q_n + \tanh\left[\frac{l_p}{L_n}\right] - q_n \operatorname{sech}\left[\frac{l_p}{L_n}\right]}{1 + q_n \tanh\left[\frac{l_p}{L_n}\right]} + L_p \frac{q_p + \tanh\left[\frac{l_n}{L_p}\right] - q_p \operatorname{sech}\left[\frac{l_n}{L_p}\right]}{1 + q_p \tanh\left[\frac{l_n}{L_p}\right]} \right)$$

$$j_s = qS_n n_{p0} \frac{1 + q_n^{-1} \tanh\left[\frac{l_p}{L_n}\right]}{1 + q_n \tanh\left[\frac{l_p}{L_n}\right]} + qS_p p_{n0} \frac{1 + q_p^{-1} \tanh\left[\frac{l_n}{L_p}\right]}{1 + q_p \tanh\left[\frac{l_n}{L_p}\right]} \quad \text{Eq. 2-25}$$

Where $q_n = L_n S_n / D_n = \tau_n S_n / L_n$, $q_p = L_p S_p / D_p = \tau_p S_p / L_p$. The saturation and generation currents with surface recombination boundary condition are now finite for thin devices. If $S_n = S_p$, for thin devices, $j_{G\lambda} \rightarrow qG(\lambda)(L_n + L_p)$ and $j_s = qS_n(n_{p0} + p_{n0})$.

Figure 2-11 compares the a) J - V characteristics and b) P - V characteristics of silicon solar cell for surface recombination (SR) and intrinsic boundary (IB) conditions for homogeneous generation under AM1.5 solar irradiation with 100 mW/cm^2 power density. The surface recombination velocity of 10 m/s was used for calculation. The surface recombination boundary condition is not only more practical to use for thin-film solar cells, but also delivers more electrical current and power from the device as shown in **Figure 2-11**.

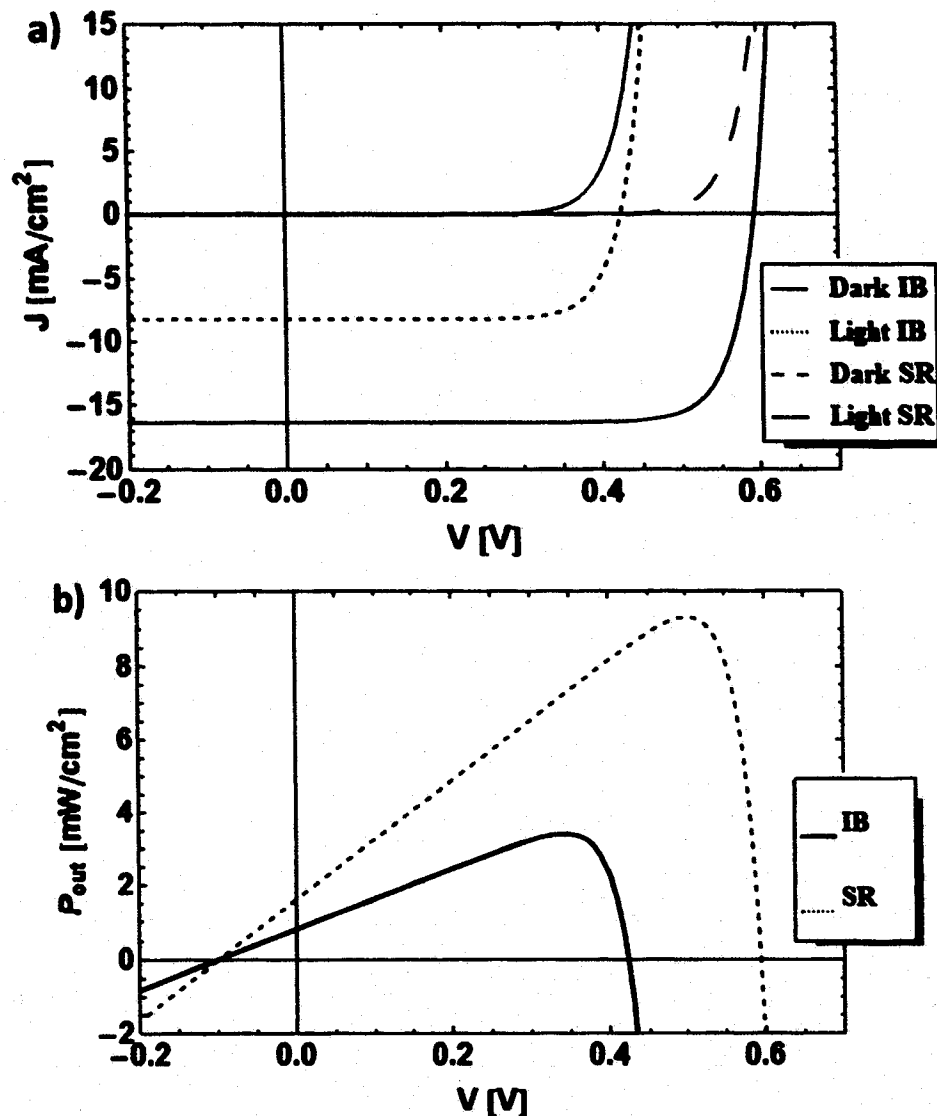


Figure 2-11: a) J - V characteristics, and b) P - V characteristics of silicon solar cell for surface recombination (SR) and intrinsic boundary (IB) conditions for homogeneous generation under AM1.5 solar irradiation with 100 mW/cm² power density.

As the analytical expression of the total electrical current from the solar cell is already obtained in Eq. 2-24, it is significant to express the optimal electrical power analytically. This optimal electrical power corresponds to the maximum power point in the J - V characteristic and peak value in the P - V characteristic of the solar cell. The output electrical power from the solar cell is given by $P_{out} = Vj_t$. As it is known that the P - V characteristic has a peak value, the optimal voltage can be obtained by using the maxima-

minima calculation. At the optimal voltage, the derivative of output electrical power with respect to the voltage is zero. Neglecting the recombination current at the depletion region in total electrical current j_t given in Eq. 2-24, the optimal voltage V_{opt} , and the optimal electrical current j_{opt} and power P_{opt} from the solar cell are given by

$$\begin{aligned} V_{opt} &= V_t(W[ej_t/j_s] - 1) \\ j_{opt} &= j_t(1 + W^{-1}[ej_t/j_s]) \\ P_{opt} &= j_t V_t(2 - W[ej_t/j_s] - W^{-1}[ej_t/j_s]) \end{aligned} \quad \text{Eq. 2-26}$$

Where W is ProductLog or Lambert W-function and e is Euler's number.

2.4.5 Inhomogeneous Generation

The homogeneous generation of charge carriers within solar cell is considered in previous section to simplify the analysis of the device operation. However, the optical power in the solar spectrum is distributed in a band of wavelength given by solar power density spectrum $P_d(\lambda)$, defined by Planck's law of black body radiation. Also, for the real solar cell device, the incident optical power decays exponentially as it progresses within the solar cell, governed by Beer-Lamberts law resulting in the position and wavelength dependent carrier generation rate and is approximated as

$$G(\lambda, x) = G(\lambda)e^{-\alpha(\lambda)x} = \frac{P_0 T(\lambda) \alpha(\lambda) \lambda P_d(\lambda) \Delta\lambda}{hc} e^{-\alpha(\lambda)x} \quad \text{Eq. 2-27}$$

Where $\alpha = (4\pi k)/\lambda$ is the absorption coefficient and k is the extinction coefficient of the solar cell material. The optical characteristics of the solar cell material are important for the device's performance. Different optical constants of crystalline silicon (c-Si) used in the model are depicted in Figure 2-12. Figure 2-12 shows the a) Refractive index and extinction coefficients of c-Si, and b) transmittance and reflectance of c-Si-Air interface.

The spectral generation rate within c-Si for inhomogeneous generation under AM1.5 solar irradiance of 100 mW/cm^2 optical power density is shown in Figure 2-13.

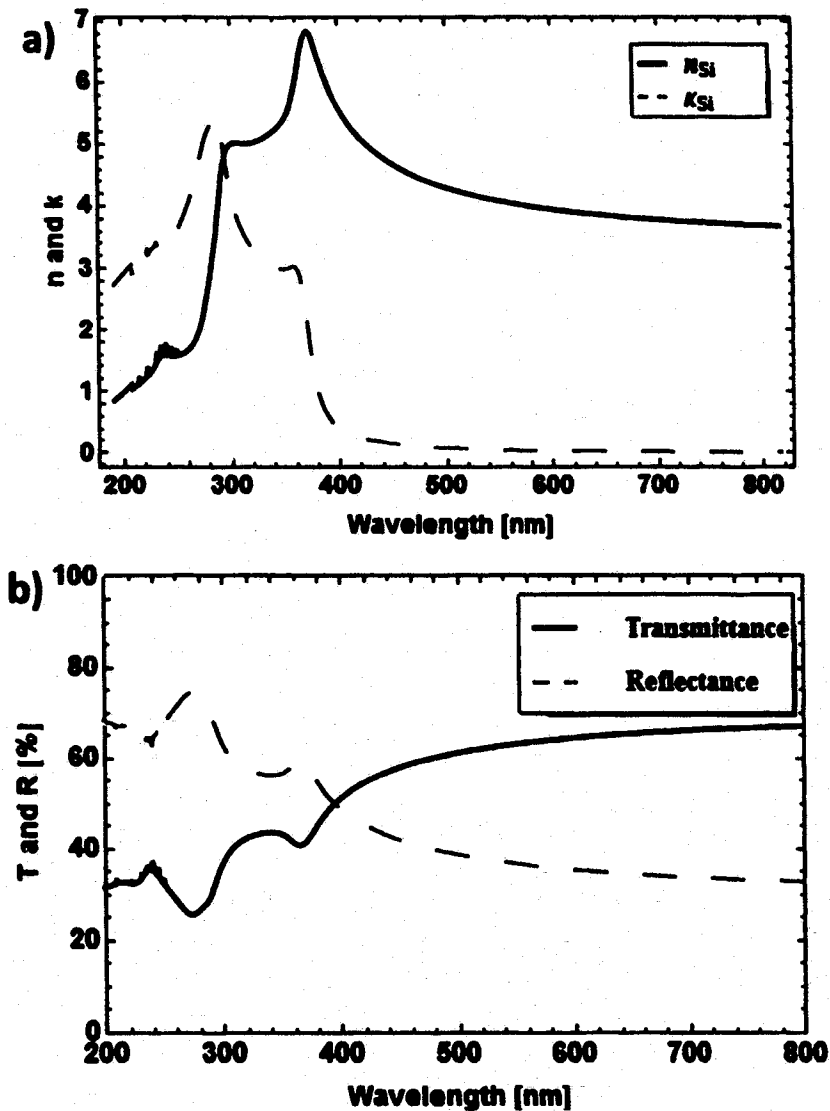


Figure 2-12: (a) Refractive index and extinction coefficients of c-Si, and (b) Transmittance and Reflectance for c-Si-Air interface.

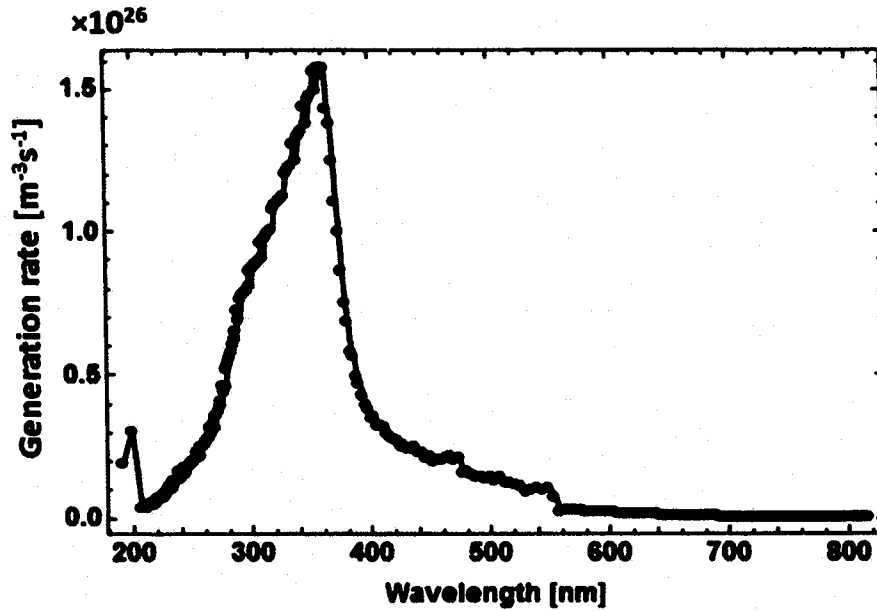


Figure 2-13: Spectral generation rate for inhomogeneous generation under AM1.5 solar irradiance of 100 mW/cm^2 optical power density.

The electron and hole transport equations in QNRs with the position and wavelength dependent inhomogeneous generation rate are given as

$$\begin{aligned} D_n n''(x) - \frac{n(x) - n_{p0}}{\tau_n} + G(\lambda)e^{-\alpha(\lambda)x} &= 0, & w_p < x < x_p \\ D_p p''(x) - \frac{p(x) - p_{n0}}{\tau_p} + G(\lambda)e^{-\alpha(\lambda)x} &= 0, & -x_n < x < -w_n \end{aligned} \quad \text{Eq. 2-28}$$

The similar approach is used here for inhomogeneous generation as in the homogeneous generation case to solve the electron and hole transport equations using intrinsic and surface recombination boundary conditions, and the total electrical current from the solar cell is calculated. The total electrical current from the solar cell is still the same as given in Eq. 2-24 where the generation ($J_{G\lambda}$, $J_{G\lambda,DR}$) and saturation (j_s) currents using intrinsic boundary condition for inhomogeneous generation are given in Eq. 2-29. From Eq. 2-29 it is discovered that even for inhomogeneous generation, the saturation

current with intrinsic boundary condition tends to attain very high unphysical value for thin devices.

$$j_{G\lambda}(\lambda) = qG(\lambda)e^{-\alpha l_n} \left(L_n \frac{e^{-\alpha w}}{1 + \alpha L_n} + L_p \frac{\alpha L_p + \coth \left[\frac{l_n}{L_p} \right] - e^{\alpha l_n} \text{csch} \left[\frac{l_n}{L_p} \right]}{1 - \alpha^2 L_p^2} \right)$$

$$j_{G\lambda,DR}(\lambda) = q \int_{-w_n}^{w_p} G(x, \lambda) dx = qG(\lambda)e^{-\alpha l_n} \frac{1 - e^{-w\alpha}}{\alpha} \quad \text{Eq. 2-29}$$

$$j_s = q \left(\frac{n_{p0} L_n}{\tau_n} + \frac{p_{n0} L_p}{\tau_p} \coth \left[\frac{l_n}{L_p} \right] \right)$$

Once again, it proved that the intrinsic boundary condition is not applicable for thin devices. Next, the surface recombination boundary condition is applied at the front where holes are the minority carriers. The total electrical current from the device in the case of surface recombination boundary condition is given by Eq. 2-24 where the generation current in depletion region $j_{G\lambda,DR}$ is given in Eq. 2-29, and generation $j_{G\lambda}$ and saturation j_s currents are given as

$$j_{G\lambda}(\lambda) = \frac{qG(\lambda)e^{-\alpha l_n} \left(L_n \frac{e^{-\alpha w}}{1 + \alpha L_n} + (q_p + \alpha L_p) \left(\cosh \left[\frac{l_n}{L_p} \right] - e^{\alpha l_n} \right) + (1 + \alpha q_p L_p) \sinh \left[\frac{l_n}{L_p} \right] \right)}{L_p (1 - \alpha^2 L_p^2) \left(\cosh \left[\frac{l_n}{L_p} \right] + q_p \sinh \left[\frac{l_n}{L_p} \right] \right)} \quad \text{Eq. 2-30}$$

$$j_s = q \frac{n_{p0} L_n}{\tau_n} + q S_p p_{n0} \frac{1 + q_p^{-1} \tanh \left[\frac{l_n}{L_p} \right]}{1 + q_p \tanh \left[\frac{l_n}{L_p} \right]}$$

Figure 2-14 shows the a) J - V characteristics and b) P - V characteristics of silicon solar cell with position and wavelength dependent inhomogeneous generation rate for intrinsic (IB) and surface recombination (SR) boundary conditions under AM1.5 solar irradiation with 100 mW/cm^2 optical power density. It is seen that the solar cell

performed better with surface recombination boundary condition and better matched with the experimental data of 8.75 cm^2 single crystalline silicon solar cell presented by Tsuno *et al.* [60].

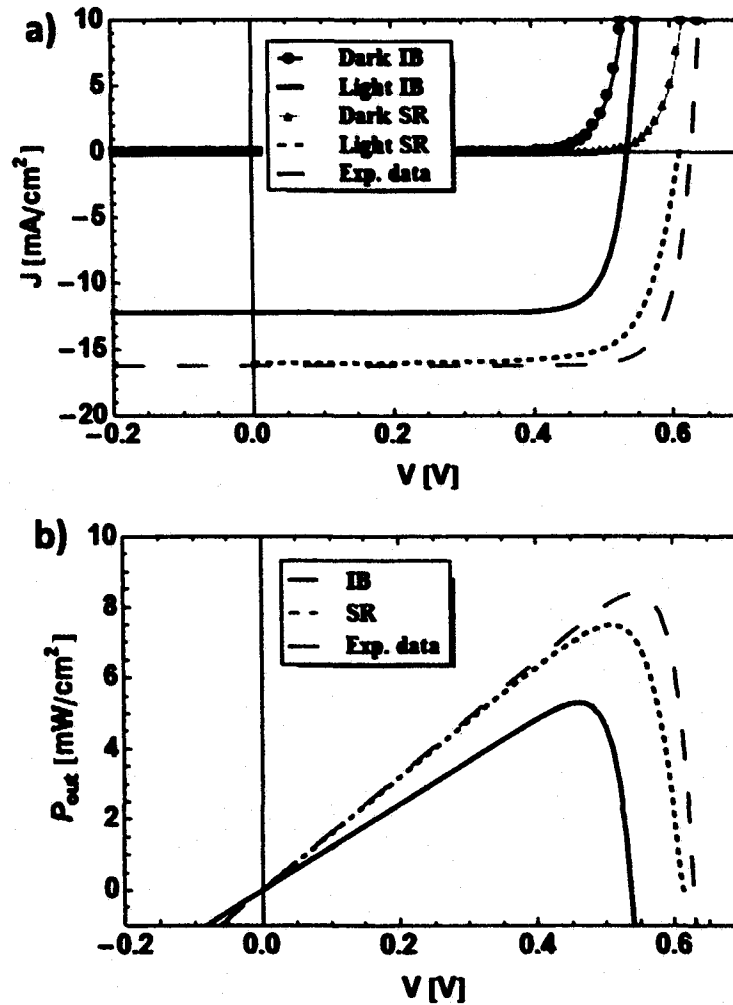


Figure 2-14: a) J - V characteristics and b) P - V characteristics of silicon solar cell for intrinsic (IB) and surface recombination (SR) boundary conditions with inhomogeneous generation rate under AM1.5 (100 mW/cm^2) solar irradiation plotted against experimental data by Tsuno *et al.* [60].

2.5 Results and Discussion

The simplified analytical model is developed for thin-film silicon solar cells for both intrinsic and surface recombination boundary conditions. It is worthy to study the

relationship between these two types of boundary conditions and their significance with physical properties of solar cells. The intrinsic boundary condition is revealed as a limiting case of surface recombination boundary condition with infinite surface recombination velocity. When the surface recombination velocity of the charge carrier approaches infinity, $S_p \rightarrow \infty \Rightarrow q_p = L_p S_p / D_p \rightarrow \infty$, the electrical currents from the solar cell with surface recombination velocity, given in Eq. 2-25 for homogeneous generation and Eq. 2-30 for inhomogeneous generation, approach the electrical currents obtained for the intrinsic boundary condition shown in Eq. 2-19 for homogeneous generation and Eq. 2-29 for inhomogeneous generation, respectively. This relation is shown in Figure 2-15 for the inhomogeneous generation case.

In Figure 2-15, as the surface recombination velocity S_p increases, the short circuit current density in the case of surface recombination (SR) boundary condition tends to reach the short circuit current density for intrinsic (IB) boundary condition. This confirms that the intrinsic boundary condition is the limiting case of surface recombination boundary condition with infinite surface recombination velocity. The electrical current obtained with intrinsic boundary condition is independent of surface recombination velocity. That is why the short circuit current is constant with IB in Figure 2-15. In the other extreme case with zero recombination velocity, $S_p \rightarrow 0 \Rightarrow q_p \rightarrow 0$, the generation current in Eq. 2-30 simplifies to

$$j_{G\lambda} = qG(\lambda)e^{-\alpha l_n} \left(L_n \frac{e^{-\alpha w}}{1 + \alpha L_n} + L_p \frac{\alpha L_p \left(1 - e^{\alpha l_n} \operatorname{sech} \left[\frac{l_n}{L_p} \right] \right) + \tanh \left[\frac{l_n}{L_p} \right]}{1 - \alpha^2 L_p^2} \right). \quad \text{Eq. 2-31}$$

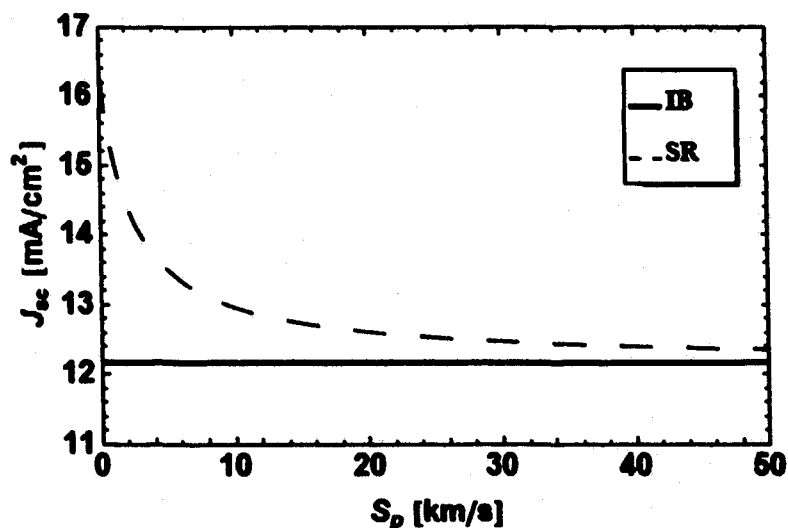


Figure 2-15: Short circuit current density for intrinsic and surface recombination boundary conditions in the case of inhomogeneous generation for various surface recombination velocities.

Another important conclusion from this analysis is that the performance of the solar cell is reduced with higher surface recombination velocity as it is shown that the short circuit current decreased for higher surface recombination velocity. **Figure 2-16** shows the J - V characteristics for different surface recombination velocities S_p for inhomogeneous generation and surface recombination boundary condition. **Figure 2-16** demonstrates that the solar cell offers higher short circuit current and open circuit voltage for small surface recombination velocity which agreed with the results in publication [40]. Higher recombination velocity could lead to higher recombination loss at the surface of solar cell material or at electrode interface resulting in lower performance, which suggests that the material for electrodes in the solar cell need to be chosen in such a way that it provides lower surface recombination velocity in order to fabricate highly efficient solar cells. The various factors influencing surface recombination velocity are surface roughness, surface contamination, oxidation temperature, ambient gases during

oxidation, post-oxidation annealing, and surface doping concentration [61]. Different passivation schemes were used to reduce the surface recombination velocity of solar cell emitters [62]–[65].

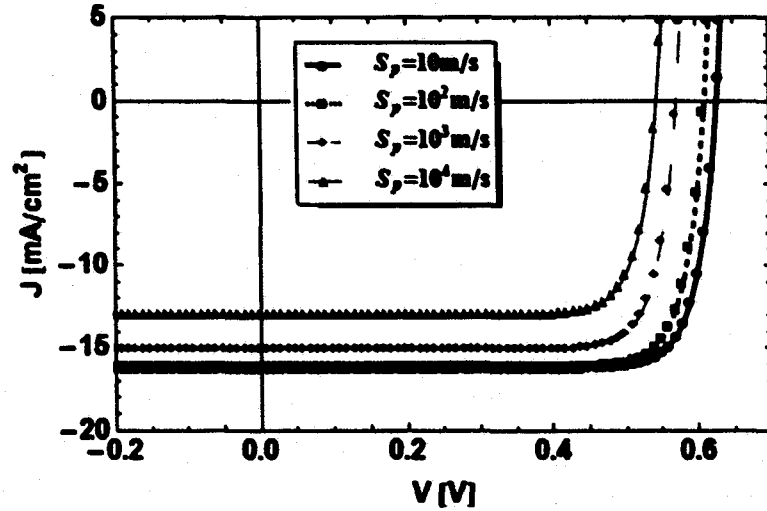


Figure 2-16: The J - V characteristics for different surface recombination velocities for inhomogeneous generation and surface recombination boundary condition.

The external quantum efficiency (EQE) gives the ratio of number of charge carriers extracted from the device to the number of incident photons of the particular wavelength λ and is given as

$$EQE(\lambda) = \frac{j_t/q}{P(\lambda)\lambda/hc} \quad \text{Eq. 2-32}$$

Where $P(\lambda)$ is the optical power density at wavelength λ in the solar spectrum. The EQE accounts for both absorption of photons within solar cell and extraction of charge carriers at the electrode. It also helps to understand the response of solar cell to different wavelengths in solar spectrum. **Figure 2-17** shows the external quantum efficiency of the silicon solar cell with inhomogeneous generation at $V = 0$ (zero bias) for intrinsic and surface recombination boundary conditions. The EQE plot shows that the surface

recombination boundary condition is more effective for lower wavelength to generate and extract charge carriers compared to intrinsic boundary condition.

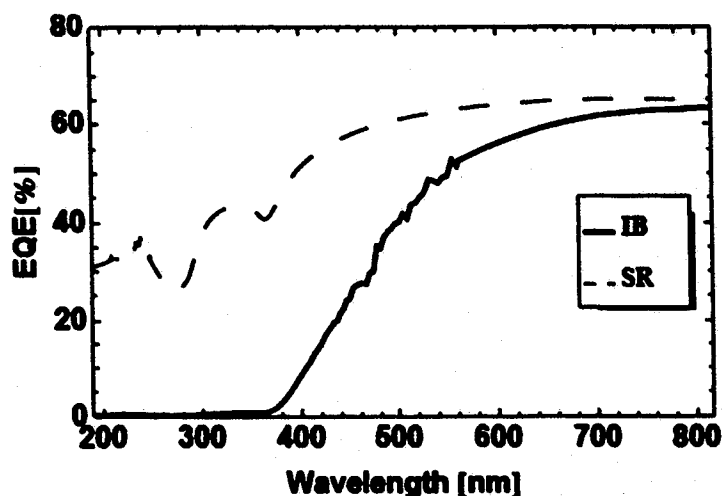


Figure 2-17: *EQE* for intrinsic and surface recombination boundary conditions with inhomogeneous generation at zero bias.

The light management scheme is very essential in thin-film solar cells. For this purpose, the front layer thickness, n-layer in this case, has a critical role in the performance of solar cell. If this layer is too thin, the depletion width reduces (if thickness is smaller than the width of depletion region in n-region), and if too thick, most of the light absorbed before reaching the depletion region and cannot contribute to the electrical current. The optimal thickness of front layer needs to be investigated to design the highly efficient thin-film solar cell. Figure 2-18 shows the optimal current density from the solar cell plotted against the thickness of the front (n-layer) and back (p-layer) layers. The optimal current j_{opt} is given in Eq. 2-26. The optimal thickness of the front layer is found to be around 300 nm; however, the back layer thickness has no optimal value. This could be due to the fact that most of the light gets absorbed within front layer and depletion region.

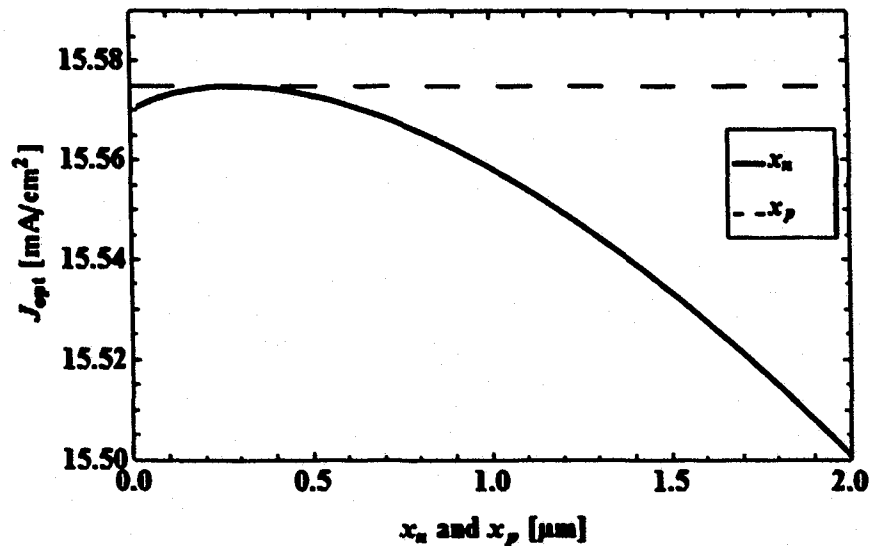


Figure 2-18: The optimal current for various front and back layers thicknesses of thin film solar cell.

Furthermore, the dependent of the performance of solar cell on minority carrier's lifetime is studied. For this purpose, the minority carrier's lifetime of five different solar cell materials are used. The minority carrier lifetime for monocrystalline silicon (mC-Si) is $37.2 \mu\text{s}$, poly-crystalline silicon (pC-Si) is $3.68 \mu\text{s}$, amorphous silicon (a-Si) is $11.29 \mu\text{s}$, gallium nitride (GaN) is 6.5 ns and indium gallium arsenide ($\text{In}_{0.14}\text{Ga}_{0.86}\text{As}$) is 110 ns [66]–[68]. **Figure 2-19** shows the J - V characteristics of p-n junction solar cell with minority carrier lifetime of monocrystalline silicon, poly-crystalline silicon, amorphous silicon, gallium nitride, and indium gallium arsenide solar cell materials. The short circuit current and open circuit voltage increased with a higher minority carrier's lifetime which can be proved analytically using total current expression given in Eq. 2-24 for any boundary condition. With a higher minority carrier's lifetime, the diffusion length increases so that many of the photo-generated charge carriers can contribute to the output electrical current.

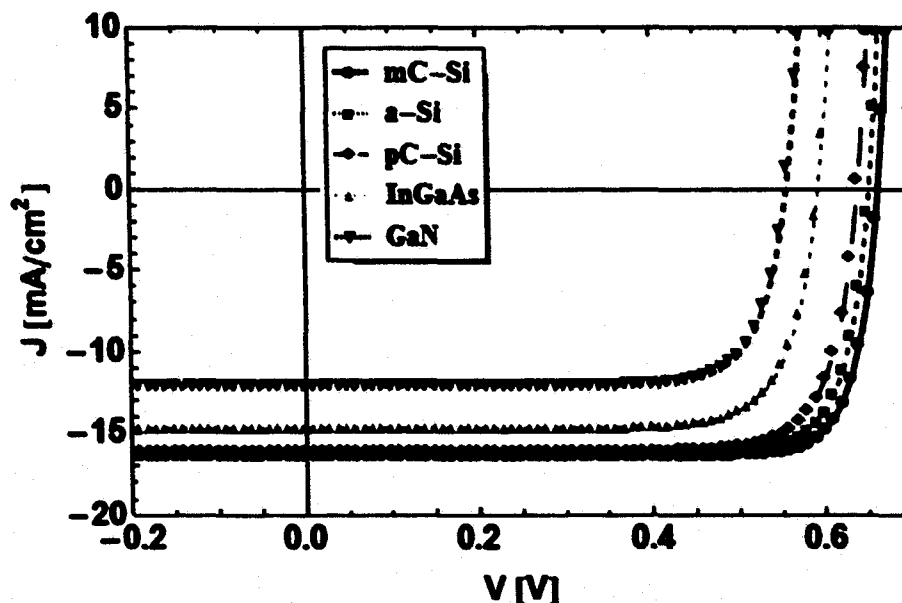


Figure 2-19: The J - V characteristics for different minority carrier lifetimes, monocrystalline Si ($37.2 \mu\text{s}$) [66], poly-crystalline Si ($3.68 \mu\text{s}$) [66], amorphous Si ($11.29 \mu\text{s}$) [66], GaN (6.5 ns) [67], $\text{In}_{0.14}\text{Ga}_{0.86}\text{As}$ (110 ns) [68].

Other important solar cell parameter to be considered for the analysis is impurity-doping concentration. The internal electric field, built-in voltage and depletion width depend on impurity doping concentration. Therefore, impurity-doping concentration influences the external voltage across the solar cell electrodes delivered to the load by a solar cell. **Figure 2-20** shows the effect of donor doping concentrations for fixed acceptor concentration, and **Figure 2-21** shows the effect of acceptor doping concentrations for fixed donor concentration, in the current density and voltage generated by a solar cell. The short circuit current density is not much affected by the doping concentration; however, the open circuit voltage increased significantly with higher doping. The important point to note from **Figures 2-20** and **2-21** is that the open circuit voltage increases when both donor and acceptor impurity are higher. For a small concentration of

one type of impurity, the open circuit voltage remains the same even as the other type of impurity is increased.

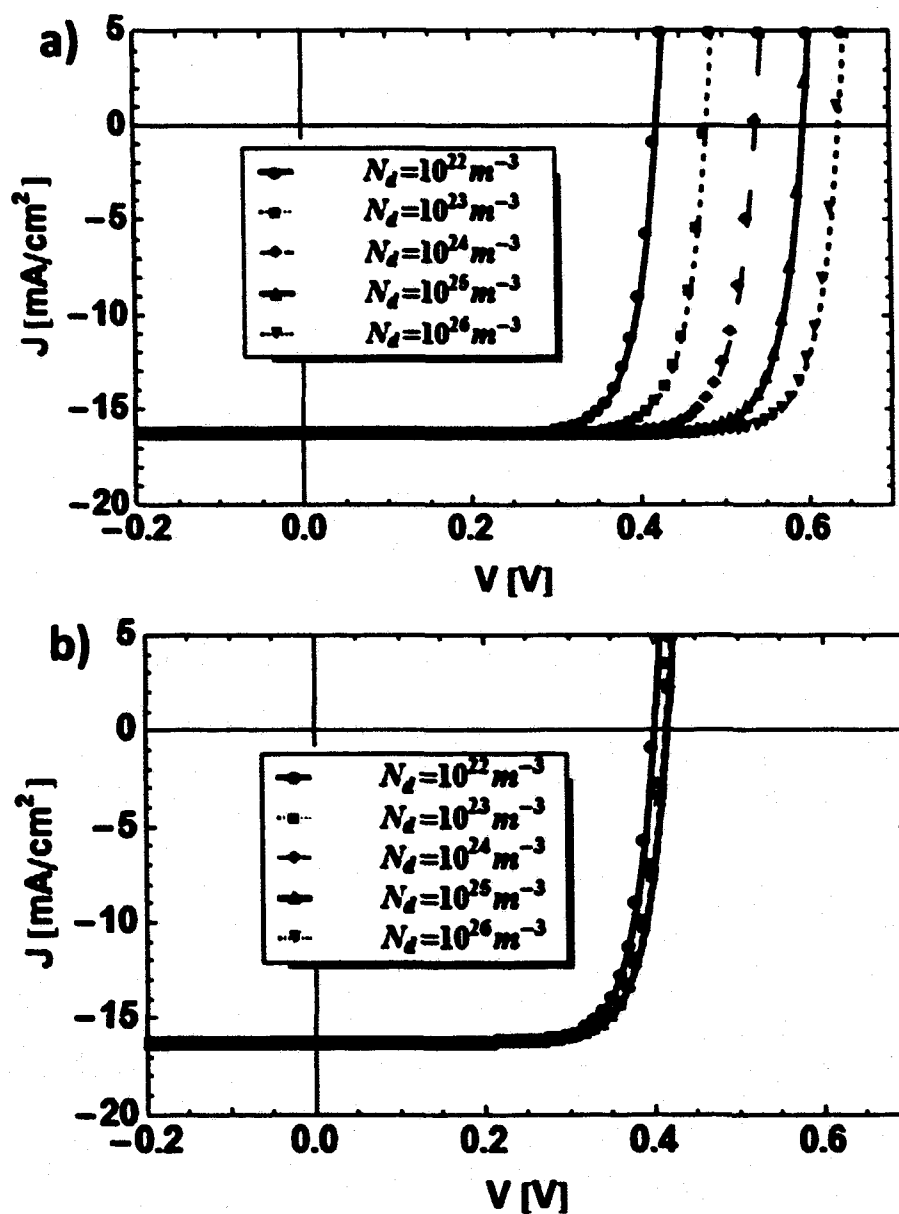


Figure 2-20: The J - V characteristics of PN junction silicon solar cell for various donor impurity concentrations N_d for a) $N_a = 10^{26} \text{ m}^{-3}$, and b) $N_a = 10^{22} \text{ m}^{-3}$.

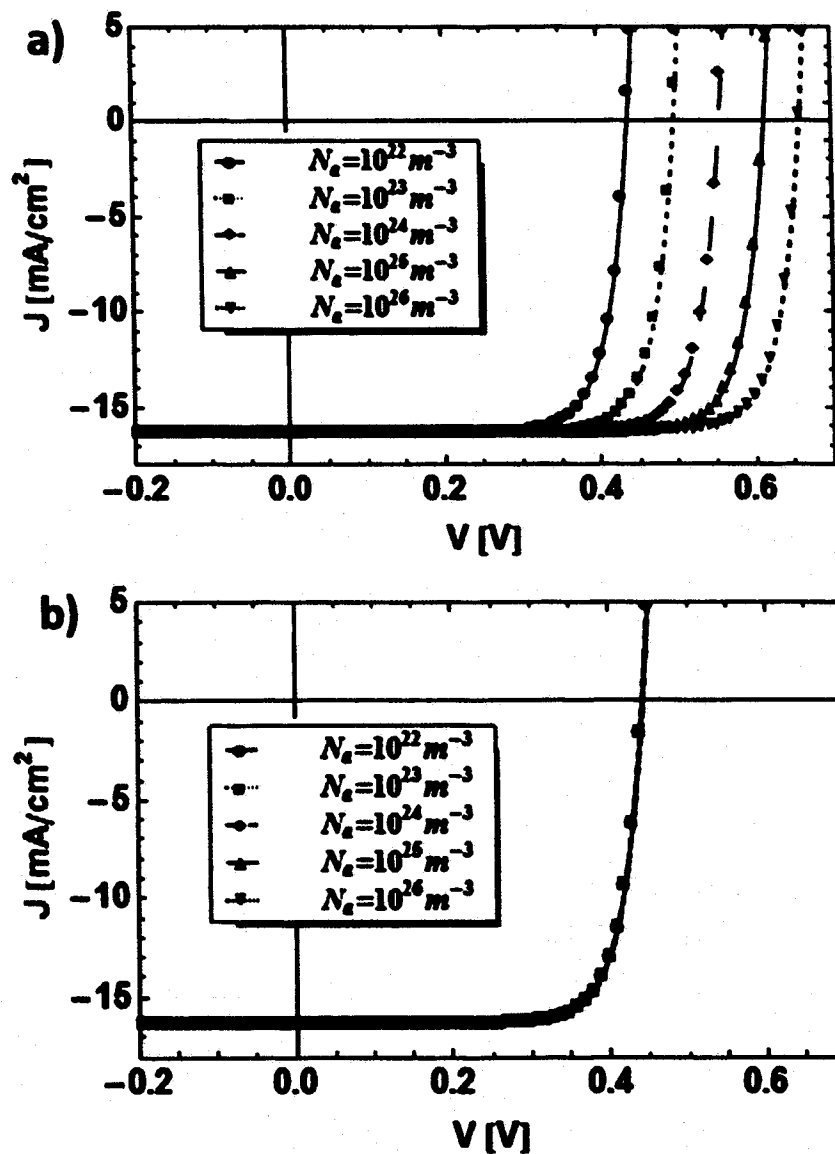


Figure 2-21: The J - V characteristics of PN junction silicon solar cell for various acceptor impurity concentrations N_a for a) $N_a = 10^{26} \text{ m}^{-3}$, and b) $N_a = 10^{22} \text{ m}^{-3}$.

2.5.1 Surface Plasmon Enhanced Thin-Film Silicon Solar Cell

The thin-film solar cell technology is emerged in the effort to reduce the cost. However, due to the thin absorber layer in thin-film solar cells, the absorption of light energy is reduced. The surface plasmon technology is one way to enhance the absorption in thin-film solar cell and enhance the performance [13]. The surface plasmon enhancement with thin inhomogeneous semi-continuous metal-dielectric composite

(MDC) was investigated using the analytical model of thin-film silicon solar cell. **Figure 2-22** shows the basic device schematic of surface plasmon enhanced thin-film silicon solar cell. The 20 nm MDC layer with silicon as dielectric and gold nanoparticles is used between ITO electrode and Si active layer to enhance the light absorption and eventually the *PCE* of solar cell. The thickness of the active layer and metal concentration in MDC were varied to observe the improvement in light absorption in the active layer.

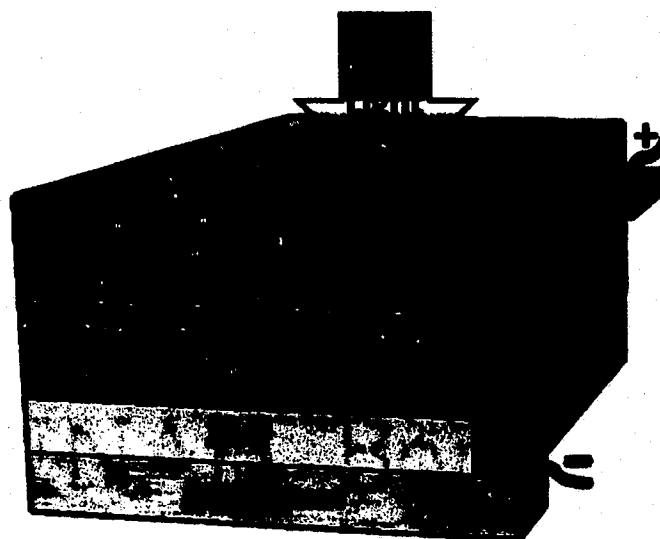


Figure 2-22: Schematic of the glass/ITO/MDC/Si/ZnO/Al based surface plasmon enhanced thin-film silicon solar cell.

The metal nanoparticles in MDC enhance the local field intensities by exhibiting energy localization under illumination which corresponds to the excitation of localized surface plasmon (SP) modes. At critical metal concentration in MDC called percolation threshold, extraordinary light absorption can be achieved. The light incidents on the glass side and reach to the MDC through the transparent ITO electrode. At MDC SP resonances trap electromagnetic radiation and enhanced optical absorption at silicon active layer. The effective permittivity of the inhomogeneous MDC layer is calculated

using the effective medium theory [69] and the optical absorption within the active layer is calculated based on effective permittivity of the MDC layer. The percentage of incident light energy absorbed in the active layer gives the optical efficiency and is varied for active layer thickness and metal concentration in MDC. **Figure 2-23** shows the optical efficiency of device structure of glass/ITO/MDC/Si/ZnO/Al as a function of active layer's (Si) thickness and metal concentration in 20 nm MDC. The maximum optical efficiency is about 35% for active layer's thicknesses of 80 nm, 180 nm, 280 nm etc. with 20% metal concentration in MDC layer. The optical efficiency enhancement is about 150% using MDC layer with periodic behavior for active layer's thickness.

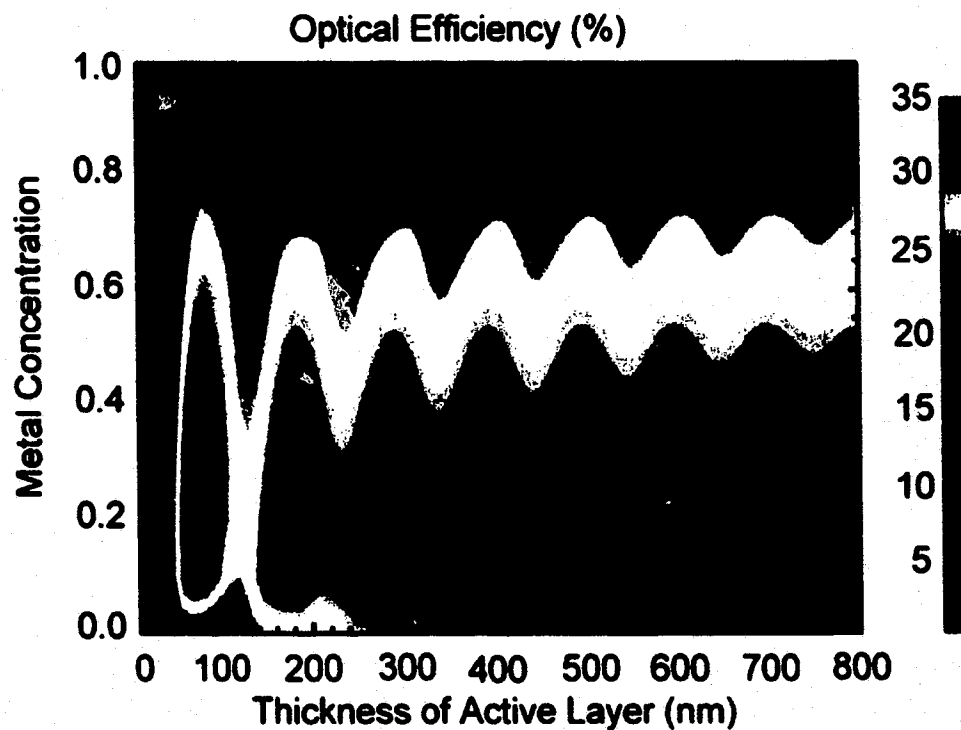


Figure 2-23: Optical efficiency of glass/ITO/MDC/Si/ZnO/Al solar cell as a function of the silicon active layer's thickness and metal concentration in 20 nm MDC layer.

Once the absorption of the light energy $A(d, m)$, as a function of the active layer thickness (d) and metal concentration (m), in the active layer is obtained from the optical model, the homogeneous generation rate is calculated as

$$G(d, m) = \frac{P_0 A(d, m)}{(hc/\lambda)d} P_a(\lambda) \Delta\lambda. \quad \text{Eq. 2-33}$$

The SP enhanced homogeneous generation rate given in Eq. 2-33 obtained from the optical model can be used in the analytical model for homogeneous generation case developed in the previous section to compute the electrical current and power generated by the solar cell. The optimal electrical power generated by the surface plasmon enhanced silicon solar cell is calculated using Eq. 2-26. The total electrical current j_t is given in Eq. 2-24, and generation and saturation currents for homogeneous generation case are given in Eq. 2-25. Once the optimal electrical power is obtained, the optimal *PCE* of surface plasmon enhanced silicon solar cell is computed with 100 mW/cm^2 input optical power density (P_{in}) as

$$\% PCE = \frac{P_{opt}}{P_{in}} \times 100 \% = P_{opt}. \quad \text{Eq. 2-34}$$

Figure 2-24 shows the optimal electrical efficiency of the surface plasmon enhanced solar cell of structure glass/ITO/ MDC/Si/ZnO/Al as function of the active layer's (Si) thickness and metal concentration in 20 nm MDC. The optimal efficiency corresponds to the maximum power point in the J - V curve. The maximum optimal *PCE* is about 14% for active layer's thickness of 80 nm with 20% to 40% metal concentrations in MDC layer. The enhancement in *PCE* is about 100% using MDC layer with periodic behavior for active layer's thickness as seen in optical efficiency enhancement.

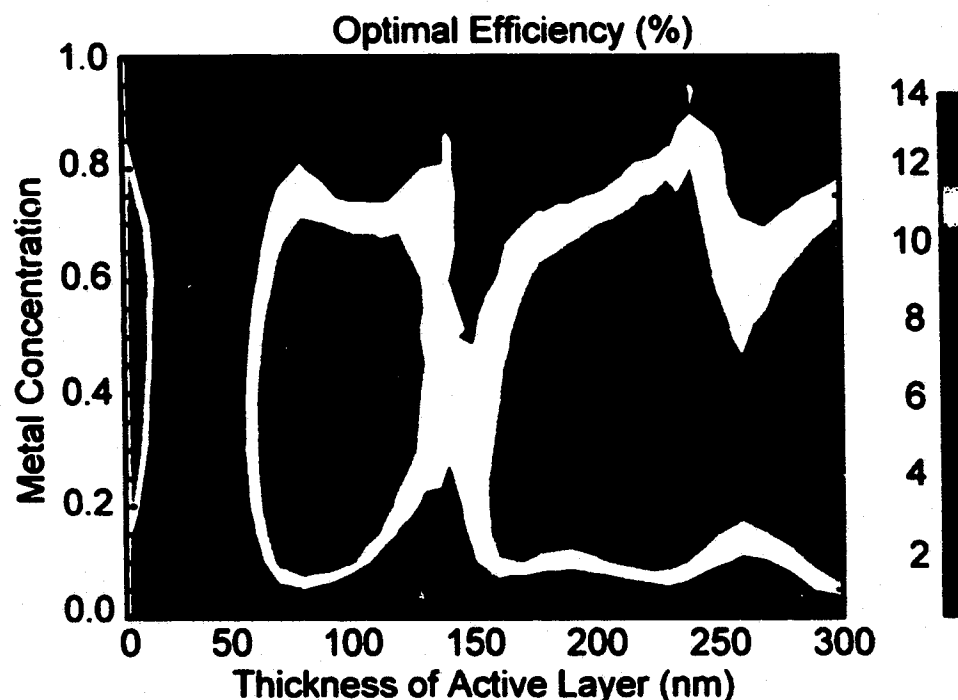


Figure 2-24: Optimal *PCE* of glass/ITO/ MDC/Si/ZnO/Al surface plasmon enhanced solar cell as a function of the silicon active layer's thickness and metal concentration in 20 nm MDC.

2.6 Conclusions

The performance of thin-film silicon solar cell is optimized by developing analytical model. Two boundary conditions, one based on surface recombination velocity and another intrinsic boundary condition are studied. The surface recombination boundary condition is more practical for thin-film solar cells and the performance of solar cell was better with surface recombination velocity boundary condition. The homogeneous and inhomogeneous generation cases are also investigated separately for both types of boundary conditions. In addition, the performance of thin-film silicon solar cell is studied for different solar cell parameters such as a device's thickness, minority carrier's lifetime, impurity doping concentration, surface recombination velocity, etc., and optimized them. The short circuit current and open circuit voltage increased with

lower surface recombination velocity. The performance of solar cells enhanced with higher minority carrier lifetime and the open circuit voltage increased when the impurity doping concentration was increased. This model can be further extended to the different solar cell architectures, such as p-i-n, multijunction, bulk heterojunction, etc. and for different solar cell materials, such as amorphous silicon, GaN, InGaAs, conjugated polymers etc.

CHAPTER 3

POLYMER SOLAR CELLS AND PHOTODETECTORS

3.1 Introduction

Photovoltaic cells based on conjugated polymers and fullerene derivatives have been explored extensively [70]–[74] in the last ten years and have attracted much attention due to their potential of harnessing solar energy in a cost effective way [75], [76]. Polymer solar cells have the advantage of low cost of fabrication, ease of processing, light weight, versatility of chemical structure, and mechanical flexibility [77]–[79]. Despite such tremendous features, the efficiency of the organic solar cell is lower than the inorganic solar cell [15]; as a result, the application of the organic solar cell has been limited in commercial use. Unlike the inorganic semiconductor, that generates free electron and hole upon absorption of photons at room temperature, an organic conjugated semiconductor generates excitons (bound electron-hole pairs) [80].

The major boost in the efficiency of the organic solar cell came up with the introduction of bulk heterojunction structure. In the bulk-heterojunction polymer solar cell, the semiconductive polymer (donor) and fullerene (acceptor) interface are required to dissociate the bound electron-hole pair (exciton) in two separate charge carriers [80] in order to release the electrical power at the load. In this structure, the semiconducting polymer is mixed with the fullerene derivative producing phase separation on a

nanometer scale [81]. The bulk heterojunction solar cell not only provides high surface contacts for charge separation, but also an efficient network for charge separation [82].

The polymer blend of poly (3-hexylthiophene) (P3HT) with fullerene derivative [6,6]-phenyl-C61-butyric acid methyl ester (PCBM) is widely used for polymer solar cells with effective blend bandgap of about 1.8 eV (maximum light wavelength absorbed around 680 nm, shown in **Figure 3-17b**). The molecular structure of P3HT and PCBM is shown in **Figure 3-1** [83], [84]. There has been a tremendous amount of research conducted to enhance the efficiency of the polymer solar cell. For example, Beck *et al.* have demonstrated the improvement in fill factor (*FF*) of organic boron subphthalocyanine chloride (SubPc)/C₆₀ photovoltaic devices using suboptical-wavelength nanostructured electrodes [85]. These nanostructured electrodes efficiently collect charge carriers, thus reducing recombination loss in low mobility organic semiconductors resulting in the improved *FF* [85]. The choice for metal electrode in organic solar cell contributes to improved performance. Vassileva *et al.* compared aluminum (Al) and silver metal electrodes for organic solar cells [86]. The thermally evaporated Al electrodes gave the best results and the post production annealing further improved the performance of P3HT:PCBM devices by eliminating S-shape in *I-V* characteristics [86]. The acidic poly(3,4-ethylenedioxythiophene):poly(styrenesulfonate) (PEDOT:PSS), which is generally deposited between indium-tin-oxide (ITO) electrode and P3HT:PCBM active layer to collect holes efficiently, etches the ITO in the long run reducing the lifetime of the polymer solar cells [87]. Graphene oxide has been used as a hole extracting layer instead of PEDOT:PSS to improve the life time of organic P3HT:PCBM solar cells [88], [89].

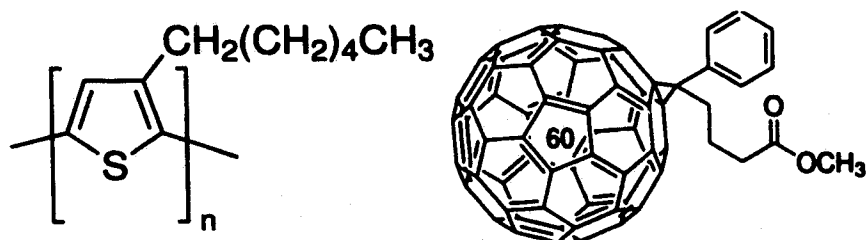


Figure 3-1: The molecular structure of P3HT (left) [83] and PCBM (right) [84].

Some novel techniques have also been used to study the loss mechanisms of polymer devices showing its promising opportunities as a competitive candidate for solar energy harvesting in the near future. Awartani *et al.* have implemented a completely new approach to study the charge recombination losses in bulk-heterojunction organic P3HT:PCBM solar cells by aligning the polymer semiconductor in the plane of the film by applying strain [90]. This study allows the investigation of the morphological origin of recombination losses providing tremendous opportunity to improve the performance of organic solar cells [90]. The new acceptor, Indene-C₆₀ Bisadduct (ICBA), has been introduced by He *et al.* for high performance polymer P3HT:PCBM solar cells [91]. The ICBA has shown stronger visible absorption and higher LUMO energy level compared to PCBM, resulting in higher open circuit voltage and greatly improving the overall performance of the solar cells [91].

In addition to the different aspects of polymer solar cells mentioned above that led to the improvement of performance, the thickness of the active polymer-fullerene layer of organic solar cell has a critical role in the performance of the P3HT:PCBM [92]–[96] and MEH-PPV:PCBM [97] devices. In order for the device to be highly efficient, the solar radiation needs to be efficiently absorbed; thus, the active layer thickness of the P3HT:PCBM device needs to be increased [98]. A substantial amount of work to

understand the effect of surface morphology, temperature, light intensity and optical absorption on the performance of the P3HT:PCBM [70], [91], [99]–[101] and MDMO-PPV:PCBM [100], [102] solar cell has been carried out. However, only several studies have been done on the influence of the active layer thickness to the P3HT:PCBM [92]–[96], MEH-PPV:PCBM [97], Si-PCPDTBT:PC₇₁BM [103] and MDMO-PPV:PCBM [104] polymer solar cell performance. Moule *et al.* in their research demonstrated the effect of active layer thickness on the performance of the bulk-heterojunction P3HT:PCBM solar cells [92]. The authors demonstrated increment in the power conversion efficiency (*PCE*) and short circuit current with P3HT:PCBM thickness with some periodic behavior, but the open circuit voltage remained almost the same [92]. It is worthy to study the dependence of the performance of polymer devices on its active layer thickness in order to achieve highly efficient polymer solar cells and photodetectors. In addition, it is least complicated and cost effective to control the thickness of the active layer of polymer devices rather than using other techniques discussed above for performance enhancement.

In this chapter, the experimental study of the dependence of the *PCE*, external quantum efficiency (*EQE*) and other characteristics of P3HT:PCBM photovoltaic and photodetecting devices are presented. This research project was aimed to address the demand of efficient and cost-effective organic solar cells and photodetectors. This was carried out by fabricating the polymer devices with the basic structure of glass/ITO/PEDOT:PSS/P3HT:PCBM/Al by a solution-processed process with various active layer thicknesses. The optical behavior of different thicknesses of P3HT:PCBM blend, which is the most important characteristics for solar cells and photodetectors, was

explored. In addition, the effect of active layer thickness on device resistance, short circuit current, fill factor, and open circuit voltage were studied.

3.2 Background

3.2.1 Conjugated Polymers

Conjugated polymers are the category of polymers having a backbone chain with alternating double and single bonds [105]. Under certain circumstances, they exhibit semiconductive properties like their inorganic counterparts. Therefore, theoretically they can be used in any optical and electronic devices, such as diodes, solar cells, photodetectors, LEDs, and transistors, the same as inorganic semiconductors [105]. In 2000, Alan J. Heeger, Alan G. MacDiarmid and Hideki Shirakawa received the Nobel Prize in chemistry for their contribution in the discovery and development of conductive polymer [106]. This discovery changed the general concept about the polymers as the insulator. The semiconducting property of a conjugated polymer is due to the movement of π -electrons from one bond to the other in their backbone chain. The conductivity of the conjugated polymers can be controlled via doping the same as inorganic semiconductors, and conjugated polymers with a wide range of conductivity can be synthesized as shown in Figure 3-2.

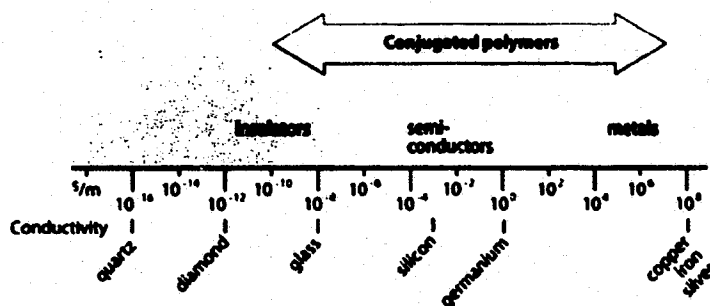


Figure 3-2: The wide range of conductivity of conjugated polymers from insulator to conductor [106].

Analogous to the valence band and conduction band in the inorganic semiconductors, organic semiconductors (conjugated polymers) have the highest occupied molecular orbital (HOMO) and the lowest unoccupied molecular orbital (LUMO). The difference between HOMO and LUMO gives the optical bandgap of these conjugated polymers [80]. The main advantage of conjugated polymer for the electronic devices is their low cost fabrication process. The thin-films of solution processed conjugated polymers used in optoelectronics devices can be fabricated using spin-coating, screen printing, doctor blades, etc. The mass production using roll-to-roll processing is feasible with these devices. In addition, these are extremely flexible and light weight. Some common conjugated polymers are polyacetylene (PA), poly(3-hexylthiophene) (P3HT), polythiophene (PT), polypyrrole (PPy), alkoxy-substituted poly(p-phenylene vinylene) (MEH-PPV), etc. The polyacetylene has metal-like conductivity but has poor thermal stability and processability [108]. MEH-PPV is used in optoelectronics devices such as optical sensors, solar cells, LEDs, etc. due to its environmental stability.

Figure 3-3 shows the common conjugated polymers. In polythiophene along with the alternate double and single bonds, carbon atom are connected by a sulfur atom forming thionyl ring resulting in the shift of the bandgap to the blue and UV range. PT has excellent thermal stability (42% weight loss at 900) and good conductivity of 3.4×10^{-4} to 1.0×10^{-1} S/cm when doped with iodine [105]. However, PT lacks processability. P3HT is the widely used conjugated polymer for organic solar cells and photodetectors. Unlike other conjugated polymers with inherent disorder causing low carrier mobility, P3HT has self-organization of the polymer chains with interchain distance on the order

of 3.8 Å and room temperature mobility up to 0.1 cm²/V.s [105]. However, the mobility of P3HT depends on the processing environment and varies from 0.2 cm²/V.s when processed in inert atmosphere to the poor mobility of 0.045 cm²/V.s when processed in ambient condition [105]. Conjugated polymers are donors in the organic photovoltaic solar cell similar to the p-type semiconductor in inorganic solar cells. These generate electron-hole pair (exciton pair) of absorption of the photon.

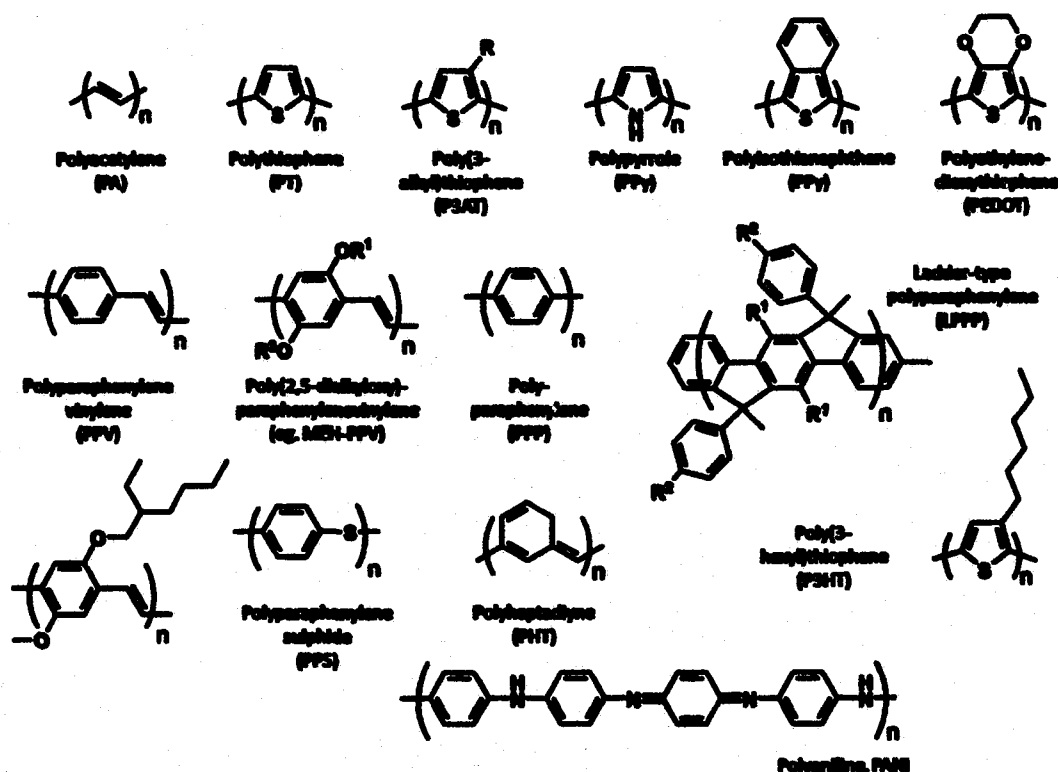


Figure 3-3: Common conjugated polymers [107].

3.2.2 Fullerene Derivatives

After diamond and graphite, fullerene (a closed shell of carbon atoms) is the third allotropic form of carbon. Robert F. Curl, Harold W. Kroto and Richard E. Smalley received the Nobel Prize in chemistry in 1996 for their discovery of fullerenes. Fullerene derivatives are used in bulk heterojunction organic devices as an acceptor similar to the

n-type semiconductor in inorganic devices. Common fullerene derivatives are [6,6]-phenyl-C₆₁-butyric acid methyl ester (PC₆₀BM), PC₇₀BM, indene C₆₀ bis-adduct (IC₆₀BA), and IC₇₀BA as shown in Figure 3-4 [109]. The major role of fullerene derivative is to provide the junction with conjugated polymer in organic devices to dissociate the exciton pair. For this reason, the fullerene derivative must possess two properties. It needs to be soluble in the same solvent as the conjugated polymer to make a solution, and it should have low LUMO energy level compared to conjugated polymer to accept electrons from conjugated polymer. PCBM is the widely used fullerene derivative, especially with P3HT due to its solubility in organic solvent like chlorobenzene and lower LUMO than P3HT. The maximum efficiency of P3HT:PCBM solar is up to 5% [105]. The new fullerene derivative, ICBA is introduced with 0.17 eV higher LUMO energy level compared to PCBM to achieve higher open circuit voltage of up to 0.84 V [91].

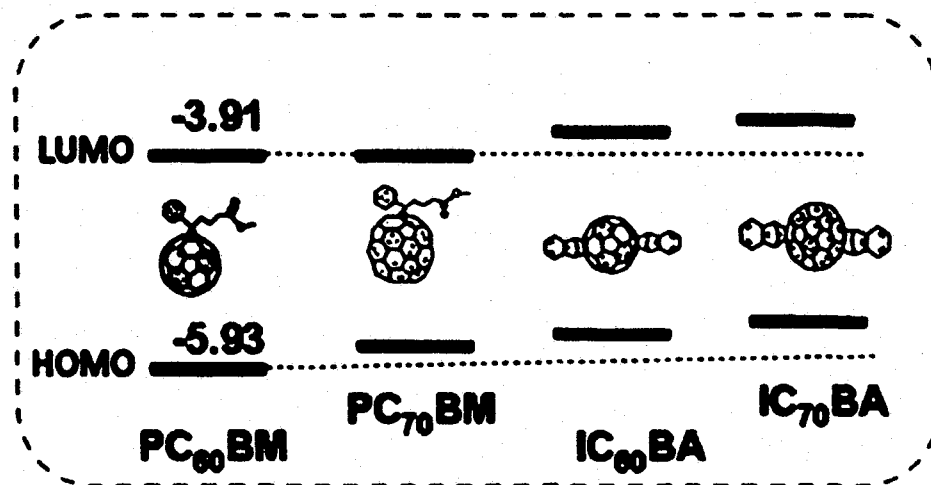


Figure 3-4: Different fullerene derivatives with LUMO and HOMO energy levels used in organic solar cells and photodetectors [109].

3.2.3 Polymer Solar Cells

The basic architecture of polymer solar cells consists of bulk heterojunction of conjugated polymer with high ionization potential (donor) and fullerene derivative with high electron affinity (acceptor) sandwiched between PEDOT:PSS coated ITO positive electrode and a low work function metal negative electrode [80]. The polymer thin-film solar cells are considered as third generation (3G) solar cells following large scale, single junction, bulk silicon wafer based first generation (1G) solar cells, and low-cost thin-film solar cells based on amorphous silicon, CuIn(Ga)Se_2 , CIGS, CdTe/CdS on low-cost substrates in second generation (2G) [80]. Four main steps in electrical power generation from the polymer solar cells are absorption of photon, generation of exciton-pair, dissociation of electron and hole at the junction of donor conjugated polymer and acceptor fullerene derivative, and collection of carriers at the electrodes. When the photon of energy equal to or higher than the bandgap of conjugated polymer incident on the active layer of the organic solar cell, it gets absorbed and generates an electron-hole pair (exciton pair). Unlike in silicon, the bond energy of exciton in conjugated polymer is higher, and it does not dissociate due to thermal energy at room temperature. This exciton pair in organic solar cells acts as a single neutral entity and diffuses to the heterojunction of polymer and fullerene, where the electron is transferred to the LUMO of the acceptor (fullerene derivative) and the hole remains in the HOMO of the donor (conjugated polymer) due to the energy level difference. Finally, the electron is collected at negative low workfunction metal electrode and the hole is collected at the ITO positive electrode. Being a neutral entity, the exciton pair does not care about the electric field. It moves towards junction only due to diffusion. Figure 3-5 shows the overall process of

electricity generation in organic solar cell following the photon absorption, exciton generation, exciton diffusion, exciton dissociation, and carrier collection at the electrodes.

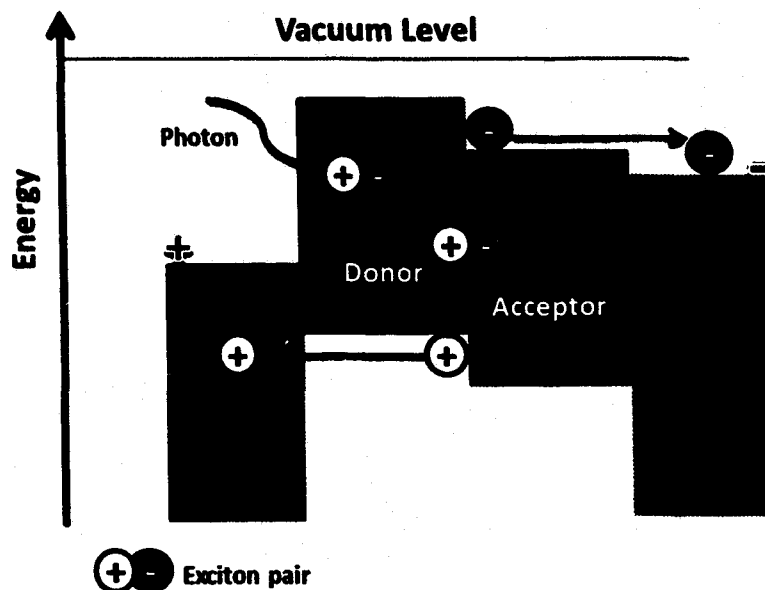


Figure 3-5: The electrical power generation process in polymer solar cell following photon absorption, exciton pair generation, exciton pair dissociation, and carrier collection.

One of the advantages of the organic solar cells compared to the inorganic counterpart is that, on one side only one type of charge carrier (either electron or hole) exists and there is no risk of recombination loss except at the junction. As the dissociation of exciton pair at the junction is key in the organic solar cells, the device architecture of polymer-fullerene active layer needs to be designed to provide proper junction. Three device structures with polymer-fullerene active layer are planer heterojunction (bilayer like in p-n junction), checkerboard type (ideal architecture) with alternate pillars of polymer and fullerene, and bulk heterojunction [110] as shown in Figure 3-6. The checkerboard type is the ideal architecture but difficult to fabricate. The planar

heterojunction has minimum junction area, and most of the exciton pairs are lost in recombination due to their short lifetime before reaching the junction.

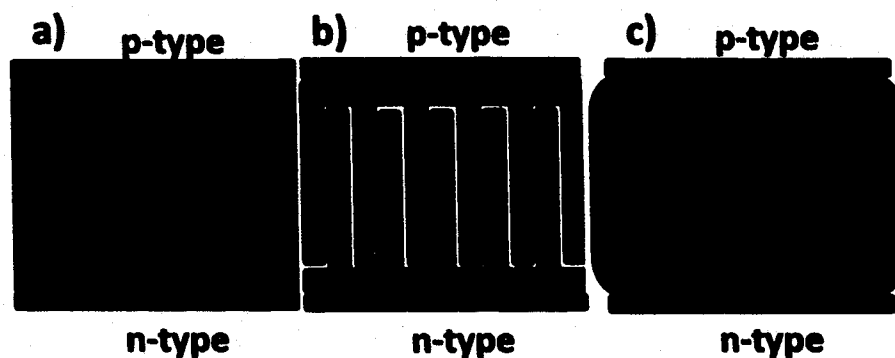


Figure 3-6: Three device architectures of polymer solar cells, a) planar heterojunction, b) checkerboard type architecture, and c) bulk heterojunction architecture.

The bulk heterojunction is most suitable as it provides junctions randomly distributed everywhere to dissociate exciton pairs efficiently, and is easy to fabricate using solution processed deposition techniques. Postproduction annealing has an important role in creation of randomly distributed junction in heterojunction. Annealing helps to segregate the same type of material together and provides the semicontinuous network of donor and acceptor to the electrodes to collect carriers avoiding charge trap islands. However, if the time and temperature of annealing is high, ultimately planar heterojunction is resulted due to the complete segregation of fullerene on one side and polymer on the other side [110]. This is the one reason for the short lifetime of the organic solar cells, as they slowly undergo segregation of donor and acceptor due to the outside temperature under the sun for a long time.

3.2.4 Polymer Photodetectors

Photodetector is the device used to detect the presence of light by converting the optical energy into an electrical signal. The device architecture and electrical power generation process in the photodetector is similar to the one in the solar cells; however, the principle of operation is different. Solar cell generates the electrical power for the external load and no external bias is required. However, in the photodetector, external reverse bias is applied and the photo-generated carriers are collected, which is proportional to the incident optical power. The fourth quadrant represents solar cell operation in I - V curve while the third quadrant is for photodetector. The Figure 3-7 shows the equivalent circuit model of the photodetector, where I_{PD} is the photocurrent, I_D is the dark current and I_{out} is the total output current released to the load [111]. Under dark condition, when the photodetector is reversed biased very small dark current flows which depends on the temperature and properties of the material. When the photodetector is illuminated with light, absorption of photons creates more charge carriers increasing the output current at the load. The photocurrent in the circuit is given by

$$I_{PD} = I_{out} - I_D. \quad \text{Eq. 3-1}$$

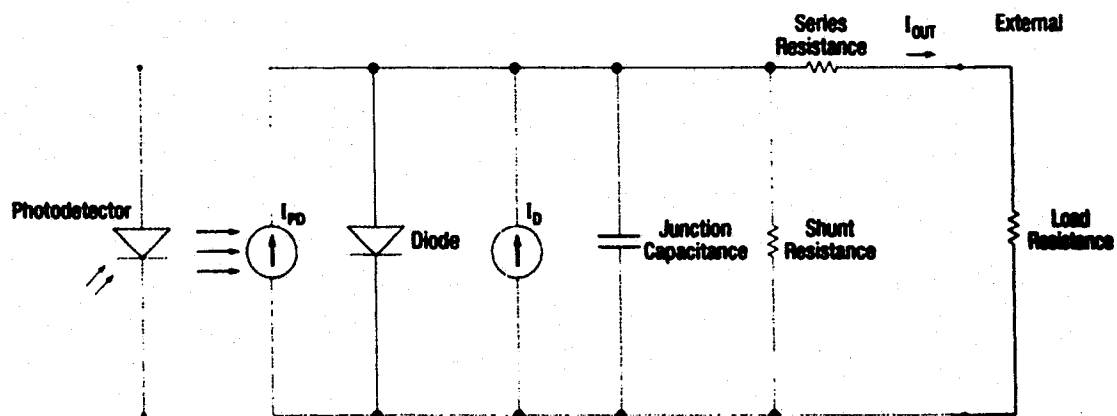


Figure 3-7: Equivalent circuit model of photodetector [111].

3.2.5 General Device Characterization and Parameters

3.2.5.1 Solar Cell

The solar cell is characterized by the J - V curve under illumination and important parameters of the solar cell are short circuit current density, open circuit voltage, maximum power current density and voltage, series and shunt resistances, fill factor, and PCE . Please see Section 2.2.2 for detail.

3.2.5.2 Photodetector

The photodetector is the device that generates electrical power when a photon with a specific wavelength incidents on it. The photodetector is characterized by the J - V curve in the third quadrant with monochromatic light. Different parameters to consider while characterizing the photodetector are photocurrent density, responsivity, internal quantum efficiency, and external quantum efficiency.

Photocurrent density, J_{ph} (A/cm^2): The photo-induced current density when the photon of a specific wavelength incidents on the photodetector. The photocurrent density depends on the wavelength of the incident photon, the incident optical power and external bias voltage. If the current density under dark is J_D and the current density under light is J_L , then the photocurrent density is

$$J_{ph} = J_L - J_D. \quad \text{Eq. 3-2}$$

Responsivity, R (A/W): It is the ratio of the electrical current generated to the incident optical power. It is the response of the photodetector per unit incident optical power. It depends on the wavelength of light and bias voltage. If P_0 is the incident optical power density at particular wavelength, then

$$R = \frac{J_{ph}}{P_0}. \quad \text{Eq. 3-3}$$

External Quantum Efficiency, EQE (%): It is the ratio of number of charge carriers extracted from the device to the number of incident photons of particular wavelength and given by

$$EQE = \frac{J_{ph}/e}{P_0\lambda/hc} = R \frac{hc}{\lambda e}. \quad \text{Eq. 3-4}$$

Where J_{ph} is the photocurrent density, P_0 is the input optical power density at particular wavelength λ , e is the elementary charge and h is the Planck's constant.

Internal Quantum Efficiency, IQE (%): The ratio of the number of charge carriers collected at the electrode to the number of absorbed photons within the photodetector. Not all incident photons get absorbed within the photodetector; some of them reflected back and some transmitted through the device. If R is the reflected and T is the transmitted portions of the incident optical power, then the IQE is given by

$$IQE = \frac{EQE}{1 - R - T}. \quad \text{Eq. 3-5}$$

3.3 Experimental Methods

3.3.1 Fabrication

The fabrication of polymer solar cells and photodetectors with P3HT:PCBM active layer was carried via microfabrication techniques. The air-processed fabrication process of the polymer devices was used [112]. The basic structure of the polymer solar cell and photodetector consists of glass/ITO/PEDOT:PSS/P3HT:PCBM/Al; the cross-section of the device is shown in **Figure 3-8**. The CB-40IN indium tin oxide (ITO), thickness of 150-200 nm and sheet resistance of 4-10 Ω /sq, on $25 \times 25 \times 1.1$ mm borosilicate glass substrate (Delta Technologies) was used as an anode [113]. The water soluble hole transport layer, poly (3,4-ethylenedioxythiophene):

poly(styrenesulfonate) (PEDOT:PSS), (Sigma-Aldrich and Heraeus Holding GmbH, shown in **Figure 3-8**) was deposited between the active layer and ITO to collect photo-generated holes at anode effectively. The blend of Poly(3-hexylthiophene):[6,6]-phenyl-C61-butyric acid methyl ester (P3HT:PCBM) (Sigma-Aldrich) [83], [84] was used as an active layer of the device. The thermally deposited aluminum thin film was used as a cathode. **Figure 3-9** shows the energy band diagram of the polymer device which explains the dissociation of photo-generated exciton pair due to the difference of works function of various layers, resulting in the collection of the hole at ITO and the electrons at aluminum. The fabrication process consists of ITO patterning, polymer-fullerene solution preparation, active layer deposition, and electrode deposition and contact wiring. Each step of the fabrication process is described in detail.

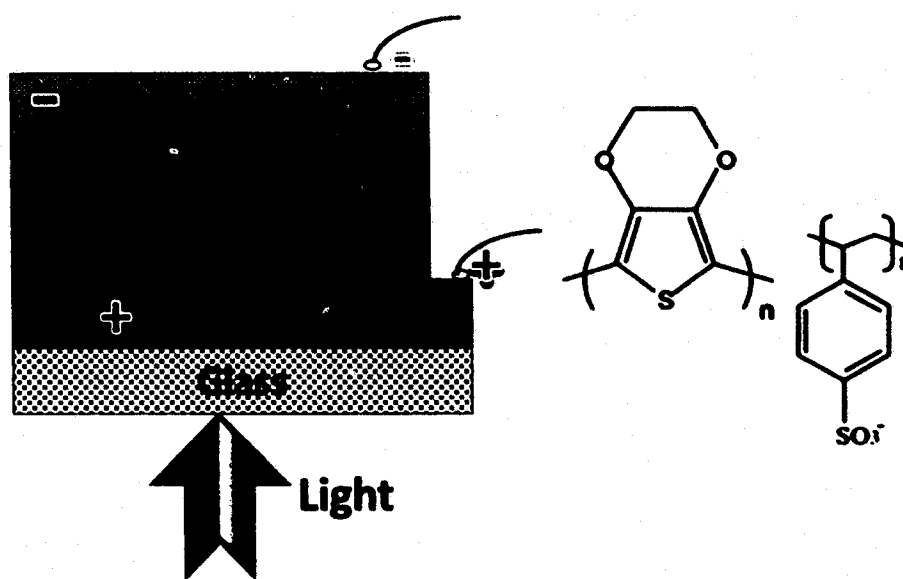


Figure 3-8: Glass/ITO/PEDOT:PSS/P3HT:PCBM/Al device cross section and charge generation and separation when illuminated with light (left) and molecular formula of PEDOT:PSS (right).

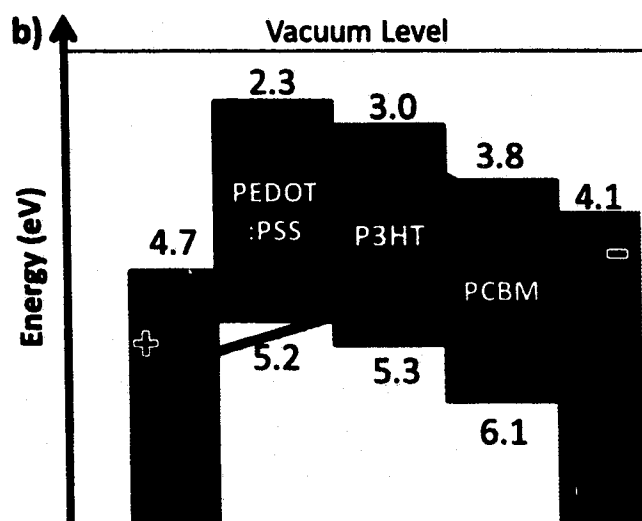


Figure 3-9: Energy level diagram of ITO/PEDOT:PSS/P3HT:PCBM/Al solar cell [80].

ITO patterning using photolithography

The standard photolithography technique was used to pattern ITO on a glass substrate such that six independent devices were fabricated on each substrate. The ITO patterning procedure follows as:

- ITO substrate cleaning by rinsing with acetone, isopropyl alcohol (IPA) and Deionized (DI) water, and drying the substrate with nitrogen blow.
- Spin-coating (CEE 100 spin coater) ITO substrate with Shipley PR 1813 positive photoresist @ 1500 RPM, 504 RPM/sec for 30 seconds.
- Soft baking (pre baking) the photoresist film on a hot plate (IKA RCT BASIC S1) @ 90°C for 5 minutes.
- Aligning the transparency plastic mask, shown in **Figure 3-10** (left), on top of the photoresist film. The white region defines the ITO etch region and ITO remains only on the dark region.
- Exposure of the photoresist film aligned with the transparency mask under 365 nm ultraviolet light (BLAK-RAY B 100 AP UV lamp) for 18 minutes.

- f. Development of the exposed photoresist film in MF-319 developer bath followed by DI water rinse, and drying with N₂ blow. The photoresist was completely removed from the exposed region. This process takes about 1-2 minutes.
- g. Hard baking of developed photoresist film on the hot plate @ 110°C for 10 minutes to remove any residue.
- h. ITO etching from exposed portions by submersing in 20% hydrochloric acid (HCl) bath warmed at 75°C for 3 minutes or until the targeted ITO etched away completely.
- i. Removing the remaining photoresist with an acetone rinse.

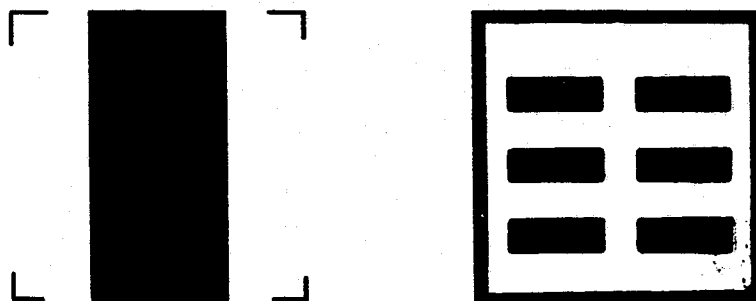


Figure 3-10: Shared anode transparency mask for photolithography to pattern ITO on glass substrate (left), and stainless steel shadow mask to define cathode regions (right).

After patterning the ITO, the substrate was cleaned thoroughly by sonicating (BRANSON 2510 Ultrasonic) with acetone, IPA and DI water baths in petri dishes, 10 minutes each. Then the substrate was dried on a hotplate @ 150°C for 15 minutes after a N₂ blow. The substrate was now ready for active layer deposition.

Polymer-fullerene (P3HT:PCBM) solution preparation

- a. P3HT and PCBM were measured (AND HR-60 scale) within N₂ glovebox in separate vials, based on the desired concentration and quantity of the solution. The same amount of P3HT and PCBM was used to get a 1:1 ratio wt. of P3HT and PCBM.

- b. Chlorobenzene solvent was added in each vial of P3HT and PCBM based on the desired concentration and quantity of the solution with magnetic stir bar.
- c. Both vials were taken out of the glovebox and placed on the stirring hotplate @ 50°C for 15-18 hours.
- d. Both solutions were then filtered with 0.45 μm polytetrafluoroethylene (PTFE) filters and mixed in a single new vial with a new magnetic stir bar, and allowed to stir for an additional 1 hour on the hotplate @ 50°C.

The amount of P3HT, PCBM and chlorobenzene were calculated based on the desired concentration and quantity of the final P3HT:PCBM blend solution. For example, to prepare 4 ml of the blend solution with 9 mg/ml concentration of both P3HT and PCBM (1:1 ratio by wt.), 4 ml of chlorobenzene and 36 mg (9 times 4) of each P3HT and PCBM is required.

Active layer deposition

The PEDOT:PSS was transferred in a new vial from the refrigerator, kept in room temperature for 30 minutes, and sonicated for 10 minutes before deposition. Approximately, 1 ml of PEDOT:PSS is required for a 25 \times 25 mm substrate.

- a. Inside a class 100 clean room, PEDOT:PSS was filtered with 0.45 μm polyvinylidene fluoride (PVDF) filter and spin-coated with a micropipette (ACURA 815) onto a substrate @ 3500 RPM for 30 seconds to deposit about 50 nm film.
- b. PEDOT:PSS was washed away at one edge to define common ITO contact as anode with water using swab.
- c. Then the PEDOT:PSS thin film was annealed @ 110°C for 10 minutes to remove water residue.

- d. The P3HT:PCBM solution was then dynamically dispensed with a micropipette (ACURA 825) while the substrate was rotating to deposit a uniform film. Approximately, 200 μ l is required for a 25 \times 25 mm substrate.
- e. P3HT:PCBM was washed away at one edge, the same location from where PEDOT:PSS was washed away in the previous step, for common ITO contact with chlorobenzene (or, chloroform) using a swab.
- f. The P3HT:PCBM thin film was baked @ 70°C for 5 minutes to remove any solvent.

The speed of spin-coating in rounds per minute (RPM), and the concentration of P3HT and PCBM in the solution influence the thickness of the active layer in the polymer device. The polymer devices of various thicknesses from 20 nm to 345 nm were fabricated by varying P3HT:PCBM concentrations from 9 mg/ml to 18 mg/ml, and spin coating speed from 600 to 2500 RPM. **Figure 3-11** shows the thickness of the polymer device for various polymer-fullerene concentrations and spin-coating RPM. The temperature and humidity inside the clean room during the device fabrication were 20.9°C \pm 1.6% and 53% \pm 6.7%, respectively. **Table 3-1** gives the fabrication parameters for solar cells and photodetectors.

Table 3-1: Fabrication parameters for solar cells and photodetectors.

Parameter/Material	Value/type
Solvent	Chlorobenzene
P3HT Concentration	9 mg/ml - 18 mg/ml
P3HT:PCBM Ratio	1:1 wt.
Additive (OT)	0% vol.
Spin Coating Recipe	600 RPM - 2500 RPM for 50 s
Thickness	20 nm - 345 nm (Surface Profiler)
PEDOT:PSS	3500 RPM, 30 s, ~ 50 nm
Ambient Conditions	20.9°C ± 1.6%, 53% ± 6.7% Humidity
Aluminum	100 nm, 0.4 nm/s, 10 ⁻⁶ Torr (Thermal evaporator)
Annealing	150°C, 15 min (Post-production)
Contact Wire	0.25 mm dia. Copper wire
Epoxy	Conductive silver epoxy

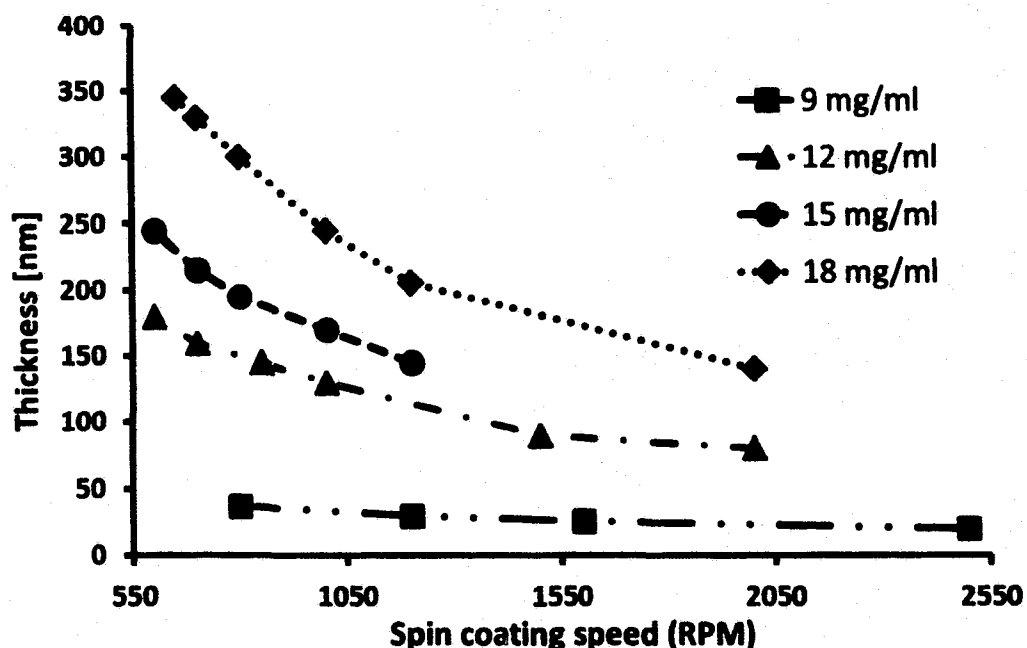


Figure 3-11: P3HT:PCBM active layer thickness, versus spin coating speed with concentration processing solution of both P3HT and PCBM in chlorobenzene as a parameter.

Electrode deposition and contact wiring

- After active layer deposition, the sample was placed on a sample holder and aligned with the stainless steel shadow mask shown in Figure 3-10 (right).

- b. The sample was transferred inside the Denton DV-502A thermal evaporator to deposit the 100 nm thin film of aluminum cathode electrode. The deposition was carried at the base pressure of 10^{-6} Torr at the rate of 4 Å/sec.
- c. Substrate was annealed @ 150°C for 15 mins.
- d. Copper wires were connected at the anode and cathode electrodes using a conductive silver epoxy (Electron Microscopy Sciences), and finally the epoxy was cured @ 75°C for 20-25 minutes.

Figure 3-12 shows the step-by-step fabrication process of P3HT:PCBM polymer device. Six independent devices each with active an area of 3 mm × 3.5 mm with shared anode architecture were fabricated on each substrate. The Figure 3-13 shows the top view of six devices on a single substrate and cross-section of a single device, and ready to test device.

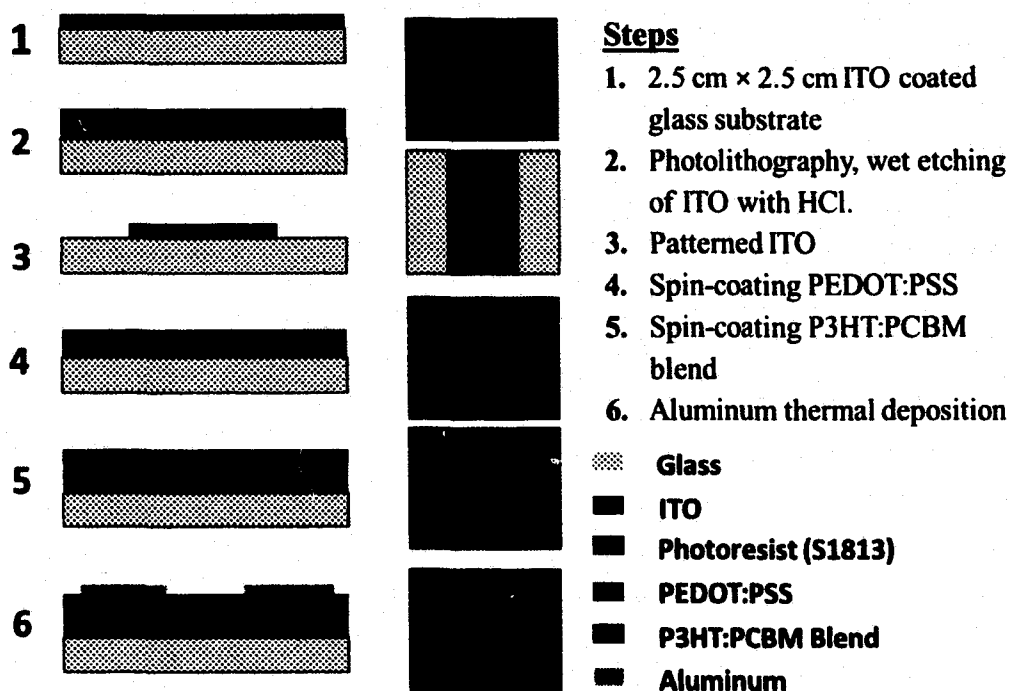


Figure 3-12: The step-by-step fabrication process of photovoltaic stack with P3HT:PCBM active layer.

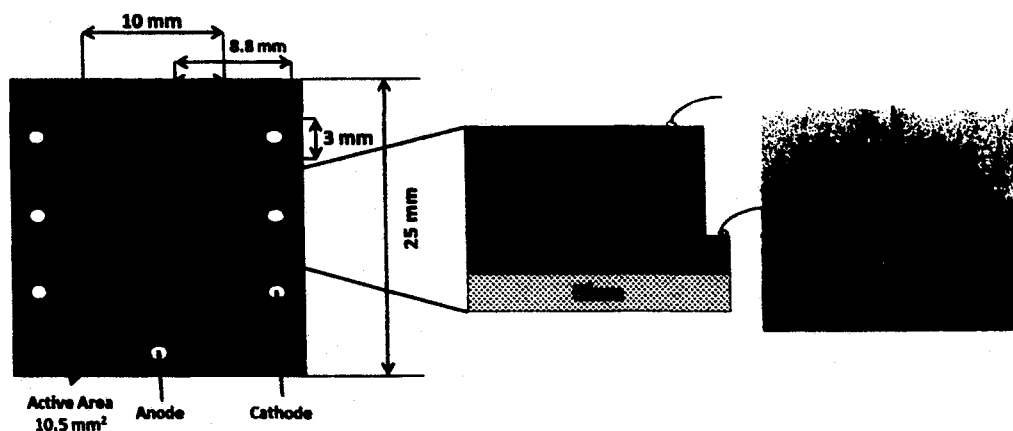


Figure 3-13: The top view of six polymer devices on a single substrate and cross section of a single device (left), and ready to test device (right).

3.3.2 Test Setup

3.3.2.1 Solar Cell Testing

The solar cells were tested under solar simulator and $I-V$ characteristics were measured with the Keithley 2400 sourcemeter. The schematic of the solar cell testing is shown in Figure 3-14. A Spectra Physics 66900 solar simulator with 100 W xenon arc lamp powered by Oriel 69907 power supply was utilized to simulate the AM1.5 solar spectrum. The AM1.5 represents the standard solar spectrum at the Earth's surface which accounts for global tilt as well as the various sources of absorption in the atmosphere. The output power density from solar simulator was measured with Oriel 91150V calibrated reference solar cell and adjusted to 1000 W/m^2 (corresponding to AM1.5). The solar cells were mounted on a sample holder and placed beneath the opening of the solar simulator where simulated solar spectrum incidents on it. The anode and cathode of the solar cells were connected with Keithley 2400 sourcemeter to measure $I-V$ characteristics of the solar cells. The Keithley sourcemeter was operated from the PC equipped with LabView program. The bias voltage was typically swept from -1 V to +1 V in increments

of 0.05 V. Then each measured current (I) value were divided by the active area of the device, 10.5 mm^2 , to obtain the current density (J). The J - V characteristics were analyzed to calculate various solar cell parameters such as short circuit current, open circuit voltage, series and shunt resistances, and fill factor and power conversion efficiency.

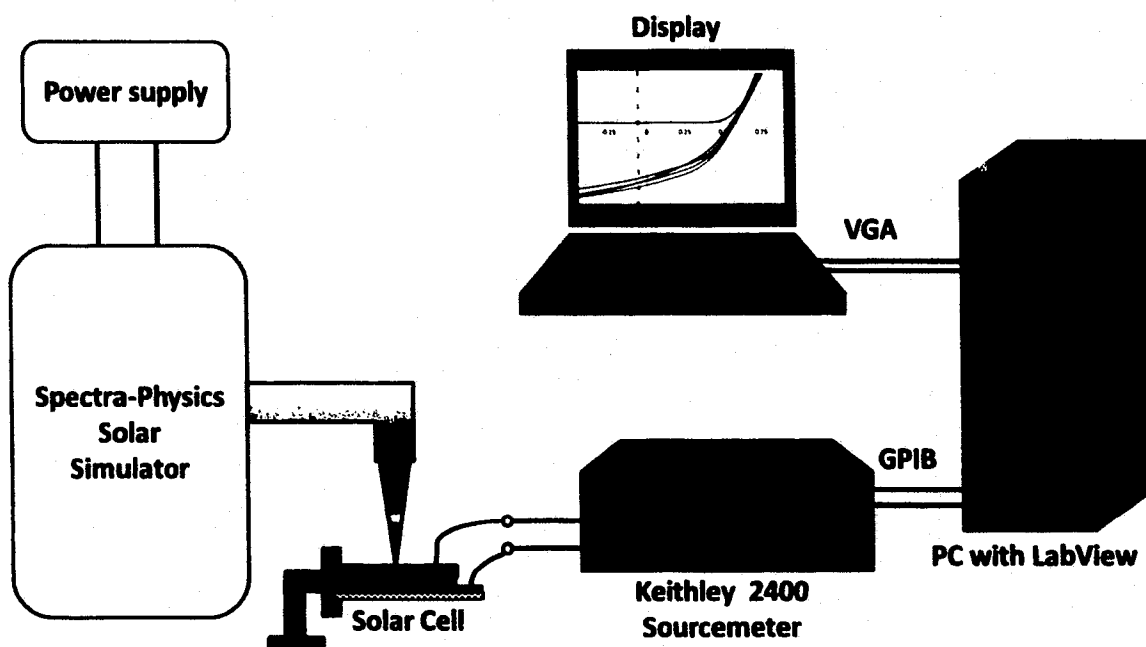


Figure 3-14: Schematic of the solar cell testing setup.

3.3.2.2 Photodetector Testing

The electrical characterization of polymer photodetectors was carried out with the monochromator, which illuminated the polymer device with selected single wavelengths ranging from 350 nm to 750 nm. The schematic for the polymer photodetector testing is shown in Figure 3-15. The light from HLX 64625 100 W quartz tungsten halogen source in an Oriel 60005 housing was launched into the Oriel Cornerstone 265 1/4m monochromator (model 74100) through a slit of 0.35 inches wide. Inside the monochromator, the mirrors and the grating system splits the light into constituent colors. The monochromatic light then exits via another 0.35-inch wide slit and focuses on the

polymer photodetector with the help of the lens setup. Before each polymer photodetector testing, the spectral optical power density was measured with Newport 818-UV calibrated silicon photodiode (placed in same position as the photodetector) and Newport 1936-R power meter, and was recorded in the PC through LabView software. During photodetector testing, the Keithley 2400 sourcemeter remotely controlled with the LabView software was used to measure the I - V characteristics from -4 V to +1 V in increments of 0.2 V for each wavelength from 750 nm to 350 nm in intervals of 10 nm. These I - V characteristics and spectral optical power density were then used to calculate the photocurrent density, responsivity and EQE of the photodetector at particular bias voltage and wavelength.

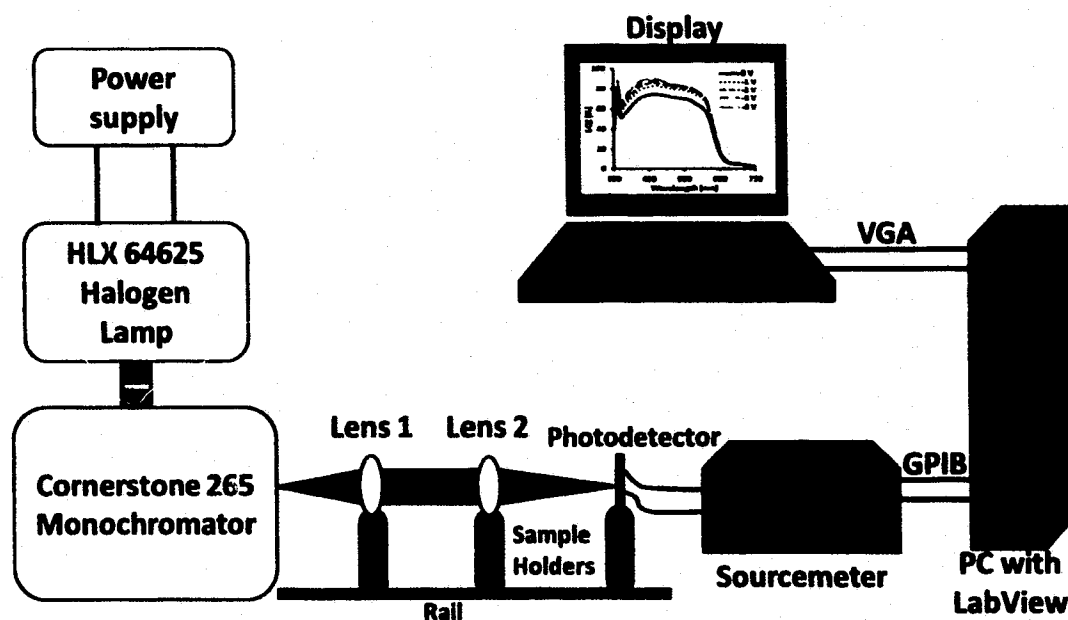


Figure 3-15: Schematic of the photodetector testing setup.

3.4 Results and Discussion

3.4.1 Imaging of Surface Morphology of P3HT:PCBM Film

The surface morphology of P3HT:PCBM thin film on the quartz substrate was studied using LEICA DM4000 M optical microscope and Hitachi S-4800 scanning electron microscope (SEM). Figure 3-16 shows, a) optical microscope image of the top view of P3HT:PCBM thin film at 100x magnification, b) optical microscope image of P3HT:PCBM and aluminum cathode interface at 20x magnification, c) SEM image of the top view of P3HT:PCBM, and d) a cross-section view of PET/ITO/PEDOT:PSS/P3HT:PCBM/Al film under SEM. The beam voltage of SEM was set to 1 kV and the working distance was 5 mm.

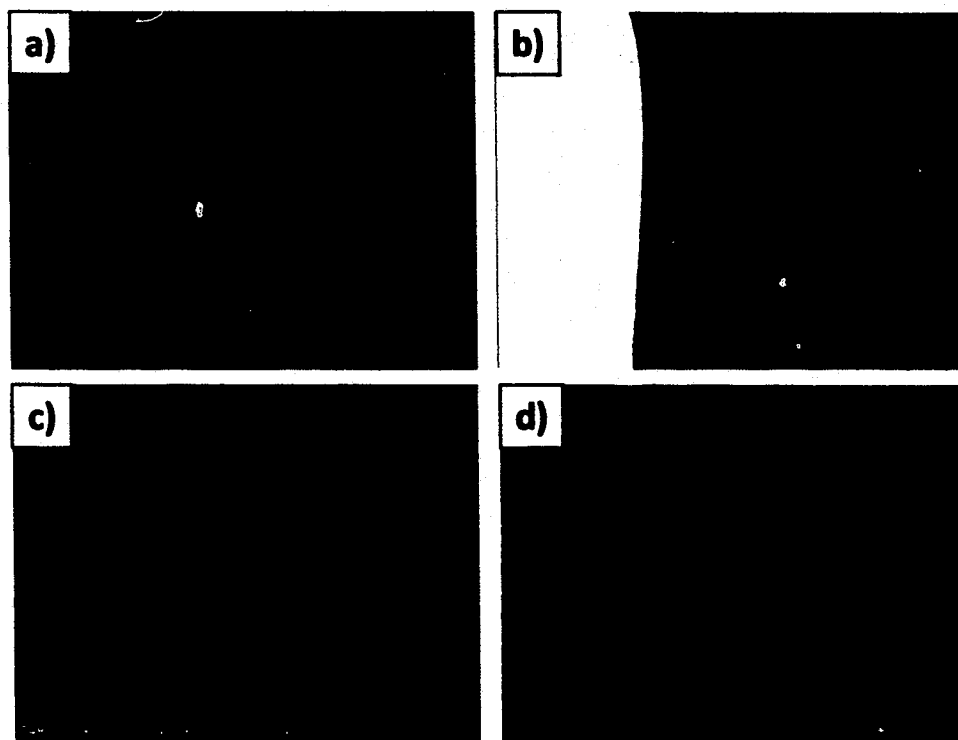


Figure 3-16: a) Optical microscope image of P3HT:PCBM thin film surface at 100x magnification, b) Optical microscope image of the interface of P3HT:PCBM film and aluminum cathode at 20x magnification, c) Top view of SEM image of P3HT:PCBM blend layer under SEM, and d) Cross-section of PET/ITO/PEDOT:PSS/P3HT:PCBM/Al film under SEM.

3.4.2 Optical Characterization

The light interaction properties of the semiconductive materials used in optical devices such as solar cell and photodetector are important to define and understand the device's performance. The optical parameters such as reflectance, transmittance, absorbance, refractive index, and extinction coefficient of the thin film material must be studied prior to their application in the solar cell and the photodetector. These optical properties determine the amount of light absorbed within the material when light incidents on it. The Filmetrics F10-RT reflectometer was used for optical characterization of P3HT:PCBM active layer. Filmetrics is easy to operate, very precise and non-destructive tool for the optical characterization of thin films. It measures the spectra of reflectance and transmittance of the sample simultaneously. It can measure the refractive index, extinction coefficient and thickness of the film precisely with the proper recipe. Different materials have their own Filmetrics recipe, which is a model developed for particular material using reflectance and transmittance information. The F10-RT model of Filmetrics can measure the thickness in the range of 15 nm to 70 μm and operates in the wavelength range of 380 nm to 1050 nm. Once the reflectance (R) and transmittance (T) spectra were obtained from Filmetrics, the absorbance (A) was calculated using $A = 1 - (R + T)$.

The effect of P3HT:PCBM active layer's thickness on the optical characteristics was investigated. **Figure 3-17** shows the transmittance and absorbance spectra of various thicknesses of P3HT:PCBM thin films on a quartz substrate, and the optical characteristics (transmittance, reflectance and absorbance) of the quartz substrate itself. As the thickness of P3HT:PCBM film increased absorption within the film is also

increased with the reduction in transmittance. Thicker film provides more material that absorbs more light compared to thinner films. This suggests that thicker films of P3HT:PCBM probably perform better as a solar cell and photodetector where high absorption of incident light is desired. The absorbance spectrum in **Figure 3-17(b)** shows that the longest wavelength absorbed by P3HT:PCBM blend is around 680 nm, which gives the effective bandgap of P3HT:PCBM blend of about 1.8 eV. The bandgap energy is the minimum photon energy that gets absorbed and can be written in terms of wavelength (λ), Planck's constant (h) and speed of light (c) as

$$E = \frac{hc}{\lambda}. \quad \text{Eq. 3-6}$$

The complex refractive index of any material is defined mathematically as [17],

$$\vec{n} = n + ik. \quad \text{Eq. 3-7}$$

Where n is the real part of the complex refractive index, called the refractive index, which indicates phase velocity, and k is the imaginary part called the extinction coefficient. The extinction coefficient is related to the absorption coefficient (α) of the material and wavelength (λ) as

$$\alpha = \frac{4\pi}{\lambda} k. \quad \text{Eq. 3-8}$$

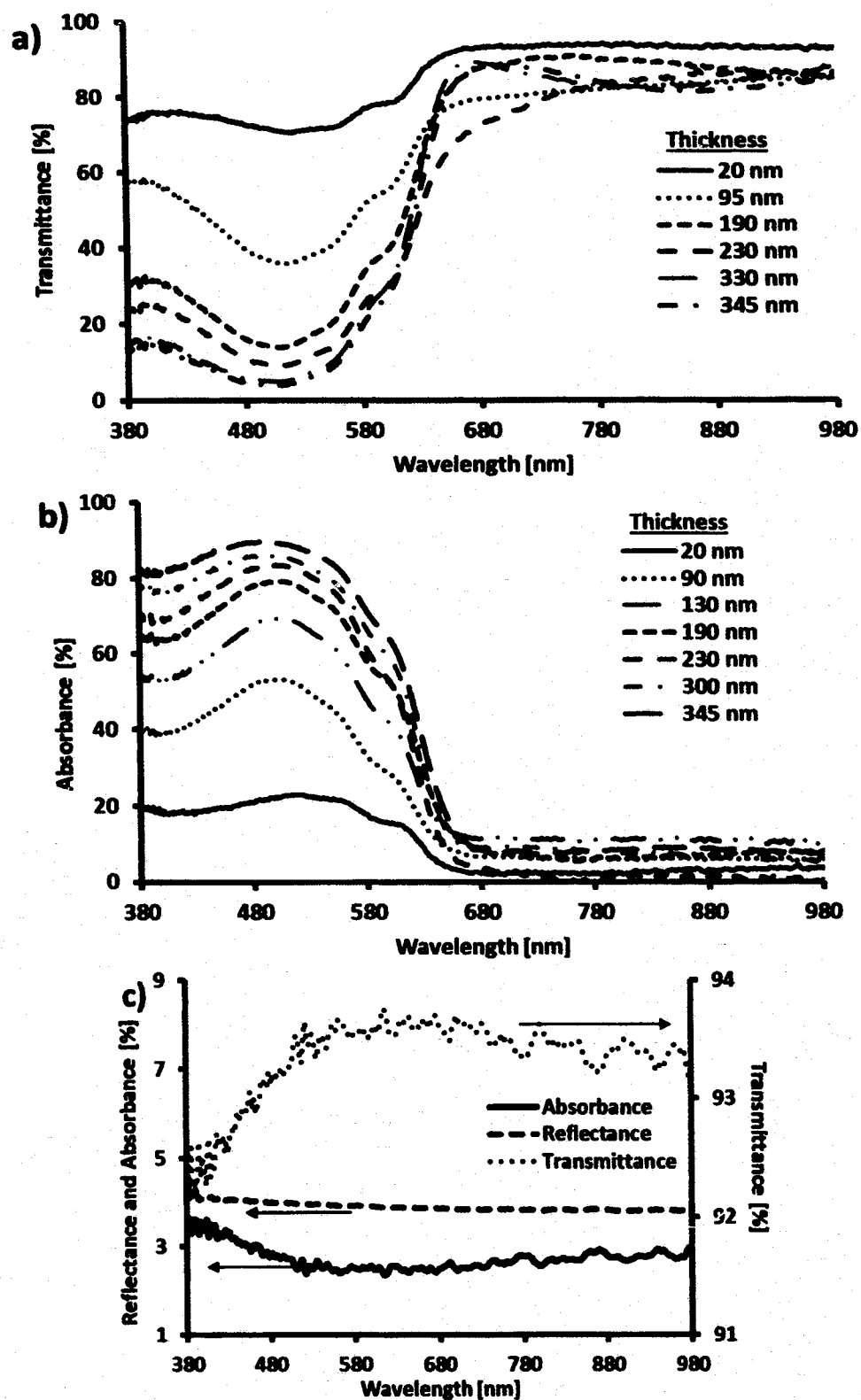


Figure 3-17: a) Transmittance, and b) Absorbance spectra of various thicknesses of P3HT:PCBM thin-films on a quartz substrate, c) Transmittance, reflectance and absorbance of quartz substrate measured with Filmetrics F10-RT reflectometer.

Figures 3-18(a) and 3-18(b) show the optical constants n and k of P3HT:PCBM blend of various thicknesses, respectively. The absorption coefficient (α) can also be calculated from transmittance knowing that the thickness (t) of the film using Beer-Lambert law as

$$\alpha = \frac{-\ln[T]}{t}. \quad \text{Eq. 3-9}$$

Figure 3-18(c) shows the absorption coefficient calculated from extinction coefficient using Eq. 3-8 and Figure 3-18(d) shows the absorption coefficient calculated from transmittance using Eq. 3-9.

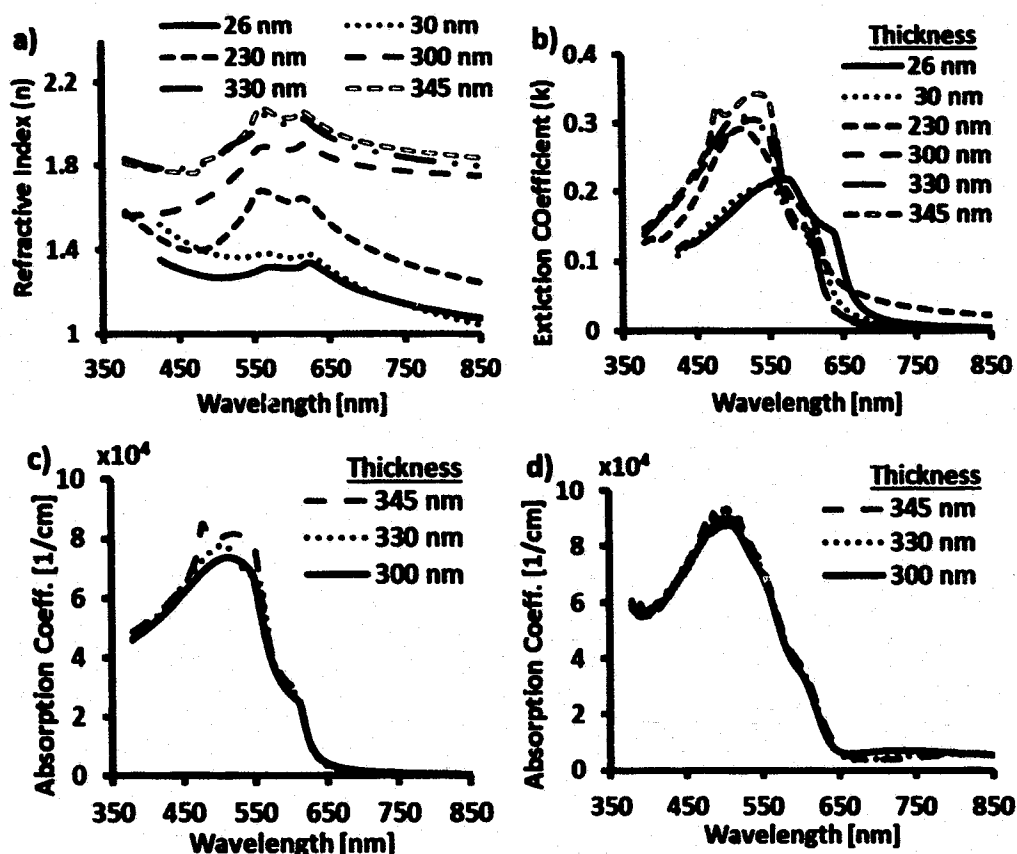


Figure 3-18: Optical constants of P3HT:PCBM blend of various thicknesses, a) refractive index (n), b) extinction coefficient (k), c) absorption coefficient (α) calculated from extinction coefficient, and d) absorption coefficient (α) calculated from transmittance.

3.4.3 Thickness Measurement

The thickness of P3HT:PCBM thin films on the quartz substrates were measured with Veeco Dektak 150 Surface Profiler and Filmetrics F10-RT using a recipe of P3HT:PCBM 1:1 wt. provided by filmetrics.com. The Veeco Dektak 150 Surface Profiler uses contact stylus technique and has a vertical resolution of 1 Å maximum. The contact profilometer has an advantage in dirty environments where contact with the surface avoids the error in measurement caused by any surface contaminants. The F10-RT model of Filmetrics can measure the thickness in the range of 15 nm to 70 µm.

3.4.4 Solar Cell Electrical Characterization

The photovoltaic J - V characteristics were measured for electrical characterization of polymer solar cells of structure glass/ITO/PEDOT:PSS/P3HT:PCBM/Al for various thicknesses of P3HT:PCBM active layer. **Figure 3-19** shows the J - V characteristics and P - V characteristics of polymer solar cell for various P3HT:PCBM active layer thickness. The J - V characteristics show the short circuit current density and the open circuit voltage, whereas P - V characteristics show the trend of the harvested output electric power density P versus the voltage across the solar cell V . The electrical current and harvested electrical power from polymer solar cell was found to have increased with the active layer's thickness. **Table 3-2** shows the solar cell characteristics, such as short circuit current density (J_{SC}), open circuit voltage (V_{OC}), maximum power point current density (J_{MP}) and voltage (V_{MP}), power conversion efficiency (PCE), fill factor (FF), series resistance (R_S) and shunt resistance (R_{Sh}), for various thickness of P3HT:PCBM active layer. The role of the active layer's thickness was investigated on various solar cell parameters. The measurement error calculation is shown in Appendix B.

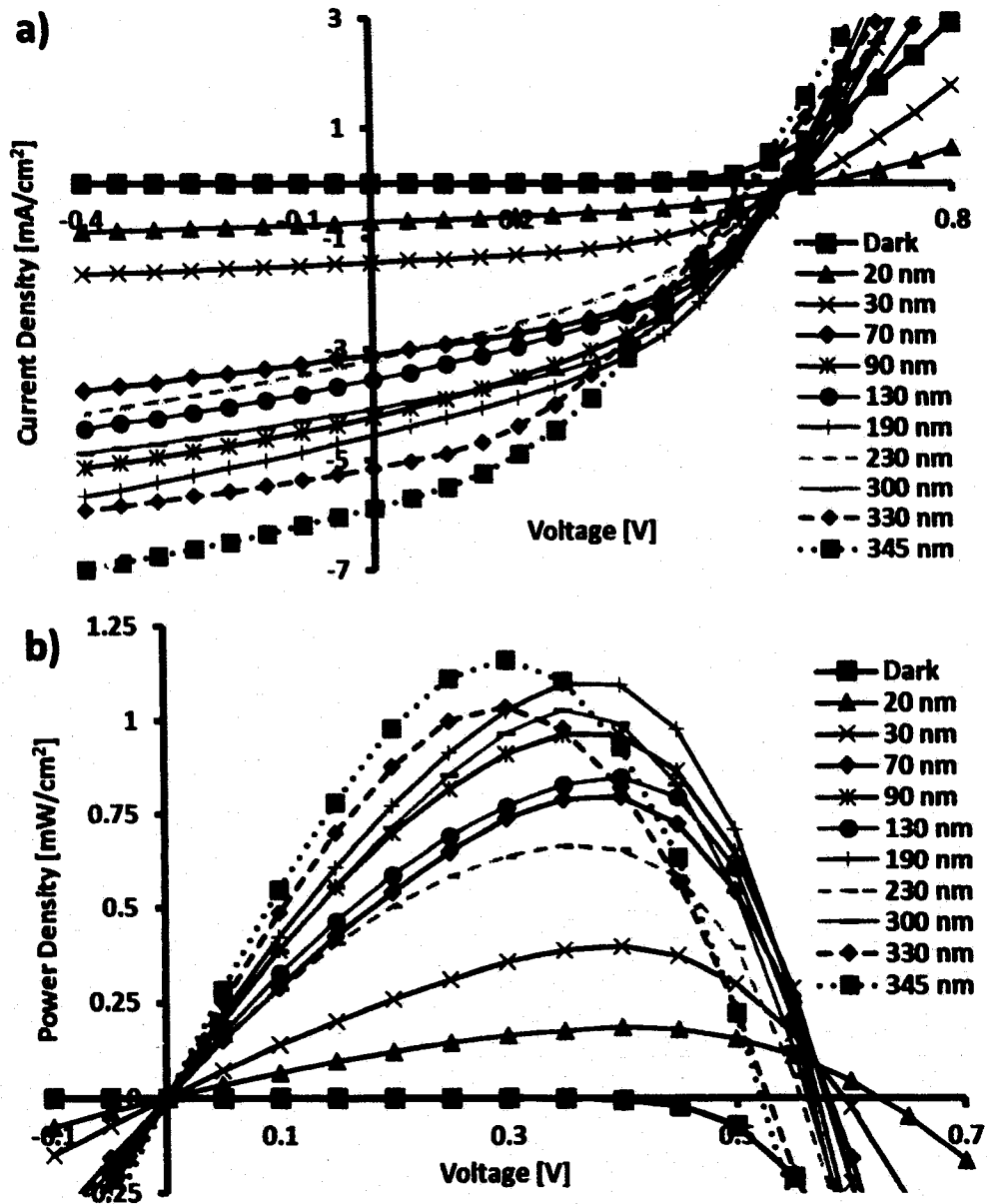


Figure 3-19: a) J - V characteristics, and b) P - V characteristics of polymer solar cells for different P3HT:PCBM active layer's thicknesses.

Table 3-2: Solar cell characteristics for different P3HT:PCBM active layer's thickness.

Thickness (nm)	J_{SC} (mA/cm ²)	V_{OC} (V)	J_{MP} (mA/cm ²)	V_{MP} (V)	PCE (%)	FF (%)	R_S (k Ω)	R_{Sh} (k Ω)
26	0.72	0.57	0.47	0.33	0.16	36.2 ±0.8	5.94	18.0
70	3.54	0.58	2.40	0.36	0.86	42.0 ±0.9	0.64	4.28
90	3.79	0.58	2.33	0.36	0.83	38.0 ±0.8	0.61	3.08
140	4.03	0.57	1.82	0.25	0.44	19.4 ±0.5	3.34	1.38
190	3.67	0.56	2.38	0.36	0.85	41.7 ±0.9	0.53	3.86
230	4.63	0.55	2.79	0.20	0.56	22.0 ±0.7	2.87	1.75
330	4.80	0.53	3.20	0.30	0.96	38.1 ±0.9	0.65	3.86

3.4.4.1 Effect of Active Layer Thickness on Short Circuit Current

The short circuit current density (J_{SC}) increased with the device's thickness. The thicker film has more semiconducting material and absorbs more light compared to a thinner film, resulting in more photo-generated exciton pairs, and more exciton generation eventually results in higher current from the solar cell. Figure 3-20 shows

increasing short circuit current density while an active layer's thickness of solar cell increases.

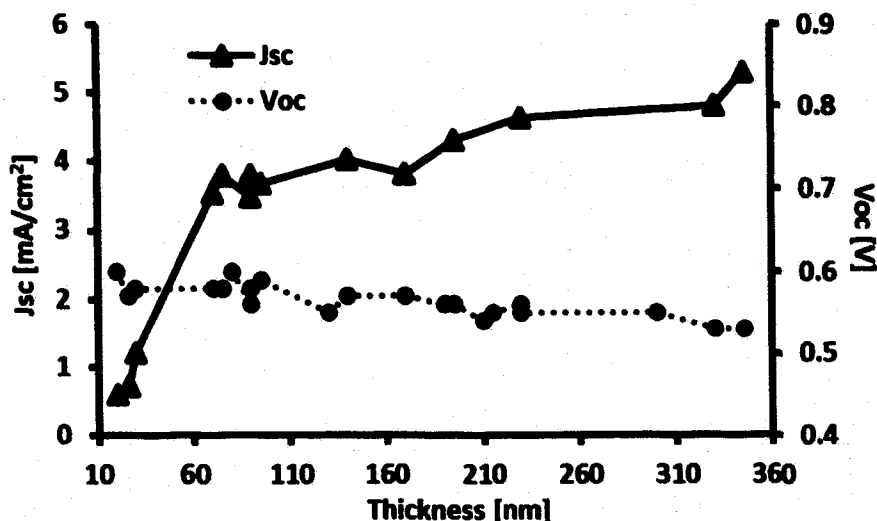


Figure 3-20: Short circuit current density (J_{SC}) and open circuit voltage (V_{OC}) of P3HT:PCBM polymer solar cells for various active layer's thicknesses.

3.4.4.2 Effect of Active Layer Thickness on Open Circuit Voltage

The open circuit voltage (V_{OC}) across the polymer solar cell was reported to have almost the same value with a small drop as thickness increased as seen in **Figure 3-20**. The energy level difference between the LUMO of PCBM and the HOMO of the P3HT limits the maximum achieved V_{OC} in P3HT:PCBM based solar cells [91], [95], [114]. Since the open circuit voltage depends mostly in the difference of work functions of electrodes, the thickness of the active layer does not affect it much. However, for thick devices, series resistance increase [92] and the internal electric field decreases due to the larger distance between electrodes, and the open circuit voltage dropped slightly. It should be noted that the internal voltage developed within the polymer device is the same for both thinner and thicker devices due to the same difference of work functions of

electrodes, but the internal electric field is determined by the distance between electrodes, which is stronger for thinner devices compared to thicker.

3.4.4.3 Effect of Active Layer Thickness on Resistance

The series resistance increased with the active layer's thickness due to the rise in the total number of charge traps within the active layer volume that increases the probability of the recombination loss of the charge carriers. Also, the thicker active layer has a more complicated and longer charge extraction network, which means there is difficulty in charge transport towards the electrodes and an increase in carrier drift length [104]. Figure 3-21 shows the increase in the series resistance with an increase in the active layer's thickness. The higher shunt resistance indicates more leakage current. The morphology of the active layer also affects the shunt resistance which could come from material and fabrication defect.

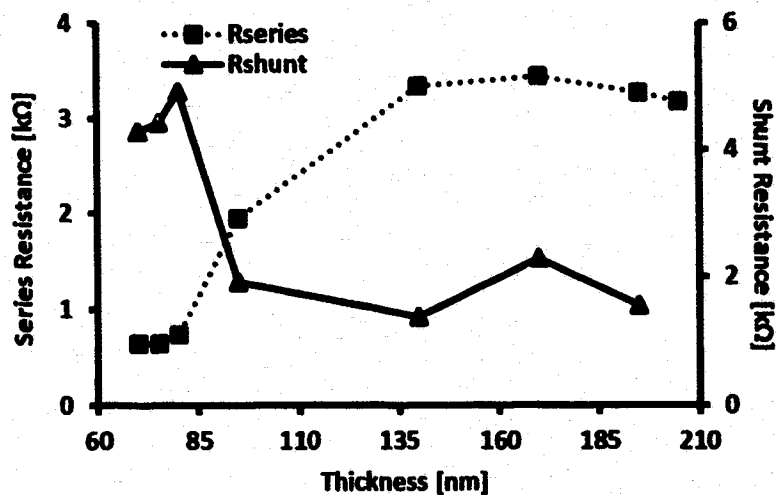


Figure 3-21: Series and shunt resistance for various active layer thicknesses of fabricated P3HT:PCBM polymer solar cells.

3.4.4.4 Effect of Active Layer Thickness on FF and PCE

The major parameter to consider for the performance of the solar cell is the power conversion efficiency (*PCE*). The *PCE* of the polymer solar cell was calculated at maximum power point using the relationship

$$PCE = \frac{V_{MP}J_{MP}}{P_{in}}. \quad \text{Eq. 3-10}$$

Where V_{MP} and J_{MP} are the voltage and current density at maximum power point, respectively, and P_{in} is the input optical power density which was set to 100 mW/cm² during device testing. **Figure 3-22** shows the *PCE* of polymer solar cells of various device thicknesses. Although the *PCE* showed some oscillatory behavior, overall it increased with the active layer thickness. The significant drop in *PCE* was seen around 150 nm active layer thickness, which could be due to the destructive interference within the device's layers at this thickness [92]. Another important metric of the solar cell is the fill factor (*FF*). The *FF* gives the charge extraction efficiency of the solar cell and was calculated as

$$FF = \frac{V_{MP}J_{MP}}{V_{oc}J_{sc}}. \quad \text{Eq. 3-11}$$

As seen in **Figure 3-22**, the fill factor remained mostly unaffected with a valley from 100 nm to 200 nm. *FF* decreased slightly after 300 nm of active layer thickness due to the increase in series resistance in thicker devices causing problems in charge extraction.

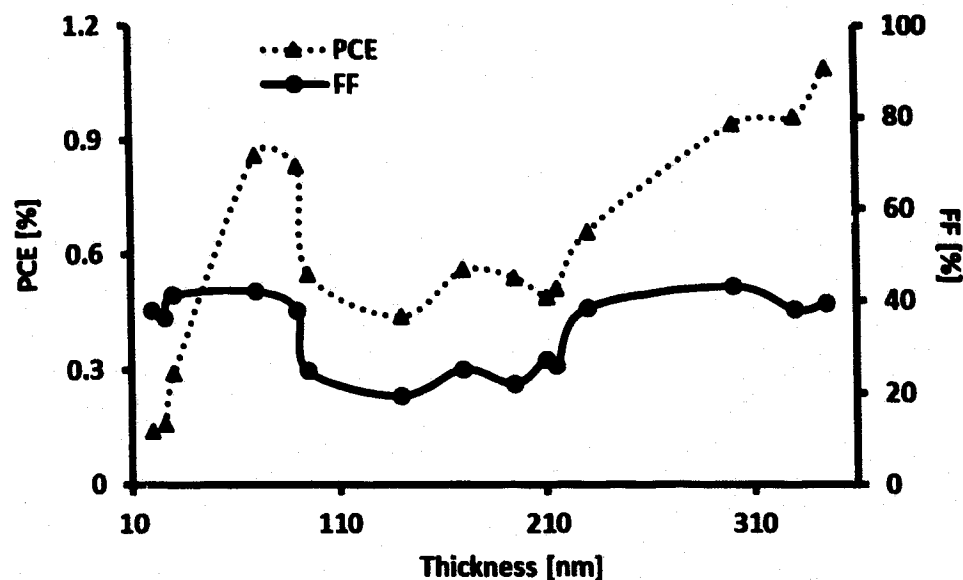


Figure 3-22: Power conversion efficiency (*PCE*) and fill-factor (*FF*) of P3HT:PCBM heterojunction polymer solar cells for various active layer thicknesses.

3.4.5 Photodetector Electrical Characterization

The polymer devices of the structure glass/ITO/PEDOT:PSS/P3HT:PCBM/Al with various P3HT:PCBM active layer thicknesses were measured separately as photodetector to study the effect of active layer thickness on photocurrent density (J_{ph}), responsivity (R) and external quantum efficiency (EQE). The expression of EQE is given in Eq. 3-4. Figure 3-23 gives the optical power density of the 100 W tungsten halogen white light source of monochromator used in photodetector testing measured with the calibrated silicon photodiode (Newport 818-UV) and power meter (Newport 1936-R). The fourth quadrant of J - V characteristics, i.e. reverse biased region, gives the photodetector response. Figure 3-24 shows the spectral photocurrent density of the photodetectors at reverse bias voltage of -4 V and J - V characteristics of each device measured with a solar simulator with various P3HT:PCBM active layer thicknesses. The photocurrent density increased with an active layer thickness. The photocurrent density

for 345 nm thick device was about 220% greater compared to 26 nm thick device at bias of -4 V and the wavelength of 580 nm. This is due to the increased absorption of photons for thick devices resulting more photo-generated charge carriers within the active layer of the devices.

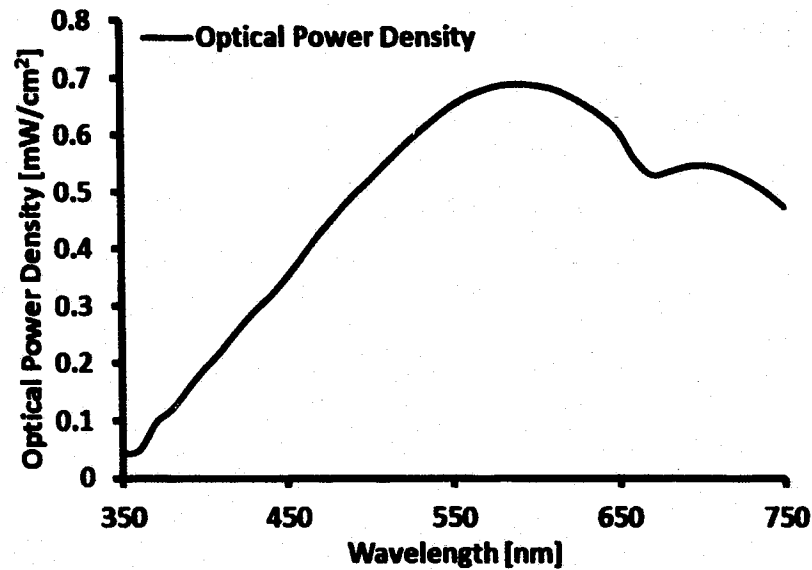


Figure 3-23: Optical power density of the 100 W tungsten halogen white light source of monochromator used in photodetector testing measured with the calibrated silicon photodiode (Newport 818-UV) and power meter (Newport 1936-R).

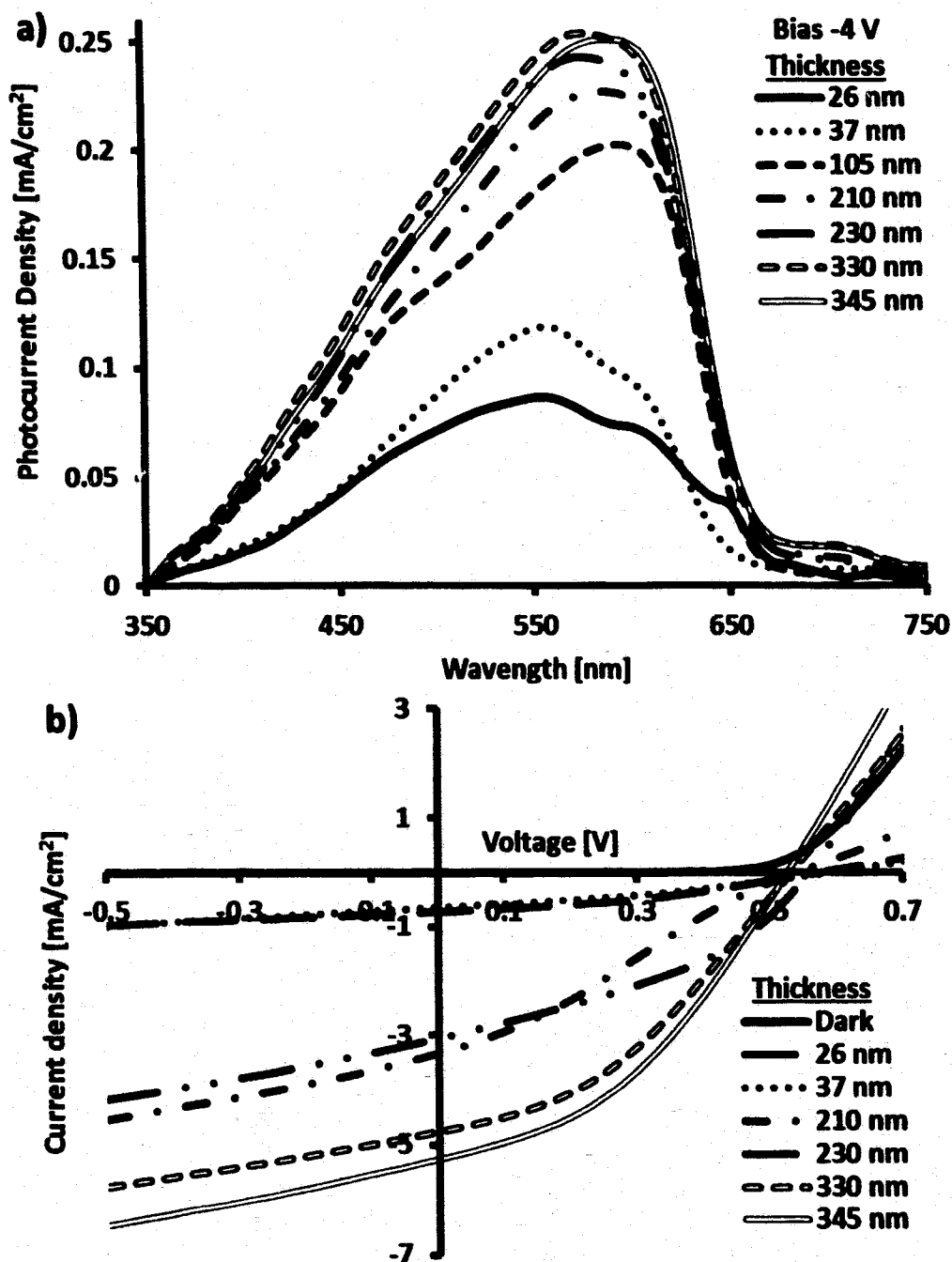


Figure 3-24: a) Spectral photocurrent density of photodetectors at reverse bias voltage of -4 V, and b) $J-V$ characteristics of each device measured with solar simulator, with various P3HT:PCBM active layer thicknesses.

3.4.5.1 Effect of Bias Voltage on EQE

Figure 3-25 shows the EQE plots of the photodetector with a) 330 nm, b) 230 nm and c) 37 nm thick P3HT:PCBM active layers for different reverse bias conditions. As

the reverse bias voltage was increased, the *EQE* also increased. This indicated that as the reverse bias voltage increased, more of the photo-generated charge carriers were swept towards the electrodes under a strong influential biased potential. With low reverse bias voltage, not all photo-generated charge carriers could make it to collect at electrodes due to low mobility and a weak electric field, and lost in the recombination process after their lifetime. With an increasing reverse bias voltage, more and more carriers collected at the electrodes and at some point all the generated carriers collected at the electrodes. This is called saturation condition and no more increase in *EQE* can be seen after this point even with an increased reverse bias voltage. The rate of increment in *EQE* with an increase in reverse bias voltage slows as it reaches the saturation point. As seen in Figure 3-25(a) for a 330 nm thick device, the *EQE* increased by 12% from 0 V to -1 V, and it increased only by 2.6% from -3 V to -4 V for 450 nm wavelength showing that it is approaching the saturation point.

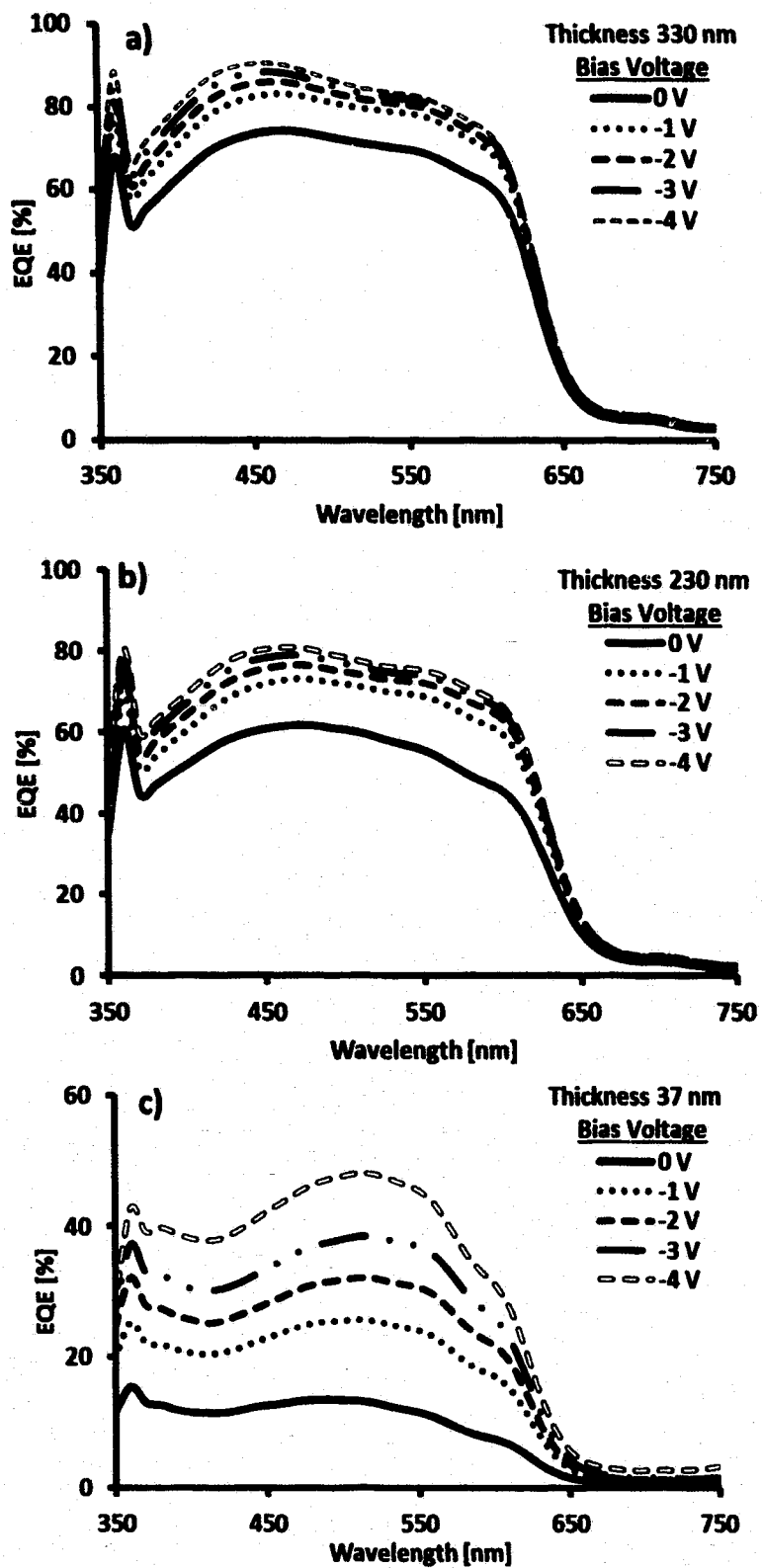


Figure 3-25: External quantum efficiency (*EQE*) of a) 330 nm, b) 230 nm and c) 37 nm thick P3HT:PCBM active layers of photodetector at various reverse bias voltages.

3.4.5.2 Effect of Active Layer Thickness on EQE

Figure 3-26 shows the *EQE* of the polymer photodetector with various active layer thicknesses at reverse bias of -4 V. This plot shows that the *EQE* increases with thickness of the active layer. The *EQE* is directly related with photocurrent density. As photocurrent density increased with the active layer's thickness due to the higher photon absorption in thicker devices, as described in the previous section, simultaneously *EQE* also increased with the active layer's thickness. The *EQE* is found to be about 125% higher in a 330 nm thick device compared to a 26 nm thick device at -4 V of reverse bias and for 450 nm wavelength. The *EQE* and responsivity plot versus active layer thickness for reverse bias of -4 V and wavelength of 580 nm is represented in Figure 3-27. This plot shows the increasing trend of *EQE* and responsivity with the active layer's thickness.

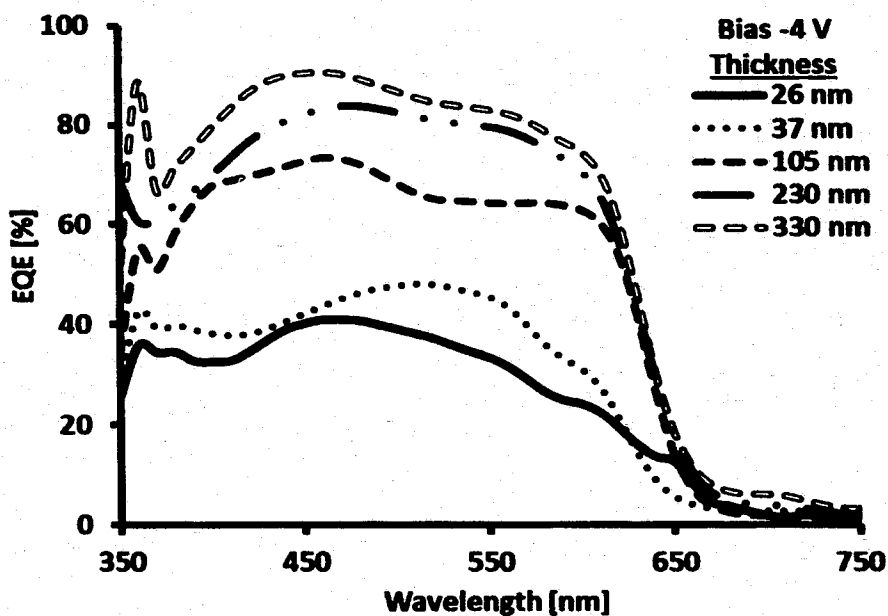


Figure 3-26: External quantum efficiency (*EQE*) of polymer photodetectors for various active layer thicknesses at reverse bias voltage of -4 V.

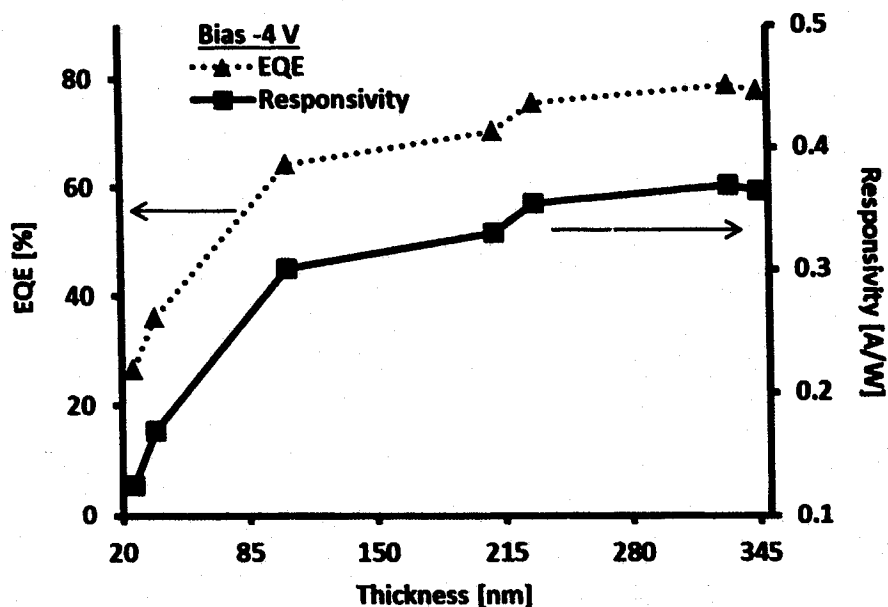


Figure 3-27: External quantum efficiency (*EQE*) and responsivity of P3HT:PCBM polymer photodetectors for various active layer thicknesses at reverse bias voltage of -4 V for 580 nm wavelength.

3.4.6 P3HT:ICBA Solar Cells with Silver Nanoparticles

The polymer solar cells of the structure glass/ITO/Ag/PEDOT:PSS/P3HT:ICBA/Al were fabricated and tested to investigate the surface plasmon enhancement using silver nanoparticles. The increased photocurrent density is reported by Kim *et al.* as a result of enhanced absorption due to excited surface plasmons by Ag nanoparticles and overall *PCE* increased from 3.05% to 3.69% [115]. Silver nanoparticles of three different thicknesses, 5 nm, 6 nm and 13 nm, were sputtered onto patterned ITO substrates using Cressington 208 HR sputter coater, and the Ag layers were annealed at 300°C for 1 hour. In one device, initially 5 nm Ag layer was sputtered and then an additional 1 nm of Ag is sputtered to create nucleated nanoparticles (mesh of small nanoparticles on the surface of a big nanoparticle) [116] which is referred to as the 6 nm Ag layer. Such nucleated nanoparticles are reported to have broadband enhancement due to the presence of the

mesh of nanoparticles with different shape and sizes [116]. **Figure 3-28** shows the SEM images of Ag nanoparticles sputtered on the ITO coated glass substrates, a) 5 nm Ag before annealing, b) 5 nm Ag after annealing at 300°C for 1 hour, c) nucleated nanoparticle with small particles attached to the sides, and d) 13 nm Ag after annealing at 300°C for 1 hour. The beam voltage of SEM was set to 3 kV and the working distance was 5 mm.

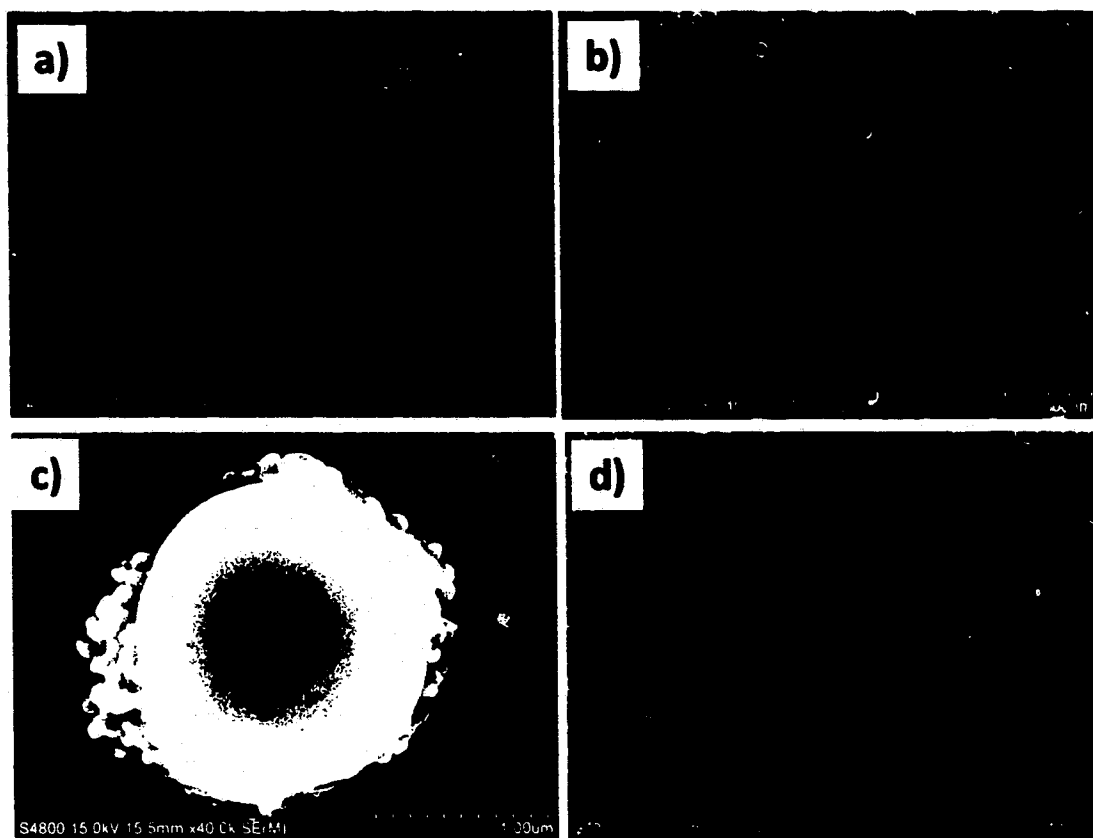


Figure 3-28: The SEM images of Ag nanoparticles sputtered on the ITO coated glass substrates, a) 5 nm Ag before annealing, b) 5 nm Ag after annealing at 300°C for 1 hour, c) nucleated nanoparticle with small particles attached to the sides, and d) 13 nm Ag after annealing at 300°C for 1 hour. The beam voltage of SEM was set to 3 kV and the working distance was 5 mm.

The 50 nm thin-layer of PEDOT:PSS and 355 nm of P3HT:ICBA polymer-fullerene blend were deposited on to the Ag sputtered ITO substrates as an active layer.

The detailed fabrication process is mentioned in Section 3.3.1. The only difference here is PCBM fullerene derivative is replaced with ICBA. The fabrication parameters are given in Table 3-3.

Table 3-3: Fabrication parameters of P3HT:ICBA solar cells with Ag nanoparticles.

Parameter/Material	Value/type
Solvent	Chlorobenzene
P3HT Concentration	24 mg/ml
P3HT:ICBA Ratio	1:1 wt.
Additive (OT)	0% vol.
Ag Layers	5 nm, 13 nm, 6 nm (nucleated 5 nm + 1 nm)
Spin Coating Recipe	700 RPM 50 s
Thickness	355 nm (Surface Profiler)
PEDOT:PSS	3500 RPM, 30 s, ~ 50 nm
Ambient Conditions	20 °C, 58% Humidity (09/01/15, 12:50 PM)
Aluminum	100 nm, 0.4 nm/s, 10^{-6} Torr (Thermal evaporator)
Annealing	150 °C, 15 min (Post-production)
Contact Wire	0.25 mm dia. Copper wire
Epoxy	Conductive silver epoxy

In these solar cells, the light is illuminated from the glass side through ITO. Part of the incident light is reflected and part of it absorbed by the Ag nanoparticles. So the presence of Ag nanoparticles on ITO decreases the transmission of light to the P3HT:ICBA active layer and this loss of light energy depends on the thickness and coverage of Ag nanoparticles. To study the effect on transmittance due to the Ag nanoparticles on ITO substrates, the optical characterization is carried out under Filmetrics F10-RT reflectometer.

Figure 3-29(a) shows the transmittance of ITO coated glass substrates with 5 nm, 6 nm and 13 nm Ag nanoparticles compared with the transmittance without any nanoparticles. The Figure 3-29(a) shows the decrease of transmittance with the increase

of Ag layer thickness especially around 450 nm wavelength. Interestingly, the transmittance increased with 6 nm nucleated nanoparticles compared with a 5 nm layer. **Figure 3-29(b)** shows the transmittance, reflectance and absorption profiles for a 355 nm P3HT:ICBA active layer on a quartz substrate. Unfortunately, the absorption of P3HT:ICBA layer has peak around 450 nm wavelength for which the transmittance is mainly decreased due to presence of Ag nanoparticles.

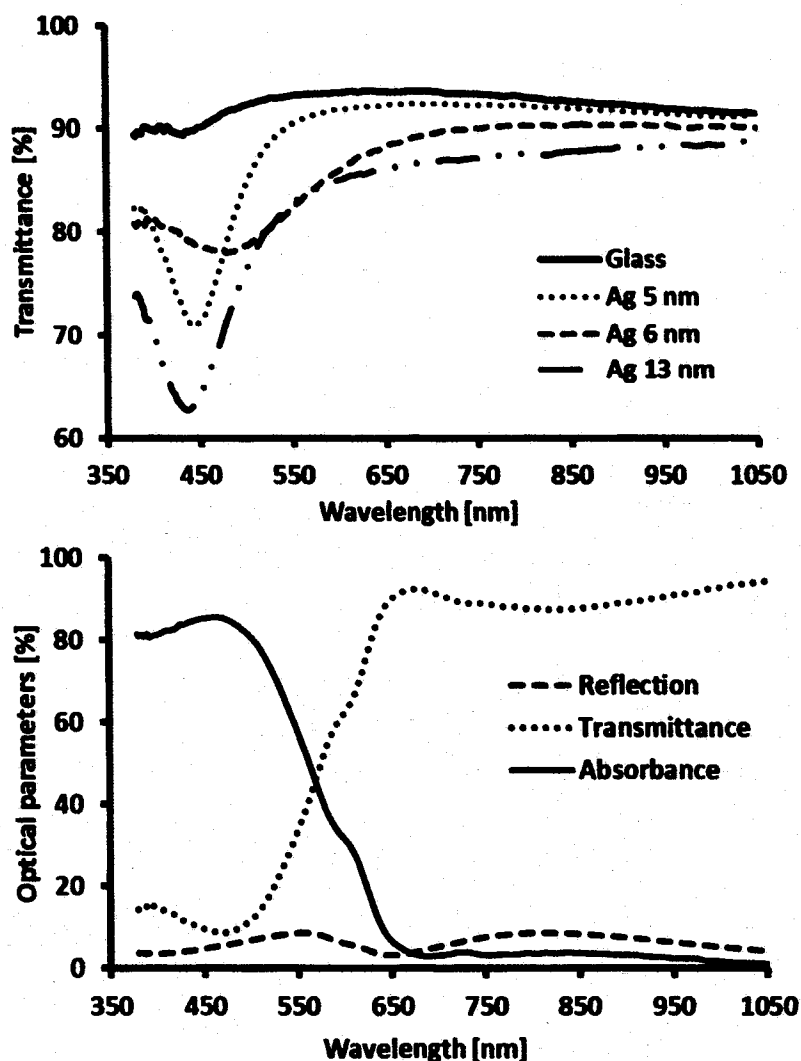


Figure 3-29: a) Transmittance profiles of 5 nm, 6 nm and 13 nm annealed Ag thin-films on ITO coated glass substrate and without Ag thin-film, and b) transmittance, reflectance and absorbance of a 355 nm thick P3HT:ICBA film on a quartz substrate.

The polymer solar cells with and without Ag nanoparticles were tested under the solar cell with an input optical power density of 97.6 mW/cm^2 . The solar cell with Ag nanoparticles is referred to as the surface plasmon (SP) device and as the benchmark (BM) device without Ag nanoparticles. Figure 3-30 shows the J - V characteristics of the benchmark device compared with surface plasmon devices with, a) 5 nm Ag layer, b) 6 nm Ag layer, and c) 13 nm Ag layer. Table 3-4 gives the solar cells' parameters of the benchmark and surface plasmon devices. The measurement error calculation is shown in Appendix B.

Table 3-4: Solar cell parameters for benchmark (BM) and surface plasmon (SP) devices.

	BM 5nm	SP 5nm	BM 6nm	SP 6nm	BM 13nm	SP 13nm
J_{sc} (mA/cm^2)	2.64	2.45	2.50	2.09	2.76	2.49
V_{oc} (V)	0.77	0.80	0.76	0.79	0.78	0.81
J_{mp} (mA/cm^2)	1.94	1.81	1.66	1.49	1.94	1.70
V_{MP} (V)	0.35	0.40	0.35	0.40	0.35	0.40
R_s ($\text{k}\Omega$)	6.60	5.57	6.39	6.35	6.54	7.40
R_{sh} ($\text{k}\Omega$)	12.3	10.7	8.40	13.3	9.60	10.9
$FF \pm 0.6$ (%)	33	37	31	36	31	34
$PCE \pm 0.008$ (%)	0.697	0.741	0.595	0.609	0.695	0.696
% PCE Enhancement	6.47		2.35		0.14	

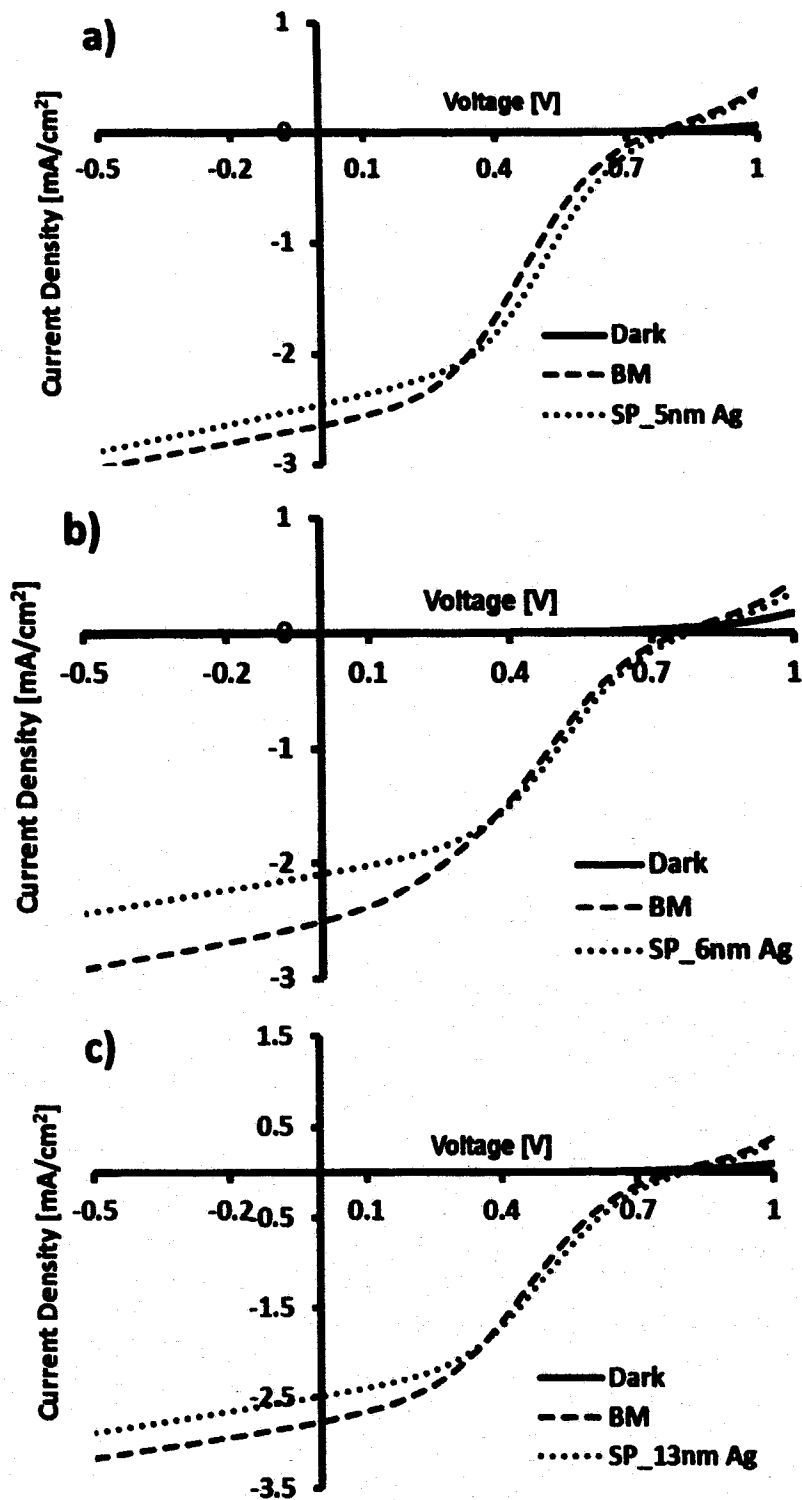


Figure 3-30: $J-V$ characteristics of benchmark (BM) devices compared with surface plasmon (SP) devices with a) 5 nm Ag, b) 6 nm Ag, and c) 13 nm Ag layers.

In each case, surface plasmon devices showed the best results with maximum *PCE* of 0.741% for 5 nm Ag nanoparticles. The *PCE* enhancement observed was 6.47% for 5 nm Ag layer, 2.35% for 6 nm Ag layer and 0.14% for 13 nm Ag layer. *PCE* enhancement decreased with an increase in Ag layer's thickness. This is due to the loss of incident optical power on thicker Ag layer (transmittance loss). The short circuit current density is lower for SP devices compared to BM devices, but open circuit voltage and fill factor are higher for SP devices. Series resistance decreased for SP devices except for 13 nm, and shunt resistance increased for SP devices except for 5 nm. Overall, the series resistance is very high and fill factor is small for all devices showing S-shaped curves. The high series resistance and low *FF* could be due to extremely thick 355 nm active layer. The short circuit current density did not show any enhancement. The overall *PCE* enhancement could be due to the improved charge transport and extraction resulted from the improved *FF* in SP devices. In conclusion, the polymer devices with thin active layer (~150 nm) and thin Ag layer (< 5 nm) might result in enhanced short circuit current density and further enhancement in *PCE*.

3.5 Conclusions

In conclusion, the effect of the active layer's thickness on the performance of polymer solar cells and photodetectors with P3HT:PCBM active layer was studied experimentally. The overall improvement of polymer devices was seen with increasing the thickness of active layer. The transmittance decreased and absorption of photons increased with thicker devices resulting generation of more charge carriers. On the other hand, as the thickness of the active layer increased the problem with the charge extraction arose due to longer and complicated network within the device and resulted in the

increase in series resistance. The electrical short circuit current through the device, as well as the device's *PCE* and *EQE*, increased with thickness. From these experimental results, it was found that the active layer's thickness has a vital role in the performance of polymer devices, which can be improved by optimizing the device's thickness. However, the increase in performance with thickness is assumed to be valid only up to a certain value, called optimal active layer thickness. In this experiment, the thickness of the device was restricted to 345 nm due to fabrication difficulty in spin-coating, and at this thickness, *PCE* of 1.09% and *EQE* of over 83% at around 460 nm wavelength was recorded. The air-processed fabrication process of polymer devices introduced the risk of exposure to moisture and oxygen degrading performance of devices. The devices with higher performance can be fabricated within an inert atmosphere.

CHAPTER 4

POLYMER BETAVOLTAIC DEVICES

4.1 Introduction

Betavoltaic devices are energy sources that can last for decades [117] and have potential applications in space missions [118]. The rapid growing space exploration requires a long duration power supply as the refueling option is not feasible for such applications. The photovoltaic energy source has been a major interest for such applications for a long time [119], [120]. However, the photovoltaic solar cells need to be exposed to sunlight all the time. This is not possible for certain circumstances in space applications such as inside the spaceship, shadow or dark regions, and the outer solar systems. For this reason, as an alternative of the solar energy source, betavoltaic power sources have a high scope for space applications.

Other applications of these devices are unattended sensors, anti-tamper devices and power supplies for biomedical devices (cardiac pacemaker [121] or prosthetic devices) [122]. Although the first betavoltaic cell was reported by Rappaport in 1954 [123], further research and development of these cells was very sparse due to the limited applications and semiconductor degradation, and high cost of suitable radioisotopes [122]. Currently, alpha/betavoltaic devices based on inorganic materials such as silicon, silicon carbide, and indium gallium phosphide are used with direct energy conversion due

to their long term stability and good power conversion efficiency (*PCE*) of 5% to 10% [124]–[128]. Cheng *et al.* achieved a high open circuit voltage of 1.64 V and 0.98% *PCE* using GaN p-i-n homojunction betavoltaic microbattery [129]. In direct energy conversion, highly energetic alpha/beta particles bombard and penetrate the semiconductor material, and a stream of free electron-hole pairs is generated. The electron-hole pairs contribute to the electrical output power generated by the alpha/betavoltaic device. Investigation of different loss mechanisms and designing ways to minimize these losses leads to the high performance betavoltaic devices [130].

Inorganic absorbers, such as silicon, silicon carbide, and indium gallium phosphide, offer good conversion efficiency and long term stability, but require complex equipment and hazardous materials, as well as high temperature process to fabricate [131]. These inorganic materials are brittle and cannot be used in flexible devices and have heavy weight restricting the portability. The betavoltaic devices of any shape can be designed with flexible materials. Radiation causes defects in the inorganic semiconductor materials resulting in shortened minority carrier diffusion lengths, increased leakage currents, and overall degradation of the device's performance [122].

The indirect energy conversion (previously explored by NASA Glenn Research Center [118] for inorganic betavoltaic cells) involves a scintillator thin film used as an intermediate layer between the alpha/beta particle source and the betavoltaic cell [127] [132]. The scintillator layer, known as a phosphor screen, converts the energy of alpha/beta particles into light, and the active layer further converts light energy into electrical energy, based on the photovoltaic principle [133]. The *PCE* of such devices depends on how well the phosphor screen generates the photons in the absorption region

of the active layer and the loss of photons generated by phosphor in different directions other than in the active layer [130]. Sychov *et al.* have demonstrated indirect converting alpha battery and generated 21 μW electrical power using 300 mCi of Pu^{238} alpha emitter, ZnS phosphor screen and AlGaAs photovoltaic cell [134]. The overall power conversion of 0.11% was achieved with short circuit current of 14 μA and open circuit voltage of 2.3 V [134]. The directional photon loss was reduced and the electrical output power was increased by 60% by applying a thin aluminum reflector layer between the alpha source and phosphor screen [134].

The radioisotope thermal generator (RTG) has been introduced to harvest thermal energy into electricity by the decay of radioisotope such as plutonium-238 (Pu-238), americium-241 (Am-241), polonium-208 (Po-208), polonium-210 (Po-210), strontium-90 (Sr-90), etc. [135]. The need of high temperature gradient (up to 1000°C) for thermoelectric generation requires powerful radioisotopes that have serious health hazard and needs proper shielding. Due to high temperature processing in RTG, usually inorganic materials such as silicon-germanium, bismuth telluride, lead telluride are used for stability at high temperature and are heavy in weight, increase production cost and lack flexibility [136]. Also, proper protection arrangements are required due to high temperature within the system [136]. Generac has developed 24" \times 13" \times 7" RTG generator, RTG16EZA1, of 36 pounds weight [137]. RTG modules are bulky and cannot be used in portable devices such as waist watches, electronic gadgets, etc. The maximum efficiency of thermoelectric generator is less than 10% [138], [139]. The betavoltaic devices with benign radioisotope such as tritium can be used as a power source for

portable devices. By using polymer active layer they can be made flexible and a low weight power source.

In order to explore some non-traditional potential materials and methods of fabrication for betavoltaic that are cost-effective, flexible, and lightweight, a photovoltaic conjugated polymer bulk heterostructure is investigated for betavoltaic application. The main advantages of conjugated polymer devices are their ease of fabrication, cost effectiveness, material flexibility, and light weight.

In this chapter, direct-conversion polymer-based betavoltaic cells, and their degradation, as well as indirect-conversion polymer-based betavoltaic cells are explored. The active polymer layer is the semiconductive conjugated polymer-fullerene P3HT:ICBA bulk heterojunction, where P3HT is poly (3-hexylthiophene), and ICBA is indene-C₆₀ bisadduct fullerene derivative. The P3HT:fullerene bulk heterostructure is widely explored for polymer-based photovoltaic cells [75], [78], [94], [98], [112], [140], [141] and the degradation of these cells can be overcome by device fabrication in inert atmosphere and device encapsulation. The alpha/betavoltaic device with organic material has not been previously explored. Kingsley *et al.* studied the radiation hardness to X-rays of a thin organic photovoltaic device based on P3HT:PCBM [142], where PCBM is the fullerene derivative phenyl-C₆₁-butyric acid methyl ester. They observed the exponential decay of the photocurrent in unencapsulated devices when exposed to a flux of 15-MV X-rays [142].

Here, the intermediate phosphor screen is explored that isolates the active polymer P3HT:ICBA layer in a polymer-based device from the electron beam (e-beam), and protects it from e-beam caused damage and degradation. The betavoltaic

performance of these batteries is demonstrated by using scanning electron microscope (SEM) as an e-beam source and for various e-beam energies. The loss mechanism in indirect-conversion polymer-based betavoltaic batteries are also investigated and tried to reduce them significantly.

4.2 Background

4.2.1 Betavoltaic

The betavoltaic is the process of generating an electric current from the kinetic energy of beta particles emitted by a radioisotope invented almost 50 years ago. This is another form of radioisotope energy (nuclear energy) harvesting unlike the widely used thermal energy harvesting in nuclear power plants. The betavoltaic power source is well suited for the low power electrical applications for long duration such as implantable medical devices, sensors, and for military and space applications. Betavoltaic batteries can be designed to use in cellphones, laptops, and other electronic gadgets that consume the considerable portions of current energy demand, as a power source for their lifetime.

The basic architecture of betavoltaic device and its operational principle is shown in **Figure 4-1** below. The radioisotope decays to emit beta particles (high-energy electrons) that hit the semiconductor p-n junction device placed underneath. The emission of beta particles from radioisotope is random in nature. When beta particles traverse through the semiconductor material, the kinetic energy of beta particles is absorbed creating the shower of free electrons and holes. These free electrons and holes are then collected at the opposite sides under the influence of an internal electric field developed at the junction of p-n junction device similar to the photovoltaic solar cells. The only

difference is, instead of photons in case of solar cells, the electron beam is used to create free electrons and holes in betavoltaic devices. Usually, radioisotopes have decades of half-life providing power to the betavoltaic devices for decades.

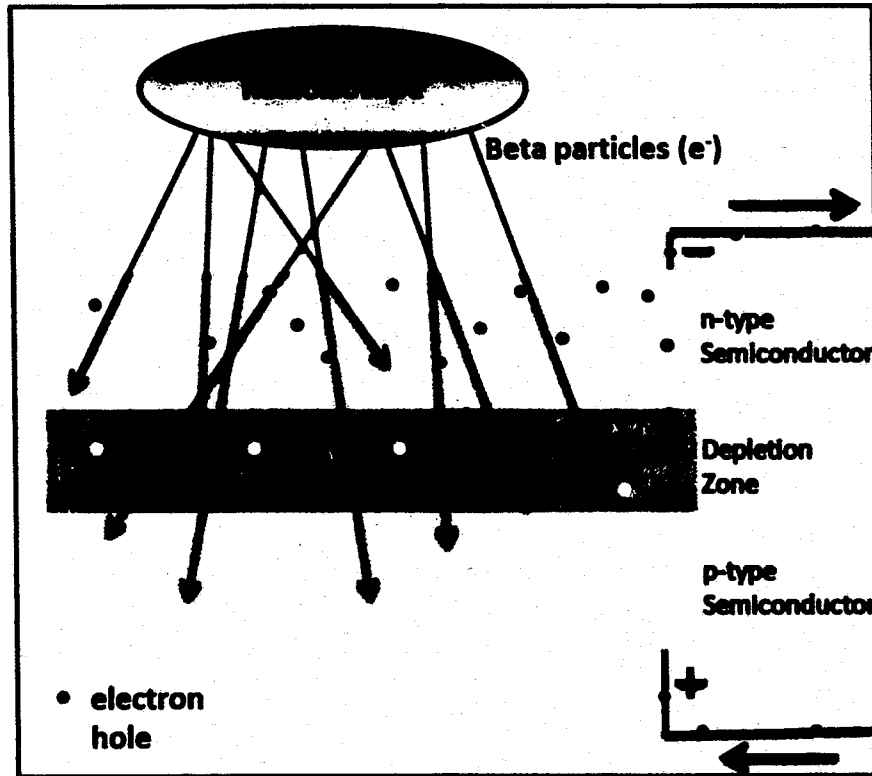


Figure 4-1: Basic device architecture and operation of betavoltaic device.

As the beta particles are continuously hitting the semiconductor material, these materials need to be tolerant enough to these energetic particles to avoid any defects and degradation. Some of the semiconductor materials used for betavoltaic devices are Si, SiC, GaAs, InGaP, etc. Having radioisotope as their source, betavoltaic devices have risk of radiation exposure to the living organism. However, using low energy isotopes such as tritium with less than 19 keV of beta emission [143], which is blocked by a thin sheet of aluminum or dead cells in human skin, the risk of health hazard can be significantly

avoided. The chemicals used in other batteries available on the market have a similar kind of health risk. In radioisotopes the activity decreases with time reducing the power of emission; therefore, during the design phase of the betavoltaic devices, it is important to consider the amount of power required at the end of the battery's life and initial radioisotope loading.

4.2.2 Organic Betavoltaic

After the discovery of semiconductive conjugated polymers, they were used in almost all kinds of optoelectronic devices as an alternative for inorganic semiconductors. Therefore, semiconductive conjugated polymers can also be used in betavoltaic devices for electrical power generation, opening the door to organic betavoltaic. In this research, the organic betavoltaic is introduced for the first time using the semiconductive conjugated polymer blend with fullerene derivative. These organic betavoltaic devices generate electricity when exposed with beta particles. However, these polymers are not radiation hardened compared to their inorganic counterparts and degrade quickly and have a limited lifetime. This problem with organic betavoltaic can be solved by designing a new architecture. **Figure 4-2** shows the schematics of organic betavoltaic with intermediate scintillator layer, also called indirect conversion architecture. The scintillator layer converts kinetic energy of beta particles into photons and then the photons are converted into electricity by the organic semiconductor material similar to the organic photovoltaic solar cells. This way the scintillator isolates the high-energy beta particles from sensitive polymer layer and increases the lifetime of the device.

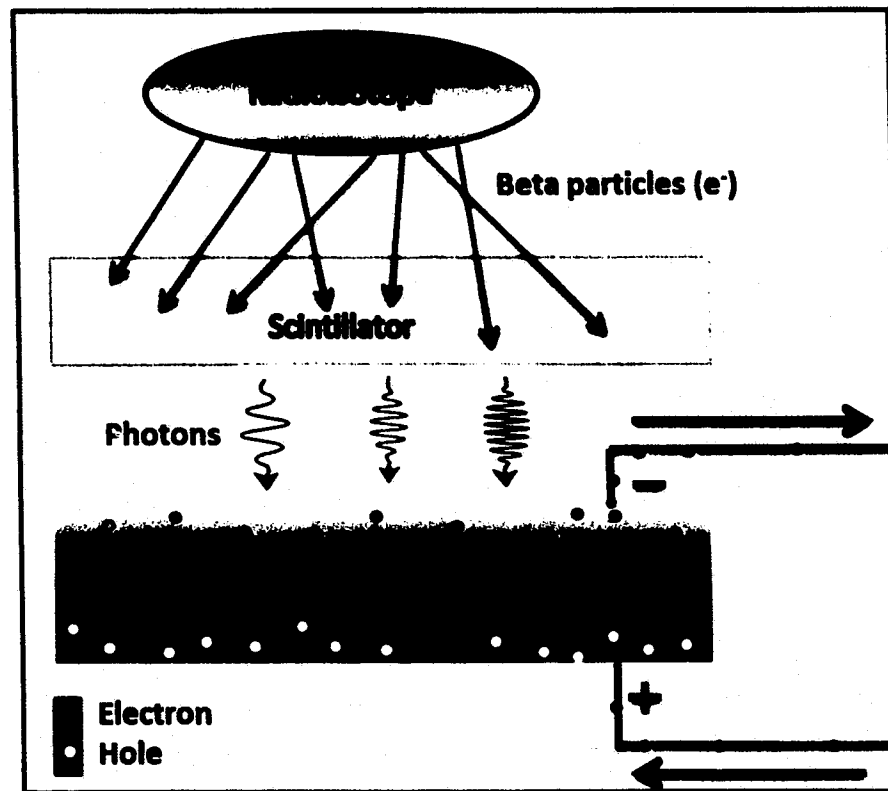


Figure 4-2: Indirect conversion device architecture of organic betavoltaic device with intermediate scintillator layer.

4.2.3 Betavoltaic Characterization and Parameters

The betavoltaic devices are characterized by measuring and plotting $I-V$ curve under the exposure of beta particles (e-beam). The output electrical power depends on the input e-beam power. Some of the betavoltaic parameters such as short circuit current and open circuit voltage are the same as in the case of photovoltaic solar cells described in Section 2.2.2. Other parameters are described below.

Electron Beam (Beta particles) Current, I_{e-beam} (pA): The e-beam or beta-particle current from the beta source is the number of electrons emitted per second. It depends on the radioisotope.

Accelerating Voltage, V_{acc} (kV): The voltage used to accelerate the electron beam as it is emitted from the beta source to hit the device. In scanning electron microscope (SEM), it is varied to change the kinetic energy of the electron beam so that the beam penetrates the sample to the desired depth. If e is the electron charge, the kinetic energy (keV) associated with accelerating voltage (kV) is

$$E_{kin} = eV_{acc}. \quad \text{Eq. 4-1}$$

Input Electron Beam (Beta particles) Power, P_{in} (nW): The input electron beam power is the product of accelerating voltage (kV) and electron beam current (pA)

$$P_{in} = V_{acc}I_{e-beam}. \quad \text{Eq. 4-2}$$

Output Electrical Power, P_{out} (nW): If V_{max} (V) and I_{max} (pA) are the voltage and current values along the I - V curve at which the maximum power is produced so that the output electrical power is given as

$$P_{out} = V_{max}I_{max}. \quad \text{Eq. 4-3}$$

Power Conversion Efficiency, PCE (%): The efficiency of betavoltaic device to convert input e-beam power into output electrical power:

$$PCE = \frac{V_{max}I_{max}}{V_{acc}I_{e-beam}} = \frac{P_{out}}{P_{in}}. \quad \text{Eq. 4-4}$$

4.2.4 Beta Sources

An ideal beta source should have a long half-life for extreme duration lifetime of betavoltaic device, emits beta particles in a range suitable for scintillator for better efficiency, and has little or no gamma and other harmful emission for safety. The common beta sources include tritium (H^3), carbon-14 (C^{14}), phosphorous-32 (P^{32}), and nickel-63 (Ni^{63}) [128] [143]. Tritium is an isotope of hydrogen with two neutrons and one

proton. Tritium decays with a half-life of 12.3 years into helium-3 by the emission of beta particles with an average energy of 5.7 keV [143] [144]. Due to its benign nature, tritium is currently the preferred beta source in commercial betavoltaic batteries, self-luminescent products, luminous paints, signage and high end wristwatches [144] [145]. Table 4-1 provides the information on different beta sources. In this research, the electron beam from AMRAY 1830 SEM was used to simulate the beta particle radiation with energy in the range of 10 keV to 30 keV.

Table 4-1: Various beta sources and their properties [128], [143]–[145].

Isotope	Average beta energy (keV)	Maximum beta energy (keV)	Half-life (years)	Price
Tritium (H^3)	5.7	18.6	12.3	~\$3.50/curie
Carbon-14 (C^{14})	49	156	5730	N/A
phosphorous-32 (P^{32})	690	1709	14.3 days	N/A
nickel-63 (Ni^{63})	18	67	92	~\$4000/curie
Promethium-147 (Pm^{147})	62	225	2.6	N/A

The nuclear waste from a nuclear power plant can be utilized as the beta source for these betavoltaic devices. The spent fuel or used fuel from the nuclear reactor is the radioactive isotope that is no more efficient to use in nuclear power plants. However,

these spent fuels are still high energetic to produce electricity if used in betavoltaic devices. Annually, a typical nuclear power plant generates about 20 metric tons of used fuel which totals about 2000 to 2300 metric tons of the nuclear waste from the nuclear industry every year [146]. There is a big challenge for the nuclear waste management because costs about 400 billion dollars over 75 years [147]. Using these spent fuels in betavoltaic batteries helps for the management of the nuclear waste on the one hand and generates revenue out of the waste on the other hand.

4.3 Direct Conversion Betavoltaic

4.3.1 Device Architecture

The direct conversion betavoltaic device consists of beta source (radioisotope) that generates beta particles continuously and the photovoltaic stack based on polymer-fullerene heterostructure that generates electrical power when bombarded with beta particles. The basic architecture of photovoltaic stack of polymer direct conversion betavoltaic device consists of glass/ITO/PEDOT:PSS/P3HT:ICBA/Al as shown in **Figure 4-3**. The ITO serves as anode and aluminum serves as cathode, PEDOT:PSS is the hole transport layer, whereas P3HT:ICBA is the active layer of the betavoltaic device. The electron beam is exposed from the aluminum cathode film as shown in **Figure 4-3**. When an energetic beta particle encounters a semiconductor conjugated polymer-fullerene blend of P3HT:ICBA, a shower of electrons and holes are generated along the path of the particle as it loses kinetic energy. As shown in **Figure 4-3**, the energetic beta particle from beta source penetrates the thin aluminum layer and reach the active layer of P3HT:ICBA, where it generates free electrons and holes. Those holes are collected at

ITO anode effectively with the help of intermediate PEDOT:PSS layer and electrons are collected at aluminum cathode, resulting the output electrical power from the betavoltaic device. This architecture of betavoltaic device is suitable for inorganic semiconductors such as silicon, GaN, etc. where the damage caused by high-energy beta particle is minimal. However, for the sensitive polymer semiconductor, the direct conversion betavoltaic are not suitable due to their vulnerability and performance degradation under direct exposure of high-energy beta particles. One of the loss mechanism in this architecture is the absorption of beta particle's kinetic energy in the aluminum layer.

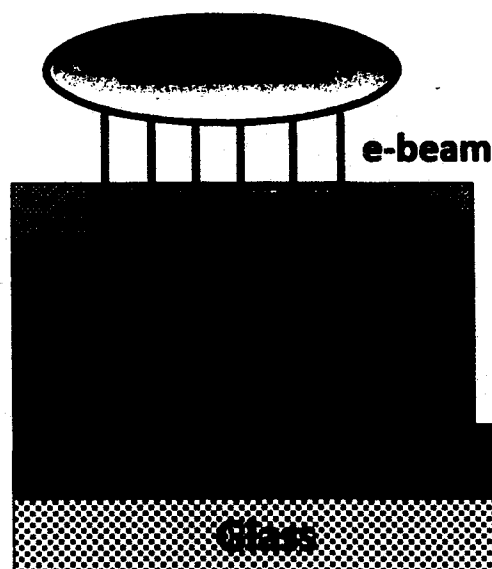


Figure 4-3: Direct conversion polymer-fullerene heterostructure betavoltaic device architecture.

4.3.2 Fabrication

The polymer betavoltaic device consists of bulk heterojunction of P3HT:ICBA thin film as an active layer, PEDOT:PSS thin film as the hole transport layer, indium tin oxide (ITO) and aluminum as the electrodes. The basic structure for such devices is glass (or PET)/ITO/PEDOT:PSS/P3HT:ICBA/Al. The PET stands for polyethylene

terephthalate. The fabrication process of polymer photovoltaic stack, similar to the air process published by Nam *et al.* [112], was carried out inside class 100 cleanroom in the Institute for Micromanufacturing (IfM). The fabrication of photovoltaic stack started with patterning of 0.14 micron ITO (sheet resistance of 5-15 Ω /sq) on 1.1 mm borosilicate glass substrates (Delta Technologies) or, ITO (sheet resistance of 60 Ω /sq) coated 175 μ m-thick PET substrates (Sheldahl) using standard photolithography process as follows.

The ITO coated glass (PET) substrates (1 inch x 1 inch) were rinsed with acetone, isopropanol (IPA) and with de-ionized (DI) water, and then dried with nitrogen (N_2) blow. Substrates were then baked on a hot plate for 15 minutes at 150°C to remove any solvent residue. The Shipley 1830 positive photoresist was spin-coated at 1500 RPM for 30 seconds. Then the photoresist was soft baked on a hot plate at 90°C for 5 minutes for drying. The transparency plastic masks as shown in **Figure 3-10** (left) were aligned to each substrate using transparent tape, and then the substrates were exposed to ultraviolet light at 365 nm for 18 minutes. After exposure, the masks were removed from the substrates and the substrates were developed using MF-319 developer for approximately 30 seconds or until all UV-exposed photoresist had clearly been removed. Due to the positive photoresist, the black part of the transparent mask defines the region where the ITO will remain after etching. After complete development of the exposed part of the photoresist, the substrates were rinsed with DI water and hard baked on a hot plate at 110°C for 10 minutes. The next step was wet etching of ITO where individually each substrate was submerged in 20% hydrochloric acid (HCl) warmed to 75°C for around 3 minutes or until the targeted ITO had been completely etched away. The presence of ITO

was checked using multimeter to ensure that ITO was etched away completely or not. Finally, substrates were ultra-sonicated in baths of acetone and IPA to remove photoresist and other contaminants, then thoroughly rinsed with DI water and dried on hot plate at 150°C for 15 minutes.

Next, the P3HT and ICBA solutions were prepared. The P3HT and ICBA, bought from Sigma Aldrich, were measured using AND HR-60 scale inside a dry nitrogen glovebox into separate vials according to desired concentration and required quantity of solution. Based on the desired concentration and quantity of the solution, the chlorobenzene solvent was added in each vial with magnetic stir bar. The amount of P3HT and ICBA were used such that the ratio of 1:1 by weight of P3HT:ICBA was achieved. Then the vials were tightly sealed and removed from the glovebox and placed onto a stirring hotplate at 50°C for 15 to 18 hours. On the day of fabrication, the two solutions of P3HT and ICBA were filtered with 0.45 µm PTFE filters and mixed together in a single vial with a new magnetic stir bar and kept on a stirring hotplate at 50°C for an additional 1 hour. The desired amount of PEDOT:PSS (approximately 1 ml for each substrate) was transferred in a vial from the refrigerator, ultra-sonicated for 5 minutes and kept at room temperature for 30 minutes.

During the device fabrication inside class 100 cleanroom, PEDOT:PSS was filtered with 0.45 µm PVDF filter and spin-coated 1 ml per substrate with micropipette onto the ITO patterned glass substrates at 3500 RPM for 30 seconds to create about a 40 nm thick film. Then the substrates were annealed at 110°C for 10 minutes. After annealing, P3HT:ICBA solution was then dynamically dispensed 200 µl per substrate with micropipette while the substrate was spinning to get a uniform layer of polymer-

fullerene blend. The polymer devices with an active layer thickness from 135 nm to 345 nm were fabricated using polymer-fullerene solution concentrations from 10 mg/ml to 18 mg/ml, and spin-coating from 650 RPM to 1000 RPM for 50 seconds. The P3HT:ICBA and PEDOT:PSS layers were washed away using chloroform and water, respectively, using a cotton swab to expose some part of ITO for anode connection. Then substrates were baked at 70°C for 5 minutes to dry on a hotplate to remove the solvent.

After drying, the substrates were placed into a sample holder and stainless steel shadow masks (see **Figure 3-10 (right)**) were placed over each substrate to define the cathode regions. Then, Denton Vacuum DV-502A or Denton 502B thermal evaporator was used to thermally deposit 100 nm thin cathode film of aluminum at a base pressure of about $10\text{E-}6$ Torr. Then the substrates were annealed at 150°C for 15 minutes. Finally, copper wires were attached to aluminum contacts (cathodes) and exposed ITO contact (anode) with conductive silver epoxy (Electron Microscopy Sciences), and epoxy was cured at 75°C for about 20 minutes. **Figure 4-4** shows the step-by-step fabrication process of photovoltaic stack with P3HT:ICBA active layer. With this fabrication process, six polymer devices, each of 3 mm \times 3.5 mm surface area, were fabricated on each substrate sharing common anode. **Figure 4-5** shows the top view of six polymer devices on a single substrate and the cross section of a single device, and ready to test device with scintillator screen.

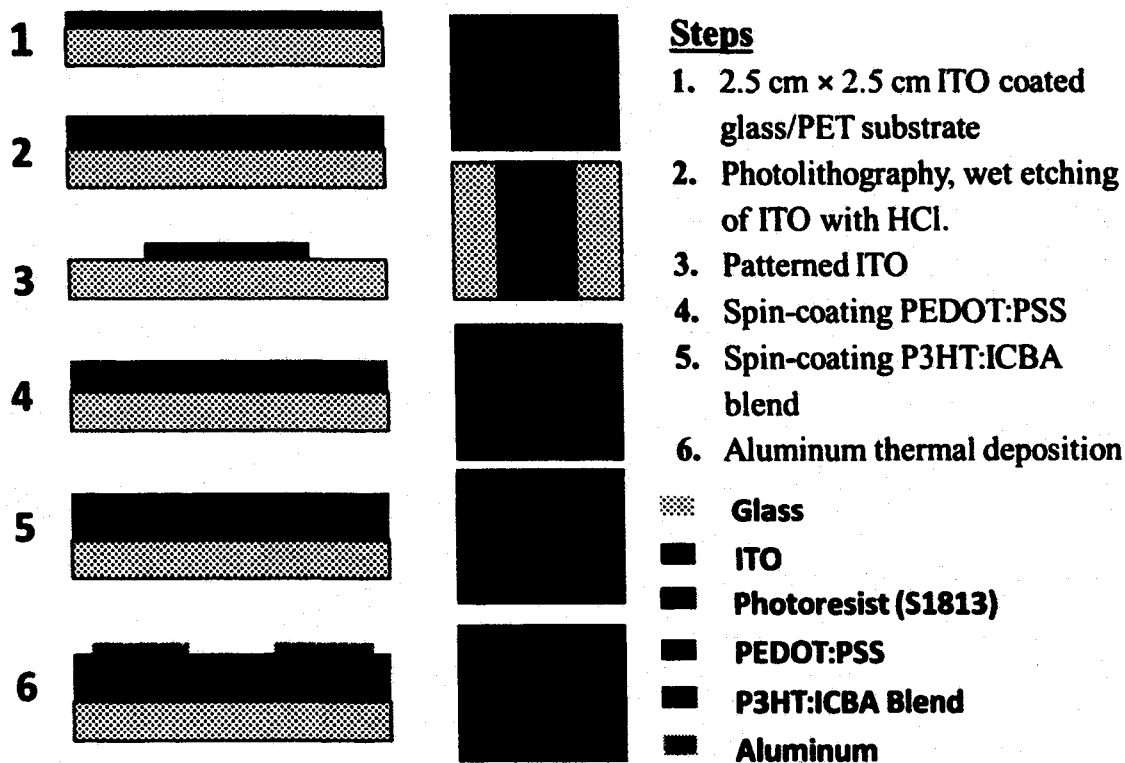


Figure 4-4: The step-by-step fabrication process of photovoltaic stack with P3HT:ICBA active layer.

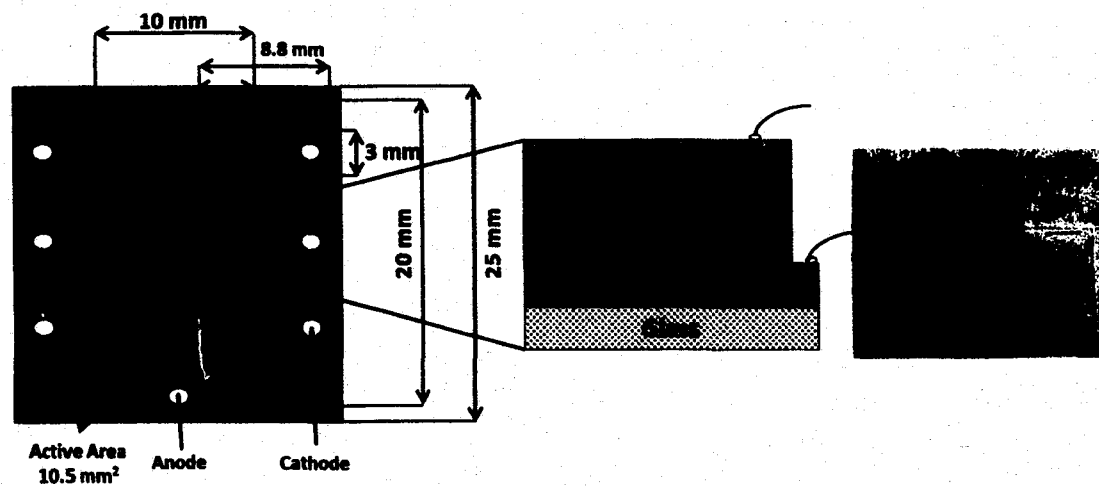


Figure 4-5: The top view of six polymer devices on a single substrate and cross section of a single device (left), and ready to test device with scintillator screen (right).

4.3.3 Test Setup

4.3.3.1 Optical Characterization

The Filmetrics F10-RT reflectometer was used for optical characterization of P3HT:ICBA blend serving as the active layer in polymer betavoltaic devices. The FilmMeasure software was used to measure optical data from Filmetrics device and recorded in the PC. This includes the measurement of reflectance and transmittance of the active layer of the betavoltaic device. For each measurement, the baseline setup was carried out using standard samples such as Al_2O_3 and light deflecting background before testing. To measure the emission spectrum of Ce:YAG scintillator, a 15 nW He-Cd 325 nm laser light using Omnichrome (Melles Griot, series 56, 45-MRS-302-120) photoluminescence laser was used to excite the scintillator and the emitted light was measured with the Ocean Optics USB 2000 spectrometer.

4.3.3.2 Input E-Beam Power

The input e-beam current at different accelerating voltages from AMRAY 1830 SEM was measured using Faraday cup (Ted Pella Inc., 651-P). The Faraday cup is a conductive cup designed to capture charged particles in the vacuum. **Figure 4-6** shows the SEM image of Faraday cup during experiment. The e-beam current is adjusted using condenser lens. The electron beam from SEM was focused on the central hole of a Faraday cup (see **Figure 4-6**), the Keithley 6487 picoammeter connected to SEM was used to measure the e-beam current, and recoded with a PC equipped with LabView software. During each measurement, initially, the e-beam current with no e-beam (i.e. zero accelerating voltage) was measured to establish any offset value of the e-beam current in the system. Later, all measured e-beam currents were corrected by subtracting

this offset value. The product of the e-beam current and accelerating voltage gives the input e-beam power.

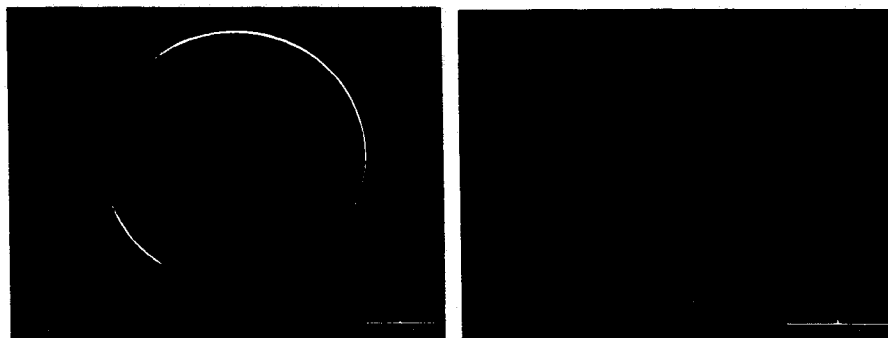


Figure 4-6: The SEM image of Faraday cup (left) and the zoomed view of central hole of Faraday cup (right) used to measure e-beam power from AMRAY 1830 SEM.

4.3.3.3 Betavoltaic Testing

AMRAY 1830 SEM was used to test direct and indirect conversion betavoltaic devices. The e-beam with kinetic energy (E_{kin}) in the range of 10-30 keV were generated using AMRAY 1830 SEM to simulate beta source isotopes of tritium (H^3) and nickel-63 (Ni^{63}) [143]. **Figure 4-7** shows the SEM images of betavoltaic devices under testing and **Figure 4-8** shows the schematic of betavoltaic device testing setup using AMRAY 1830 SEM. The e-beam is exposed from the Al side. The Keithley 6487 picoammeter was used to measure $I-V$ curves of betavoltaic devices and recorded in a PC equipped with LabView software. Initially, dark $I-V$ of each betavoltaic device was measured and recorded. Then the noise current was obtained by adjusting the zero current at zero bias voltage for the dark $I-V$. This noise current was then subtracted from each current values at all bias voltage in $I-V$ curve to get final dark $I-V$. After this, light $I-V$ of betavoltaic devices were measured and recorded at different e-beam energies. A similar procedure was used to subtract the noise current from all light $I-V$ curves as done in dark $I-V$.

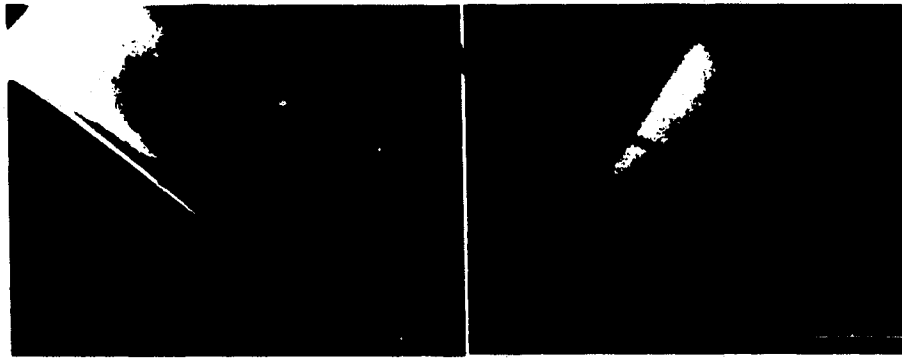


Figure 4-7: SEM images of betavoltaic devices under testing.

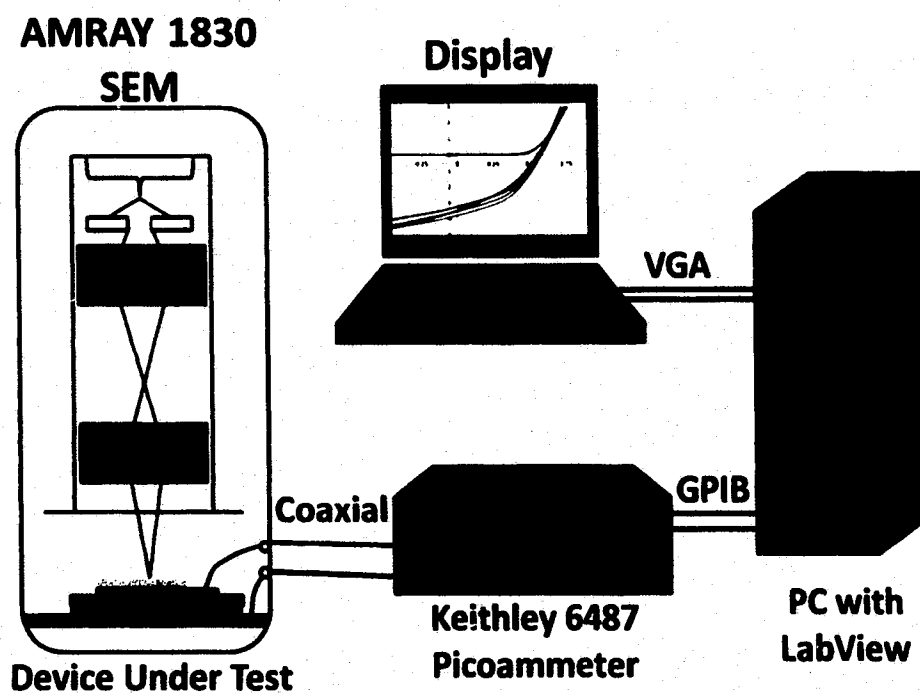


Figure 4-8: Schematic of betavoltaic device testing setup using AMRAY 1830 SEM.

4.3.3.4 *Raman Spectroscopy*

In direct conversion betavoltaic devices, the thin-film of P3HT-ICBA blend is directly exposed to the high-energy electron beam. The Raman spectroscopy (Horiba XploRA PLUS Raman microscope) was used to analyze the effect of direct e-beam exposure to the P3HT:ICBA thin film. Raman analysis was targeted to study any

morphological or molecular changes occur within the P3HT:ICBA film under the direct exposure to e-beam and its consequences to the performance of direct conversion betavoltaic devices. The Raman spectrum is a plot of the intensity of Raman scattered radiation, when the light incidents on a sample, as a function of the Raman shift (frequency difference of scattered radiation from the incident radiation in units of wavenumbers, cm^{-1}). The Raman spectrum gives the chemical fingerprint of a sample. It provides a qualitative assessment of the chemical composition of the sample [148]–[150]. Some functional groups are more Raman active than others [149]. So, if the chemical composition or functional group changes within the sample, the difference in Raman spectrum can be seen. With the change in functional group, the bond characteristics also changes, resulting in different intensity in Raman spectrum. For example, if the high-energy e-beam breaks the backbone of the polymer chain, the intensity change can be seen in Raman spectrum.

4.3.4 Results and Discussion

The direct conversion betavoltaic devices of structure Al/P3HT:ICBA/PEDOT:PSS/ITO/glass (structure shown in **Figure 4-3**) were tested within AMRAY 1830 SEM. The e-beam is exposed from Al side. In the direct energy conversion, the input high-energy e-beam from SEM penetrates the top aluminum (cathode) layer and reaches the active layer to generate a shower of electrons and holes (exciton pairs) within the P3HT:ICBA film. The e-beam generated exciton pairs were then dissociated at the P3HT:ICBA polymer-fullerene heterojunction and collected at opposite electrodes, holes at ITO anode and electrons at aluminum cathode, to generate electrical potential difference between these two electrodes of betavoltaic devices. **Table**

4-2 gives the fabrication parameters for direct conversion polymer betavoltaic devices and Figure 4-9 shows the measured I - V characteristics of a typical direct conversion polymer betavoltaic device on glass substrate under a direct e-beam.

Table 4-2: Fabrication parameters for direct conversion betavoltaic devices.

Parameter/Material	Value/type
Solvent	Chlorobenzene
P3HT Concentration	18 mg/ml
P3HT:PCBM Ratio	1:1 wt.
Additive (OT)	0% vol.
Spin Coating Recipe	650 RPM for 50 s
Thickness	345 nm (Surface Profiler)
PEDOT:PSS	4000 RPM, 30 s, ~ 50 nm
Ambient Conditions	20.8°C, 56% Humidity
Aluminum	100 nm, 0.4 nm/s, 10^{-6} Torr (Thermal evaporator)
Annealing	150°C, 15 min (Post-production)
Contact Wire	0.25 mm dia. Copper wire
Epoxy	Conductive silver epoxy

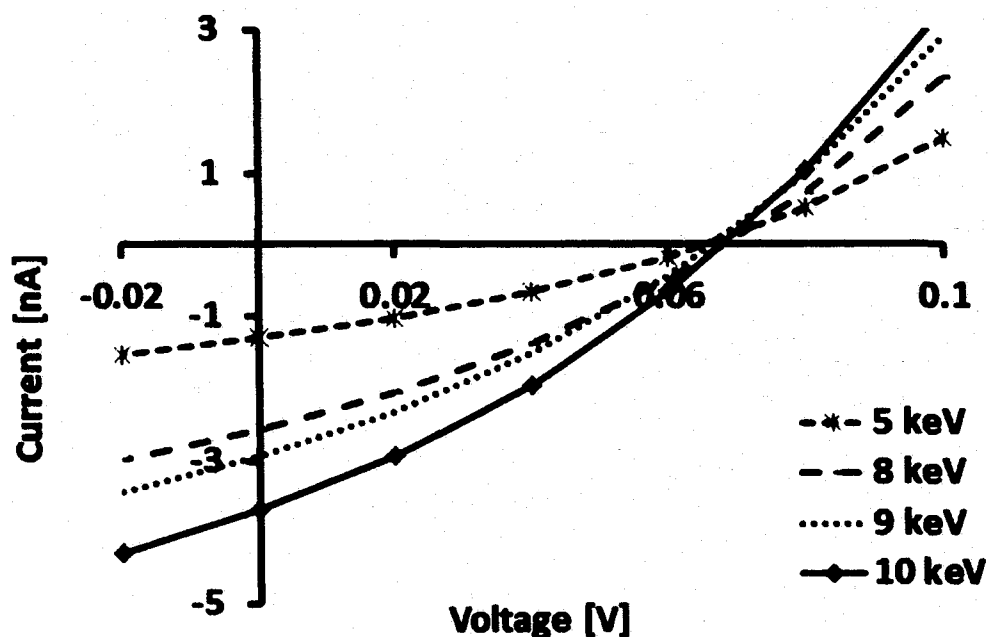


Figure 4-9: I - V characteristics of glass/ITO/PEDOT:PSS/P3HT:ICBA/Al, direct conversion betavoltaic devices for electron kinetic energies of 5, 8, 9, and 10 keV.

The *PCE* of betavoltaic device is defined as

$$PCE = \frac{V_{max} \cdot I_{max}}{V_{acc} \cdot I_{e-beam}} * 100. \quad \text{Eq. 4-5}$$

Where V_{max} and I_{max} are the device voltage and current at maximum power point, at which the maximum electric power of the device is obtained. V_{acc} is the accelerating voltage of the e-beam and I_{e-beam} is the measured e-beam current. The maximum *PCE* obtained for direct conversion betavoltaic devices shown in **Figure 4-9** is 0.068% for $E_{kin} = 5$ keV at which the e-beam current (I_{e-beam}) was 7.74 pA, and the value measured for V_{max} and I_{max} were 40 mV and 659 pA, respectively. The electrical output power P_{out} and short circuit current I_{SC} increased with E_{kin} . The P_{out} and I_{SC} at 10 keV are 78.4 pW and 3.67 nA, respectively.

Since the P3HT in the air is reported to degrade under exposure to X-rays [142], the degradation of polymer betavoltaic cells upon exposure to the e-beam was investigated. The polymer betavoltaic devices on glass with three different thicknesses of the active P3HT:ICBA layer, 225 nm, 180 nm, and 55 nm, were tested under direct 10 keV e-beam. The *I-V* characteristics were measured in time during the continuous direct e-beam exposure. Degradation was observed in all devices and the results are shown in **Figure 4-10**. The analysis of the data shows that the device with the thinnest active layer (55 nm) degrades fastest, especially in terms of the open circuit voltage V_{OC} , which reduces to 31% of the initial V_{OC} value in 13 minutes. In comparison, the V_{OC} for the 180 nm device reduces to 44% of the initial value, and for the 225 nm device, it reduces to 57% of the initial value in 13 minutes. It is also noticed that the degradation of active polymer material increased with E_{kin} .

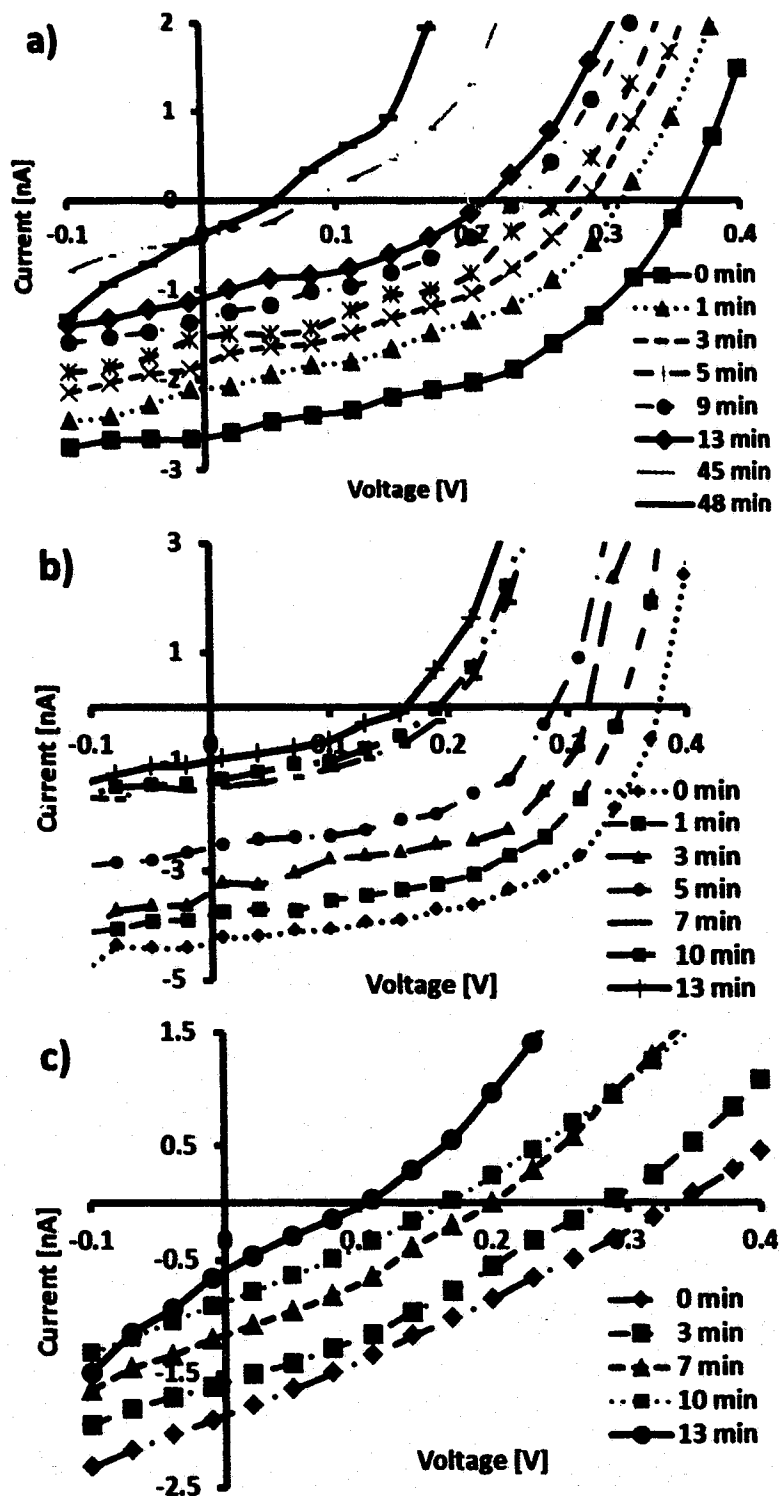


Figure 4-10: *I-V* characteristics of direct conversion polymer betavoltaic devices with a) 225 nm , b) 180 nm , or c) 55 nm thick P3HT:ICBA active layer measured in different time intervals under direct exposure of 10 keV e-beam. The e-beam current from the SEM was 69 pA.

One of the causes of low performance of direct conversion devices could be the interaction between the input energetic electron beam from the beta-source with the collecting electrons at the aluminum cathode. The energetic e-beam could deflect and minimize the electron collection efficiency at aluminum electrode. In addition, the exposure of e-beam over time could create damage on aluminum, reducing its conductivity, as well as breaking the backbone chain of the conjugate semiconductive polymer.

Figure 4-11 shows the Raman spectrum of P3HT-ICBA thin-films on quartz substrates with different thicknesses, 120 nm (2000 RPM, 50 seconds) and 160 nm (1000 RPM, 50 seconds) prepared with spin coating P3HT:ICBA solution (1:1 wt.), with and without e-beam exposure. Each sample was exposed to 20 kV e-beam for 15 minutes inside AMRAY 1830 SEM. The Raman spectrum is acquired for 30-45 seconds. With 25 mW laser power, initially 50% and 25% neutral density (ND) filters were used. The ND filter allows only a certain percentage of laser power to incident on the sample. However, the sample was damaged instantly with this power. Then the 10% ND filter was used to reduce the incident power on P3HT:ICBA sample further which corresponds to about 2 mW incident power on the sample out of 25 mW laser power. In both cases, change in the Raman spectrum is noticed around 1500 to 2000 cm^{-1} and 2500 to 3000 cm^{-1} Raman shifts. The Raman peak around 1447 cm^{-1} Raman shift corresponds to P3HT [151], [152], thiophene C = C bond [153]. The change in the Raman spectrum around 1500-1900 cm^{-1} corresponds to the C = C, 1600 cm^{-1} corresponds to C - C in aromatic ring chain vibrations, and 2800 to 3000 cm^{-1} corresponds to the C - H vibrations [154]. These results show that the e-beam is affecting the bonding chain in the polymer, which could

degrade its semiconductive property with long exposure. This effect is more pronounced in thinner films shown in **Figure 4-11**, as the change in the Raman spectrum is larger in 120 nm film than 160 nm film.

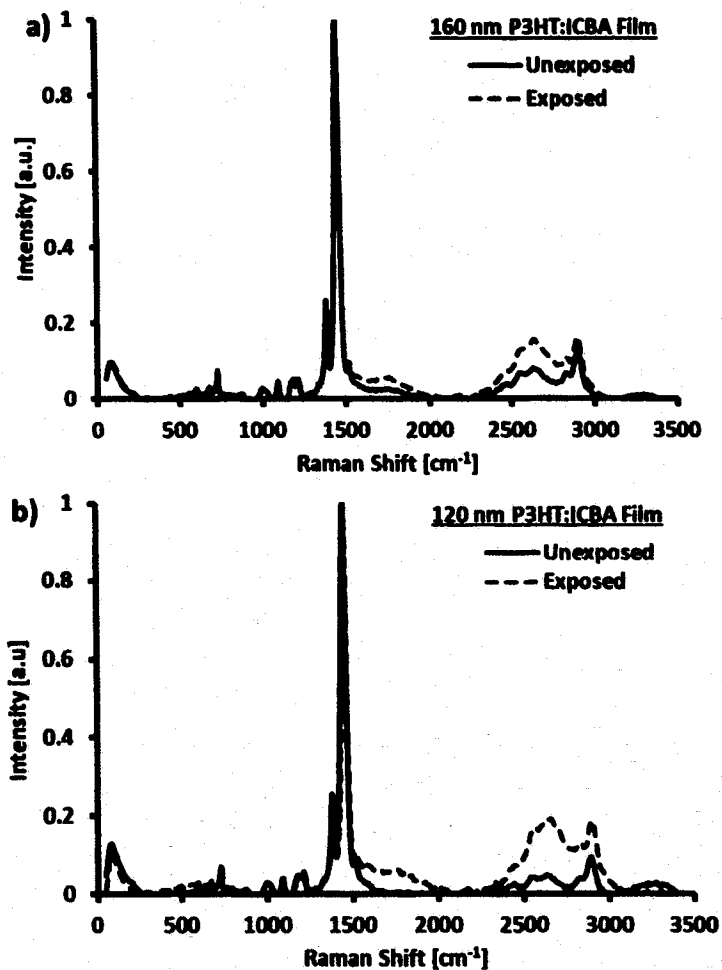


Figure 4-11: Raman spectrum of a) 160 nm, and b) 120 nm, P3HT:ICBA thin-films with and without e-beam exposure. The samples were exposed under 20 kV e-beam for 15 minutes inside AMRAY 1830 SEM.

The low *PCE* of devices with direct conversion method and their performance degradation over time confirms the need of a scintillator intermediate layer that will avoid the direct device exposure to the e-beam and will convert the electron kinetic energy into light energy.

4.4 Indirect Conversion Betavoltaic

4.4.1 Device Architecture

The basic architecture of indirect conversion polymer-fullerene heterostructure betavoltaic device consists of Al/P3HT:ICBA/PEDOT:PSS/ITO/glass (or PET)/quartz (or PET)/scintillator as shown in **Figure 4-12**. Unlike direct conversion betavoltaic device, in the case of the indirect conversion betavoltaic device, the energetic beta particles from beta source (radioisotope) encounter scintillator material. As these beta particles penetrate the scintillator, their kinetic energy generates shower of electrons and holes along the path they travel. The scintillator is special kind of material in which the generated electrons and holes recombine momentarily to generate photons (usually visible spectrum of light). These photons then travel towards the photovoltaic stack placed underneath the scintillator and get absorbed in an active layer of P3HT:ICBA to generate electrical current similarly as in photovoltaic solar cell. In this way, the indirect conversion betavoltaic devices are modified forms of photovoltaic solar cells. Here, the scintillator-generated photons are isotropic in nature and not necessarily travel only towards the active layer to get absorbed. In reality, they travel in all directions and only part of it gets absorbed in the active layer to generate usable output electrical power. The overall *PCE* of indirect conversion betavoltaic device is the efficiency of the scintillator to convert beta particle's kinetic energy to intermediate light energy times the *PCE* of photovoltaic stack to convert scintillator-generated light energy into electrical power. The different loss mechanisms in this case include the directional loss (photons travelling to other directions than active layer), internal interaction loss (photons lost due to absorption

within scintillator material itself) and external interaction loss (photons lost due to absorption in surrounding media before reaching the active layer).

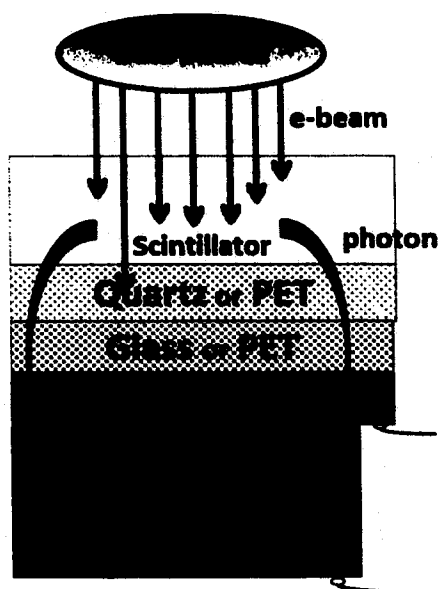


Figure 4-12: Indirect conversion polymer-fullerene heterostructure betavoltaic device architecture.

4.4.2 Scintillator for Indirect Conversion Betavoltaic

The performance of indirect conversion betavoltaic devices strongly depends on the efficiency of scintillator to convert beta particle's kinetic energy into photons. Therefore, it is desired that the scintillator material be as efficient as possible. The two best candidates for inorganic scintillators are cerium-doped yttrium aluminum garnet (Ce:YAG) and thallium-doped cesium iodide (CsI:Tl). The emission spectrums of these scintillators match well with the absorption spectrum of many semiconducting polymers including the polymer-fullerene blend of P3HT:ICBA. The Ce:YAG is a non-hygroscopic, chemically inert inorganic scintillator having emission range from 500 nm to 700 nm with an emission peak around 550 nm and a decay time of 70 ns [155]–[157].

The CsI:Tl is known as the brightest scintillator and has the greatest light output of all scintillator emitting 54 photons/keV [158]. The CsI:Tl has a large emission range from 375 nm to 725 nm with peak emission at 550 nm and decay time of 1 μ s [157], [158]. The CsI:Tl exhibits somewhat plastic mechanical properties which makes it very durable in situations of extreme acceleration.

However, it is somewhat hygroscopic and would need to be well-encapsulated to ensure long term efficiency [157]. Figure 4-13 shows the normalized emission spectrums of Ce:YAG and CsI:Tl [159] scintillators, and normalized absorption spectrum of 260 nm thick P3HT:ICBA polymer-fullerene blend on a quartz substrate. The absorption spectrum of P3HT:ICBA blend was measured with Filmetrics F10-RT reflectometer. The emission spectrum of Ce:YAG was acquired by exciting a Ce:YAG screen with a 325 nm laser and measuring the emitted light with an Ocean Optics USB 2000 spectrometer. Figure 4-13 shows that emission of CsI:Tl is better matched with absorption of the P3HT:ICBA blend.

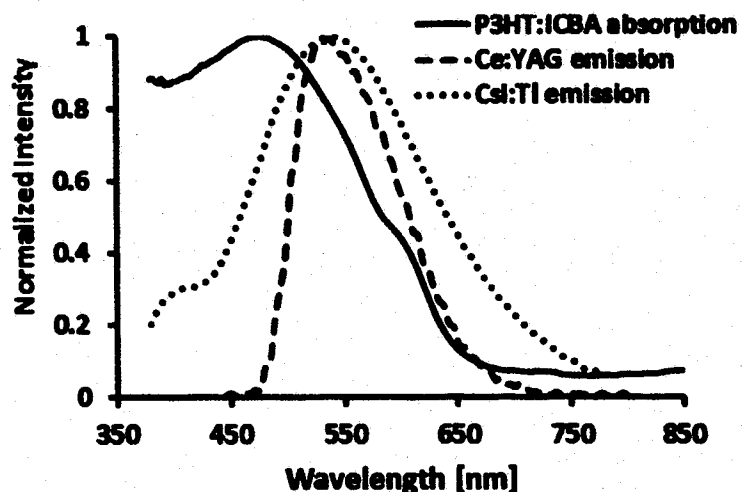


Figure 4-13: The absorption spectrum of 260 nm thick P3HT:ICBA blend on a quartz substrate, the emission spectrum of Ce:YAG and CsI:Tl scintillators. The emission spectrum of CsI:Tl is obtained from Phosphor Technology Ltd. [159].

4.4.3 Test Setup

The test setup for characterization of indirect conversion betavoltaic devices is similar to that of the direct conversion devices already mentioned in Section 4.3.3. Specifically, the testing setup of betavoltaic device is shown in **Figure 4-8**. The only difference is, in the case of direct conversion devices, e-beam is exposed from Al side while in indirect conversion from the scintillator side and photons pass through glass substrate to the active layer.

4.4.4 Fabrication

The indirect conversion betavoltaic device consists of a scintillator layer and a photovoltaic stack of polymer-fullerene blend. The detailed fabrication process of photovoltaic stack is given in Section 4.3.2. The deposition of the scintillator layer is described below.

4.4.4.1 Scintillator Deposition

The 10 μm Ce:YAG scintillator screen was deposited on a 1.58 mm quartz substrate (Technical Glass Products) and on a 175 μm -thick PET substrate using sedimentation process. A 1.58 mm quartz substrate was kept in the glass dish (16.4 cm diameter and 8.0 cm depth) with barium chloride solution. The glass rod with a diameter of 0.5 cm was placed under one end to give drainage tilt as shown in **Figure 4-14**. A total of 150 ml barium chloride solution was prepared by mixing 2.9 ml of analytical reagent (A.R.) grade barium chloride solution (0.4g/L $\text{BaCl}_2\cdot 2\text{H}_2\text{O}$ in demineralized water) and 147.1 ml water. The Ce:YAG phosphor (PhosphorTech Corp.) suspension was prepared in a conical flask with potassium silicate solution diluted with demineralized water. The 136 ml suspension was prepared by mixing 322.87 mg of Ce:YAG phosphor powder, 30

ml of potassium silicate solution (sg 1.057) and 106 ml of water. The suspension was then poured in the glass dish with quartz substrate and barium chloride solution, using a funnel. The solution was allowed to settle for 2 hours and was sucked off gently, using a pipette. Finally, the quartz substrate with phosphor layer on it was removed carefully from the glass dish and dried completely on a hot plate. A similar procedure was followed to deposit the Ce:YAG screen on the PET substrate. **Figure 4-14** shows the experimental setup for the Ce:YAG screen deposition.

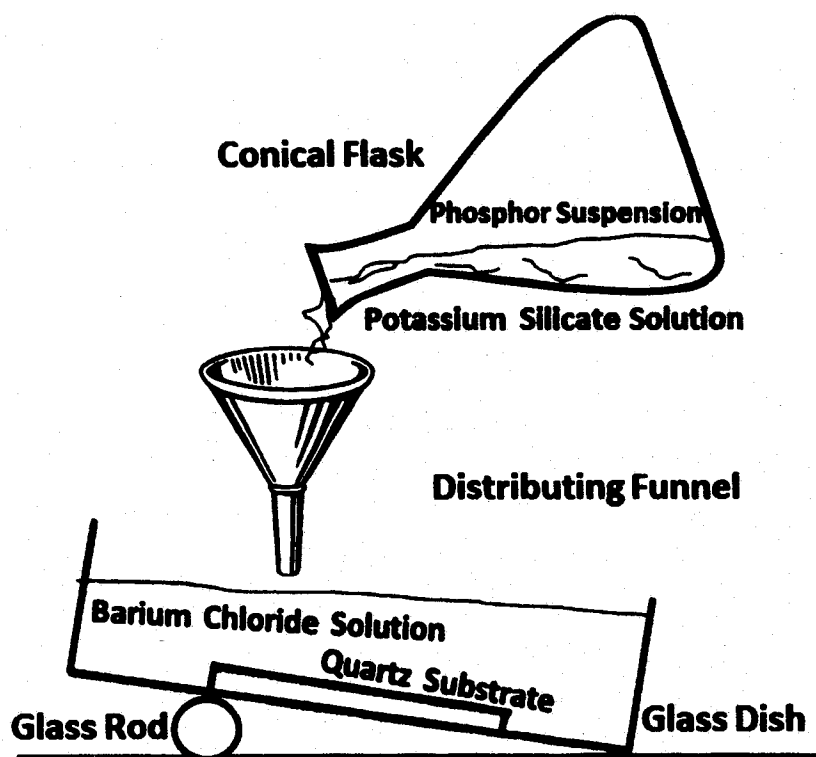


Figure 4-14: Ce:YAG scintillator screen deposition on quartz substrate using sedimentation process.

4.4.5 Results and Discussion

The indirect conversion betavoltaic devices of structure scintillator/quartz(PET)/glass(PET)/ITO/PEDOT:PSS/P3HT:ICBA/Al (structure shown in **Figure 4-12**) were

fabricated and tested to overcome any shortcomings of direct conversion betavoltaic devices. Such indirect conversion betavoltaic devices offer stability and high performance. In these devices, the intermediate scintillator screen is introduced as shown in Figure 4-12, which converts the e-beam kinetic energy into photons. So the optical characteristics of the P3HT:ICBA layer such as absorption profile is important in this case. Figure 4-15 shows the optical characteristics of P3HT:ICBA 1:1 ratio by weight thin film on a quartz substrate measured with Filmetrics F10-RT reflectometer. The emission spectrum of Ce:YAG scintillator, as shown in Figure 4-13, indicates a good match with the absorption spectrum of P3HT:ICBA blend.

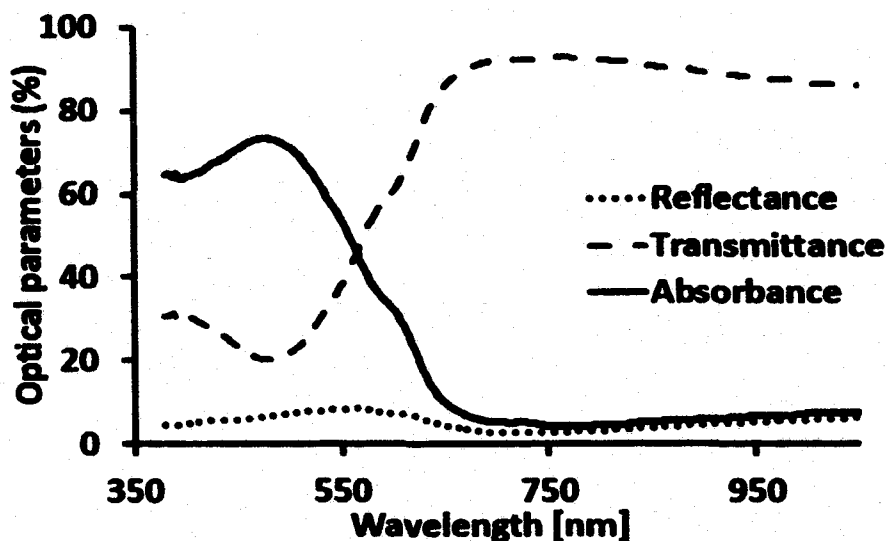


Figure 4-15: Optical characteristics of the 160 nm thick P3HT:ICBA 1:1 wt. thin film on a quartz substrate.

Table 4-3 shows the fabrication parameters of photovoltaic stack for I - V curves in Figure 4-16. The P3HT:ICBA polymer device on 1.1 mm boro-aluminosilicate glass (Delta Technologies) with Ce:YAG scintillator intermediate layer on 1.58 mm quartz substrate is denoted by symbol G. As shown in Figure 4-16, I - V curves were acquired for

two accelerating voltages of 7 kV and 10 kV at low and high e-beam current modes. The output electric current of the betavoltaic device increased with the e-beam current. For the same accelerating voltage, the input e-beam power increases with the increase of e-beam current. Data in Table 4-4 and Figure 4-17 show that the *PCE* of G devices increases with the e-beam input power and in almost a linear fashion.

Table 4-3: Fabrication parameters for indirect conversion betavoltaic devices.

Parameter/Material	Value/type
Solvent	Chlorobenzene
P3HT Concentration	10 mg/ml
P3HT:PCBM Ratio	1:1 wt.
Additive (OT)	0% vol.
Spin Coating Recipe	800 RPM for 50 s
Thickness	135 nm (Filmetrics)
PEDOT:PSS	3500 RPM, 30 s, ~ 50 nm
Aluminum	100 nm, 0.4 nm/s, 10^{-6} Torr (Thermal evaporator)
Annealing	150°C, 15 min (Post-production)
Contact Wire	0.25 mm dia. Copper wire

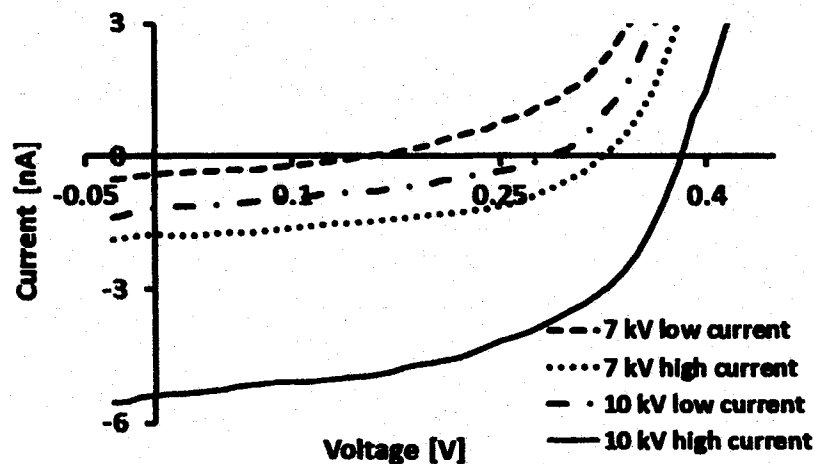


Figure 4-16: *I-V* characteristics of indirect conversion betavoltaic G devices (polymer device on glass substrate and scintillator on quartz) for 7 kV (low current 27 pA, high current 158 pA) and 10 kV (low current 60 pA, high current 300 pA).

Table 4-4: Input e-beam current, accelerating voltage, e-beam power and *PCE* for indirect conversion G devices.

V_{acc} (kV)	I_{e-beam} (pA)	P_{in} (μ W)	<i>PCE</i> (%)
7	27	0.19	0.0112
10	60	0.60	0.0214
20	130	2.60	0.0420
30	110	3.30	0.0492

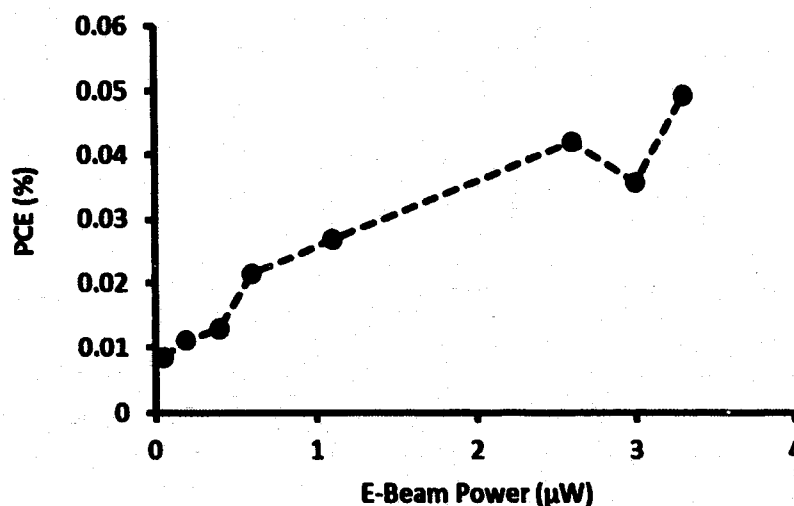


Figure 4-17: Betavoltaic *PCE* at different e-beam powers of G devices (polymer device on glass substrate and scintillator on quartz).

As mentioned before, G denotes the polymer device on glass substrate with scintillator on quartz substrate, P denotes the polymer device on PET substrate with scintillator on a quartz substrate, and the polymer device on PET substrate with phosphor on PET is denoted by PP. In general, the indirect energy conversion polymer-based devices with scintillator performed better compared to the direct conversion polymer-based devices without scintillator. However, the *PCE* of indirect conversion betavoltaic

G devices is still low as shown in **Figure 4-17**. One of the reasons for the low performance of these indirect conversion betavoltaic devices is the directional loss. Here, in G devices, the 1.58 mm quartz and 1.1 mm glass substrate significantly separate the Ce:YAG scintillator from the P3HT:ICBA active layer. This results in directional and external interaction losses since a significant number of scintillator-generated photons was lost in lateral directions and absorbed in glass and quartz substrates instead of being absorbed in the P3HT:ICBA active layer of the betavoltaic device.

These losses can be minimized by reducing the distance between photon-generating scintillator and photon-absorbing polymer active layer. These losses were considerably reduced by replacing 1.1 mm glass substrate by thin 175 μm PET substrate for polymer device fabrication. At $E_{kin} = 10$ keV, the P_{out} , I_{SC} , and the PCE were almost doubled in P device compared to G device (see **Figure 4-18** and **Table 4-6**). **Figure 4-18** shows the $I-V$ characteristics of several different types of betavoltaic devices. **Table 4-5** gives the fabrication parameters for photovoltaic stack of devices with $I-V$ curve in **Figure 4-18**. The performance indirect conversion betavoltaic device was further improved by using scintillator layer on thin PET substrate called RadiantFlex (PhosphorTech). The RadiantFlex, a proprietary scintillator of PhosphorTech Company, has a 10 μm -thick layer of Ce:YAG on a 60 μm -thick PET substrate. The short circuit current increased by 19 times, output electrical power increased by 23 times and PCE increased by 39 times at 10 keV in PP device compared to G device (see **Figure 4-18** and **Table 4-6**). **Table 4-6** gives the I_{SC} , V_{OC} , P_{out} , and the PCE for G, P, and PP betavoltaic devices for $E_{kin}=10$ keV, 20 keV and 30 keV. The measurement error calculation is shown in Appendix B. The improvement in device performance is due to further reducing

distance between scintillator and polymer layers that significantly minimized the directional and external interaction losses.

Table 4-5: Fabrication parameters for G, P, PP indirect conversion betavoltaic devices.

Parameter/Material	Value/type
Solvent	Chlorobenzene
P3HT Concentration	15 mg/ml
P3HT:PCBM Ratio	1:1 wt.
Additive (OT)	0% vol.
Spin Coating Recipe	700, 800, 900, 1000 RPM for 50 s
Thickness	180, 165, 160, 150 nm (Surface Profiler)
PEDOT:PSS	3500 RPM, 30 s, ~ 50 nm
Ambient Conditions	20°C, 50% Humidity
Aluminum	100 nm, 0.4 nm/s, 10^{-6} Torr (Thermal evaporator)
Annealing	150°C, 15 min (Post-production)
Contact Wire	0.25 mm dia. Copper wire
Epoxy	Conductive silver epoxy

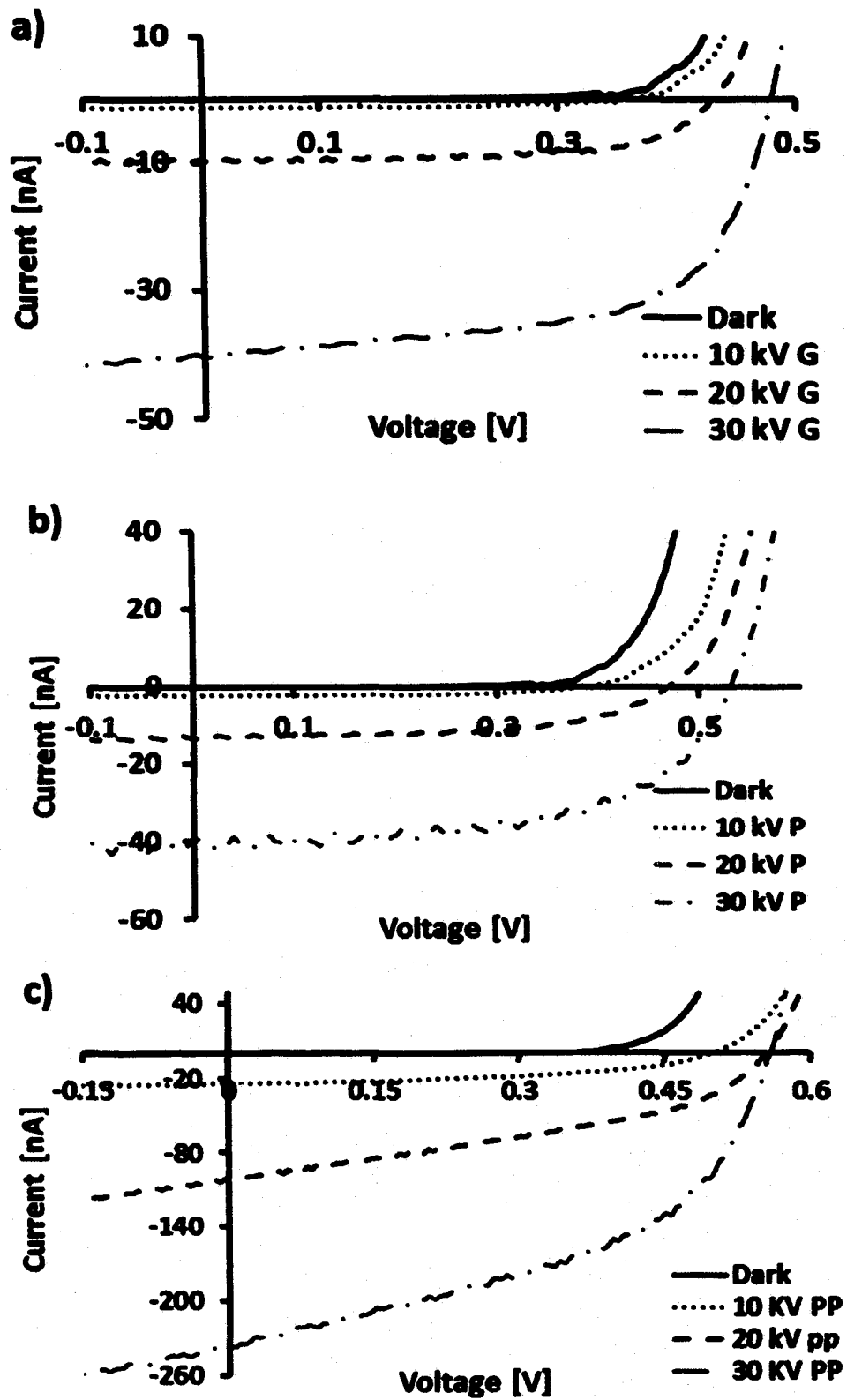


Figure 4-18: I - V characteristics of indirect conversion betavoltaic devices: a) G device, b) P device, c) PP device in dark (i.e. no e-beam) and for 10, 20 and 30 keV e-beams.

Table 4-6: Different betavoltaic device parameters of indirect conversion G, P and PP devices.

Electron Beam Energy →		10 keV	20 keV	30 keV
G Polymer device on glass with phosphor on quartz	I_{e-beam} (pA)	120 ± 0.5	390 ± 1.8	750 ± 3.4
	P_{in} (μW)	1.2 ± 0.05	7.8 ± 0.7	23 ± 3.1
	I_{SC} (nA)	1.2	9.6	40.0
	V_{OC} (V)	0.29	0.43	0.48
	P_{out} (nW)	0.24 ± 0.01	2.7 ± 0.1	11.8 ± 0.5
	PCE (%)	0.020 ± 0.002	0.035 ± 0.004	0.052 ± 0.009
P Polymer device on PET with phosphor on quartz	I_{e-beam} (pA)	120 ± 0.5	390 ± 1.8	750 ± 3.4
	P_{in} (μW)	1.2 ± 0.05	7.8 ± 0.7	23 ± 3.1
	I_{SC} (nA)	2.2	13	41
	V_{OC} (V)	0.38	0.47	0.53
	P_{out} (nW)	0.49 ± 0.2	3.6 ± 0.1	13 ± 0.4
	PCE (%)	0.040 ± 0.003	0.050 ± 0.006	0.060 ± 0.009
PP Polymer device on PET with phosphor on PET	I_{e-beam} (pA)	73 ± 0.3	260 ± 1.2	330 ± 1.5
	P_{in} (μW)	0.73 ± 0.03	5.1 ± 0.5	9.7 ± 1.3
	I_{SC} (nA)	24	100	240
	V_{OC} (V)	0.50	0.55	0.56
	P_{out} (nW)	5.7 ± 0.2	22 ± 0.6	62 ± 1.6
	PCE (%)	0.78 ± 0.06	0.43 ± 0.05	0.6 ± 0.05

4.4.5.1 Comparison of Ce:YAG and CsI:Tl Scintillators

So far, the indirect conversion betavoltaic devices with Ce:YAG scintillator are presented. Although Ce:YAG is non-hygroscopic and a stable scintillator, the light emitting capabilities of CsI:Tl is better compared to Ce:YAG as it is known as the brightest scintillator, discussed in Section 5.2.1.2.1. Slightly hygroscopic in nature, CsI:Tl if used with proper encapsulation can provide better performance with indirect conversion betavoltaic devices. Also, from **Figure 4-13**, the emission spectrum of CsI:Tl is wider in the visible regions and better matched with the absorption spectrum of active P3HT:ICBA layer compared to Ce:YAG. Next, the behavior of energetic electron beams were simulated in these two, Ce:YAG and CsI:Tl, scintillators and indirect conversion betavoltaic devices were fabricated and tested with these two scintillators to compare the performances.

4.4.5.1.1 Monte-Carlo Simulations of Ce:YAG and CsI:Tl. The Monte Carlo simulations can be used to study the random physical phenomenon such as electron beam interaction with solid materials [160], [161]. These simulations help to understand the light generation nature of different scintillator materials and optimize them for specific application such as betavoltaic batteries with organic active layer. The betavoltaic device architecture with the intermediate scintillator layer offers the indirect energy conversion process for the betavoltaic device [127], [132], discussed in Section 5.2.1.2.

The Monte Carlo simulations using CASINO, a free software for simulating electron trajectory in solid for low energy electron beam (0.1 to 30 keV) [162] [163], for two different scintillators, Ce:YAG and CsI:Tl, were conducted. The simulations provided the penetration depth of the input electron beam and catholuminescence

intensities of these two scintillators. The 10,000 electrons were used in the simulation at 30 kV electron beam accelerating voltage. **Figure 4-19** shows the electron beam trajectories in XZ plane within (a) Ce:YAG film and (b) CsI:Tl film. From **Figure 4-19**, it is seen that most of the electron beam energy get absorbed by 3 μm depth of Ce:YAG and 3.5 μm depth of CsI:Tl. These being optimized thicknesses of scintillators to be used for the best performance at 30 kV of electron beam accelerating voltage.

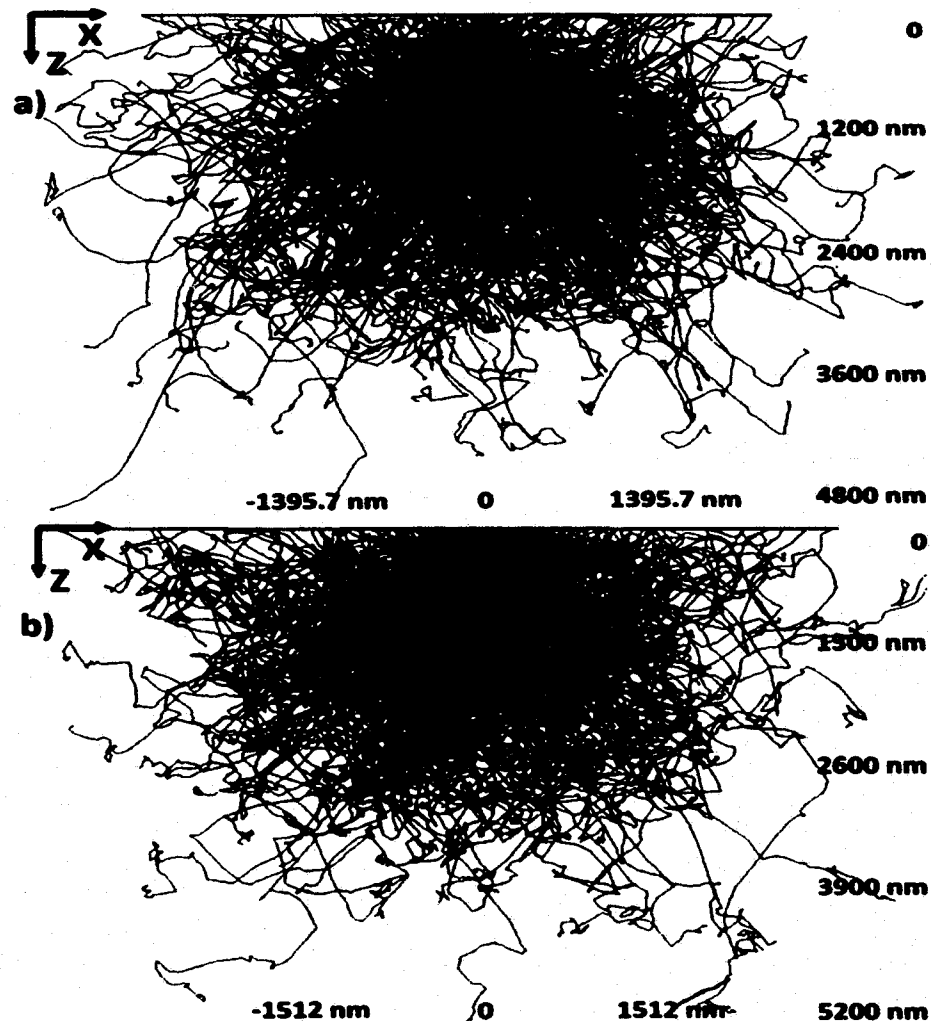


Figure 4-19: The 30 keV electron beam trajectories of 10,000 electrons in (a) Ce:YAG and (b) CsI:Tl obtained from CASINO Monte Carlo simulations.

The use of a thicker layer of a scintillator could lead towards the photon loss due to self-absorption within scintillator material before those photons get released towards the active P3HT:ICBA layer [134]. In addition, if a thinner layer is used, some of the e-beam penetrates through the scintillator and reach the glass substrates losing part of their kinetic energy with no use. **Figure 4-20** shows the catholuminescence intensity comparison between Ce:YAG and CsI:Tl scintillators at 30 kV electron beam accelerated voltage. The catholuminescence intensity provides the photon generation capability of scintillators when these are bombarded with energetic electron beam. The simulation results at 30 kV e-beam accelerated voltage show that CsI:Tl is comparatively more efficient for photon generation than Ce:YAG shown in **Figure 4-20**, which is further verified with the experimental results shown in Section 4.4.5.1.2.

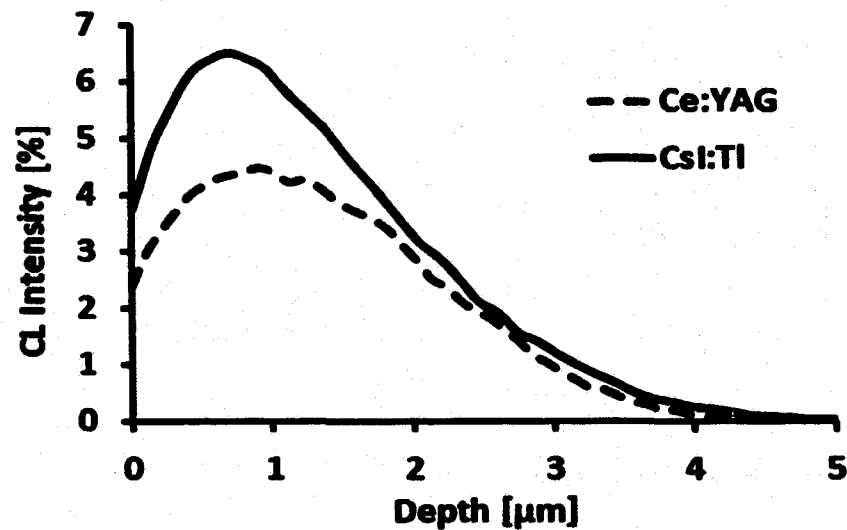


Figure 4-20: The Catholuminescence intensity profile of Ce:YAG and CsI:Tl scintillators for 30 kV electron kinetic energy obtained from CASINO Monte Carlo simulations.

4.4.5.1.2 **Experimental Results.** The optical properties of scintillators and polymer P3HT:ICBA thin film were measured before testing betavoltaic devices. **Figure 4-21** shows the measured reflectance, transmittance and estimated absorbance of P3HT:ICBA thin film on quartz substrate. The measurement was done with spectral reflectometer Filmetrics F10-RT.

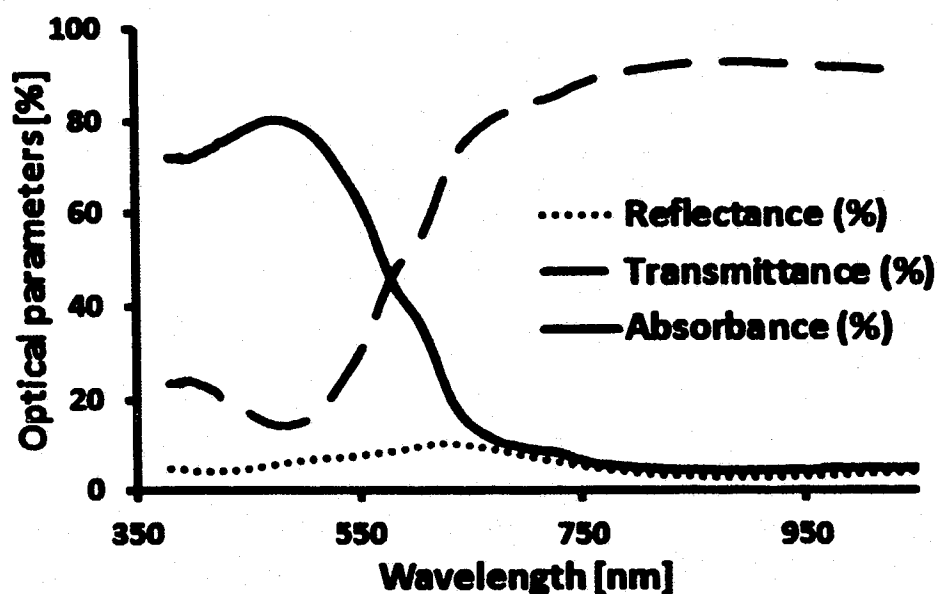


Figure 4-21: The optical characteristics of the 260 nm thick P3HT:ICBA (1:1 wt.) thin film on a quartz substrate obtained from Filmetrics F10-RT reflectometer.

Next, the betavoltaic devices were tested under a scanning electron microscope (SEM) using AMRAY 1830 SEM to simulate the beta particles with two different scintillators. **Figure 4-9** shows the testing setup of the betavoltaic device. **Table 4-7** shows the fabrication parameters of the photovoltaic stack.

Table 4-7: Fabrication parameters for indirect conversion betavoltaic devices with Ce:YAG and CsI:Tl scintillators.

Parameter/Material	Value/type
Solvent	Chlorobenzene
P3HT Concentration	18 mg/ml
P3HT:PCBM Ratio	1:1 wt.
Additive (OT)	0% vol.
Spin Coating Recipe	700 RPM for 50 s
Thickness	260 nm (Surface Profiler)
PEDOT:PSS	3500 RPM, 30 s, ~ 50 nm
Ambient Conditions	21.39°C, 43% Humidity
Aluminum	100 nm, 0.4 nm/s, 10^{-6} Torr (Thermal evaporator)
Annealing	150°C, 15 min (Post-production)
Contact Wire	0.25 mm dia. Copper wire
Epoxy	Conductive silver epoxy

The electron beams with 10 keV, 20 keV and 30 keV electron energies were used to test polymer betavoltaic devices with two scintillators, Ce:YAG and CsI:Tl. The Keithley 6487 picoammeter connected with SEM was used to measure the betavoltaic I - V characteristics of devices placed inside SEM and recorded with a PC equipped with LabView software. **Figure 4-22** shows the betavoltaic I - V characteristics, and **Table 4-8** gives the betavoltaic parameters, of polymer betavoltaic devices with Ce:YAG and CsI:Tl scintillators for (a) 10 kV, (b) 20 kV and (c) 30 kV e-beam kinetic energies.

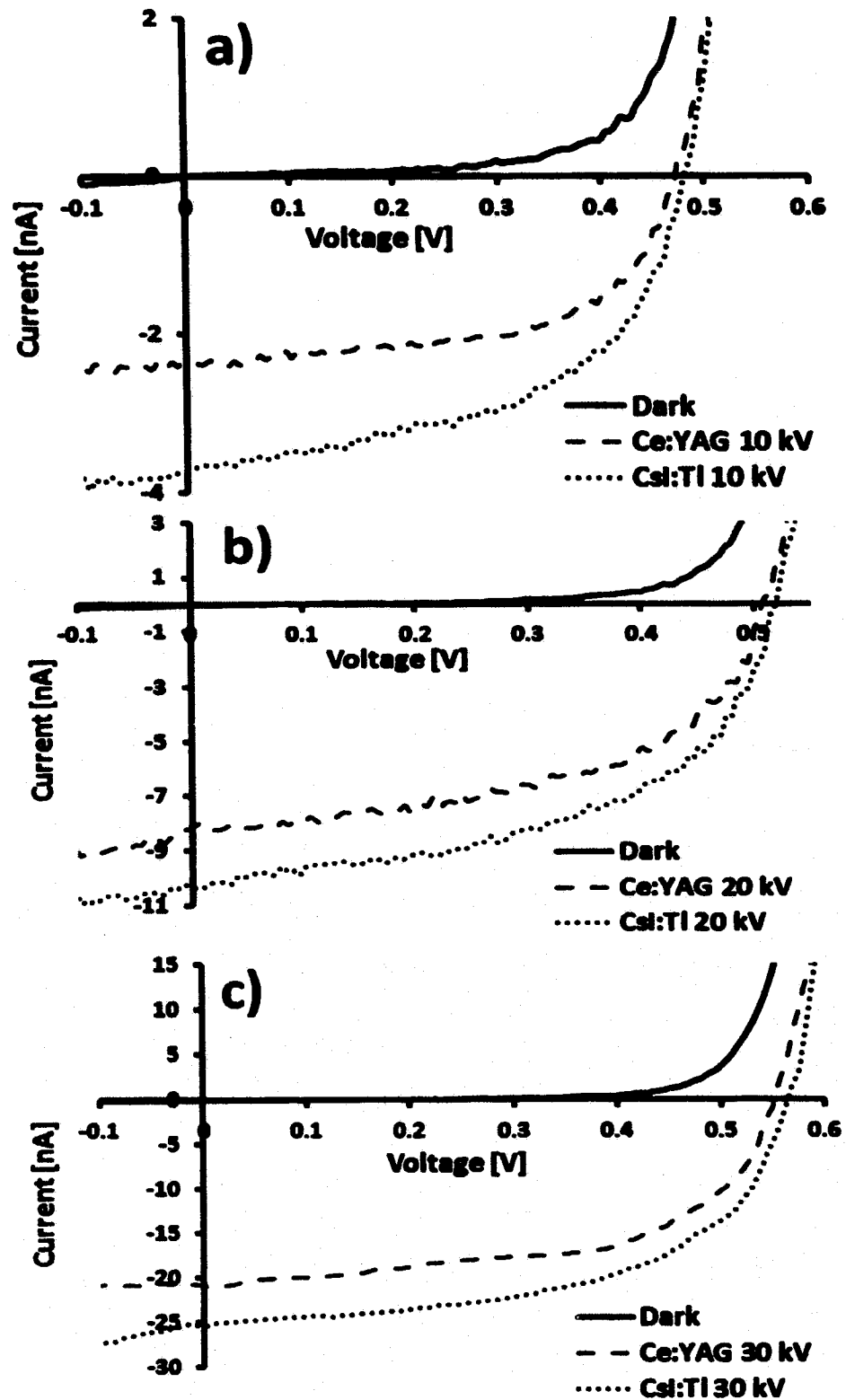


Figure 4-22: The betavoltaic $I-V$ characteristics compared with Ce:YAG and CsI:Tl scintillators at (a) 10 kV, (b) 20 kV and (c) 30 kV e-beam accelerated voltage.

Table 4-8: Electron beam and betavoltaic device parameters obtained when tested with Ce:YAG and CsI:Tl scintillators.

V_{acc} (kV)		10	20	30
I_{e-beam} (pA)		39.5 ± 0.2	124 ± 0.6	228 ± 1
P_{in} (μ W)		0.4 ± 0.02	2.5 ± 0.2	6.8 ± 0.9
With Ce:YAG	I_{sc} (nA)	2.38	8.17	20.9
	V_{oc} (V)	0.47	0.51	0.55
	P_{out} (nW)	0.65 ± 0.02	2.21 ± 0.07	6.5 ± 0.1
	PCE (%)	0.16 ± 0.01	0.09 ± 0.01	0.10 ± 0.02
	FF (%)	58 ± 3	53 ± 3	57 ± 3
With CsI:Tl	I_{sc} (nA)	3.74	10.4	25.4
	V_{oc} (V)	0.48	0.52	0.56
	P_{out} (nW)	0.93 ± 0.03	2.75 ± 0.08	7.90 ± 0.2
	PCE (%)	0.24 ± 0.02	0.11 ± 0.01	0.12 ± 0.02
	FF (%)	52 ± 3	51 ± 3	55 ± 3

From Figure 4-22, it is seen that the betavoltaic devices performed better with CsI:Tl than Ce:YAG at 10 kV, 20 kV and 30 kV electron beams. The better catholuminescence intensity result from the Monte Carlo simulation of CsI:Tl and better match of emission profile of CsI:Tl with absorption profile of P3HT:ICBA compared to Ce:YAG is verified with these experimental results. The increase in short circuit current by 57% at 10 kV, 27% at 20 kV and 21% at 30 kV by using CsI:Tl compared to Ce:YAG demonstrated the promising opportunities of CsI:Tl scintillator for polymer betavoltaic devices. The small increase in open circuit voltages is also observed by replacing Ce:YAG with CsI:Tl scintillator. However, the fill factor (FF) is observed better in the case of Ce:YAG. With V_{MP} and I_{MP} being the voltage and current at maximum power

point, the open circuit voltage V_{OC} , and the short circuit current I_{SC} , the FF factor is calculated using the formula

$$FF = \frac{V_{MP}I_{MP}}{V_{OC}I_{SC}} \quad \text{Eq. 4-6}$$

In all cases, the output electrical power from the betavoltaic devices increased with input electron beam energy showing that the active polymer-fullerene layer performs better in the presence of high input light energy. Also, at high electron kinetic energies, the electron beam can penetrate deeper into the scintillator that is closer to the polymer device placed underneath, thus reducing photon loss within the scintillator, i.e. internal interaction loss. The various electron beam parameters used in experiment, such as e-beam accelerated voltage, e-beam current, e-beam power, and other betavoltaic device parameters obtained from experiment are listed in **Table 4-8**. Using CsI:Tl, the PCE is greater by 50% at 10 kV, 22% at 20 kV and 20% at 30 kV compared with Ce:YAG. The maximum PCE of 0.24% is obtained at 10 kV with CsI:Tl scintillator. The measurement error is shown in Appendix B.

4.4.5.2 Role of Thin Reflecting Film on Scintillator

In case of indirect conversion betavoltaic devices, the photons generated within scintillator due to electron beam excitation are isotropic in nature. That means the photon can travel in any direction. Ideally, it is required that all generated photons should reach and absorbed within the active layer, and contribute to the generation of the exciton pairs. It can be presumed that almost 50% of generated photons travel in an upward direction, see **Figure 4-12**, which is opposite of the active layer. Such loss of photons due to isotropic nature can be minimized to a certain extent by applying a thin reflecting layer

on top of the scintillator that will reflect all the photons traveling upwards back to the active layer and help to enhance the incident optical power on the active layer [134]. It is required that such thin film needs to be highly reflecting and at the same time should ensure minimal loss of e-beam kinetic energy, as the e-beam has to pass this thin film to reach the scintillator. Aluminum is well-known as a good reflector of both visible light and radiated heat [164], [165]. Additionally, aluminum is non-toxic, and light metal with a density of 2.7 g/cm^3 causes minimal loss to e-beam energy [165]. Therefore, the aluminum thin film is perfect fit for this application. **Figure 4-23** shows the cross-section of the indirect conversion betavoltaic device.

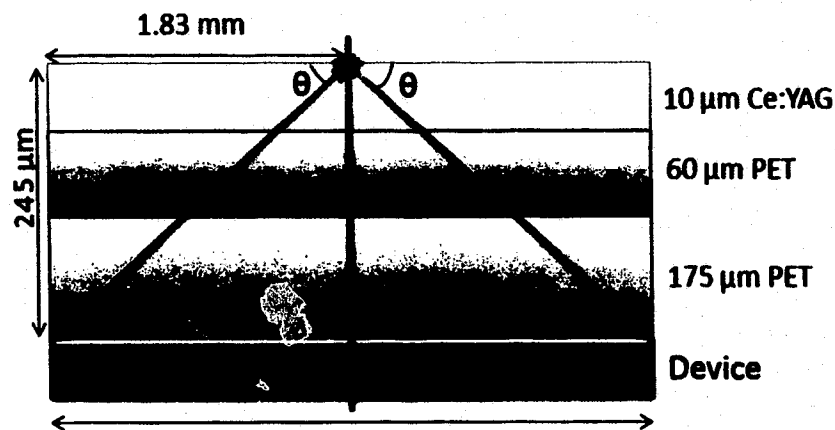


Figure 4-23: Cross section of indirect conversion betavoltaic device without thin reflecting film on top of the scintillator to study the directional loss.

The area of betavoltaic device is 10.5 mm^2 ($3 \text{ mm} \times 3.5 \text{ mm}$), so the equivalent radius of the device is 1.83 mm ($\text{Area} = 10.5 \text{ mm}^2 = \pi r^2$). Consider the case without the reflecting film on top of the scintillator and suppose the e-beam generates a photon at the center of the scintillator as shown in **Figure 4-23**. The minimum angle θ that the photon makes with the device's surface (horizontal plane) such that it hits the device and

gets absorbed is $\theta = \tan^{-1}\left(\frac{0.245}{1.83}\right) = 7.6^\circ$ (see **Figure 4-23**). This means that only photons within a cone of angle $180-2\theta$ reach the device and the others are lost. Hence, the percentage of optical power that reaches the device without the reflecting film on top of the scintillator is $\frac{180-2\theta}{360} = 45.78\%$ (without Al).

Now consider the case with a 30 nm aluminum thin-film reflector on top of Ce:YAG scintillator as shown in **Figure 4-24**. Here, the angle θ is the same as in the previous case, i.e. 7.6° (see **Figure 4-23**). The minimum angle α that the photon makes with the device's surface (horizontal plane) such that it reflects back from the aluminum thin film and hits the polymer device is $\alpha = \tan^{-1}\left(\frac{0.24503}{0.92}\right) = 14.9^\circ$ (see **Figure 4-24**). Since the reflectance of a 32 nm thin aluminum film at $546 \mu\text{m}$ wavelength is 90.4% [166], almost 90% of all photons within the cone of the angle, $180-2\alpha$, reflect back and hit the polymer active layer. Therefore, the percentage of optical power that reaches active layer with the thin aluminum reflecting film is $\frac{0.9[(180-2\alpha)+(180-2\theta)]}{360} = 83.3\%$ (with Al).

Hence, by neglecting other losses, the percentage enhancement in the incident optical power on the polymer device with a 30 nm of aluminum thin reflecting layer on top of the scintillator can be written as

$$\% \text{ Enhancement in incident optical power} = \frac{0.833 - 0.4578}{0.4578} = 82\%. \quad \text{Eq. 4-7}$$

This shows that neglecting other photon losses and with 30 nm aluminum thin-film of 90% reflectance on top of the scintillator, up to 82% enhancement in the incident optical

power onto the active layer of betavoltaic devices can be achieved, which would significantly enhance the overall performance of the device.

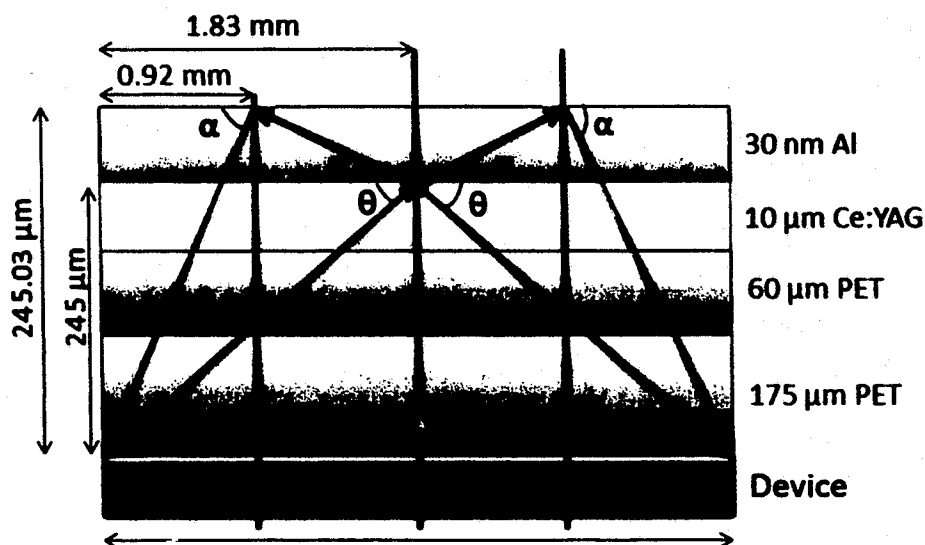


Figure 4-24: Cross section of indirect conversion betavoltaic device with a 30 nm aluminum thin reflecting film on top of the scintillator to study the directional loss.

4.4.5.2.1 Monte-Carlo Simulations with Al Thin-Film on Scintillator. The mathematical calculations in Section 5.3.2.2 show the enhancement in the incident optical power on the active layer by applying a thin reflection film on top of the scintillator. However, the loss in electron beam kinetic energy needs to be studied due to the presence of such reflecting film. Here, electron beams were simulated for Ce:YAG scintillator with a 30 nm aluminum thin film on top of it to investigate the e-beam energy loss caused by the aluminum layer using CASINO Monte-Carlo simulations. In these simulations, 120 nm of e-beam radius was used and 100,000 electrons were used for 10 kV, 20 kV and 30 kV accelerating voltages. The device architecture for simulation was Al (30 nm)/Ce:YAG (10 μm)/PET (60 μm). **Figure 4-25** shows the catholuminescence intensity profiles of Al/Ce:YAG/PET architecture for 10 kV, 20 kV and 30 kV accelerating voltages. The e-

beam kinetic energy absorbed by 10 nm and 30 nm Al thin films on top of Ce:YAG are 2.50% and 3.37%, respectively, obtained from catholuminescence profiles. **Figure 4-26** shows the cross-sectional view of absorbed e-beam energy in Al/Ce:YAG/PET device architecture for a) 10 kV, b) 20 kV and c) 30 kV accelerating voltages. So the calculations and simulations show that the presence of a 30 nm aluminum film offers about 82% incident optical power enhancement, whereas only less than 4% e-beam kinetic energy loss. This means the enhancement in overall performance of indirect conversion betavoltaic devices can be achieved with the thin reflecting film (30 nm of Al) on top of the scintillator. In the next section, the experimental results presented verify the calculation and simulation results. Also, in the next section, these simulation results are used to calculate the overall efficiency of indirect conversion betavoltaic device with and without thin aluminum reflecting film on top of the scintillator.

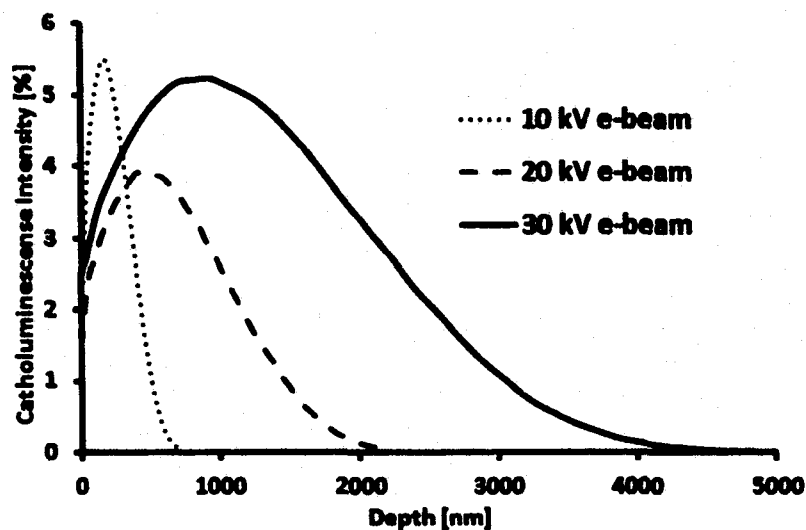


Figure 4-25: Catholuminescence intensity profiles of Al/Ce:YAG/PET device architecture for 10 kV, 20 kV and 30 kV accelerating voltages obtained from CASINO Monte-Carlo simulations.

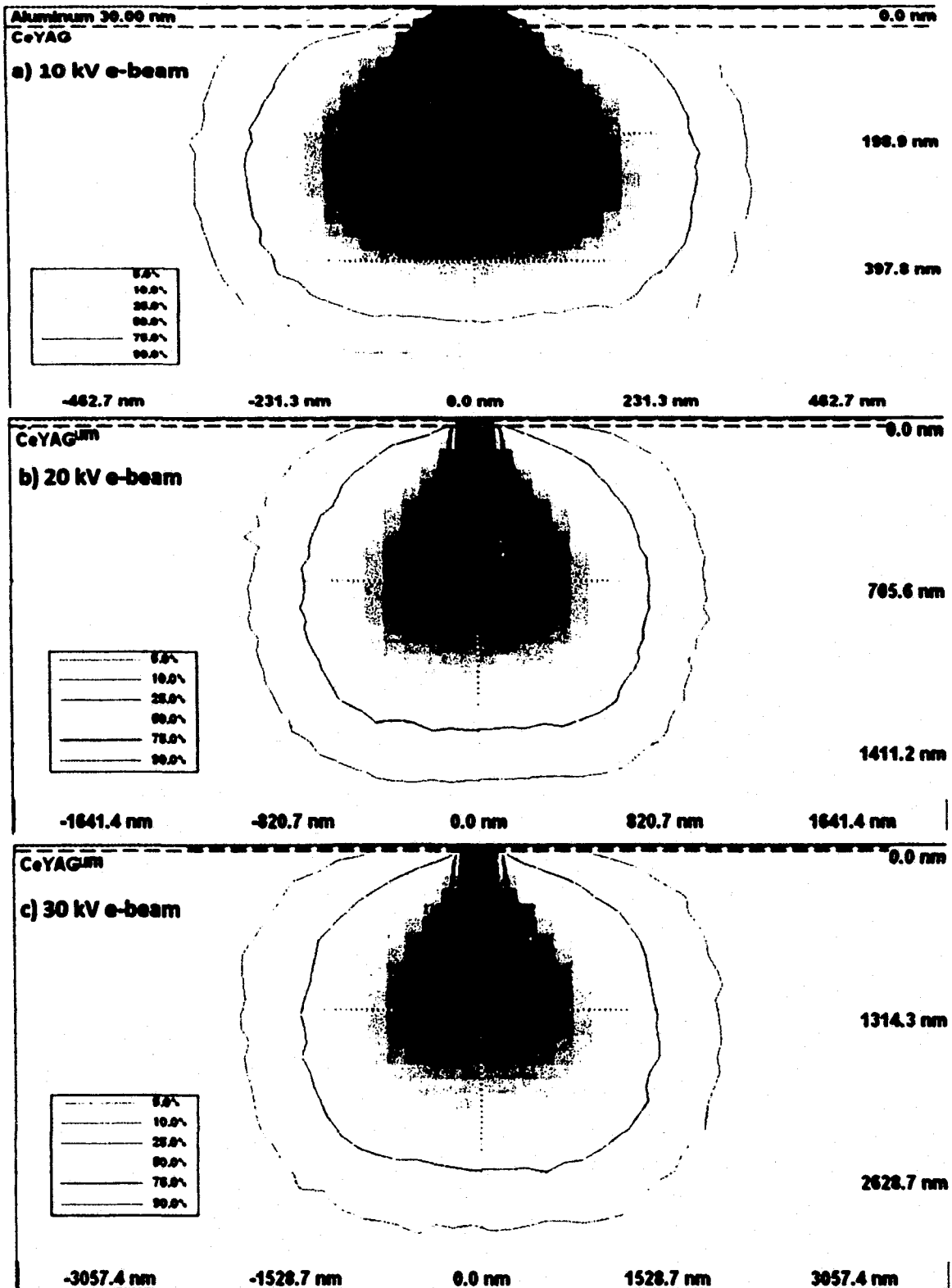


Figure 4-26: Cross-sectional view of absorbed e-beam energy in Al/Ce:YAG/PET device architecture for a) 10 kV, b) 20 kV, and c) 30 kV accelerating voltages.

4.4.5.2.2 **Experimental Results.** The 10 nm and 30 nm thin-films of aluminum were deposited on top of Ce:YAG scintillator using Denton 502B thermal evaporator and used to test the indirect conversion betavoltaic devices. **Figure 4-27** shows the Ce:YAG films used in device testing. The polymer betavoltaic devices with a 235 nm thick active layer of P3HT:ICBA were fabricated on PET substrates. **Figure 4-28** shows the optical characteristics of a 235 nm thick P3HT:ICBA active layer on quartz substrate measured in Filmetrics F10-RT reflectometer.

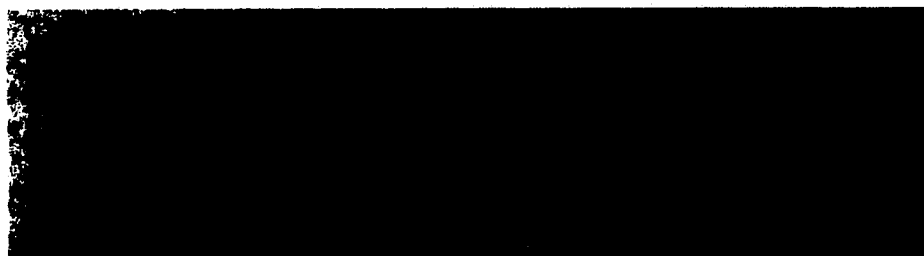


Figure 4-27: a) Ce:YAG film, b) Ce:YAG with a 10 nm aluminum film, and c) Ce:YAG with a 30 nm aluminum film.

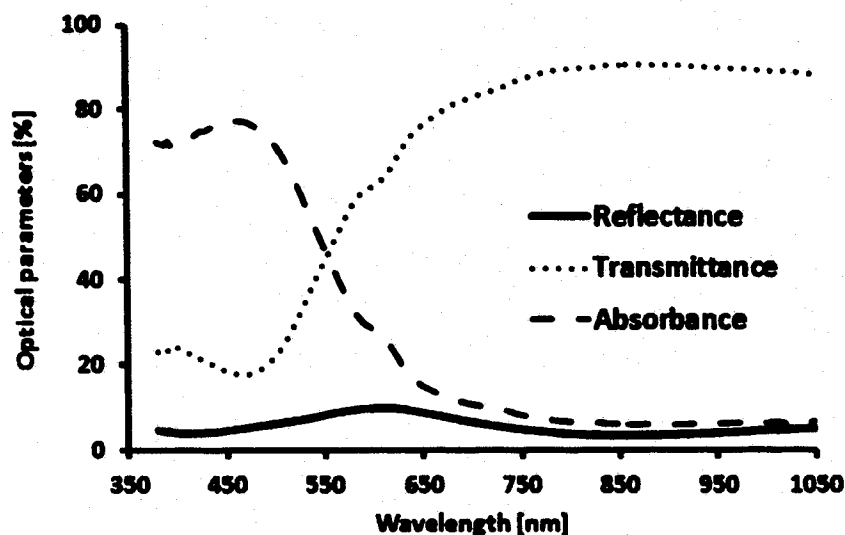


Figure 4-28: Transmittance, reflectance and absorbance of 235 nm P3HT:ICBA film on a quartz substrate.

Devices were tested in AMRAY 1830 SEM with 10 keV, 20 keV and 30 keV e-beam energies. The short circuit currents and open circuit voltages increased with Al reflecting films on top of Ce:YAG scintillators. The enhancement in *PCE* was obtained with Al layer on Ce:YAG for all accelerating voltages. The maximum *PCE* of 0.33% is obtained with 30 nm of Al on Ce:YAG for 20 kV. The enhancement with a 30 nm Al on Ce:YAG for 10 kV was 18.5%, for 20 kV was 26.9% and for 30 kV was 26.7% when compared with devices with pristine Ce:YAG scintillator. Over 80% enhancement in incident optical power on the active layer due to aluminum reflecting film calculated above and less than 4% e-beam energy loss in aluminum film obtained from Monte-Carlo simulations were confirmed with these experimental results. **Table 4-9** shows the fabrication parameters of photovoltaic stack. **Figure 4-29** shows the betavoltaic *I-V* characteristics with and without Al reflecting layer on Ce:YAG scintillator for a) 10 kV, b) 20 kV, and c) 30 kV accelerating voltages. **Table 4-10** provides the e-beam parameters and **Table 4-11** gives the various betavoltaic device parameters. The measurement error calculation is given in Appendix B.

Table 4-9: Fabrication parameters for indirect conversion betavoltaic devices with Al thin-film on top of Ce:YAG scintillator.

Parameter/Material	Value/type
Solvent	Chlorobenzene
P3HT Concentration	18 mg/ml
P3HT:PCBM Ratio	1:1 wt.
Additive (OT)	0% vol.
Spin Coating Recipe	700 RPM for 50 s
Thickness	235 nm (Surface Profiler)
PEDOT:PSS	3500 RPM, 30 s, ~ 50 nm
Ambient Conditions	21.88°C, 54% Humidity
Aluminum	100 nm, 0.4 nm/s, 10^{-6} Torr (Thermal evaporator)
Annealing	150°C, 15 min (Post-production)

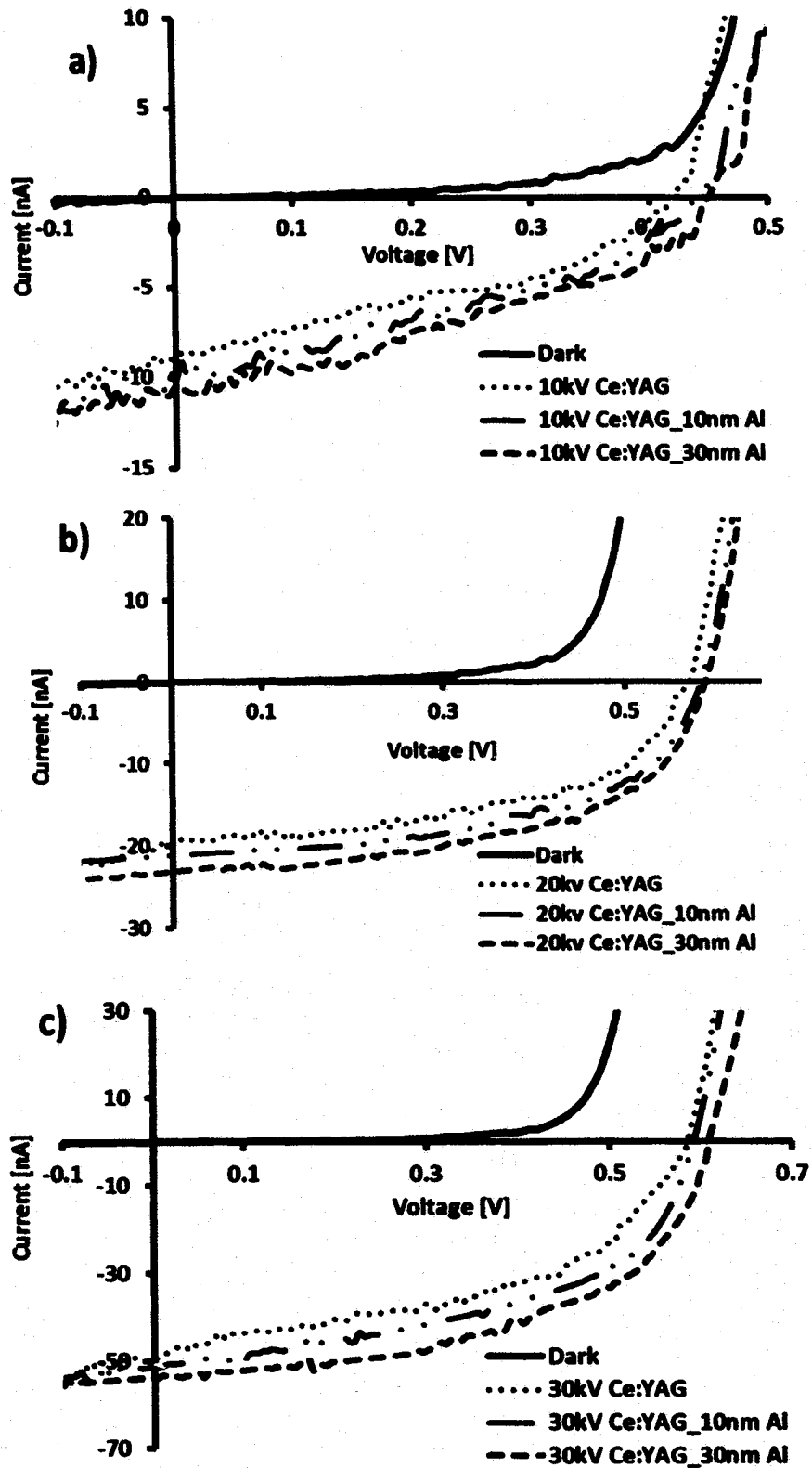


Figure 4-29: Betavoltaic $I-V$ characteristics with and without Al reflecting layer on Ce:YAG scintillator for a) 10 kV, b) 20 kV, and c) 30 kV accelerating voltages.

Table 4-10: Accelerating voltage, e-beam current and e-beam power used to test indirect conversion betavoltaic devices with and without aluminum reflecting film on top of Ce:YAG scintillator.

Accelerating voltage (kV)	10	20	30
E-beam Current (pA)	52.9 ± 0.2	115.0 ± 0.5	293 ± 1
E-beam Power (μW)	0.529 ± 0.002	2.30 ± 0.01	8.79 ± 0.04

Table 4-11: PCE and other betavoltaic device parameters with and without thin aluminum reflecting film on top of Ce:YAG scintillator.

kV	Scintillator	I_{SC} (nA)	V_{OC} (V)	I_{MP} (nA)	V_{MP} (V)	FF ±2 (%)	PCE ±0.01 (%)
20	Ce:YAG 10nm Al	10.17	0.44	4.75	0.34	36	0.31
	Ce:YAG	19.92	0.57	14.01	0.43	52	0.26
	Ce:YAG 30nm Al	23.14	0.59	17.11	0.45	56	0.33
	Ce:YAG 10nm Al	51.27	0.59	32.99	0.46	49	0.17

The overall PCE of indirect conversion betavoltaic device (η) is the product of efficiency of the scintillator to convert e-beam kinetic energy to photons (η_1) and PCE of photovoltaic stack to convert photon energy to the electrical output power (η_2) as shown in Figure 4-30. The following is the overall PCE calculation for 10 kV accelerating voltage with and without Al thin-film on top of Ce:YAG scintillator.

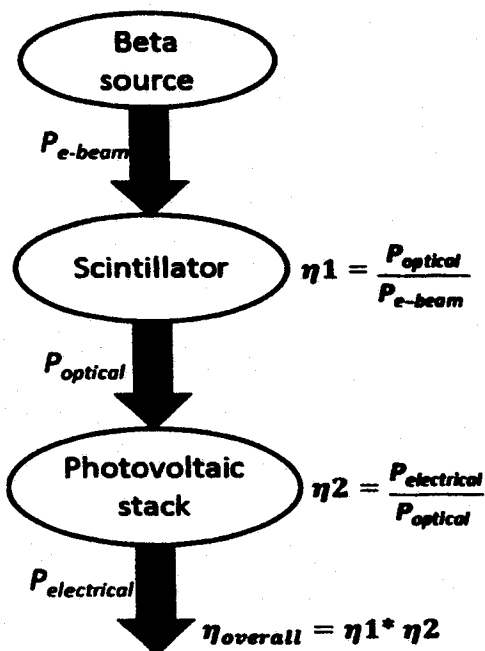


Figure 4-30: Power conversions in indirect conversion betavoltaic devices and overall efficiency calculation.

For 10 kV e-beam without Al layer

The input e-beam power (P_{e-beam}) is the product of e-beam current measured from 1830 AMARAY SEM using Faraday cup and accelerating voltage, provided in Table 4-10, which is 528.9 nW for 10 kV. Assuming that the light generating efficiency of Ce:YAG with e-beam excitation being $\eta_1 = x$, the optical power generated by the Ce:YAG is $P_{optical} = xP_{e-beam} = 528.9x$ nW. The output electrical power from the betavoltaic device was obtained from $I-V$ curves listed in Table 4-11. For 10 kV and without Al, the electrical output power is $P_{electrical} = I_{mp}V_{mp} = 4.85 * 0.29 = 1.41$ nW.

Therefore, the PCE of photovoltaic stack is $\eta_2 = \frac{P_{electrical}}{P_{optical}} = \frac{1.41}{528.9x}$. Now, the overall

PCE of betavoltaic device can be obtained as

$$\eta = \eta_1 * \eta_2 = \left(x * \frac{1.41}{528.9x} \right) * 100\% = 0.27\% \text{ (without Al)}. \quad \text{Eq. 4-8}$$

For 10 kV e-beam with 10 nm Al layer

In the case of a 10 nm Al thin film on top of Ce:YAG, the e-beam power lost in Al film is 2.5%, as obtained from the CASINO simulation. So the e-beam power incident on Ce:YAG for 10 kV is $P_{e-beam} = (1 - 0.025) * 528.9 \text{ nW} = 516 \text{ nW}$. Then the optical power generated by the scintillator with e-beam excitation is $P_{optical} = xP_{e-beam} = 516x \text{ nW}$. The *PCE* of photovoltaic stack can be written as $\eta_2 = \frac{P_{electrical}}{P_{optical}} = \frac{4.75 * 0.34}{516x} = \frac{1.615}{516x}$ (from Table 4-11). Now the overall *PCE* of betavoltaic device is

$$\eta = \eta_1 * \eta_2 = \left(x * \frac{1.615}{516x} \right) * 100\% = 0.31\% \text{ (with 10nm Al)}. \quad \text{Eq. 4-9}$$

For 10 kV e-beam and with 30 nm Al layer

In the case of a 30 nm Al thin film on top of Ce:YAG, the e-beam power lost in Al film is 3.37%, as obtained from the CASINO simulation. So the e-beam power incident on Ce:YAG for 10 kV is $P_{e-beam} = (1 - 0.0337) * 528.9 \text{ nW} = 511 \text{ nW}$. Then the optical power generated by scintillator with e-beam excitation is $P_{optical} = xP_{e-beam} = 511x \text{ nW}$. The *PCE* of photovoltaic stack can be written as $\eta_2 = \frac{P_{electrical}}{P_{optical}} = \frac{4.88 * 0.35}{511x} = \frac{1.708}{511x}$ (from Table 4-11). Now the overall *PCE* of betavoltaic device is

$$\eta = \eta_1 * \eta_2 = \left(x * \frac{1.708}{512x} \right) * 100\% = 0.33\% \text{ (with 30nm Al)}. \quad \text{Eq. 4-10}$$

4.5 Conclusion

The polymer betavoltaic devices with P3HT:ICBA active layer are demonstrated for the first time using the direct and indirect energy conversion methods. Direct energy conversion, where the energetic beta particle directly hits the betavoltaic device, is not suitable for polymer betavoltaic devices due to their vulnerability and degradation upon direct exposure to the e-beam. In addition, the low performance of such direct conversion polymer betavoltaic devices was observed. The indirect conversion method, which incorporates the scintillator intermediate layer, is more suitable for polymer betavoltaic devices as this intermediate layer isolates energetic e-beam from the polymer active layer and avoids any possible damage. The photons generated by the scintillator layer are absorbed by the active layer of the polymer device and cause much less damage to the polymer layer.

It is observed that the betavoltaic *PCE* increases proportionally with the incident e-beam power for polymer devices on glass or PET with phosphor on quartz. We have reduced directional and external interaction losses significantly in PP device on PET with phosphor on PET by reducing the distance between phosphor screen and active layer of polymer device. The maximum betavoltaic *PCE* of 0.78% is achieved at 10 keV e-beam energy for PP device using the indirect energy conversion method. The output electrical power increases with the input beam power and the maximum achieved output electrical power is 62 nW at 30 keV.

Due to the limitation of e-beam power from the SEM, e-beam with a maximum energy of 30 keV was used to test the devices. However, it is expected that more electrical power can be achieved at higher e-beam energies. The performance of indirect

conversion betavoltaic devices with two different scintillators, Ce:YAG and CsI:Tl, was investigated. The optical characteristics of scintillators showed that the emission profile of CsI:Tl is better matched with absorption profile of P3HT:ICBA active layer. Also, the Monte Carlo simulations indicated that CsI:Tl is more efficient in light generation with e-beam excitation compared to Ce:YAG. These results were verified with the experimental resulting by testing indirect betavoltaic devices with Ce:YAG and CsI:Tl scintillators, where the devices with CsI:Tl performed better at 10 kV, 20 kV and 30 kV e-beam energies. The performance of indirect conversion betavoltaic device is further enhanced by applying a thin aluminum-reflecting layer on top of the scintillator reducing directional loss. Degradation results suggest that the whole device encapsulation should be considered in the future device design. The self-absorption loss in scintillator is another important factor that needs to be considered for the future development of high performance betavoltaic devices. The Monte Carlo simulations provided the optimal thickness of Ce:YAG and CsI:Tl scintillator that can help to reduce internal interaction and self-absorption losses.

CHAPTER 5

CONCLUSIONS AND FUTURE RECOMMENDATIONS

5.1 Conclusions

In conclusion, a simplified analytical model of a p-n junction silicon solar cell is developed for homogeneous and inhomogeneous generation rates. Two different types of boundary conditions, intrinsic boundary condition for thick devices and surface recombination boundary condition, were explored. Surface recombination was found to be more physical for thin-film solar cells. The effect of different solar cell parameters such as the device layer's thickness, impurity doping concentration, surface recombination velocity, and minority carrier's lifetime on the solar cell performance was studied. The performance increased with decreasing surface recombination velocity. The open circuit voltage increased with impurity doping concentrations and the minority carrier's lifetime. The device has the optimal front layer thickness at which maximum power is harvested.

The polymer solar cells based on conjugated polymer P3HT and fullerene derivative PCBM were studied as a cost effective alternate to the inorganic solar cells. The active layer thickness of widely used polymer solar cells and photodetectors with P3HT:PCBM active layer was experimentally optimized. The P3HT:PCBM solar cells

with various thicknesses from 20 nm to 345 nm were fabricated using the air-processed spin-coating technique. The optical characterization of P3HT:PCBM thin films with various thicknesses on quartz substrates was carried out to investigate the role of active layer thickness on absorption, transmittance and reflectance of incident optical power from 380 nm to 1050 nm wavelength band. The absorption of light energy increased and transmittance decreased with the increase of thickness of the active layer. Then the electrical characterization was conducted on the polymer solar cells with various P3HT:PCBM active layer thickness by plotting $J-V$ curves, calculating short circuit current density, open circuit voltage, series and shunt resistances, fill factor and PCE . The short circuit current and PCE increased with the thickness of the device, however, the series resistance decreased. The overall performance of the solar cell and photodetector increased with active layer thickness.

The polymer betavoltaic devices with P3HT:ICBA active layer with direct and indirect conversion device architecture were introduced as a long duration power source. These self-powered betavoltaic devices best suit for the applications where solar cells have limitations due to the absence of sunlight inside buildings, spaceships, shadow regions, space in outer solar system, etc. The degradation of direct conversion betavoltaic devices under exposure of e-beam was studied and indirect conversion approach was implemented. The electrical power was successfully generated from these betavoltaic devices with two different scintillators, Ce:YAG and CsI:Tl. The loss mechanism was investigated and minimized by modifying the device's design. The optimal thickness of the scintillator layer was calculated using Monte-Carlo simulations and the directional

loss of scintillator-generated photons was minimized using thin reflecting film on top of the scintillator.

This research was mainly focused on investigating various novel clean energy sources as an alternate of the current carbon emission causing energy sources to address the increasing future energy demand with minimal negative environmental impact.

5.2 Future Recommendations

The analytical model of p-n junction thin-film solar cell developed in this research helps to optimize the various solar cell parameters. The maximum *PCE* of thin-film silicon solar cell obtained is less than 10%. This is due to the thin absorber layer. The *PCE* of these devices can be further enhanced by applying surface plasmon enhancement scheme incorporating metal nanoparticles. Usually, amorphous silicon is used for thin-film solar cells with p-i-n structure. This analytical model can be extended to such p-i-n structure and for various other semiconductors such as a-Si, InGaAs, GaN, etc. The model can be modified to apply to the polymer solar cells to study the role of various parameters on their performances and optimize them.

The experimental optimization of polymer solar cells and photodetectors attempts to optimize the active layer's thickness. Further enhancement can be obtained by investigating the optimal postproduction annealing time and temperature. Fabrication of the polymer devices in inert atmosphere and proper encapsulation is another recommendation to increase the *PCE*. The acidic PEDOT:PSS etches the ITO cathode in the long run reducing the lifetime of the solar cells [87]. Use of non-acidic graphene oxide interfacial layer could improve the lifetime of these devices [88], [89]. The graphene film offers high transparency, electrical conduction and mechanical flexibility,

which makes it a good candidate as a transparent electrode for polymer solar cells as a replacement for ITO. Replacing PCBM fullerene derivative with ICBA increases the open circuit voltage and *PCE* of polymer devices [91]. Similarly, high performing polymer devices are introduced by replacing P3HT conjugated polymer with new donors PCPDT-BT, PCPDT-DFBT, PDTP-DFBT, PBDTT-DPP, etc. [140]. The tandem polymer solar cell architecture with low bandgap polymers can be implemented to enhance the performance further [140], [167].

The primary investigations and application of conjugated polymer in polymer betavoltaic devices is presented in this dissertation. The performance of such devices has room to increase. To develop the technology further and establish it as a long duration energy source, the following future recommendations are suggested:

- Fabrication of polymer photovoltaic stack in inert atmosphere and proper encapsulation.
- Using single thin and flexible transparent substrate to deposition photovoltaic stack on one side and scintillator layer on the other side to reduce the gap further between the active layer and the scintillator layer, and thus photon loss.
- Investigation and application of other more efficient scintillator materials.
- Optimization of the active layer's thickness of photovoltaic stack and scintillator.
- Investigation of the effect of high-energy e-beam on polymer-fullerene active layer in direct conversion betavoltaic devices.
- Testing betavoltaic devices with radioisotope instead of e-beam under SEM.
- Investigation of other device architectures such as cylindrical or spherical with radioisotope at the center to reduce the directional loss.

APPENDIX A
KEITHLEY INSTRUMENTS SPECIFICATION

Table A-1: Keithley 2400 sourcemeter voltage measurement accuracy (local or remote sense) [168].

Range	Accuracy (1 Year) 23°C ± 5°C ± (% rdg. + volts)
200 V	0.015% + 10 mV

Table A-2: Keithley 2400 sourcemeter current measurement accuracy (local or remote sense) [168].

Range	Accuracy (1 Year) 23°C ± 5°C ± (% rdg. + amps)
10 μA	0.027% + 700 pA
1 mA	0.027% + 60 nA
100 mA	0.055% + 6 μA

Table A-3: Keithley 6487 picoammeter specifications [169].

Range	Accuracy (1 Year) ± (% rdg. + offset)
2 nA	0.3% + 400 fA

APPENDIX B
MEASUREMENT ERROR CALCULATION

B.1 Solar Cell

The error in the voltage measurement is calculated using the Keithley 2400 Sourcemeter voltage measurement accuracy for 20 V range provided in Table A-1 and is given as

$$\Delta V = \pm(0.015\% \text{ of } 20 \text{ V} + 1.5 \text{ mV}) = \pm 4.5 \text{ mV}.$$

The error in the current measurement is calculated using the Keithley 2400 Sourcemeter current measurement accuracy for 100 μA range provided in Table A-2 and is given as

$$\Delta I = \pm(0.025\% \text{ of } 100 \mu\text{A} + 6 \text{ nA}) = \pm 31 \text{ nA}.$$

The observed error in input optical power density is $\Delta P_{in}/P_{in} = 0.02\%$. Then the error in FF calculation is obtained as

$$\frac{\Delta FF}{FF} = \left| \frac{\Delta J_{MP}}{J_{MP}} \right| + \left| \frac{\Delta V_{MP}}{V_{MP}} \right| + \left| \frac{\Delta J_{SC}}{J_{SC}} \right| + \left| \frac{\Delta V_{OC}}{V_{OC}} \right|.$$

Similarly, the error in PCE calculation is obtained as

$$\frac{\Delta PCE}{PCE} = \left| \frac{\Delta J_{MP}}{J_{MP}} \right| + \left| \frac{\Delta V_{MP}}{V_{MP}} \right| + \left| \frac{\Delta P_{in}}{P_{in}} \right|.$$

B.2 Betavoltaic Device

The errors in voltage and current measurements are calculated using the Keithley 6487 picoammeter specifications provided in Table A-3 and are given as

$$\Delta V = \pm(0.1\% \text{ of } 10.1 \text{ V} + 1 \text{ mV}) = \pm 11.1 \text{ mV}.$$

$$\Delta I = \pm(0.3\% \text{ of } 2 \text{ nA} + 400 \text{ fA}) = \pm 6.4 \text{ pA}.$$

The observed error in e-beam current is $\Delta I_{e\text{-beam}}/I_{e\text{-beam}} = 0.45\%$. Then the error in input e-beam power, output power and PCE are calculated as

$$\frac{\Delta P_{in}}{P_{in}} = V_{acc} \left| \frac{\Delta I_{e-beam}}{I_{e-beam}} \right|.$$

$$\frac{\Delta P_{out}}{P_{out}} = \left| \frac{\Delta I_{MP}}{I_{MP}} \right| + \left| \frac{\Delta V_{MP}}{V_{MP}} \right|.$$

$$\frac{\Delta PCE}{PCE} = \left| \frac{\Delta I_{MP}}{I_{MP}} \right| + \left| \frac{\Delta V_{MP}}{V_{MP}} \right| + \left| \frac{\Delta P_{in}}{P_{in}} \right|.$$

Where I_{MP} and V_{MP} are the current and voltage at the maximum power point.

BIBLIOGRAPHY

- [1] EIA, "International Energy Outlook 2014," 2014.
- [2] IEA, "IEA - Energy Access." [Online]. Available: <http://www.worldenergyoutlook.org/resources/energydevelopment/>. [Accessed: 29-Feb-2016].
- [3] EIA, "What is U.S. electricity generation by energy source? - FAQ - U.S. Energy Information Administration (EIA)." [Online]. Available: <https://www.eia.gov/tools/faqs/faq.cfm?id=427&t=3>. [Accessed: 29-Feb-2016].
- [4] CDIAC, "2013 Global Carbon Project," 2013. [Online]. Available: <http://cdiac.ornl.gov/GCP/carbonbudget/2013/>. [Accessed: 01-Mar-2016].
- [5] M. Tao, "Inorganic Photovoltaic Solar Cells: Silicon and Beyond," *The Electrochemical Society Interface*, 2008.
- [6] M. A. Green, K. Emery, Y. Hishikawa, W. Warta, and E. D. Dunlop, "Solar cell efficiency tables (version 47)," *Prog. Photovoltaics Res. Appl.*, vol. 24, no. 1, p. n/a–n/a, Nov. 2015.
- [7] A. Globus, "Tango III : A Space Settlement Design," *NASA Ames Space Settlement Page*, 2002. [Online]. Available: <http://settlement.arc.nasa.gov/Contest/Results/96/winner/index.html>. [Accessed: 23-Jul-2015].
- [8] T. Saga, "Advances in crystalline silicon solar cell technology for industrial mass production," *NPG Asia Mater.*, vol. 2, no. 3, pp. 96–102, Jul. 2010.
- [9] NREL, "Best Research-Cell Efficiencies," 2015. [Online]. Available: http://www.nrel.gov/ncpv/images/efficiency_chart.jpg. [Accessed: 20-Feb-2016].
- [10] A. F. Hepp, S. G. Bailey, and R. P. Raffaele, "Inorganic Photovoltaics Materials and Devices: Past, Present, and Future," Aug. 2005.
- [11] A. Blakers, N. Zin, K. R. McIntosh, and K. Fong, "High Efficiency Silicon Solar Cells," *Energy Procedia*, vol. 33, pp. 1–10, 2013.
- [12] A. Shah, *Thin-Film Silicon Solar Cells*. EPFL Press, 2010.
- [13] S. Pillai, K. R. Catchpole, T. Trupke, and M. A. Green, "Surface plasmon enhanced silicon solar cells," *J. Appl. Phys.*, vol. 101, no. 9, p. 093105, May 2007.

- [14] "Crystalline Silicon Photovoltaics Research | Department of Energy." [Online]. Available: <http://www.energy.gov/eere/sunshot/crystalline-silicon-photovoltaics-research>. [Accessed: 22-Jul-2015].
- [15] M. A. Green, K. Emery, Y. Hishikawa, W. Warta, and E. D. Dunlop, "Solar cell efficiency tables (Version 45)," *Prog. Photovoltaics Res. Appl.*, vol. 23, no. Version 45, pp. 1–9, Jan. 2015.
- [16] International Renewable Energy Agency, "Renewable Energy Technologies: Cost Analysis Series," *Sol. Photovoltaics*, vol. 1, no. 4/5, 2012.
- [17] R. E. I. Schropp and M. Zeman, *Amorphous and Microcrystalline Silicon Solar Cells: Modeling, Materials and Device Technology*. USA: Kluwer Academic Publishers, 1998.
- [18] A. Shah, "Photovoltaic Technology: The Case for Thin-Film Solar Cells," *Science* (80-.), vol. 285, no. 5428, pp. 692–698, Jul. 1999.
- [19] J. Carabe and J. J. Gandia, "Thin-film-silicon solar cells," *Opto-Electronics Rev.*, vol. 12, no. 1, pp. 1–6, 2004.
- [20] K. Yamamoto, A. Nakajima, M. Yoshimi, T. Sawada, S. Fukuda, T. Suezaki, M. Ichikawa, Y. Koi, M. Goto, T. Meguro, T. Matsuda, M. Kondo, T. Sasaki, and Y. Tawada, "A high efficiency thin film silicon solar cell and module," *Sol. Energy*, vol. 77, no. 6, pp. 939–949, Dec. 2004.
- [21] U.S. Department of Energy, "PV FAQs," *Energy Efficiency and Renewable Energy*, 2004. [Online]. Available: <http://www.nrel.gov/docs/fy04osti/35489.pdf>. [Accessed: 22-Jul-2015].
- [22] F.-J. Haug and C. Ballif, "Light management in thin film silicon solar cells," *Energy Environ. Sci.*, vol. 8, no. 3, pp. 824–837, Mar. 2015.
- [23] P. J. McElheny, S. S. Nag, S. J. Fonash, C. R. Wronski, M. Bennett, and R. Arya, "Role of film thickness in amorphous silicon solar cell characterization," in *IEEE Conference on Photovoltaic Specialists*, 1990, pp. 1459–1464 vol.2.
- [24] D. L. Crook and J. R. Yeagan, "Optimization of silicon solar cell design for use under concentrated sunlight," *IEEE Trans. Electron Devices*, vol. 24, no. 4, pp. 330–336, Apr. 1977.
- [25] A. Tamang, A. Hongsingthong, P. Sichanugrist, V. Jovanov, M. Konagai, and D. Knipp, "Light-Trapping and Interface Morphologies of Amorphous Silicon Solar Cells on Multiscale Surface Textured Substrates," *IEEE J. Photovoltaics*, vol. 4, no. 1, pp. 16–21, Jan. 2014.
- [26] Y. P. Singh, A. Jain, and A. Kapoor, "Localized Surface Plasmons Enhanced Light Transmission into c-Silicon Solar Cells," *J. Sol. Energy*, vol. 2013, Jul. 2013.
- [27] A. Bozzola, M. Liscidini, and L. C. Andreani, "Broadband light trapping with disordered photonic structures in thin-film silicon solar cells," *Prog. Photovoltaics Res. Appl.*, vol. 22, no. 12, pp. 1237–1245, Dec. 2014.

- [28] Z. Yu, A. Raman, and S. Fan, "Fundamental limit of nanophotonic light trapping in solar cells," *Proc. Natl. Acad. Sci. U. S. A.*, vol. 107, no. 41, pp. 17491–17496, Oct. 2010.
- [29] Z. Yu, S. Sandhu, and S. Fan, "Efficiency above the shockley-queisser limit by using nanophotonic effects to create multiple effective bandgaps with a single semiconductor," *Nano Lett.*, vol. 14, no. 1, pp. 66–70, 2014.
- [30] F. Priolo, T. Gregorkiewicz, M. Galli, and T. F. Krauss, "Silicon nanostructures for photonics and photovoltaics," *Nat. Nanotechnol.*, vol. 9, no. 1, pp. 19–32, Jan. 2014.
- [31] R. W. Rostron, "Short-circuit current in silicon solar cells; Dependence on cell parameters," *IEEE Trans. Electron Devices*, vol. 19, no. 9, pp. 1024–1028, Sep. 1972.
- [32] P. P. Altermatt, "Models for numerical device simulations of crystalline silicon solar cells - a review," *Journal of Computational Electronics*, vol. 10, no. 3. Springer US, pp. 314–330, Jul-2011.
- [33] C. Ringhofer and C. Schmeiser, "A modified Gummel method for the basic semiconductor device equations," *IEEE Trans. Comput. Des. Integr. Circuits Syst.*, vol. 7, no. 2, pp. 251–253, 1988.
- [34] J. Shi and Z. C. Holman, "Micro-concentrated silicon heterojunction solar cells: Basic concept, device simulation, and system modeling," in *2014 IEEE 40th Photovoltaic Specialist Conference (PVSC)*, 2014, pp. 0641–0644.
- [35] S. Degraeve, M. Burgelman, and P. Nollet, "Modelling of polycrystalline thin film solar cells: new features in SCAPS version 2.3," vol. 1. pp. 487–490 Vol.1, 2003.
- [36] Y. Liu, Y. Sun, and A. Rockett, "A new simulation software of solar cells—wxAMPS," *Sol. Energy Mater. Sol. Cells*, vol. 98, pp. 124–128, Mar. 2012.
- [37] P. A. Basore, "Numerical modeling of textured silicon solar cells using PC-1D," *IEEE Trans. Electron Devices*, vol. 37, no. 2, pp. 337–343, Feb. 1990.
- [38] M. S. Lundstrom, "Numerical analysis of silicon solar cells," Purdue University, 1980.
- [39] A. Neculae and M. Paulescu, "Numerical simulation for the current density of p-n like-type solar cells," *J. Optoelectron. Adv. Mater.*, vol. 10, no. 9, pp. 2438–2440, 2008.
- [40] F. Y. R. El Faituri and A. Y. Darkwi, "Computer simulation for current density in pn-silicon solar cells," in *International Symposium on Solar Physics and Solar Eclipses (SPSE)*, 2006, pp. 163–171.
- [41] M. Zeman, "Solar Cells : 2. Solar Radiation." [Online]. Available: <http://ocw.tudelft.nl/courses/microelectronics/solar-cells/readings/2-solar-radiation/>. [Accessed: 20-Feb-2016].
- [42] S. J. Fonash, *Solar Cell Device Physics*, Second. Burlington: Academic Press, 2010.
- [43] L. Fraas and L. Partain, *Solar Cells and Their Applications*, Second. New Jersey: Wiley, 2010.

- [44] B. Parida, S. Iniyar, and R. Goic, "A review of solar photovoltaic technologies," *Renew. Sustain. Energy Rev.*, vol. 15, no. 3, pp. 1625–1636, Apr. 2011.
- [45] L. El Chaar, L. A. Lamont, and N. El Zein, "Review of photovoltaic technologies," *Renew. Sustain. Energy Rev.*, vol. 15, no. 5, pp. 2165–2175, Jun. 2011.
- [46] D. C. Jordan and S. R. Kurtz, "Photovoltaic Degradation Rates-an Analytical Review," *Prog. Photovoltaics Res. Appl.*, vol. 21, no. 1, pp. 12–29, Jan. 2013.
- [47] M. Khamooshi, H. Salati, F. Egelioglu, A. H. Faghiri, J. Tarabishi, and S. Babadi, "A Review of Solar Photovoltaic Concentrators," *Int. J. Photoenergy*, vol. 2014, p. 17, 2014.
- [48] R. W. Miles, G. Zoppi, and I. Forbes, "Inorganic photovoltaic cells," *Mater. Today*, vol. 10, no. 11, pp. 20–27, Nov. 2007.
- [49] M. Zeman, "Solar Cell Conversion-Efficiency Limits," in *Solar Cells*, TU Delft OpenCourseWare.
- [50] M. Zeman, "Solar Cells : 7. Thin-film silicon solar cells." [Online]. Available: <http://ocw.tudelft.nl/courses/microelectronics/solar-cells/readings/7-thin-film-silicon-solar-cells/>. [Accessed: 12-Feb-2013].
- [51] "Solar Technology." [Online]. Available: <http://www.techinvestingdaily.com/report/solar-technology/1409>. [Accessed: 22-Feb-2016].
- [52] T. Takamoto, M. Kaneiwa, M. Imaizumi, and M. Yamaguchi, "InGaP/GaAs-based multijunction solar cells," *Prog. Photovoltaics Res. Appl.*, vol. 13, no. 6, pp. 495–511, Sep. 2005.
- [53] J. O. Schumacher and W. Wetling, *Device Physics of Silicon Solar Cells*, vol. 3. London: Imperial College Press, 2000.
- [54] S. S. Li, *Semiconductor Physical Electronics*, Second Edi. USA: Springer, 2006.
- [55] D. A. Neamen, *Semiconductor Physics and Devices: Basic Principles*, Fourth. New York, USA: McGraw-Hill, 2011.
- [56] C. Honsberg and S. Bowden, "Solving for Quasi Neutral Regions," *PVEducation.org*, 2013. [Online]. Available: <http://pveducation.org/pvcdrom/pn-junction/solving-for-qnr>. [Accessed: 17-Sep-2013].
- [57] V. K. Tewary and S. C. Jain, "Surface boundary condition for solar cell diffusion equation," *J. Phys. D. Appl. Phys.*, vol. 13, no. 5, pp. 835–837, May 1980.
- [58] A. McEvoy, L. Castaner, and T. Markvart, *Solar Cells - Materials, Manufacture and Operation*, Second. Elsevier, 2013.
- [59] "Physical properties of Silicon (Si)." [Online]. Available: <http://www.ioffe.ru/SVA/NSM/Semicond/Si/>. [Accessed: 24-Mar-2016].

- [60] Y. Tsuno, Y. Hishikawa, and K. Kurokawa, "Temperature and Irradiance Dependence of the I-V Curves of Various Kinds of Solar Cells," in *15th International Photovoltaic Science & Engineering Conference*, 2005, pp. 422–423.
- [61] R. R. King, R. A. Sinton, and R. M. Swanson, "Studies of diffused phosphorus emitters: saturation current, surface recombination velocity, and quantum efficiency," *IEEE Trans. Electron Devices*, vol. 37, no. 2, pp. 365–371, 1990.
- [62] M. J. Kerr, J. Schmidt, A. Cuevas, and J. H. Bultman, "Surface recombination velocity of phosphorus-diffused silicon solar cell emitters passivated with plasma enhanced chemical vapor deposited silicon nitride and thermal silicon oxide," *J. Appl. Phys.*, vol. 89, no. 7, p. 3821, Apr. 2001.
- [63] G. Agostinelli, A. Delabie, P. Vitanov, Z. Alexieva, H. F. W. Dekkers, S. De Wolf, and G. Beaucarne, "Very low surface recombination velocities on p-type silicon wafers passivated with a dielectric with fixed negative charge," *Sol. Energy Mater. Sol. Cells*, vol. 90, no. 18–19, pp. 3438–3443, Nov. 2006.
- [64] J. Schmidt, A. Merkle, R. Brendel, B. Hoex, M. C. M. van de Sanden, and W. M. M. Kessels, "Surface passivation of high-efficiency silicon solar cells by atomic-layer-deposited Al₂O₃," *Prog. Photovoltaics Res. Appl.*, vol. 16, no. 6, pp. 461–466, Sep. 2008.
- [65] R. Hezel, "Low-Temperature Surface Passivation of Silicon for Solar Cells," *J. Electrochem. Soc.*, vol. 136, no. 2, p. 518, Feb. 1989.
- [66] U. Stutenbaumer, "Minority carrier lifetime in monocrystalline, polycrystalline and amorphous silicon solar cells using photo-induced open circuit voltage decay (OCVD) technique," *SINET Ethiop. J. Sci.*, vol. 22, no. 1, pp. 15–30, 1999.
- [67] Z. Z. Bandić, P. M. Bridger, E. C. Piquette, and T. C. McGill, "Minority carrier diffusion length and lifetime in GaN," *Appl. Phys. Lett.*, vol. 72, no. 24, p. 3166, Jun. 1998.
- [68] C. Z. Carlin, G. K. Bradshaw, J. P. Samberg, P. C. Colter, and S. M. Bedair, "Minority Carrier Transport and Their Lifetime in InGaAs/GaAsP Multiple Quantum Well Structures," *IEEE Trans. Electron Devices*, vol. 60, no. 8, pp. 2532–2536, Aug. 2013.
- [69] D. A. GENOV, A. K. SARYCHEV, and V. M. SHALAEV, "METAL-DIELECTRIC COMPOSITE FILTERS WITH CONTROLLED SPECTRAL WINDOWS OF TRANSPARENCY," *J. Nonlinear Opt. Phys. Mater.*, vol. 12, no. 04, pp. 419–440, Dec. 2003.
- [70] V. Shrotriya, J. Ouyang, R. J. Tseng, G. Li, and Y. Yang, "Absorption spectra modification in poly(3-hexylthiophene):methanofullerene blend thin films," *Chem. Phys. Lett.*, vol. 411, no. 1–3, pp. 138–143, Aug. 2005.
- [71] J. D. Kotlarski, P. W. M. Blom, L. J. A. Koster, M. Lenis, and L. H. Slooff, "Combined optical and electrical modeling of polymer:fullerene bulk heterojunction solar cells," *J. Appl. Phys.*, vol. 103, no. 8, p. 084502, 2008.

- [72] R. N. Chauhan, C. Singh, R. S. Anand, and J. Kumar, "Effect of sheet resistance and morphology of ITO thin films on polymer solar cell characteristics," *Int. J. Photoenergy*, vol. 2012, Mar. 2012.
- [73] T. Kuwabara, T. Nakashima, T. Yamaguchi, and K. Takahashi, "Flexible inverted polymer solar cells on polyethylene terephthalate substrate containing zinc oxide electron-collection-layer prepared by novel sol-gel method and low-temperature treatments," *Org. Electron. physics, Mater. Appl.*, vol. 13, no. 7, pp. 1136–1140, Jul. 2012.
- [74] S. Günes, H. Neugebauer, and N. S. Sariciftci, "Conjugated polymer-based organic solar cells," *Chem. Rev.*, vol. 107, no. 4, pp. 1324–1338, Apr. 2007.
- [75] G. Li, R. Zhu, and Y. Yang, "Polymer solar cells," *Nat. Photonics*, vol. 6, no. 3, pp. 153–161, Mar. 2012.
- [76] A. C. Mayer, S. R. Scully, B. E. Hardin, M. W. Rowell, and M. D. McGehee, "Polymer-based solar cells," *Mater. Today*, vol. 10, no. 11, pp. 28–33, Nov. 2007.
- [77] C. J. Brabec, N. S. Sariciftci, and J. C. Hummelen, "Plastic solar cells," *Adv. Funct. Mater.*, vol. 11, no. 1, pp. 15–26, 2001.
- [78] B. C. Thompson and J. M. J. Fréchet, "Polymer-fullerene composite solar cells," *Angewandte Chemie - International Edition*, vol. 47, no. 1, pp. 58–77, Jan-2008.
- [79] J. P. Petrović, P. S. Matavulj, L. R. Pinto, A. Thapa, and S. R. Živanović, "Thickness dependent absorption and polaron photogeneration in poly-(2-methoxy-5-(2'-ethyl-hexyloxy)-1,4-phenylene-vinylene)," *J. Appl. Phys.*, vol. 111, no. 12, 2012.
- [80] F. C. Krebs, *Polymer Solar Cells: Materials, Design, Manufacture*. Lancaster, Pennsylvania, USA: DEStech Publication, Inc., 2010.
- [81] W. C. H. Choy, *Organic Solar Cells - Materials and Device Physics*. Springer, 2012.
- [82] S. K. M. Jönsson, E. Carlegrim, F. Zhang, W. R. Salaneck, and M. Fahlman, "Photoelectron spectroscopy of the contact between the cathode and the active layers in plastic solar cells: The role of LiF," *Japanese J. Appl. Physics, Part 1 Regul. Pap. Short Notes Rev. Pap.*, vol. 44, no. 6 A, pp. 3695–3701, Jun. 2005.
- [83] "Poly(3-hexylthiophene-2,5-diyl) regioregular | Sigma-Aldrich." [Online]. Available: <https://www.sigmaaldrich.com/catalog/product/aldrich/445703?lang=en®ion=US>. [Accessed: 20-Jan-2016].
- [84] "[6,6]-Phenyl C61 butyric acid methyl ester >99% | Sigma-Aldrich." [Online]. Available: https://www.sigmaaldrich.com/catalog/product/aldrich/684430?lang=en®ion=US&cm_sp=Insite_-_prodRecCold_xorders_-_prodRecCold2-1. [Accessed: 20-Jan-2016].
- [85] J. H. Beck, B. Ray, R. R. Grote, R. M. Osgood, C. T. Black, M. A. Alam, and I. Kymissis, "Nanostructured electrodes improve the fill factor of organic photovoltaics," *IEEE J. Photovoltaics*, vol. 4, no. 4, pp. 1100–1106, Jul. 2014.

- [86] M. Sendova-Vassileva, G. Popkirov, P. Vitanov, D. Ch, V. Gancheva, D. Tsocheva, and P. Mokreva, "Influence of the Type of Metal Contact and Post-deposition Treatment on the Performance of P3HT:PCBM Organic Solar Cells," *J. Phys. Conf. Ser.*, vol. 398, no. 1, p. 12049, Dec. 2012.
- [87] H. Kim, S. Nam, H. Lee, S. Woo, C.-S. Ha, M. Ree, and Y. Kim, "Influence of Controlled Acidity of Hole-Collecting Buffer Layers on the Performance and Lifetime of Polymer:Fullerene Solar Cells," *J. Phys. Chem. C*, vol. 115, no. 27, pp. 13502–13510, Jul. 2011.
- [88] S. S. Li, K. H. Tu, C. C. Lin, C. W. Chen, and M. Chhowalla, "Solution-processable graphene oxide as an efficient hole transport layer in polymer solar cells," *ACS Nano*, vol. 4, no. 6, pp. 3169–3174, Jun. 2010.
- [89] Y. Park, K. Soon Choi, and S. Young Kim, "Graphene oxide/PEDOT:PSS and reduced graphene oxide/PEDOT:PSS hole extraction layers in organic photovoltaic cells," *Phys. status solidi*, vol. 209, no. 7, pp. 1363–1368, Jul. 2012.
- [90] O. Awartani, M. W. Kudenov, R. J. Kline, and B. T. O'Connor, "In-Plane Alignment in Organic Solar Cells to Probe the Morphological Dependence of Charge Recombination," *Adv. Funct. Mater.*, vol. 25, no. 8, pp. 1296–1303, Feb. 2015.
- [91] Y. He, H. Y. Chen, J. Hou, and Y. Li, "Indene - C60 bisadduct: A new acceptor for high-performance polymer solar cells," *J. Am. Chem. Soc.*, vol. 132, no. 4, pp. 1377–1382, 2010.
- [92] A. J. Moulé, J. B. Bonekamp, and K. Meerholz, "The effect of active layer thickness and composition on the performance of bulk-heterojunction solar cells," *J. Appl. Phys.*, vol. 100, no. 9, p. 094503, Nov. 2006.
- [93] P. Morvillo, E. Bobeico, S. Esposito, and R. Diana, "Effect of the Active Layer Thickness on the Device Performance of Polymer Solar Cells Having [60]PCBM and [70]PCBM as Electron Acceptor," *Energy Procedia*, vol. 31, pp. 69–73, 2012.
- [94] Ž. Jelić, J. Petrović, P. Matavulj, J. Melancon, A. Sharma, C. Zellhofer, and S. Živanović, "Modeling of the polymer solar cell with a P3HT:PCBM active layer," *Phys. Scr.*, vol. 2014, no. T162, p. 014035, Sep. 2014.
- [95] R. Blumenthal, "Experimenting With Polymer Blend Solar Cells and Active Layer Thickness," *Physics*, 2013. [Online]. Available: <http://digitalcommons.calpoly.edu/physsp/90>. [Accessed: 20-Aug-2015].
- [96] G. Li, V. Shrotriya, Y. Yao, and Y. Yang, "Investigation of annealing effects and film thickness dependence of polymer solar cells based on poly(3-hexylthiophene)," *J. Appl. Phys.*, vol. 98, no. 4, p. 043704, Aug. 2005.
- [97] D. W. Sievers, V. Shrotriya, and Y. Yang, "Modeling optical effects and thickness dependent current in polymer bulk-heterojunction solar cells," *J. Appl. Phys.*, vol. 100, no. 11, p. 114509, Dec. 2006.

- [98] G. Li, V. Shrotriya, J. Huang, Y. Yao, T. Moriarty, K. Emery, and Y. Yang, "High-efficiency solution processable polymer photovoltaic cells by self-organization of polymer blends," *Nature Materials*, vol. 4, no. 11, pp. 864–868, Nov-2005.
- [99] Y.-M. Shen, C.-S. Chen, S.-Y. Ma, and C.-F. Lin, "Improve the thin film morphology and efficiency performance of P3HT:PCBM based solar cells by applying external electric fields," in *2011 37th IEEE Photovoltaic Specialists Conference*, 2011, pp. 001200–001202.
- [100] S. Bertho, G. Janssen, T. J. Cleij, B. Conings, W. Moons, A. Gadisa, J. D'Haen, E. Goovaerts, L. Lutsen, J. Manca, and D. Vanderzande, "Effect of temperature on the morphological and photovoltaic stability of bulk heterojunction polymer:fullerene solar cells," *Sol. Energy Mater. Sol. Cells*, vol. 92, no. 7, pp. 753–760, Jul. 2008.
- [101] F. Padinger, R. S. Rittberger, and N. S. Sariciftci, "Effects of Postproduction Treatment on Plastic Solar Cells," *Adv. Funct. Mater.*, vol. 13, no. 1, pp. 85–88, Jan. 2003.
- [102] L. J. A. Koster, V. D. Mihailetschi, R. Ramaker, and P. W. M. Blom, "Light intensity dependence of open-circuit voltage of polymer:fullerene solar cells," *Appl. Phys. Lett.*, vol. 86, no. 12, p. 123509, Mar. 2005.
- [103] T. Kirchartz, T. Agostinelli, M. Campoy-Quiles, W. Gong, and J. Nelson, "Understanding the Thickness-Dependent Performance of Organic Bulk Heterojunction Solar Cells: The Influence of Mobility, Lifetime, and Space Charge.," *J. Phys. Chem. Lett.*, vol. 3, no. 23, pp. 3470–5, Dec. 2012.
- [104] M. Lenes, L. J. A. Koster, V. D. Mihailetschi, and P. W. M. Blom, "Thickness dependence of the efficiency of polymer:fullerene bulk heterojunction solar cells," *Appl. Phys. Lett.*, vol. 88, no. 24, p. 243502, Jun. 2006.
- [105] T. A. Skotheim and J. R. Reynolds, *Conjugated Polymers: Theory, Synthesis, Properties, and Characterization*, Third. CRC Press, 2006.
- [106] "The 2000 Nobel Prize in Chemistry - Popular Information," *Nobelprize.org*, 2000. [Online]. Available: http://www.nobelprize.org/nobel_prizes/chemistry/laureates/2000/popular.html. [Accessed: 22-Feb-2016].
- [107] "File:Conjugated polymer common.png - CMDITRWIKI." [Online]. Available: http://photonicswiki.org/index.php?title=File:Conjugated_polymer_common.png#filelinks. [Accessed: 23-Feb-2016].
- [108] S. S. Shinde and J. A. Kher, "A Review on Polyaniline and Its Noble Metal Composites," *Int. J. Innov. Res. Sci. Eng. Technol.*, vol. 3, no. 9, 2014.
- [109] Y. He and Y. Li, "Fullerene derivative acceptors for high performance polymer solar cells.," *Phys. Chem. Chem. Phys.*, vol. 13, no. 6, pp. 1970–83, Feb. 2011.
- [110] M. A. Alam, "Solar Cells Lecture 5: Organic Photovoltaics," 2011. [Online]. Available: <https://nanohub.org/resources/11950>. [Accessed: 22-Feb-2016].

- [111] "Thorlabs.com - Tutorials." [Online]. Available: <http://www.thorlabs.com/tutorials.cfm?tabID=31760>. [Accessed: 23-Feb-2016].
- [112] C. Y. Nam, D. Su, and C. T. Black, "High-performance air-processed polymer-fullerene bulk heterojunction solar cells," *Adv. Funct. Mater.*, vol. 19, no. 22, pp. 3552–3559, Nov. 2009.
- [113] "Delta Technologies Limited - Products." [Online]. Available: <http://www.deltatechnologies.com/products.asp?C=1>. [Accessed: 20-Jan-2016].
- [114] I. Lange, J. Kniepert, P. Pingel, I. Dumsch, S. Allard, S. Janietz, U. Scherf, and D. Neher, "Correlation between the Open Circuit Voltage and the Energetics of Organic Bulk Heterojunction Solar Cells," *J. Phys. Chem. Lett.*, vol. 4, no. 22, pp. 3865–3871, Nov. 2013.
- [115] S.-S. Kim, S.-I. Na, J. Jo, D.-Y. Kim, and Y.-C. Nah, "Plasmon enhanced performance of organic solar cells using electrodeposited Ag nanoparticles," *Appl. Phys. Lett.*, vol. 93, no. 7, p. 073307, Aug. 2008.
- [116] X. Chen, B. Jia, J. K. Saha, B. Cai, N. Stokes, Q. Qiao, Y. Wang, Z. Shi, and M. Gu, "Broadband enhancement in thin-film amorphous silicon solar cells enabled by nucleated silver nanoparticles," *Nano Lett.*, vol. 12, no. 5, pp. 2187–92, May 2012.
- [117] K. Bourzac, "A 25-Year Battery," *MIT Technology Review*, Nov-2009. [Online]. Available: <http://www.technologyreview.com/news/416312/a-25-year-battery/>. [Accessed: 22-May-2014].
- [118] G. A. Landis, S. G. Bailey, E. B. Clark, M. G. Myers, M. F. Piszczor, and M. S. Murbach, "Non-solar photovoltaics for small space missions," in *38th IEEE Photovoltaic Specialists Conference*, 2012, pp. 002819–002824.
- [119] M. T. Dang, L. Hirsch, and G. Wantz, "P3HT:PCBM, Best Seller in Polymer Photovoltaic Research," *Adv. Mater.*, vol. 23, no. 31, pp. 3597–3602, Aug. 2011.
- [120] M. Taguchi, A. Yano, S. Tohoda, K. Matsuyama, Y. Nakamura, T. Nishiwaki, K. Fujita, and E. Maruyama, "24.7 % Record Efficiency HIT Solar Cell on Thin Silicon Wafer," *IEEE J. Photovoltaics*, vol. 4, no. 1, pp. 96–99, Jan. 2014.
- [121] M. Mohamadian, S. A. H. Feghhi, and H. Afarideh, "Conceptual design of GaN betavoltaic battery using in cardiac pacemaker," in *13th International Conference on Emerging Nuclear Energy Systems*, 2007.
- [122] S. T. Revankar and T. E. Adams, "Advances in Betavoltaic Power Sources," *ETHAN Publ.*, vol. 1, no. 6, pp. 321–329, Dec. 2014.
- [123] P. Rappaport, "The Electron-Voltaic Effect in p-n Junctions Induced by Beta-Particle Bombardment," *Phys. Rev.*, vol. 93, no. 1, pp. 246–247, Jan. 1954.
- [124] L. Da-Rang, J. Lan, Y. Jian-Hua, T. Yuan-Yuan, and L. Nai, "Betavoltaic Battery Conversion Efficiency Improvement Based on Interlayer Structures," *Chinese Phys. Lett.*, vol. 29, no. 7, p. 078102, Jul. 2012.

- [125] M. A. Prelas, C. L. Weaver, M. L. Watermann, E. D. Lukosi, R. J. Schott, and D. A. Wisniewski, "A review of nuclear batteries," *Prog. Nucl. Energy*, vol. 75, pp. 117–148, Aug. 2014.
- [126] M. V. S. Chandrashekhar, C. I. Thomas, and M. G. Spencer, "Betavoltaic cell," US Patent 7663288 B2, 2010.
- [127] S. G. Bailey, D. M. Wilt, S. L. Castro, C. D. Cress, and R. P. Raffaele, "Photovoltaic development for alpha voltaic batteries," in *Thirty-first IEEE Photovoltaic Specialists Conference*, 2005, pp. 106–109.
- [128] R. Bao, P. J. Brand, and D. B. Chrisey, "Betavoltaic Performance of Radiation-Hardened High-Efficiency Si Space Solar Cells," *IEEE Trans. Electron Devices*, vol. 59, no. 5, pp. 1286–1294, May 2012.
- [129] Z. Cheng, X. Chen, H. San, Z. Feng, and B. Liu, "A high open-circuit voltage gallium nitride betavoltaic microbattery," *J. Micromechanics Microengineering*, vol. 22, no. 7, p. 074011, Jul. 2012.
- [130] T. Wacharasindhu, B. R. Nullmeyer, J. W. Kwon, J. D. Robertson, and A. Y. Garnov, "Mechanisms Leading to Losses in Conventional Betavoltaics and Evolution: Utilizing Composite Semiconductor With Infused Radioisotope for Efficiency Improvement," *J. Microelectromechanical Syst.*, vol. 23, no. 1, pp. 56–65, Feb. 2014.
- [131] T. Takamoto, E. Ikeda, H. Kurita, and M. Ohmori, "Structural optimization for single junction InGaP solar cells," *Sol. Energy Mater. Sol. Cells*, vol. 35, pp. 25–31, Sep. 1994.
- [132] A. Sharma, J. M. Melancon, S. G. Bailey, and S. R. Zivanovic, "Betavoltaic Cells Using P3HT Semiconductive Conjugated Polymer," *IEEE Trans. Electron Devices*, vol. 62, no. 7, pp. 2320–2326, Jul. 2015.
- [133] K. E. Bower, Y. A. Barbanel, Y. G. Shreter, and G. W. Bohnert, *Polymers, Phosphors, and Voltaics for Radioisotope Microbatteries*. New York: CRC Press, 2002.
- [134] M. Sychov, A. Kavetsky, G. Yakubova, G. Walter, S. Yousaf, Q. Lin, D. Chan, H. Socarras, and K. Bower, "Alpha indirect conversion radioisotope power source.," *Appl. Radiat. Isot.*, vol. 66, no. 2, pp. 173–7, Feb. 2008.
- [135] R. C. O'Brien, R. M. Ambrosi, N. P. Bannister, S. D. Howe, and H. V. Atkinson, "Safe radioisotope thermoelectric generators and heat sources for space applications," *J. Nucl. Mater.*, vol. 377, no. 3, pp. 506–521, Jul. 2008.
- [136] S. LeBlanc, "Thermoelectric generators: Linking material properties and systems engineering for waste heat recovery applications," *Sustain. Mater. Technol.*, vol. 1–2, pp. 26–35, Dec. 2014.
- [137] "Generac RTG16EZA1 Generator." [Online]. Available: <https://www.gexpro.com/transfer-switches-automatic/generac/rtg16eza1/generac-rtg16eza1-generator-automatic-transfer-switch-load-center-100a-16-circuit/product/580317>. [Accessed: 24-Mar-2016].

- [138] G. R. Schmidth, T. J. Sutliff, and L. A. Dudzinski, "Radioisotope Power: A Key Technology for Deep Space Exploration," *Radioisot. - Appl. Phys. Sci.*, 2011.
- [139] National Research Council, *Energy-Efficient Technologies for the Dismounted Soldier*. National Academies Press, 1998.
- [140] J. You, L. Dou, K. Yoshimura, T. Kato, K. Ohya, T. Moriarty, K. Emery, C.-C. Chen, J. Gao, G. Li, and Y. Yang, "A polymer tandem solar cell with 10.6% power conversion efficiency," *Nat. Commun.*, vol. 4, p. 1446, Feb. 2013.
- [141] F. C. Krebs, "Fabrication and processing of polymer solar cells: A review of printing and coating techniques," *Sol. Energy Mater. Sol. Cells*, vol. 93, no. 4, pp. 394–412, Apr. 2009.
- [142] J. W. Kingsley, S. J. Weston, and D. G. Lidzey, "Stability of X-Ray Detectors Based on Organic Photovoltaic Devices," *IEEE J. Sel. Top. Quantum Electron.*, vol. 16, no. 6, pp. 1770–1775, Nov. 2010.
- [143] L. C. Olsen, P. Cabaay, and B. J. Elkind, "Betavoltaic power sources," *Phys. Today*, vol. 65, no. 12, pp. 35–38, Dec. 2012.
- [144] P. Ridden, "Commercially-available NanoTritium battery can power microelectronics for 20+ years," *Gizmag*, 2012. [Online]. Available: <http://www.gizmag.com/city-labs-nanotritium-betavoltaic-battery/23720/>. [Accessed: 08-Oct-2015].
- [145] Michigan State University, "Radiation Safety Manual," *Environmental Health & Safety*, 2013. [Online]. Available: http://www.ehs.msu.edu/radiation/programs_guidelines/radmanual/radmanual.pdf. [Accessed: 08-Oct-2015].
- [146] NEI, "Nuclear Waste Amounts & On-Site Storage - Nuclear Energy Institute." [Online]. Available: <http://www.nei.org/Knowledge-Center/Nuclear-Statistics/On-Site-Storage-of-Nuclear-Waste>. [Accessed: 26-Feb-2016].
- [147] National Geographic, "Nuclear Waste Article, Radioactive Garbage Information, Plutonium Facts -- National Geographic." [Online]. Available: <http://science.nationalgeographic.com/science/earth/inside-the-earth/nuclear-waste/#page=2>. [Accessed: 26-Feb-2016].
- [148] "Raman Spectroscopy - A Tutorial." [Online]. Available: http://www.kosi.com/na_en/products/raman-spectroscopy/raman-technical-resources/raman-tutorial.php. [Accessed: 10-Jul-2015].
- [149] "FunctionalGroupsTeachingLab.pdf." [Online]. Available: <http://www.wysri.com/wp-content/uploads/2014/12/FunctionalGroupsTeachingLab.pdf>. [Accessed: 10-Jul-2015].
- [150] M. J. Walter, J. M. Lupton, K. Becker, J. Feldmann, G. Gaefke, and S. Höger, "Simultaneous Raman and Fluorescence Spectroscopy of Single Conjugated Polymer Chains," *Phys. Rev. Lett.*, vol. 98, no. 13, p. 137401, Mar. 2007.

- [151] E. Klimov, W. Li, X. Yang, G. G. Hoffmann, and J. Loos, "Scanning Near-Field and Confocal Raman Microscopic Investigation of P3HT-PCBM Systems for Solar Cell Applications," *Macromolecules*, vol. 39, no. 13, pp. 4493-4496, Jun. 2006.
- [152] W. C. Tsoi, D. T. James, J. S. Kim, P. G. Nicholson, C. E. Murphy, D. D. C. Bradley, J. Nelson, and J.-S. Kim, "The nature of in-plane skeleton Raman modes of P3HT and their correlation to the degree of molecular order in P3HT:PCBM blend thin films.," *J. Am. Chem. Soc.*, vol. 133, no. 25, pp. 9834-43, Jun. 2011.
- [153] M. W. Meyer, K. L. Larson, R. C. Mahadevapuram, M. D. Lesoine, J. A. Carr, S. Chaudhary, and E. A. Smith, "Scanning angle Raman spectroscopy of poly(3-hexylthiophene)-based films on indium tin oxide, gold, and sapphire surfaces.," *ACS Appl. Mater. Interfaces*, vol. 5, no. 17, pp. 8686-93, Sep. 2013.
- [154] "Raman Data and Analysis - Raman Bands - bands.pdf." [Online]. Available: <http://www.horiba.com/fileadmin/uploads/Scientific/Documents/Raman/bands.pdf>. [Accessed: 10-Jul-2015].
- [155] Saint-Gobain, "YAG(Ce) Yttrium Aluminum Garnet Scintillator Material." [Online]. Available: <http://www.crystals.saint-gobain.com/uploadedFiles/SG-Crystals/Documents/YAG Data Sheet.pdf>. [Accessed: 08-Oct-2015].
- [156] D. Cavouras, I. Kandarakis, D. Nikolopoulos, I. Kalatzis, G. Kagadis, N. Kalivas, A. Episkopakis, D. Linardatos, M. Roussou, E. Nirgianaki, D. Margetis, I. Valais, I. Sianoudis, K. Kourkoutas, N. Dimitropoulos, A. Louizi, C. Nomicos, and G. Panayiotakis, "Light emission efficiency and imaging performance of Y3Al5O12: Ce (YAG: Ce) powder screens under diagnostic radiology conditions," *Appl. Phys. B*, vol. 80, no. 7, pp. 923-933, Apr. 2005.
- [157] Hilger Crystals, "Materials." [Online]. Available: <http://hilger-crystals.co.uk/materials-index/index-bismuth-germanate.html>. [Accessed: 08-Oct-2015].
- [158] Saint-Gobain, "CsI(Tl), CsI(Na) Cesium Iodide Scintillator Material." [Online]. Available: [http://www.crystals.saint-gobain.com/uploadedFiles/SG-Crystals/Documents/CsI\(Tl\) and \(Na\) data sheet.pdf](http://www.crystals.saint-gobain.com/uploadedFiles/SG-Crystals/Documents/CsI(Tl) and (Na) data sheet.pdf). [Accessed: 08-Oct-2015].
- [159] Phosphor Technology, "Phosphor Technology Scintillation Phosphors." [Online]. Available: <http://www.phosphor-technology.com/products/scint.htm>. [Accessed: 08-Oct-2015].
- [160] M. Ljungberg and S.-E. Strand, "A Monte Carlo program for the simulation of scintillation camera characteristics," *Comput. Methods Programs Biomed.*, vol. 29, no. 4, pp. 257-272, Aug. 1989.
- [161] S. Yao, Z. Song, X. Wang, H. San, and Y. Yu, "Design and simulation of betavoltaic battery using large-grain polysilicon," *Appl. Radiat. Isot.*, vol. 70, no. 10, pp. 2388-2394, Oct. 2012.
- [162] D. Drouin, "CASINO: Monte Carlo Simulation of electron trajectory in solids." [Online]. Available: <http://www.gel.usherbrooke.ca/casino/index.html>. [Accessed: 08-Apr-2015].

- [163] D. Drouin, A. R. Couture, D. Joly, X. Tastet, V. Aimez, and R. Gauvin, "CASINO V2.42—A Fast and Easy-to-use Modeling Tool for Scanning Electron Microscopy and Microanalysis Users," *Scanning*, vol. 29, no. 3, pp. 92–101, May 2007.
- [164] Xiaoming Ling, D. Fan, and Fan Yang, "A study of the organization and performance of thermally evaporated aluminum reflector for solar energy system," in *2010 The 2nd Conference on Environmental Science and Information Application Technology*, 2010, vol. 3, pp. 558–561.
- [165] Sapa, "The properties of aluminium - Aluminium Design." [Online]. Available: <http://www.aluminiumdesign.net/why-aluminium/properties-of-aluminium/>. [Accessed: 12-Oct-2015].
- [166] G. HASS and J. E. WAYLONIS, "Optical Constants and Reflectance and Transmittance of Evaporated Aluminum in the Visible and Ultraviolet," *J. Opt. Soc. Am.*, vol. 51, no. 7, p. 719, Jul. 1961.
- [167] L. Dou, J. You, J. Yang, C.-C. Chen, Y. He, S. Murase, T. Moriarty, K. Emery, G. Li, and Y. Yang, "Tandem polymer solar cells featuring a spectrally matched low-bandgap polymer," *Nat. Photonics*, vol. 6, no. 3, pp. 180–185, Mar. 2012.
- [168] "Model 2400 Series SourceMeter User's Manual - Keithley2400Manual.pdf." [Online]. Available: <http://research.physics.illinois.edu/bezryadin/labprotocol/Keithley2400Manual.pdf>. [Accessed: 27-Feb-2016].
- [169] "6487-900-01 (B - Jan 2003).book - 6485-6487-m.pdf." [Online]. Available: <http://www.testequity.com/documents/pdf/keithley/manuals/6485-6487-m.pdf>. [Accessed: 27-Feb-2016].